The X-ray Point Source Population of Spiral and Star-forming Galaxies

Roy E. Kilgard

Supervisors:

Martin Ward

Robert Warwick

Thesis to be submitted for the degree of
Doctor of Philosophy
at the University of Leicester.

X-ray & Observational Astronomy Group
Department of Physics and Astronomy
University of Leicester

August 16, 2007

Declaration

I hereby declare that no part of this thesis has been previously submitted to this or any other University as part of the requirement for a higher degree. The work described herein was conducted by me except for contributions from colleagues as acknowledged here: Parts of chapters 4, 5 and 6 were published in Kilgard et al. (2005 ApJS, 159, 214). Much of chapter 7 was published in Kilgard et al. (2002 ApJ, 573, 138) in collaboration with Phil Kaaret. The modeling of the ultraluminous X-ray source M74 X-1 was done in collaboration with Miriam Krauss, and published in Krauss et al. (2005 ApJ, 630, 228). The development of the colour-classification scheme for X-ray sources was done in collaboration with Andrea Prestwich, with parts published in Prestwich et al. (2003 ApJ, 595, 719). In addition, material presented herein was also presented at numerous academic conferences by myself and the above collaborators.

Roy E. Kilgard,
July, 2007

Roy E. Kilgard

The X-ray Point Source Population of Spiral and Star-forming Galaxies

Abstract

In this thesis, I study a sample of 11 nearby "normal" spiral galaxies and one starburst galaxy with the *Chandra X-ray Observatory* and supporting ground-based telescopes, with particular emphasis on the characterisation of the discrete X-ray point source population.

Emission from discrete point sources dominates the X-ray flux from spiral galaxies. This survey spans the Hubble sequence for spirals and, hence, a range in star formation, allowing insights into the X-ray source population of many diverse systems. The inclusion of M82, the prototypical starburst galaxy in the nearby universe, allows for comparison with a system at the extreme of star formation.

Presented here is a detailed catalogue of the source population of these galaxies. For each source, I have derived fluxes, luminosities, X-ray colours, and variability properties. I have also searched for optical and radio counterparts. For the most luminous sources, detailed spectral and temporal analyses have been performed.

For galaxies as a whole, I have examined X-ray point source luminosity functions and how these relate to star formation of those galaxies. I have also devised a strategy for initial classification of X-ray sources based upon their position within a colour-colour diagram. The luminosity function analysis has then been performed on each class of sources, showing 1) that the method of classification appears to be robust to the first order, and 2) that the old and young (i.e. low-mass X-ray binary and high-mass X-ray binary) populations can be segregated, providing insight into the star formation history of each individual galaxy.

I have also studied the environments in which the sources fall within their host galaxies and what this can tell us about the nature of the sources. I have included a discussion of the enigmatic ultraluminous X-ray sources (ULXs), which may be candidates for intermediate mass (100-10,000 $M_{\odot}$) black holes.

CONTENTS

LIST OF FIGURES

LIST OF TABLES

Chapter 1

X-rays from Galaxies–A Brief History

In the beginning the Universe was created. This has made a lot of people very angry and been widely regarded as a bad move.

Douglas Adams

1.1 The Rocket Years

The rocket flights of the early 1960s established that there were extraordinary "X-ray stars" in our galaxy. This discovery was remarkable because the existence of objects with such extreme X-ray luminosities had not been predicted. Thus began a whole new branch of observational astronomy: high energy astronomy. Herein I will briefly discuss some of the highlights of this young branch of astronomy. In particular, I will focus on the science topics of most relevance to this thesis. A more complete chronology of events is located in appendix 9.

In 1968-1970, two rocket flights detected X-ray emission from the Large and Small Magellanic Clouds (LMC, SMC). The luminosity of the LMC was 6×10^{38} erg s^{-1} with two strong emission regions, one of which was close to the star cluster 30 Doradus. The SMC has an X-ray luminosity of 5×10^{38} erg s^{-1}. It seemed likely that the X-ray emission from the Magellanic clouds was similar to the Milky Way in that it was dominated by a few discrete sources with luminosities close to 10^{38} erg s^{-1} (Price et al., 1971).

Confirmation that this was indeed the case came from a remarkable series of observations with the *Uhuru* satellite in the early 1970s. *Uhuru* detected three discrete sources in the LMC (dubbed LMC X-1, X-2, and X-3). It also detected periodic variations in the flux of the source SMC X-1. Even more importantly, an optical counterpart to SMC X-1 with the same period was discovered. The period discovered was an eclipse period, which allowed for orbital parameters and a mass function to be obtained. Spectroscopic identification of the companion star allowed for a mass determination. Hence, a mass estimate could be obtained for the compact object. The extremely high X-ray luminosity for such a compact object led to the conclusion that these "X-ray stars" must be accretion-powered, radiating close to the Eddington limit for a $1.4\ \mathrm{M}_{\odot}$ neutron star. In addition to the periodic variability, SMC X-1 was identified as the first X-ray pulsar in 1970. The rapid variability of pulsars was theorized to be due to rapid rotation of the optically invisible object, and such high rotations could only be achieved by a very small (compact) object–a neutron star or black hole.

In 1973, Bowyer et al. (1974) detected M31 in X-rays. Although this was not an imaging observation, the X-ray luminosity and integrated spectrum was similar to that of the Milky Way. Thus by the mid-1970s, a clear picture was emerging: the X-ray emission of our galaxy, the Magellanic clouds, and M31 was dominated by a few bright, discrete X-ray point sources, and that these sources were almost certainly all X-ray binaries.

1.2 The *Einstein* Observatory

By the mid-1970s, it was clear that the burgeoning field of X-ray astronomy needed a long-term space-based telescope with high spatial resolution to avoid the problems of source confusion that were plaguing the field. The *Einstein* Observatory was launched in 1978. Prior to its launch, only 5 non-AGN, non-Syefert (that is to say, "normal") galaxies had been detected in X-rays: M31, M82, the Miky Way, and the Large and Small Magellanic Clouds.

In the late 1970s and early 1980s, X-ray eclipses (1.4 day), flux modulations (30.5 day), and pulsations (13.5s) were all observed in the source LMC X-4, thus confirming it as an X-ray binary. In addition, bursts in excess of $10^{39}\ \mathrm{erg\ s^{-1}}$ were seen in LMC X-5, and an outburst recurrence scale of 16.7 days is determined (with not all predicted outbursts occuring). Shortly thereafter, a B star counterpart to LMC X-5 was found. From the period and companion identification, LMC X-5 was determined to be

a neutron star.

Einstein allowed for the first true surveys of external galaxies in the X-ray. The *Einstein* survey of M31 revealed 69 discrete X-ray sources. Many of these sources are within the bulge, implying that they are largely Population II (low-mass X-ray binaries, LMXBs). In addition, many of the sources lie in globular clusters, contrary to the bright X-ray sources in the Milky Way.

Surveys of the Magellanic clouds with *Einstein* allowed for the detection of optical counterparts to many X-ray sources, most of which are X-ray binaries (XRBs). These surveys also uncovered a new class of soft sources for which counterparts cannot be found. *Einstein* also observed the first extra-galactic supernova remnant, N132D in the LMC, and determined that its spectrum is softer than that of XRBs.

For the first time, galaxies beyond the local group could be studied in detail with *Einstein*. In these galaxies, both discrete point sources and diffuse emission are observed. The first highly luminous, non-nuclear point sources are also observed. These sources exceed the Eddington luminosity for pure hydrogen accretion onto a neutron star, and are likely black holes.

In 1984, Cowley et al. (1984) determine that LMC X-3 is a black hole with mass between 7 and 13 $\mathrm{M}_{\odot}$. This is the first confirmed detection of an extragalactic stellar-mass black hole. Around the same time, it is demonstrated that there is a strong correlation correlation between L_X and L_B in normal galaxies (where L_X is the X-ray luminosity and L_B the B-band optical luminosity), indicating that the X-ray population is predominantly Population I objects associated with young star formation. Discrete source luminosity functions are discussed for the first time and are plotted as cumulative functions with $\mathrm{N} > \mathrm{L_X vs. L_X}$. High-mass X-ray binaries (HMXBs) dominate the high luminosity end of the luminosity function of galaxies and contribute the most to the total X-ray luminosity.

Towards the end of the *Einstein* era, the first X-ray point source luminosity functions (LFs or XLFs) are presented. They are well fit by power-laws and it is determined that there is a difference between the power-law slope for different galaxies: the LF of M101 appears flatter than that of M31, suggesting that M101 contains a population of HMXBs on top of an M31-like population of LMXBs.

1.3 *ROSAT* and *ASCA*

The 1990s brought a new round of X-ray telescopes, first with the German and U.S. *ROSAT*, then the Japanese satellite *ASCA*. While *Einstein* can be seen as the true predecessor to *Chandra*, due primarily to its high spatial resolution, *ROSAT* and *ASCA* also made important discoveries in X-ray galaxy observations.

ROSAT allowed for a theory to be formulated about the "supersoft sources" (SSSs) in the LMC. It is postulated that the sources are binaries with white dwarf primaries accreting matter at a super-Eddington rate. The X-ray emission would result from nuclear burning directly on the surface of the white dwarf. This would explain the high luminosity, extreme variability, and lack of observed optical counterparts to these sources. This theory is stengthened when ionization nebulae are found associated with many SSSs: the nebulae may be planetary nebulae, since one would expect to see supernova remnants (SNRs) around compact objects from more massive parent stars.

Also in the mid-90s, the term "ultra-luminous X-ray source" (ULX) is used to describe a source with $L_x > 10^{39}\ \mathrm{erg\ s^{-1}}$. The *ASCA* results for ULXs show that the source spectra are well fit by cool disc blackbody models. A well-known proportionality relation exists between the disc temperature and the radius of the inner accretion disc–the higher the temperature, the closer the accretion disc and thus the lower mass the compact object ($L_X \propto \sigma T^4$, Mitsuda et al. (1984)). Thus, a cool disc temperature implies a large inner accretion disc radius and a more massive compact object. The sources may then be black holes with $M > 50\ \mathrm{M_\odot}$. Roberts & Warwick (2000) show that there are a large number of ULXs in nearby galaxies. Confusing the issue, further results from *ASCA* show that many ULXs also have high T_{in}, incomatible with the theory that the sources are black holes with very high masses. It is suggested that a Kerr (rotating) black hole can explain both these properties, and that the sources may be similar to Galactic microquasars like GRS 1915+105 and GRO J1655-40.

1.4 The Story thus far...

Before the launch of *Chandra*, X-ray sources in galaxies were determined to be primarily X-ray binaries with compact objects accreting matter from more normal stars. These discoveries were made through

orbital modulation and pulsations as well as spectral modeling of disc emission. In addition, supersoft sources were modeled as white dwarfs accreting at high rates (near-Eddington to super-Eddington) and ULXs were theorized as black holes with masses from 10 to 100,000 $M_{\odot}$.

However, little was known about the fractions of LMXBs, HMXBs, and SNRs and how (or if) these fractions change with galaxy morphology, star-formation rate, star-formation history, stellar environment, etc. The fraction of discrete sources compared with hot gas was also poorly understood. Largely this was a problem of angular resolution and effective area. Point source confusion prevented study of the discrete sources in all but the most nearby local group galaxies. Low effective area prevented spectral study of sources beyond a few hundred kiloparsecs, even if the discrete sources could be resolved. Though *ROSAT* and *ASCA* were making valuable contributions to the field, the need for a telescope with high angular resolution and throughput had become obvious. The answers to all of these questions are extremely important for understanding star-formation both in the Milky Way and in external galaxies. These high resolution X-ray observations can place constraints on star formation models. *Chandra* was needed if any real progress was to be made in this important area of astrophysics.

Chapter 2

The *Chandra* X-ray Observatory

TELESCOPE, n. A device having a relation to the eye similar to that of the telephone to the ear, enabling distant objects to plague us with a multitude of needless details. Luckily it is unprovided with a bell summoning us to the sacrifice.

Ambrose Bierce

The *Chandra* X-ray Observatory is the third mission of four in the *NASA* Great Observatories program, whose aim was to cover many different wavelengths with simultaneous space-based observatories. The other missions are the *Hubble Space Telescope*, the *Compton Gamma Ray Observatory* (now de-orbited), and the *Spitzer* Space Telescope(formerly *SIRTF*). *Chandra* was launched on 23 July, 1999 by *NASA*'s space shuttle Columbia and placed into a highly elliptical orbit by an inertial upper stage booster. *Chandra* features two primary focal plane instruments: *ACIS*, the Advanced CCD Imaging Spectrometer (see section 2.1.1), and *HRC*, the High Resolution Camera (see section 2.1.2).

Chandra is in a highly elliptical 64 hour orbit with perigee at 16,000km and apogee at 160,000km. This allows for a maximum amount of time above the radiation belts for continuous observing of up to 55 hours and overall observing efficiency of around 70%.

The most outstanding feature of *Chandra* is the HRMA, or mirror assembly. The Wolter type grazing-incidence reflection mirrors (see figure 2.2) are the most precisely polished mirrors ever constructed. The *Chandra* HRMA allows for resolution of objects smaller than $0.5''$. Combined with the excellent

Figure 2.1 *Chandra* (artists impression) from *Chandra Proposer's Observatory Guide, v6.0.*

aspect solution of *Chandra*, source positions can be determined with absolute astrometric accuracy to better than $0.3''$, which is comparable to that achieved with the *Hubble Space Telescope*.

2.1 *Chandra* Instruments

In this thesis, I utilize data from both the *ACIS* and *HRC* instruments. Here I discuss the main properties of these instruments. Each instrument has two principal components: an imaging detector and an array intended for reading out dispersed spectra from the two sets of onboard transmission gratings. The science instrument module (SIM), which contains both detectors, can move along both the X- and Z-axes for focus and instrument selection (see figure 2.3).

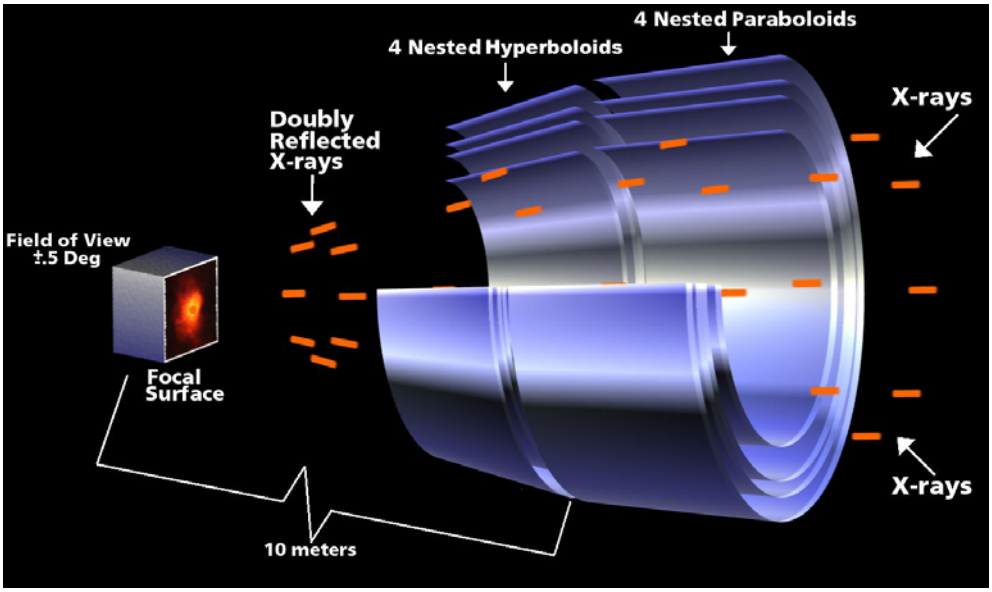

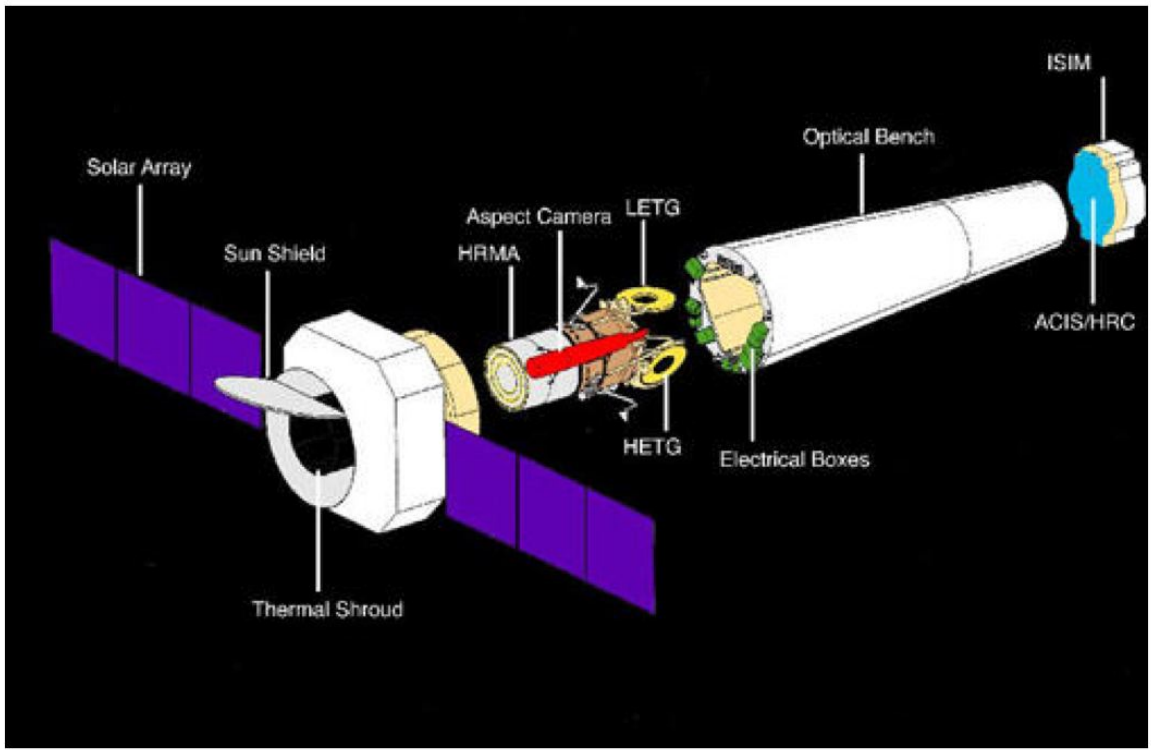

Figure 2.3 Schematic of the *Chandra* observatory. with parts labeled.

2.1.1 *ACIS*: the Advanced CCD Imaging Spectrometer

The *ACIS* instrument consists of two separate charge-coupled device (CCD) arrays: the *ACIS-I*, intended for imaging, and the *ACIS-S*, intended for dispersed grating spectroscopy (see figure 2.4). Each array is made of 1024×1024 pixel CCDs; four arranged in a 2×2 grid (*ACIS-I*), and 6 in a long array (*ACIS-S*). Any combination of up to 6 CCDs may be read out simultaneously. In imaging mode, the default is to read out chips I0-I3 and S2-S3 for *ACIS-I* and chips I2-I3 and S1-S4 for *ACIS-S*. The *ACIS* pixels are $\sim 0.49'' \times 0.49''$, slightly larger than the on-axis point-spread function (PSF) of the HRMA. The PSF degrades with off-axis angle however, due both to the differentiation of CCD layout from the ideal focal surface and to the intrinsic increase in PSF with off-axis angle due to mirror aberrations (It should be noted that the latter is energy dependent (for further discussion, see the *Chandra* Proposers' Observatory Guide, POG (2003), section 4.2.3).

The CCDs have intrinsic energy resolution determined by measuring the pulse height amplitude of the charge displaced by each incident photon. The calibrated energy range is $\sim 0.3 - 10$keV, with resolution on the order of ~ 100eV at 1keV.

The *ACIS* detector has two CCDs which are back-illuminated (BI) and 8 that are front-illuminated (FI). The BI CCDs (chips S1 and S3) have had a treatment applied to the back side of the chip to remove insensitive, bulk silicon and leave the photo-sensitive region exposed. These chips are then installed with the back of the chip facing the optical bench. This configuration allows for a much higher sensitivity at low photon energies as compared with the FI CCDs, since less X-rays are absorbed or scattered by the detector material before striking the photo-sensitive surface. Most of the data discussed in this thesis comes from the *ACIS* S3 chip, though some data makes use of the FI CCDs. As time has progressed, the *ACIS* detector has developed a contaminant build-up on the optical blocking filter. This contaminant severely effects the low-energy effective area of ACIS; however, since most of the data discussed here was taken early in the *Chandra* mission, the contamination presents minimal difficulty for our work.

Each *ACIS* CCD has an active region which is exposed to incident photons and an inactive frame store region, which is shielded. After a single exposure (nominally 3.2s for the full chip), the data is transferred to the frame store in 41ms. The next exposure then begins and the data is transferred from the frame store to a processor that records the position and amplitude of the event along with

information from the surrounding pixels (used for grading, see below), and passes the data into the telemetry stream.

One can choose to read out a portion of an *ACIS* chip or chips in a subarray. Since the exposure time is largely dictated by the processing time of events from the frame store, using a subarray allows one to reduce the frame time, and hence increase the timing resolution, of the data. The frame time is given by the following equation:

$$T(msec) = 41 \times m + 2.84 \times n + 5.2 + 0.040 \times (m \times q)$$

where m is the number of active CCDs, n is the number of rows in the subarray, and q is the number of rows separating the subarray from the frame store region.

During onboard processing, each *ACIS* event is assigned a grade using the *ASCA* grading scheme. This method examines the information in the 3×3 pixel region surrounding the event and utilizes that information to determine whether the event is a real incident photon, a cosmic ray, detector noise, etc. For further details on grading, see the POG (2003). For each of the *ACIS* modes, one can also choose graded, faint, or very faint telemetry format. The difference between these formats is in what is telemetered to the ground. In very faint mode, a 5×5 event island is telemetered to the ground rather than the standard 3×3. This allows the expert user to perform further grade rejection in post-processing but has the disadvantage of requiring more bits of data and therefore cannot be used for very bright sources without risking a saturation of the telemetry stream. Graded mode only transfers the event grade and not the 3×3 island, so events cannot be regraded on the ground. Graded mode allows for 375.0 events/sec, faint mode 170.2 events/sec, and very faint mode allows only 68.8 events/sec. Nominal operating mode for *ACIS* is TE/Faint mode.

ACIS also has a few problems that diverge from optimal operation. These are: pileup, increased charge transfer inefficiency, and contamination. Each will be discussed briefly, as each impacts some of the data to be discussed.

- Pileup occurs when two or more photons are detected in a single pixel during a single frame. The detector cannot register each as a separate event, but rather registers the sum of the charge displaced by each event, roughly equal to the sum of the incident photon energies. This naturally has an impact on the spectrum of the source. The more "piled" photons there are, the harder the

spectrum appears. Pileup is discussed more fully in chapter 5.

- The FI CCDs on *ACIS* have had an increase in the charge transfer inefficiency (CTI) since launch, resulting in a loss of energy resolution. This CTI increase was due to radiation damage caused by low energy protons, encountered when *Chandra* was passing through the Earth's radiation belts. The protons were reflected off the X-ray telescope and onto the focal plane. Once this degradation was discovered, procedures were changed to remove *ACIS* from the focal plane whilst passing through the radiation zone. The BI CCDs were not affected by the proton flux. A correction for the energy resolution changes has been implemented in the standard data processing and all data discussed herein have been reprocessed to perform this correction.

- Since the *ACIS* CCDs are sensitive to both optical and X-ray photons, optical blocking filters are positioned between the CCDs and the mirrors. Observations of calibration sources have determined that the *ACIS* effective area has been slowly but steadily decreasing since launch. This has now been attributed to a buildup of contamination on the outside (opposite the detector) of the optical blocking filters. The effect is seen primarily at event energies below 1keV. There are two models for the contamination available to users: one from the *Chandra* Science Center, and the other from Pennsylvania State University, the co-developers of the *ACIS* CCDs. The *Chandra* Science Center model was chosen for this analysis and has been applied to all data discussed herein (see section 4.1).

2.1.2 *HRC*: the High Resolution Camera

The High Resolution Camera, *HRC*, is a microchannel plate (MCP) detector with two arrays: an imaging array (*HRC-I*) and an array for reading out dispersed spectra from the low energy gratings (*HRC-S*). All of the *HRC* data presented herein was taken using the *HRC-I*, so the *HRC-S* will not be discussed further. The *HRC-I* is a wide-field imager, providing imaging over a field $\sim 30' \times 30'$. Although the *HRC* records the pulse-height amplitude (PHA) of events, the actual energy resolution of the detector is extremely poor and thus not useful for spectral analysis. A diagram of the *HRC* can be seen in figure 2.5.

In a MCP detector, an incident X-ray photon strikes a charged surface (in this case, cesium iodine), producing a cloud of electrons which strikes a charge detector. The position of the photon is then

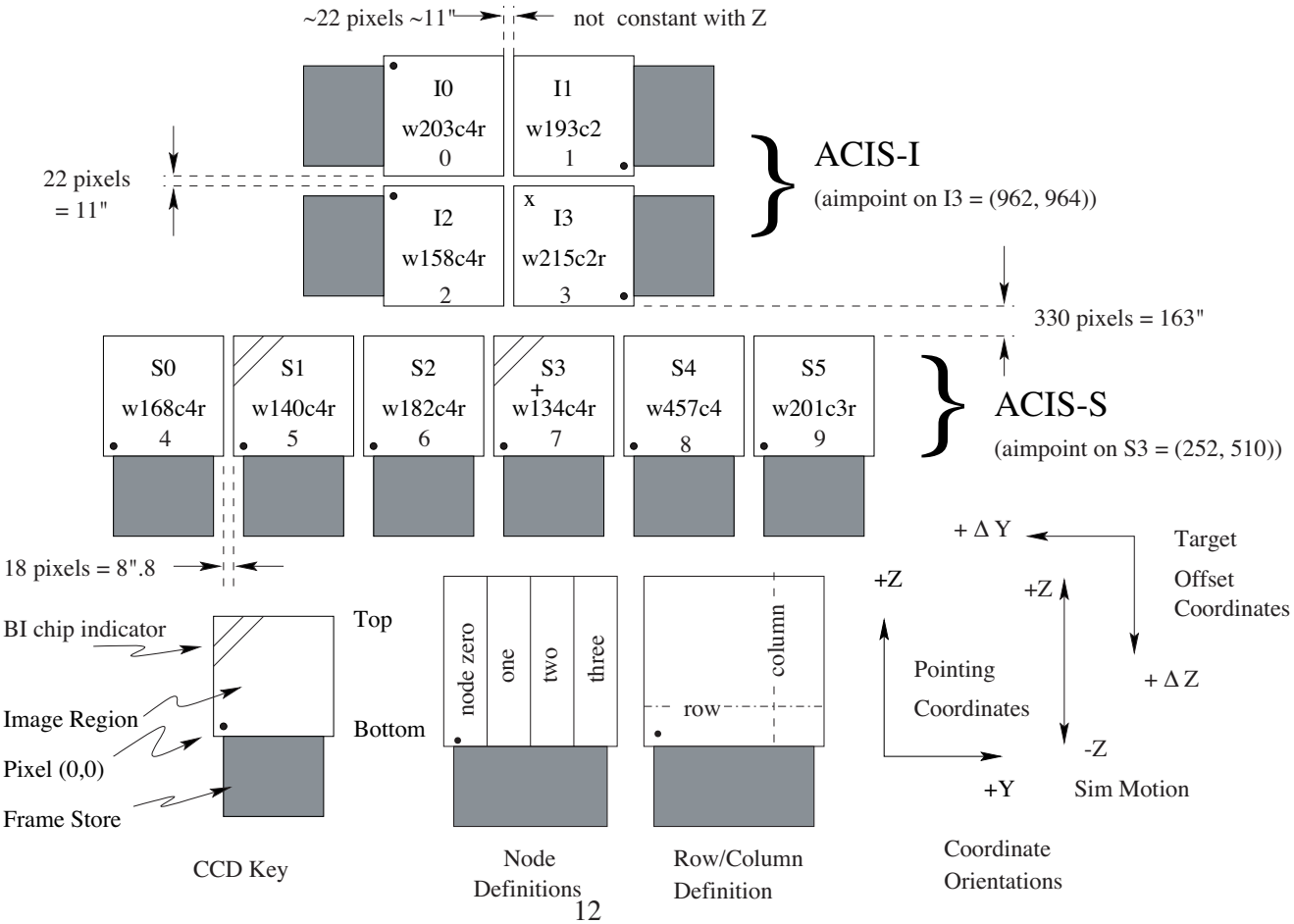

Figure 2.4 Diagram of the *ACIS* instrument. At top is the *ACIS-I* array and at bottom the *ACIS-S*. The X and + symbols denote the nominal aimpoints of each array in imaging mode. From POG (2003), Figure 6.1.

determined by measuring the centroid of the charge cloud. Thus, the spatial resolution of the detector is determined by the size of the charge detector rather than the grid of the MCP. The *HRC* detector has spatial resolution of $\sim 0.13''$, which is considerably superior to *ACIS* and is the only instrument onboard *Chandra* to fully take advantage of the small PSF of the mirrors.

Like *ACIS*, the *HRC* resolution degrades with off-axis angle for the same reasons: deviation from the ideal focal plane and HRMA aberrations.

The *HRC* was intended to have high timing resolution of $\sim 16\mu s$ but a problem in-orbit has been found that limits this timing resolution to the mean time between events. The *HRC* instrument background is 250-300 events/sec, so the timing resolution is typically on the order of 4ms.

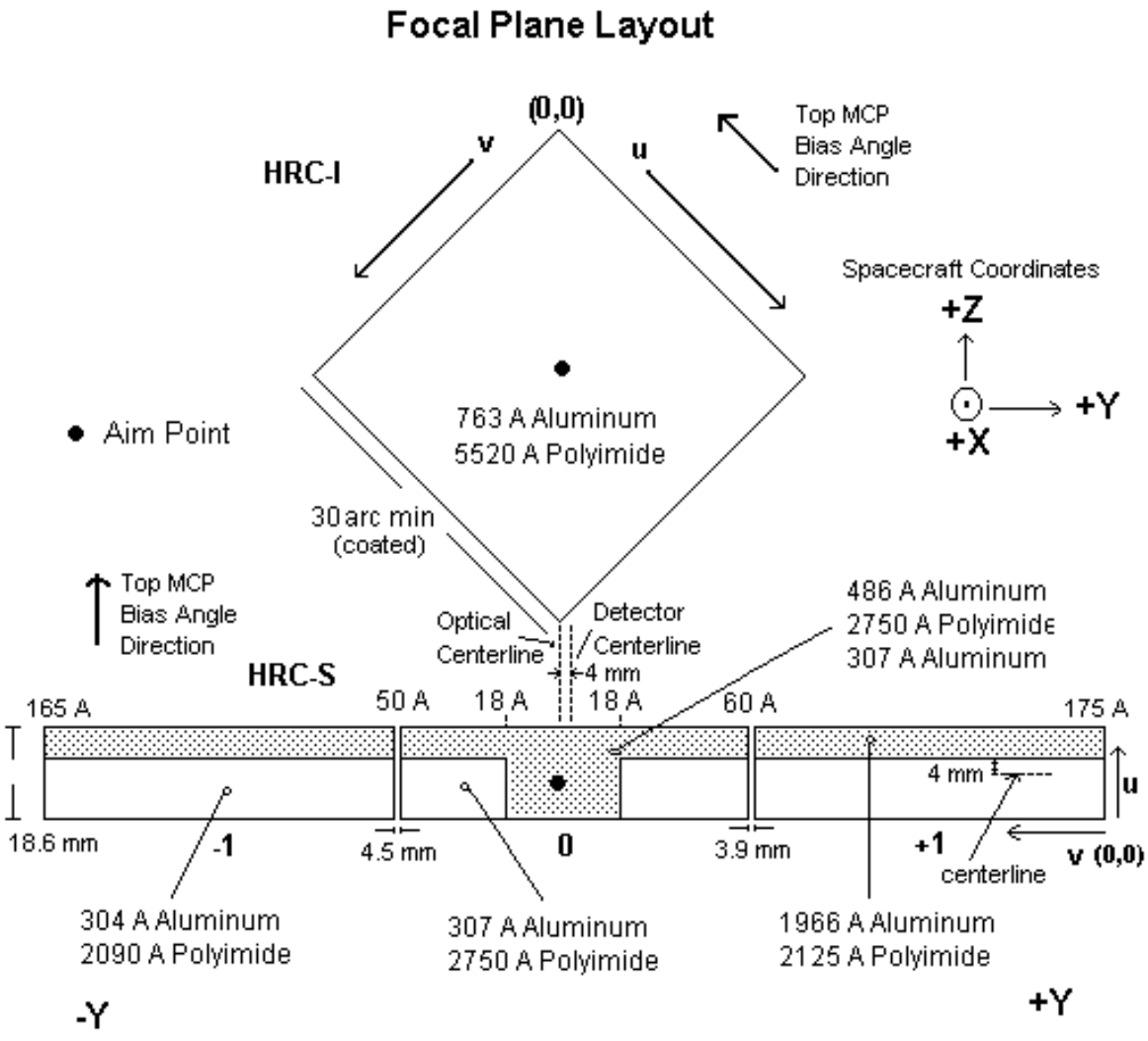

Figure 2.5 Layout of the *HRC* focal plane. Figure 7.2 from POG (2003).

Chapter 3

Data Overview and Science Background

> There is something fascinating about science. One gets such wholesale returns of conjecture out of such a trifling investment of fact.
>
> Mark Twain

3.1 Data Introduction

In this thesis, I examine the properties of X-ray sources in spiral and star-forming galaxies. In particular, I relate the characteristics of X-ray sources–such as X-ray luminosity, variability, and colour–to what is known about the global star formation properties of the host galaxies. The observations in this thesis come from two different projects: a *Chandra* large observing proposal in observing cycle 2 to study X-ray emission from normal galaxies, and a series of *Chandra* observations of the prototypical starburst galaxy M82.

3.1.1 Nearby Spiral Galaxies

This work proposes to take advantage of the unique spectro-imaging capabilites of *Chandra* to study nearby galaxies in the X-ray in unprecedented detail. Prior to Chandra, it was known that the X-ray emission from normal galaxies is composed of two distinct components: diffuse emission from hot

gas and a discrete source component which dominates the integrated emission in spiral galaxies. As previously discussed, the brightest sources were known to be largely a mix of accreting binaries and supernova remnants. However, many questions remained unanswered. What fraction of the sources were binaries vs. SNR? What kinds of binaries were present and in what fractions: LMXBs, HMXBs, white dwarf accretors, etc.? How do these properties change with star formation history or with metallicity? Are there differences in the source populations of galactic bulges and discs? How does the source population of normal spirals compare with that of starbursts? Since starbursts are at the extreme end of the star-formation sequence, are they a natural extension of the Hubble tuning fork beyond Sd galaxies, or should Hubble class be removed from the picture entirely?

Our sample is shown in Table 4.1. The normal spiral component was derived from the *Nearby Galaxies Catalog*, and consists of galaxies spanning the Hubble sequence for spirals (types 0-7), inclinations $i < 35\,\mathrm{deg}$, distances $R \lesssim 10Mpc$, and low galactic extinction ($N_H < 5 \times 10^{20} cm^{-2}$). Note that 2 of the galaxies, NGC 1291 and NGC 4314, have distances slightly larger than 10 Mpc, but they were felt to be strong candidates for other reasons; NGC 1291 (an S0 galaxy) because of the already present archival data and the sparsity of nearby early-type spirals, and NGC 4314 because of the large number of detailed optical studies available in the literature. In addition, NGC 278 has an $N_H = 1.29 \times 10^{21} cm^{-2}$, but we relaxed this requirement because the only other Sb galaxy with $i < 25\,\mathrm{deg}$ within 15 Mpc in the *Nearby Galaxies Catalog* is NGC 1068, which has an extremely luminous Seyfert nucleus. These galaxies also have a relatively narrow range in L_B to distinguish trends due to luminosity from trends due to morphology. We chose to study face-on galaxies for a number of reasons: 1) we minimize effects of intrinsic galactic absorption on soft sources, 2) we minimize source confusion by effectively "spreading the sources out" across the disc, 3) we improve the ability to identify multi-wavelength counterparts by minimizing confusion due to dust. At the distance of our sample galaxies, we are able to locate sources to an accuracy $\lesssim$ 50pc. This allows us, for example, to place a binary source within a giant HII region in a spiral arm.

3.1.2 The Prototypical Starburst Galaxy M82

Starburst galaxies are galaxies with extraordinarily high rates of star formation. This star formation occurs when the density and rate of supernovae are so high that the expanding remnants collide and merge before they have time to lose their energy radiatively. The resulting shocks create a hot (typically

a few keV), low-density, high-pressure plasma (Chevalier & Clegg (1985); Strickland (2004)). This expanding plasma forms a bipolar outflow above and below the plane of the galaxy–a superwind. M82 is the prototypical starburst galaxy in the nearby universe (Rieke et al. (1980)). It is an irregular galaxy located at a distance of $3.9 \pm 0.3 Mpc$ (Sakai & Madore (1999)) in the M81 system, which also includes the dwarf galaxy NGC 3077 and numerous smaller galaxies. M82 has extensive evidence for violent star formation throughout the electromagnetic spectrum (see, e.g., de Grijs et al. (2001); Gallagher & Smith (1999)). 21 cm radio observations have revealed HI loops connecting M81, M82 and NGC 3077, triggering massive star formation not just in M82 but also in the tidal interaction regions (Feldmeier et al. (2003); Durrell et al. (2003); DeCesar et al. (2003)). This demonstrated that the likely cause of the extremely high star-formation is due to interaction in the system and N-body simulations have presented a likely interaction scenario of the system (Yun et al. (1993)).

M82 has been extensively studied in X-ray, with the first high-resolution X-ray images coming from the *Einstein* observatory (Watson et al. (1984)). It was these first observations of M82 with *Einstein* that discovered the now famous ULX in M82, henceforth M82 X-1. Further observations with *ROSAT* and *ASCA* (Collura et al. (1994) and Ptak & Griffiths (1999)) demonstrated the source to be both extremely luminous and highly variable, leading to the conclusion (by Ptak & Griffiths (1999)) that M82 X-1 is an accreting black hole with mass in excess of 460 $\mathrm{M}_{\odot}$. Due to the confusion caused by both the number density of luminous sources near the nucleus of M82 and the presence of X-ray emission due to hot gas from the starburst, the overall point source population of M82 remained poorly studied prior to the launch of *Chandra*.

Since M82 is very nearby, our data allow detailed spectra/temporal analysis of the most luminous X-ray sources for the first time. In addition, the multi-epoch observations allow for analysis of the spectral/temporal evolution of the entire source population. M82 is also one of the most observed nearby galaxies at all wavelengths; we therefore get the multi-wavelength data "for free".

3.2 Detailed Science Goals

3.2.1 Identify Point Sources

Individual point sources dominate the X-ray emission in normal spiral galaxies. We have identified ~ 900 sources in our 11 normal galaxies and ~ 80 source in M82. We have classified many of these sources by X-ray luminosity, spectra, colours, and variability characteristics. In addition, we have found multi-wavelength counterparts to many sources, allowing further classification.

3.2.2 Ultraluminous X-ray Sources

In our galaxy sample, there are 18 of the enigmatic ultraluminous X-ray sources (ULXs). ULXs are point sources whose luminosities exceed, often by an order of magnitude or more, the Eddington luminosity for a $10\ \mathrm{M}_{\odot}$ black hole ($L_X > 10^{39}\ \mathrm{erg\,s^{-1}}$). These objects may be similar to Galactic microquasars or other Galactic binary sources, with instantaneous super-Eddington luminosities or apparent super-Eddington luminosities; they may be intermediate mass black holes (IMBH), with masses $> 100\ \mathrm{M}_{\odot}$; or they may be a new class of objects. Studies have shown that there are numerous ULXs in starburst galaxies such as the Antennae and NGC 3256 (see Fabbiano et al. (2001); Lira et al. (2002)), with fewer in normal spirals. Our sample allows us to study the sources in normal spirals and compare them with those found in starburst galaxies.

3.2.3 Luminosity Functions

Understanding the discrete source luminosity function (LF) is a key to a number of important questions: How much of the diffuse emission in galaxies is due to hot gas and how much to unresolved sources? Does this vary from galaxy to galaxy? Does the LF slope change with star formation rates? Does the LF slope differ for bulge and disc sources? Are there breaks in the LF due to episodic star formation or due to the separation between neutron star and black hole binaries (the so-called Eddington break)? Can we derive information about the star formation history of galaxies from the LF? Is there a universal LF for all galaxies? We will attempt to answer these questions.

3.3 Science Introduction

Of the 824 sources in the normal spiral galaxies discussed, 64 sources have sufficient counts to investigate both the spectra and the short-term variability of the sources in detail. These sources represent the high luminosity end of the normal galaxy luminosity function, above $\sim 2 \times 10^{38}$ erg s^{-1}. Naively, based entirely on X-ray luminosity, one would assume these sources are black hole binaries, as the luminosities are greater than pure Eddington accretion onto a 1.4 M$_{\odot}$ neutron star. As we shall see, however, that is not necessarily the case.

In order to interpret the spectral and temporal characteristics of these sources, we must first discuss the spectra and variability of Galactic X-ray binaries and how those sources might look if located within our target galaxies. In section 3.4 we discuss general properties of X-ray binaries. In section 3.5, we discuss a method to degrade the spectra of Galactic sources to determine how they would appear if in our target galaxies. In section 5.1 we discuss the spectra of our sources and what they tell us about the nature of the sources.

3.4 X-ray Binary Overview

X-ray binaries are binary star systems in which a compact object, either white dwarf, neutron star, or black hole, accretes matter from a normal main sequence or post-main sequence star. X-ray binaries are broadly divided into two classes based on the mass of the companion star: low-mass X-ray binaries (LMXBs) and high-mass X-ray binaries (HMXBs). This method of classification is immediately advantageous as the spectral type of the mass donor star can be easily determined for XRBs with identified counterparts. We will discuss these two types in turn.

3.4.1 High Mass X-ray Binaries

High mass X-ray binaries are those systems in which a high-mass, early-type star transfers material onto a compact object. The compact object can be either a neutron star or black hole. In these systems, powerful stellar winds from the mass-donor deliver material to the compact object. The stellar winds from early-type stars typically expel 10^{-6} M$_{\odot}$ per year, with values as high as 10^{-4} M$_{\odot}$ yr^{-1} in some

cases. Since the wind is isotropic, not all of the material will be deposited on the compact object (typically 0.1%), but this is sufficient material to power the observed X-ray luminosities.

Neutron Stars and Pulsars

As the gas from stellar winds approaches the compact object, it will form an accretion disc as a result of conservation of angular momentum. However, if the compact object is a neutron star with strong magnetic fields, the gas will move along the field lines of the source towards the magnetic polar caps. As material approaches the pole of the neutron star, a hot shock forms in which the X-rays are produced. If the orbit is viewed off-axis from the earth, as the neutron star rotates, pulses of emission will occur when the emission cone from the hotspot faces the earth. Since this process would occur inside the event horizon of a black hole, if a pulse period is detected in an HMXB, the compact object must be a neutron star.

Many of these neutron star HMXBs also exhibit eclipses in the X-ray emission as the companion star passes in front of the neutron star. From the eclipse, one can determine an inclination and an orbital period. By observing the Doppler shifted lines of the primary, one now has enough information (from Kepler's third law) to determine the masses of the two systems, the separations of the systems, and the physical sizes of the early-type stars. By way of an example:

$$f(M_o) = \frac{P(V_x \sin i)^3}{2\pi G} = \frac{(M_o \sin i)^3}{(M_x + M_o)^2} \tag{3.1}$$

is the mass function of the optical counterpart in a binary as derived using Kepler's third law. P is the orbital period, $V_x \sin i$ is the radial velocity of the neutron star, and M_o and M_x are the masses of the optical counterpart and the neutron star, respectively. Clearly, $f(M_x)$ can be derived similarly. $V_x \sin i$ is determined from the Doppler shifts of the X-ray pulse period and $V_o \sin i$ is determined from the Doppler shifted lines of the optical counterpart. This provides a mass ratio. If the inclination $\sin i$ can be determined by the eclipse, the masses can be determined. This has allowed for the determination of the classical neutron star mass of $1.4\ \mathrm{M}_\odot$ (Thorsett et al. (1993), see figure 3.1).

Neutron star HMXBs are typically associated with regions of star formation, since the massive donor stars are short-lived O and B stars. It is theorized that these systems begin with a binary made of two

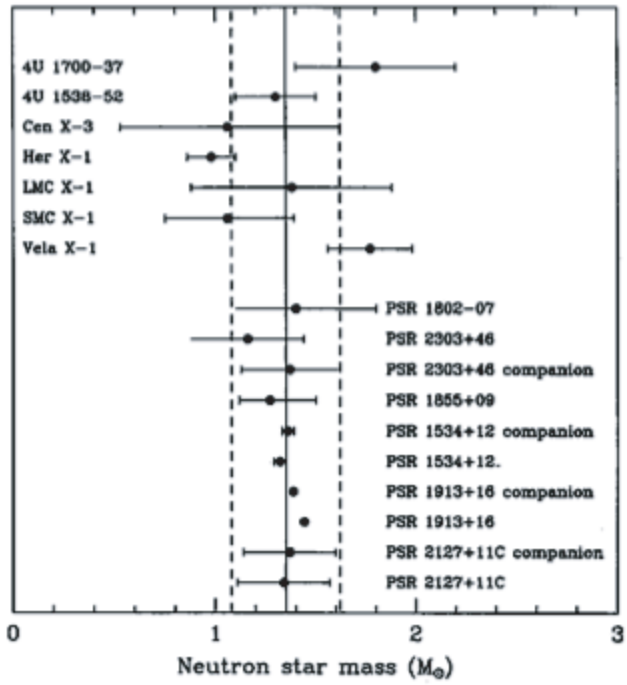

Figure 3.1 Figure 3 from Thorsett et al. (1993) showing the determination of the classical neutron star mass.

massive stars. The more massive star will evolve more quickly, and begin helium burning. After this, it will expand to fill its Roche lobe and begin transferring matter to the less massive star. In a few tens of thousands of years, almost all the material will have transferred to the less massive star, leaving only a helium core of the original. Helium fusion in this core proceeds rapidly, and soon the star overflows its Roche lobe again, initiating a second mass transfer. The mass transfer stage is very short (only a few thousand years), leaving a carbon core behind. Shortly thereafter, the carbon star will collapse and detonate as a supernova, leaving a neutron star.

Black Hole HMXBs

These are the most rare class of XRBs in the Galaxy. The compact object masses can be quite hard to determine, since only the mass function can be determined and the mass of the companion star must be determined by optical spectroscopy. In the case of these systems, mass is not always transferred by stellar winds. Rather, these binaries can emit via Roche lobe overflow as described in section 3.4.2. X-ray luminosities of these sources can be quite high, in excess of $10^{39}\ \mathrm{erg\,s^{-1}}$, due to high mass-accretion rates.

3.4.2 Low Mass X-ray Binaries

Low mass X-ray binaries are characterised by stars which have evolved to fill their Roche lobes and are transferring material through the inner Lagrangian point in their orbits into an accretion disc around the compact object; due to the angular momentum of the material, it cannot fall directly onto the compact object.

X-ray bursts and Quasi-periodic Oscillations

X-ray bursts were first observed in the 1970s. X-ray bursts are characterised by a rapid burst seen at all energies followed by an exponential decline (referred to as "FRED" for fast rise, exponential decline). They occur when unstable nuclear burning occurs on the surface of the neutron star. Hydrogen is deposited by the accretion disc onto the surface of the neutron star. Hydrogen burning will occur, leading to a layer of helium under the hydrogen. Eventually helium burning will occur, but this helium burning is unstable and the helium will be rapidly consumed, leading to a thermonuclear flash. This flash is observed as an X-ray burst. In order for helium burning to occur, a critical mass of helium must accrete onto the surface. If accretion is happening at a constant rate, this process will have a characteristic timescale; hence X-ray bursts occur semi-periodically. However, if a period of time passes without a predicted burst, the next burst will likely be more intense due to the larger mass of helium accumulated on the neutron star surface.

The short timescales (on the order of a few seconds) of, and oscillations (lasting only milliseconds) in, X-ray bursts rule out alternate explanations in which the compact object is a black hole. The short timescales of the bursts would take place within the event horizon of a black hole; thus, if an X-ray burst is observed, the source must be a neutron star. Luminosities in the X-ray can approach the Eddington limit for accretion onto a neutron star of $\approx 2 \times 10^{38}\ \mathrm{erg\ s^{-1}}$ (Strohmayer & Bildsten (2003)).

In many LMXBs, quasi-periodic oscillations in the flux are observed. These QPOs are characterised by broad peaks in the power spectrum of the source, rather than the delta function one would expect from a purely periodic phenomenon. QPOs were first observed in known neutron stars, but the QPO frequencies, whilst high, were not as high as the predicted neutron star rotation periods. It was theorized that, in the presence of weak magnetic fields, clumpy material accreting onto the neutron star would

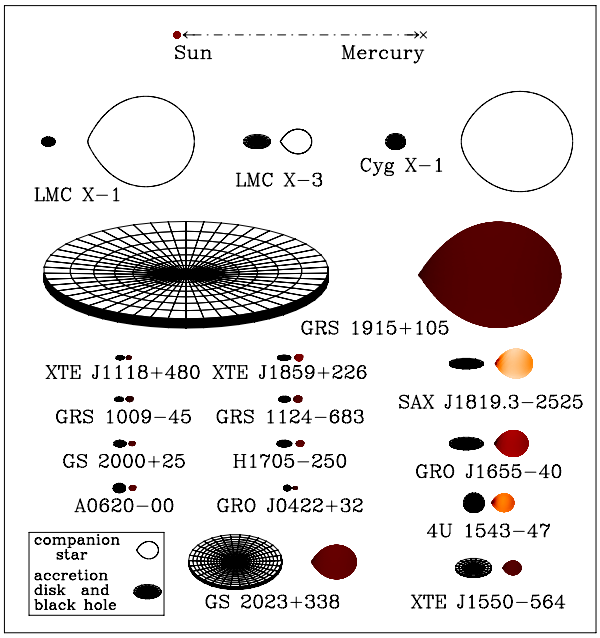

Figure 3.2 Relative sizes of all known black hole X-ray binaries. Figure courtesy of Jerome Orosz.

only be able to penetrate the magnetosphere at the pole. This occurs at the beat frequency of the neutron star's spin frequency and the orbital frequency of the inner disc. Since this process is dependent upon the magnetic field, it cannot take place within a black hole system.

High frequency QPOs can occur in both neutron stars and black holes. The mechanism for black hole QPOs is less clear than for the QPOs discussed above and several models have been proposed. Many of these models involve oscillations or perturbations in the accretion disc. See McClintock & Remillard (2004) section 4.4 for a review of these sources. Since detection of these phenomena would require considerably higher signal-to-noise than is present in our data, I will not discuss them further.

Black Hole LMXBs

Shown in figure 3.2 are the relative sizes of all currently known black hole X-ray binaries. In figure 3.3 are shown the masses of these black holes as compared with known neutron stars. As can be seen, these sources are a diverse class of objects.

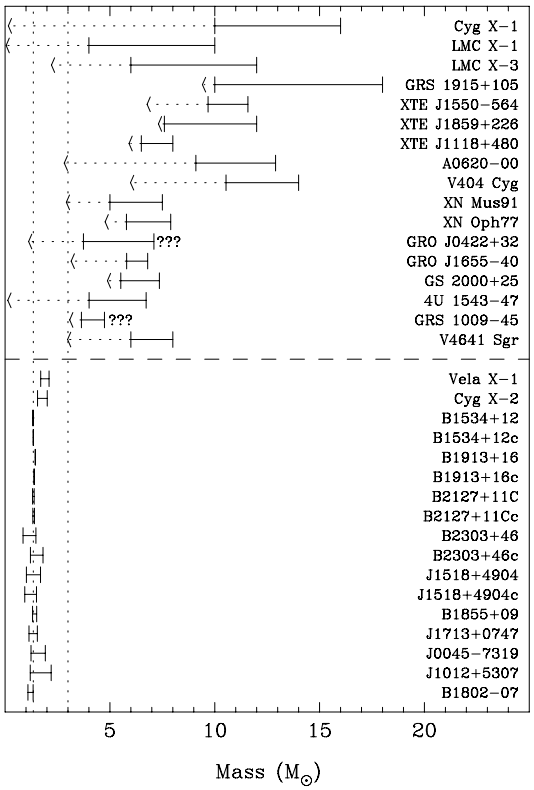

Figure 3.3 Masses of all known black hole XRBs as compared with neutron star masses. Figure courtesy of Jerome Orosz.

Soft X-ray Transients

Soft X-ray transients, also called X-ray novae, are LMXBs, frequently observed with black hole primaries in the Galaxy, though the compact objects can also be neutron stars. They are characterised by bright X-ray and optical outbursts (often accompanied by radio emission) followed by periods of quiescence. These systems occur when there is a slow rate of mass accretion from the companion star. Material builds up in the compact object (usually a black hole) accretion disc until a critical surface density is reached, at which point material rapidly spirals into the black hole. As the material approaches the event horizon, the temperature increases until it reaches X-ray emitting temperatures (see Tanaka & Shibazaki (1996) for a review). The sources are called "soft" because the spectrum is dominated by a soft disc blackbody component. Soft X-ray transients are the brightest sources in the Milky Way and experience high-frequency QPOs during their outbursts, often with frequencies in 3:2 ratio pairs (Remillard (2004)).

3.4.3 Ultraluminous X-ray Sources

Ultraluminous X-ray sources (ULXs) are not a homogeneous class of sources: ULXs are classically defined as sources whose X-ray luminosities exceed the Eddington luminosity for a 10 $\mathrm{M}_{\odot}$black hole, around $10^{39}\ \mathrm{erg\ s^{-1}}$, often by an order of magnitude or more. The dividing line is drawn at this luminosity as it is difficult to produce black holes of greater mass via evolution of a single parent star. It was therefore postulated that many ULXs may be a heretofore unknown category of object: intermediate mass black holes: that is, black holes whose masses are between those of black holes resultant from single parent stars and those of supermassive black holes at the centres of galaxies. These sources also frequently exhibit cool disc temperatures as were seen in *ASCA* spectra (1.3), lending further support to the idea that they may be intermediate-mass black holes, since inner disc temperature scales inversely with black hole mass.

As more data becomes available, it is clear that, via various mechanisms, neutron star and stellar-mass black hole binaries can produce luminosities over $10^{39}\ \mathrm{erg\ s^{-1}}$, but it is difficult to produce luminosities greater than $10^{40}\ \mathrm{erg\ s^{-1}}$ without more massive black holes. Thus, sources classified as ULXs likely represent a heterogeneous class of objects. Confusing the issue, however, is the clear tie between ULXs and star formation (see chapter 7).

3.5 Spectra of Galactic Binaries

3.5.1 Spectra of Black Hole XRBs

Black hole XRBs go through 4 distinct spectral states which correspond to different mass accretion rates (see Fig. 3.4). The lowest accretion rate state, called the quiescent state, is the state in which black hole XRBs spend most of their time. It is characterised by a very faint ($L_x \sim\ 10^{30-33}\ \mathrm{erg\ s^{-1}}$), hard ($\Gamma = 1.5 - 2.1$), non-thermal spectrum. Since this is well below the detection threshold of any of our observations, it is not necessary to discuss this state further other than to note that the behaviour of binaries in this state will become important with further *Chandra* and *XMM* observations of Local Group galaxies.

The high/soft state of BH binaries, also referred to as the thermal-dominant state, occurs at much higher

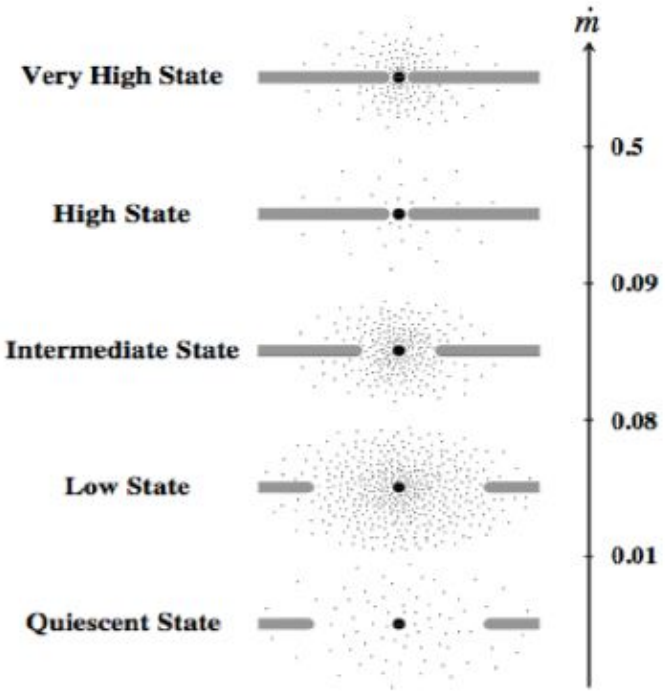

Figure 3.4 Diagram of the accretion flow in different spectral states of black hole XRBs as a function of mass accretion rate $\dot{M}$, expressed as a fraction of Eddington luminosity. Figure from McClintock & Remillard (2004).

mass accretion rates. The emission comes from thermal radiation from the inner accretion disc (Shakura & Sunyaev (1973) and the spectra in this state are well modeled by multi-temperature accretion disc models (henceforth multi-colour disc, or MCD, models). These sources also exhibit a hard X-ray tail which is typically modeled by a power-law, but this component typically does not become spectrally significant until above 10 keV, outside the *Chandra* energy range. For stellar mass (3-50 $\mathrm{M}_{\odot}$) black holes, the typical temperature is in the range $0.7-1.5$ keV with the hard power-law component spectral index of $\Gamma = 2.1 - 4.8$.

The low/hard state of BHXBs is characterised by a hard, non-thermal spectrum with photon index typically ~ 1.7. The low/hard state appears to be correlated with jet emission, and many binaries in the low/hard state exhibit clear, persistent radio jets with flat spectra. It should be noted that, though the luminosity is typically lower in the low/hard state than in the high/soft (hence the naming convention), this is not always the case.

The very high state, also called the steep power-law state, occurs at luminosities approaching the Eddington luminosity for BHXBs. Like the low/hard state, the spectrum is highly nonthermal with a much

harder power-law photon index ($\Gamma \geq 2.4$). The strength of the power-law component is closely tied to the onset of QPOs (see section 3.4.2).

In addition to the 4 main states, black hole XRBs go through many intermediate states. However, with the poor statistics provided by our observations, it would be speculative at best to discuss any states beyond the 3 easily distinguishable in our observations: the high/soft, low/hard, and very high states.

3.5.2 Spectra of Neutron Star XRBs

In order to discuss neutron star spectra, it must first be stated that there are two states of neutron star sources: the high state, characterised by persistent luminosities above 10^{38} erg s^{-1}, and the low state, with luminosities around a few times 10^{37} erg s^{-1}. It was initially proposed that high state NSXBs have three distinct spectral modes: a horizontal, a normal, and a flaring branch. These sources are called 'Z' sources due to the shape they trace on a colour-colour diagram (see, e.g., Schulz et al. (1989)). More recently it has been demonstrated that the low state sources (previously called 'Atoll' sources because of the shape traced on the colour-colour diagram) also exhibit this same Z shape, though on a much longer timescale and over a larger range in intensity (Muno et al. (2002)).

Sources seem to follow along the Z in spectral variation from the horizontal branch into the normal branch and then the flaring branch (or vice versa). The spectra of all three branches are well characterised by a multicolour disc plus thermal component model. Spectral changes along the horizontal branch are due to variations in the blackbody flux, with temperature typically $\sim 1.3keV$ and electron temperature component at $\sim 5keV$. Normal branch spectra are characterised by variations in the electron temperature, decreasing from $\sim 6.5\ to \sim 3.8keV$, and a decrease in blackbody temperature from $\sim 1.3\ to \sim 1.1$. Flaring branch spectra are more complex, with blackbody temperature increases up to $\sim 1.6keV$ and very strong electron temperature increases to $\sim 10 - 17keV$ (Schulz et al. (1989)). These variations in spectra are believed to be the result of changing mass accretion rate ($\dot{M}$) but the exact mechanism is not known.

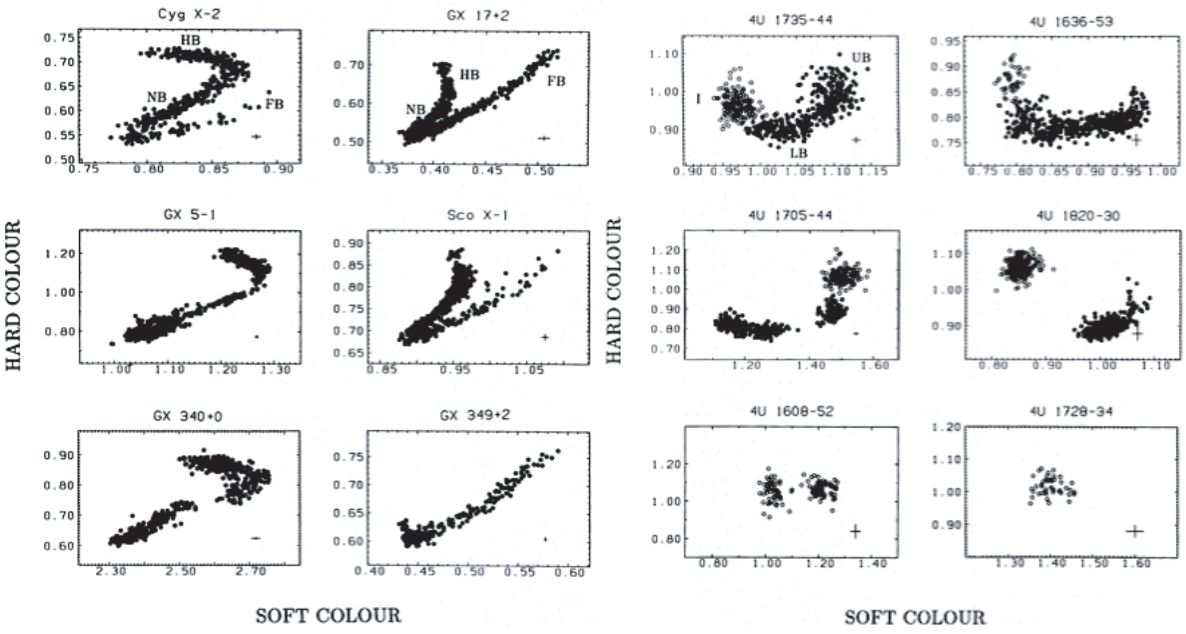

Figure 3.5 Z sources (left) and atoll sources (right) from Hasinger & van der Klis (1989). The colour bands used for each source are slightly different, but are typically 1-3 keV and 3-5 keV for the soft colour and 4.5-7 keV and 7-20 keV for the hard colour. Future observations in the hard X-ray (above 10 keV) will be useful in studying these types of sources in external galaxies.

Chapter 4

Data Analysis

> I went on to test the program in every way I could devise. I strained it to expose its weaknesses. I ran it for high-mass stars and low-mass stars, for stars born exceedingly hot and those born relatively cold. I ran it assuming the superfluid currents beneath the crust to be absent – not because I wanted to know the answer, but because I had developed an intuitive feel for the answer in this particular case. Finally I got a run in which the computer showed the pulsar's temperature to be less than absolute zero. I had found an error. I chased down the error and fixed it. Now I had improved the program to the point where it would not run at all.
>
> George Greenstein

4.1 X-ray Data Analysis

4.1.1 Observations

All spirals observations were performed on the *ACIS* instrument with the aimpoint falling on the back-illuminated S3 chip. This was chosen because the S3 chip has excellent low energy response, better sensitivity, and does not suffer as much form the effects of charge transfer inefficiency (CTI) as do the front-illuminated CCDs. In addition, the calibration of the S3 chip is more complete than that of the

other ACIS chips. The observations were conducted in regular graded/faint mode with the standard 3.2 second frametime and 6 chips on (I2, I3, S2, S3, S4, S5). The one exception is M94, which was observed in a 1/4 subarray on S3 during the longer (49ks) observation and a 1/8 subarray on S3 during the shorter (2ks) observation. This yields much shorter frame times of 0.84 and 0.42 seconds, respectively, and was done to mitigate the effects of pileup in data from the bright nuclear source, but it reduces the field of view to a strip of $8' \times 2'$ for the 1/4 subarray and $8' \times 1'$ for the 1/8 subarray. The fraction of D_{25} covered in each galaxy is listed in table 4.1.

The observations of M82 were taken on several different detectors. Five observations during *Chandra* AO1 were made on the *ACIS-I* detector before the detrimental effects of CTI were completely understood. In addition, a set of two observations were made with the *HRC*, allowing for higher spatial/temporal resolution at the sacrifice of all spectral information. The field of view of the *ACIS-I* observations is $16' \times 16'$ and the field of view of the *HRC* is $30'$ on a side. A further observation was made in 2002 using the *ACIS-S* instrument as described for the normal spirals.

Analyses were performed using the *Chandra* Interactive Analysis of Observations software (*CIAO*) v2.2.1 and the *Chandra* Calibration database v2.11. Standard data processing was performed at the *Chandra* X-ray Center. Data were then reprocessed using the latest calibration files available, utilizing new gain maps, improved plate scale*, and applying PHA randomization (for *ACIS* data only). The PHA randomization removes statistically coincident spikes sometimes seen in the instrumental spectra of point sources due to quantization of PHA calculations. Real spectral features will not be removed by this randomization. The S4 data were additionally cleaned using the tool *destreak*, which removes linear streaks which are due to a detector artifact †.

4.1.2 Source Detection

For the purposes of source detection, the observations were screened for periods of high background due to increased solar activity, and background levels above the mean level in each observation by 20% were excluded. The observations of each galaxy were then merged using the CIAO script *merge_all*, which reprojected the events files into a common coordinate plane and created a merged events list.

*The new plate scale is a consequence of a better calculation of the *Chandra* focal length and was implemented in the CALDB v2.9. *http://cxc.harvard.edu/cal/Hrma/optaxis/platescale/foc_len_public.html*

†For details on *destreak*, see http://cxc.harvard.edu/ciao/download/scripts/destreak.ps

Source lists were constructed using *wavdetect* (Freeman et al., 2002), the Mexican-hat wavelet source detection routine that is part of CIAO. The detection was run on full-resolution images with a restricted energy filter of 0.3-6.5 keV using wavelet scales of 2, 4, 8, and 16 pixels and again in the energy range 0.5-6.5 keV using scales 1, 2, 4, 8, and 16 pixels, with the latter used in regions where confusion due to unresolved emission or close spacing of sources may be a problem. The *wavdetect* significance threshold was 10^{-6} and sources with significance less than 3σ were excluded unless they were visibly obvious point sources. This combination of energy bands and wavelet scales yielded the fewest spurious detections and found all visually obvious point sources. The output source regions were visually inspected to remove the artifacts that sometimes occur with wavdetect: regions where the ellipse minor axis is zero, regions containing 2 sources, and sources detected twice. The D_{25} ellipse of the galaxy is the distance at which the B-band isophote has a surface brightness of 25.0 mag arcsec^{-2}. This is generally considered to be a good estimate of the diameter of a galaxy. Colbert & Ptak (2002) (and in subsequent papers) consider sources beyond D_{25} and determine that the X-ray sources detected are predominantly background sources. As such, sources outside the galaxy D_{25} ellipses were also removed. The number of sources excluded in each case is listed in Appendix 10.

Each source has been assigned a name following the *Chandra* naming convention. This is presented in the catalog tables for each galaxy. If this or another name has been used for the source in an existing publication, it is also noted in the table. For galaxies whose D_{25} radii extended beyond the S3 chip, source detection was performed on flanking chips as necessary. Details are given in the notes on individual galaxies found in appendix 10.

4.1.3 Spectral Extraction

For each source, pulse height analysis (PHA) spectra were extracted from the unfiltered, reprocessed *ACIS* events lists and response matrix files (RMFs) and ancillary response functions (ARFs) were constructed. Corresponding background spectra were extracted for each source, and background responses were generated. The ARFs were then corrected for the *ACIS* low energy degredation using the tool *corrarf* by Alexey Vikhlinin[‡]. The region for each background spectrum was taken to be an ellipse with radius equal to 4 times the source radius and excluding the source regions and any other overlapping source regions. To limit contamination from unresolved emission, the background ellipse radii were

[‡]The corrarf tool can be found at http://hea-www.harvard.edu/ alexey/

not allowed to exceed 50 pixels (about 25″).

4.1.4 Colours

Because of potential overlaps in PHA to energy mapping, counts must be determined using a tool capable of analysis in channel-space. We chose to use *Sherpa* for this purpose. Background subtracted counts in 4 bands were determined for each source using the CXC spectral fitting tool *Sherpa*: a soft band (S) of 0.3-1 keV, medium band (M) of 1-2 keV, hard band (H) 2-8 keV, and the total band (T) of 0.3-8 keV. Events below 0.3 keV and above 8 keV were exlcuded because they tend to be dominated by background and intrinsic detector noise. As an example, a PHA channel is defined as having low and high energy bounds of 0.98 and 1.02 keV, respectively (for example). Two photons are detected with energies 0.99 and 1.01 keV. Both these detections fall within that single PHA channel and will therefore be counted in both the 0.3-1 keV and 1-2 keV bands if one specifies the count extraction using energies rather than specific channels. Instead, for each source, we determine the PHA channels most closely corresponding to the energies 0.3, 1.0, 2.0, and 8.0 keV. We will refer to them as PHA channels A, B, C, and D, for convenience. Counts are then extracted in the PHA regions A to B, B+1 to C, C+1 to D, and A to D.

Hardness ratios were then calculated from these values using the following form:

$$HC = \frac{(H - M)}{(H + M)} \tag{4.1}$$

and:

$$SC = \frac{(M - S)}{(M + S)} \tag{4.2}$$

with errors based on standard error propagation:

$$HC\_ERR = \frac{2\sqrt{H^2 \times \ M\_ERR^2 + M^2 \times \ H\_ERR^2}}{(H + M)^2} \tag{4.3}$$

and:

$$SC\_ERR = \frac{2\sqrt{M^2 \times \ S\_ERR^2 + S^2 \times \ M\_ERR^2}}{(M+S)^2} \tag{4.4}$$

where the error on the counts was taken to be the statistical error using the Gehrels approximation (Gehrels, 1986):

$$ERR = 1 + \sqrt{COUNTS + 0.75} \tag{4.5}$$

These values are presented in the electronic catalog table for each galaxy published in Kilgard et al. (2005). For the sources that fall on the front-illuminated CCDs, weights were applied to correct the source counts to the value expected on the S3 chip using a conversion factor equal to the difference between the effective area for the front-illuminated CCD as compared with the S3 aimpoint. These weighted counts were used for colour calculation, not for the count values listed in the catalog and not for the flux and luminosity calculations where the differences are taken into account by appropriate response files. The colours were then used to determine inital classifications for each source.

We have changed our colour definitions from the work of Prestwich et al. (2003) to be more consistent with other work in the literature and to use a more statistically correct error propagation. The advantage of our method over the Prestwich et al. (2003) definition (e.g. $SC = M - S/H + M + S$) is that the colours are independent: the hard-band counts do not affect the soft colour and vice versa. We present our coarse bins in table 4.3. In figure 4.1, we show the curves of constant photon index and the Galactic reference sources from Prestwich et al. (2003), plotted in the colour-space defined in table 4.3. We choose our colour bands to include all the sources as classified by Prestwich et al. (2003), and, as we are interested here in only bulk trends across our sample, we include both high- and low-mass X-ray binaries in the same bin.

Since most sources do not have sufficient counts for detailed spectral analysis, it is necessary to assume some spectral model for flux and luminosity calculations. For each source, fluxes were calculated for 3 assumed spectral models: a simple power law with $\Gamma = 1.5$ and photoelectric absorption, a disc blackbody with $T_{in} = 1.0\ keV$ and photoelectric absorption, and a thermal bremsstrahlung model with $kT = 5.0\ keV$ and photoelectric absorption. These models were chosen as characteristic of the best-fit

spectra to bright point sources in the sample. In all cases, the absorption was set to the Galactic value; since most of our galaxies are face-on, line-of-sight absorption in the host galaxy should be minimal. Fluxes were then calculated in *Sherpa* by rescaling the normalization of the models to the observed count rates. Luminosities were calculated using the distances listed in Table 4.1. This method of normalization to fixed model parameters allows some model types to be rejected for any given source. For example, if a source has a very hard spectrum (e.g. a 5 keV blackbody) and one normalizes a l.0 keV disc blackbody model to the data, the normalization will be unrealistically high and the residuals of the fit will be very large at low energies. If one then uses the model spectrum to compute a flux, the flux will in turn be unrealistically high. This error can be uncovered using a simple PIMMS calculation: if one determines the flux using PIMMS over the full energy band and the same assumed model (1.0 keV disc blackbody), one will arrive at a considerably lower flux than that determined by the Sherpa method. This is because PIMMS does not know anything about the intrinsic spectrum of the source, but only the count rate in the full band. Thus, to reject a spectral model, a rejection criterion of $3\times$ or $1/3$ the PIMMS vs. *Sherpa* flux was used. The rejection of some models is potentially useful in source classification.

Cepheid or other high quality distance indicators were used, where available. However, only distances based on recessional velocities were available for several galaxies within the sample. Since all galaxies in our sample are nearby, distances from recessional velocities are not particularly accurate and, indeed, can be incorrect by a factor of 2 or more. Distances used and references can be found in table 4.1.

It should be noted that the detection threshold differs greatly between the FI and BI ACIS chips due to the low-energy degradation of the FI chips. This has impacts on, for example, the construction of luminosity functions, since the completeness limit differs from chip to chip. In the discussions of individual galaxies, we consider only those sources on the back-illuminated S3 chip unless otherwise noted.

Though the *Chandra* astrometry is generally good to $\sim 1''$ on the aimpoint ACIS chip, the sources on other chips will have decreasing accuracy with increasing off-axis angle. In addition, our utilization of the newer plate scale produces a slight discrepancy between the *Chandra* coordinates in the literature for some of the sources and the coordinates presented here, as many of those catalogues were published before the new plate scale was available.

4.2 Luminosity Functions

The cumulative luminosity functions for each observation of each galaxy are presented in chapter 7. In order to avoid incompleteness, we consider only the high luminosity range of the luminosity functions. We set an overall conservative completeness limit determined by the data available for each galaxy. The completeness limits for each galaxy are cited in the subsections on each galaxy in appendix 10.

We derive power law fits to the unbinned differential luminosity functions using a maximum likelihood statistic following Crawford et al. (1970). We evaluate the goodness of fit using a Monte Carlo technique. The fitted slopes, Γ, and estimate of goodness of fit are shown in Table 4.1. In fitting the LFs, we include a background component from Giacconi et al. (2001), scaled to the area of each galaxy and the flux detection limit of each observation. This is represented as a solid red line in the XLF plots in Appendix 10. For galaxies spanning more than one ACIS chip, we include a separate background component per chip, as both the area and the completeness limit will be different. The plots each show the complete data and best-fit LF slope (indicated with a solid black line), background-subtracted data and best-fit LF slope (indicated with a solid blue line), and red line indicating the distribution of background sources. The background is subtracted by simulating a random distribution of background sources (scaled as described above) and removing discrete sources that match that sample distribution from the data via a nearest-neighbour approximation. The goodness of fit estimate is performed by simulating a luminosity distribution with the best-fit slope. One million iterations are performed and the mean slope and mean deviation of the simulated luminosity distributions are found. The goodness of fit estimate comes from Crawford et al. (1970) and is defined as:

σ^2_{MC}/σ^2

where σ_{MC} is the mean deviation of the simulated LFs and σ is the observed deviation, as defined in Crawford et al. (1970) equation 13. If the data are well fit by a single, unbroken powerlaw distribution, then the goodness of fit value should approach 1. It should be noted that, for several of the galaxies, the exposure times of the separate observations are quite different and, thus, the detection thresholds are also different. As such, the range of luminosities fit will be different for those galaxies. For example, in the case of M101, the luminosity thresholds are $4.4 \times\ 10^{36} erg\ s^{-1}$ and $4.6 \times\ 10^{37} erg\ s^{-1}$ for the 100ks and 10ks observations, respectively; the best fit slopes are 0.69 and 1.70, respectively; and the goodness of fit values are 1.60 and 1.06, respectively. The fit to the shorter data set is much steeper,

but also a better fit, suggesting that the high luminosity end of the LF may be better fit with a steeper component or a high luminosity cut-off.

In the catalog table for each galaxy, we also present variability information for each source. This includes both long-term variability (statistically significant variability between each observation) and short-term, statistically significant variability during each observation.

4.3 Optical Data Analysis

Except where noted, all optical observations were obtained with the Fred L. Whipple Observatory 48″ telescope located at Mt. Hopkins, Arizona. Data were obtained during two observing runs, 2001 February 19-21 and 2001 December 15-16. Filters used were U, B, V, R, I, and wide $H\alpha$ and [SII]. Observations of M83 were obtained using the Southeastern Association for Research in Astronomy (SARA) 0.9 meter telescope at Kitt Peak National Observatory, Arizona. Data were obtained on 2001 May 29 using V, $H\alpha$, and $H\alpha$ continuum filters. Data were reduced in the standard fashion using *IRAF* v2.12 and the *MSCRED* package, used for analysis of data taken with the 4-shooter CCD on the FLWO 48″ telescope. Astrometric alignment of images was performed using the *WCSTools* software from the SAO Telescope Data Center using objects identified in both X-ray and optical observations as either foreground stars or background AGN, as identified in SIMBAD catalog queries. For the galaxies NGC 1291 and IC 5332, which are located in the southern hemisphere, we utilized data from the Digitized Sky Survey and no further registration was performed. None of the optical data were taken simultaneously with the X-ray, but all data was obtained within a year of the X-ray observations. For the FLWO and SARA data, image resolution is determined by atmospheric stability from the sites in Arizona. Typical observations have 2″ seeing. All optical images presented here are V band unless otherwise noted.

Table 4.1 Global properties of sample galaxies. Columns are galaxy name, morphologic type, inclination, distance, D_{25} ellipse, the fraction of D_{25} covered in the *Chandra* observations, line-of-sight Galactic neutral hydrogen column density, *Chandra* observation IDs, *Chandra* observation durations, best-fit luminosity function power-law slope, error of LF slopes, goodness-of-fit for LF slopes, number of detected X-ray sources within D_{25}, and number of ultraluminous X-ray sources per galaxy.

Galaxy	**Morph.**	**i (deg)**	**R (Mpc)**	D_{25} **(arcmin)**	**frac.** D_{25}	N_H $(10^{20} cm^{-2})$	**ObsID 1/2**	**Duration 1/2 (s)**	Γ **1/2**	σ **1/2**	**GOF 1/2**[1]	**No. srcs**	**No. ULXs**
NGC 278	Sb	0	8.5[2]	2.1	1.00	12.9	2055/2056	38258/37269	0.89/1.03	0.33/0.39	0.55/0.22	14	1
M74 (NGC 628)	Sc	0	8.8[2]	10.5	0.88	4.81	2057/2058	46352/46169	1.03/1.08	0.16/0.15	1.96/1.79	67	1
NGC 1291	S0/a	28	8.9[3]	9.8	0.94	2.24	795/2059	39168/36533 (22906)[4]	0.74/1.01	0.09/0.14	1.85/1.56	93	2
NGC 2681	S0/a	0	9.2[5]	3.6	1.00	2.48	2060/2061	80898/78977	0.63/0.62	0.15/0.15	1.46/0.67	23	1
NGC 3184	Scd	26	11.1[6]	7.4	1.00	1.15	805/1520	42122/23731	1.11/0.84	0.21/0.15	1.03/1.31	49	0
NGC 4314	Sa	15	12.8[7]	4.2	1.00	1.62	2062/2063	16075/16044	1.20/1.19	0.38/0.36	0.61/0.89	19	0
M94 (NGC 4736)	Sab	33	4.1[8]	11.2	0.20	1.44	310/808	47366/2314	0.48/0.69	0.08/0.21	1.18/0.66	50	0
M51 (NGC 5194/95)	Sbc	20	8.4[9]	11.2	0.87	1.53	354/1622	14865/26808	0.86/0.66	0.12/0.08	0.81/1.14	116	3
M83 (NGC 5236)	Sc	24	4.2[10]	12.9	0.0.81	3.70	793/2064	50978/9845	0.57/0.84	0.05/0.10	1.27/1.00	131	3
M101 (NGC 5457)	Scd	0	7.2[11]	28.8	0.78	1.15	934/2065	98244/9633	0.69/1.70	0.07/0.47	1.60/1.06	208	3
IC 5332	Sd	25	9.4[12]	7.8	1.00	1.38	2066/2067	52134/55247	1.12/1.26	0.22/0.23	1.59/1.04	50	0
M82 (NGC 3034)	I0 Sbst		3.9[13]	11.2	1.00	4.03	[14]	[14]	[14]	[14]	[14]	107	3

Table 4.2. Properties of M82 from individual observations. Values for LF fits are presented for each observation down to its completeness limit and for the 4×10^{37} erg s^{-1}, the highest completeness limit of all the M82 observations.

ObsID	Primary Detector	Duration	Γ_{all}	σ_{all}	GOF_{all}	Completeness	Γ_{4E37}	σ_{4E37}	GOF_{4E37}
1302	ACIS-I	15516	0.81	0.16	0.52	1E37	0.59	0.09	1.01
1411A	HRC-I	36207							
1411B	HRC-I	17609							
361	ACIS-I	33253	1.18	0.24	1.27	5E36	0.51	0.07	0.90
378	ACIS-I	4116	0.71	0.12	1.33	4E37	–	–	–
379	ACIS-I	8931	0.73	0.13	1.08	2E37	0.59	0.10	1.17
380	ACIS-I	5001	0.87	0.15	1.15	4E37	–	–	–
2933	ACIS-S	18024	1.10	0.25	1.91	7E36	0.60	0.10	1.80

[1]An estimate of the goodness of fit derived from Monte Carlo simulations as defined in section 4.1. The quantity measures the deviation as compared with that from a pure powerlaw distribution; thus the quantity should approach unity as the data approaches a pure powerlaw distribution.

[2]Huchra et al. (1999)

[3]de Vaucouleurs (1975)

[4]This observation contains a large flare starting at 23ks. The flare data was filtered out for the purposes of analysis.

[5]de Vaucouleurs et al. (1991)

[6]Leonard et al. (2002)

[7]Benedict et al. (1996)

[8]Mulder & van Driel (1993)

[9]Feldmeier et al. (1997)

[10]Thim et al. (2003)

[11]Stetson et al. (1998)

[12]da Costa et al. (1991)

[13]Sakai & Madore (1999)

[14]Parameters for the eight observations of M82 are presented in table 4.2.

Table 4.3. Colour-colour classifications. Whilst these are the boundaries used for assigning a classification to each source, it must be noted that there is much overlap between the actual populations. For the class of supersoft sources, we choose to include only those sources with zero net counts above 1 keV, thus M and H band values of 0 net counts.

Classification	definition
supernova remnant	$HC < -0.2, SC < -0.3$
X-ray Binary	$-0.8 < HC < 0.8, -0.3 < SC < 0.6$
indeterminate source	$HC > -0.2, SC < -0.3$
absorbed source	$SC > 0.6$
indeterminate soft source	$HC < -0.8, -0.3 < SC < 0.6$
indeterminate hard source	$HC > 0.8, -0.3 < SC < 0.6$
supersoft source	$M = 0, H = 0$

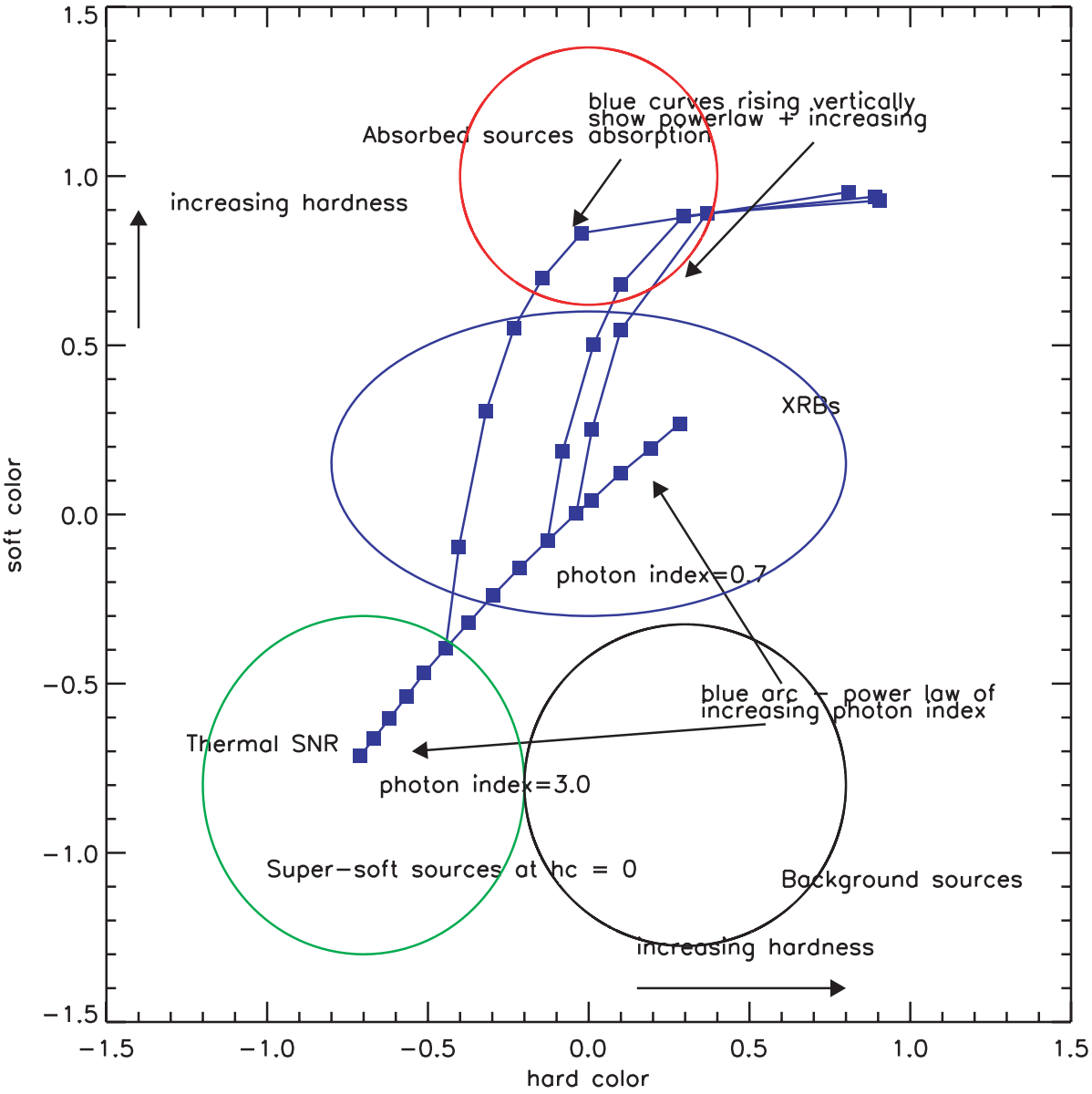

Figure 4.1 Colour-colour diagram following Prestwich et al. (2003). The blue points represent power laws of different photon index, with photon index increasing (spectrum hardening) as one moves from the upper-right to the lower left. As absorption is added, sources travel up and to the right along the blue curves. Ellipses outline the major source categories. Though we use different colour definitions from Prestwich et al. (2003), we plot the same curves here as in Prestwich Figure 4 for reference.

Chapter 5

The Most Luminous X-ray Sources

> We must avoid here two complementary errors: on the one hand that the world has a unique, intrinsic, pre-existing structure awaiting our grasp; and on the other hand that the world is in utter chaos. The first error is that of the student who marvelled at how the astronomers could find out the true names of distant constellations. The second error is that of the Lewis Carroll's Walrus who grouped shoes with ships and sealing wax, and cabbages with kings...
>
> R. Abel

5.1 Introduction

X-ray spectroscopy has been important in understanding the nature of Galactic stellar evolution, since sources in the Galaxy become X-ray bright at the end-point of stellar life: X-ray binaries, neutron stars, and supernova remnants. With all X-ray telescopes prior to *Chandra*, confusion and high background made it impossible to determine discrete sources spectra beyond the Milky Way and Magellanic Clouds. With the unprecedented spatial resolution of *Chandra*, it becomes possible for the first time to perform what was traditionally "Galactic" X-ray astronomy on extragalactic sources.

Though most of our sources are too faint to use spectroscopy as a means of determining the nature of the source, the most luminous sources in our sample allow for fitting of at least simple spectral models.

Approximately 10% of all sources have sufficient counts for a simple fit, $\gtrsim 300$ counts, in at least one observation. Since it is known that most, if not all, X-ray point sources in galaxies will be XRBs, SNR, and background sources, we chose to use simple models characteristic of those sources, focusing in particular on the X-ray binary sources (see 3.4).

In the following sections, example spectra are presented for each source class. In addition, I present timing analysis of some of the most luminous sources where that information can aide in source classification.

5.2 Spectral Fitting

All spectra were fit over the energy ranges $0.5-8.0keV$ and $0.7-8.0keV$ (for spirals and M82, respectively) using the *CIAO* spectral fitting package *Sherpa*. The different energy bands were used because the M82 data was taken during the first few months of *Chandra* observations. During this period, the focal plane temperature was changing and insufficient calibration data was taken at the higher focal plane temperatures to allow for proper calibration of low-energy *ACIS* spectra. The extracted spectra were grouped with a minimum of 15 counts per bin to allow for Poisson statistics to apply. Goodness-of-fit values were computed using chi-squared statistics with variance computed from the data (chi dvar in *Sherpa*). Background spectra were constructed as described in Section 4.1. The background spectra were subtracted rather than using simultaneous fitting, as the latter is primarily advantageous in the energy ranges dominated by detector noise, below 0.5 keV and above 8 keV, which are excluded from our data. Bad PHA values were ignored. Errors presented are 90% confidence values computed with *projection* except for sources with insufficient counts for good error projection (around 400, based on trial-and-error) where *covariance* was used. All model parameters were allowed to freely vary except for the N_H, which had the minimum frozen to the foreground Galactic value for each source. All source spectra were fit individually, not via automated fitting routines. This allows for more flexibility in finding the best fit model based both upon visual inspection and experience.

Since most sources are believed to be XRBs, we fit each source with 3 simple models: a power-law plus photoelectric absorption, a disc blackbody (multi-colour disc or MCD) with photoelectric absorption, and a simple blackbody with photoelectric absorption. In all cases, the absorption minimum was set to the foreground Galactic column and all parameters were allowed to vary. If none of these models

provided satisfactory fits, more complicated models were considered as necessary. The more complex models and motivations for using them are discussed below.

5.3 Short-term Variability

In addition to long-term variability, we performed tests for short-term variability within each observation. Two methods were utilized: a Bayesian block routine following the method of Scargle (1998) and a simple Kolmogorov-Smirnov (KS) test. The Bayesian block method is efficient at detecting localized structures in the lightcurve (bursts), but is also somewhat sensitive to larger-scale variability. The KS test compares the photon arrival times for a source with the flat lightcurve of mean flux for that source in that observation and is thus sensitive to large-scale variability across an observation (brightening or dimming). Results of the tests for individual sources are presented in the catalog in Kilgard et al. (2005). As determined by the Bayesian block method, 7 of the 64 luminous spirals sources are variable at the 99% confidence level. From the KS test, 33 of the sources are variable at the 99.5% confidence level. Of the 16 luminous sources in M82, only two exhibit variability that is detectable in either the KS or Bayesian block tests. These tests are highly dependent upon both the number of counts in each source and the duration of the observations, so are necessarily lower limits to the number of sources that experience short-term variability. In addition, it is likely that fewer M82 sources have detectable short-term variability due to the high background from diffuse emission.

5.4 Spiral Galaxy Sources

Since the normal spiral galaxies in our sample cover a wide range of star formation histories, one would expect a diverse assortment of sources, and that is indeed what we see. There are 64 sources in our sample of normal spirals with sufficient counts for detailed spectral fitting. Best fit spectral parameters are presented in Tables 5.1 and 5.2. Below, I discuss the broad spectral categories into which these sources fall, giving examples of each. In addition, I discuss several sources which do not fall clearly into one of the categories.

It should be noted that, since the normal galaxy component of our survey was designed to reach equal

luminosity detection limits across the sample, the luminosity at which we have sufficient counts for spectral fitting is also approximately equal across the sample, at 2×10^{38} erg s^{-1}. Naively one would assume, based entirely upon the argument of Eddington luminosity, that these sources would all be black hole binaries, since 2×10^{38} erg s^{-1} corresponds to the Eddington luminosity of a $1.4\,M_{\odot}$ neutron star. However, whilst many of the sources are certainly black hole candidates, several are also neutron star candidates.

5.4.1 Single-component spectral models and short-term variability

The majority of sources are well fit by either a power-law with spectral index $\Gamma \sim 1.5 - 2.5$ or a warm disc blackbody model with temperature index $T_{in} \sim 1.0 - 2.0keV$. The former are likely black hole binaries in the low/hard state or very high state (as discussed in section 3.5.1, whereas the latter are likely black hole binaries in the high/soft state (sec. 3.5.1), though they could be neutron star binaries as well (sec 3.5.2). In particular, if these sources were neutron stars in the flaring branch, the thermal component of the spectrum would be well outside the *Chandra* energy range. Variability will add another important clue in determining source type. I discuss short-term variability of several individual sources below; long-term variability will be discussed in section 6.2.

Of the 7 sources with variability found via the Bayesian block method, 6 have luminosities above 2×10^{38} erg s^{-1} and 5 are included in the tables of detailed spectral fits. The two sources not included are CXOU J013647.4+154745 in M74 and CXOU J031736.8-410901 in NGC 1291. Each clearly exhibit flaring variability in their lightcurves but have insufficient counts to allow for spectral fitting. CXOU J013647.4+154745 exceeds 2×10^{38} erg s^{-1} but has slightly fewer than 300 counts, so no detailed fitting is performed. CXOU J031736.8-410901 has a persistent luminosity of 7×10^{37} erg s^{-1} in both *Chandra* observations. Figure 5.2 shows the lightcurves of these two sources.

5.4.2 M51 X-7 (CXOU J133001.0+471344): flaring variability as a diagnostic tool

M51 X-7 (Roberts & Warwick (2000)) is another source which exhibits flaring variability on a timescale of a few thousand seconds. M51 has been observed three times with *Chandra*, including an observation too recent to be included in the bulk of the analysis for this thesis. In the first and third observations,

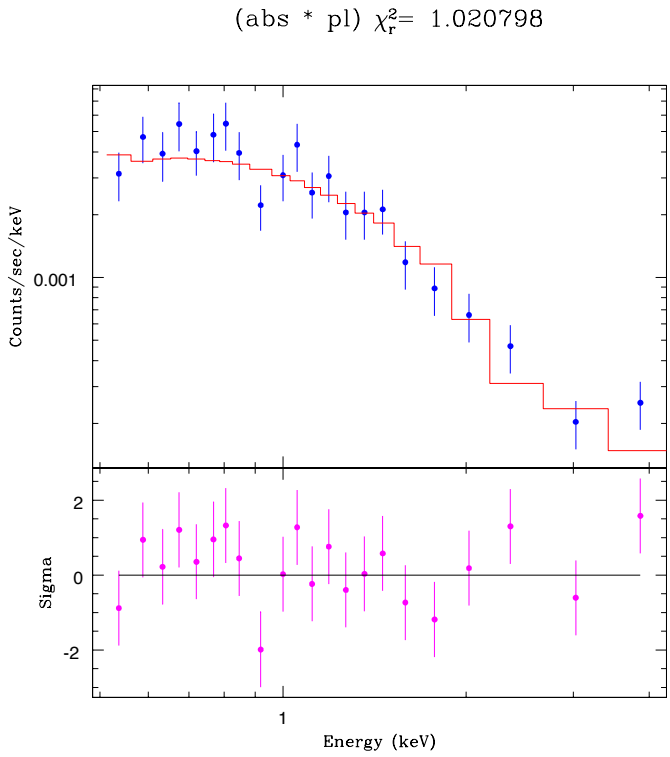

Figure 5.1 Spectrum of source CXOU J085333.3+511705 in NGC 2681. The source is well fit by a power-law with $\Gamma = 1.84$. The spectrum of this source is characteristic of most of the bright source population.

the flaring variability is clearly seen (see figure 5.3). In the second observation, the flux is reduced by a factor of about 19.

M51 X-7 is also located near, but not directly in a bright cluster (number 839 from Larsen (2000)). As discussed in section 6.3, this type of association with clusters is common amongst ULXs and indicates that the sources are likely HMXBs that have been kicked out of the clusters due to N-body interactions.

The spectrum of M51 X-7 is well-fit by a simple absorbed power-law with slope of 1.2-1.5. This is consistent with the interpretation of the source as a neutron star binary (Liu et al., 2002), or as an HMXB in a Comptonization-dominated state (low/hard or very high). Liu et al. (2002) claim there to be a coherent period at around 7000 seconds. They use this interpretation to calculate a mass of the stellar counterpart of $0.3\ M_\odot$. This interpretation is suspect, since the lightcurve does not have an eclipse profile and hence would not necessarily be related to the binary orbit. Further, whilst the source appears periodic in the first *Chandra* observation lightcurve, the more recent observations suggests that the period is not coherent (see figure 5.3). In addition, unlike M74 X-1, the flaring is not quasi-

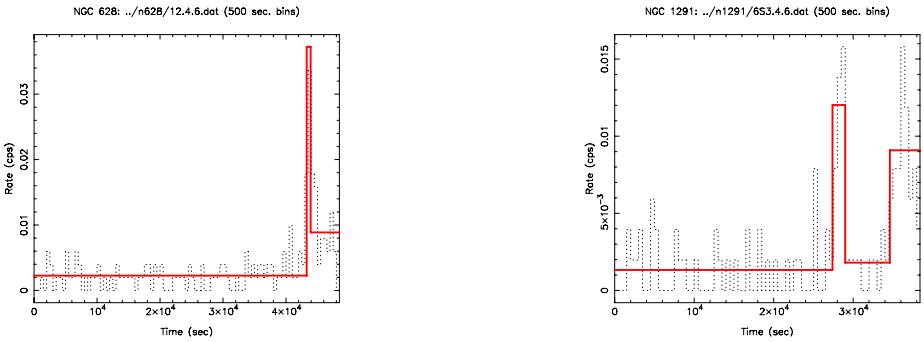

Figure 5.2 Lightcurves for CXOU J013647.4+154745 in M74 (left) and CXOU J031736.8-410901 in NGC 1291 (right) with 500 second time bins. Overplotted in red are the Bayesian block fits to the lightcurves. As can be seen, both observations show clear flaring variability with no obvious periods or quasi-periods.

periodic, as is evident in the power-density spectra shown in figure 5.4. However, the possibility that periodicity is masked due to flaring in the third observation cannot be ruled out. Given the luminosity of the source, the period could be easily detected by the XRT on the SWIFT Observatory, and would be a good candidate for follow-up study. Based on the spectrum, the flaring non-periodic variability, and the position near a young massive star cluster, M51 X-7 is likely a HMXB.

5.4.3 Cool disc blackbodies: intermediate-mass black hole candidates

Three of the sources are well modeled by cool disc blackbodies with $T_{in} \sim 0.1 - 0.3keV$. Two of these three sources have peak $L_x > 10^{39}\,\mathrm{erg\,s^{-1}}$. Five additional sources are equally well fit with either a cool disc or soft power-law. These sources are considered to be good IMBH candidates. As discussed earlier, the disc temperature in stellar-mass black holes is indicative of the temperature of the inner edge of the accretion disc. A lower temperature would indicate a larger inner disc radius and thus

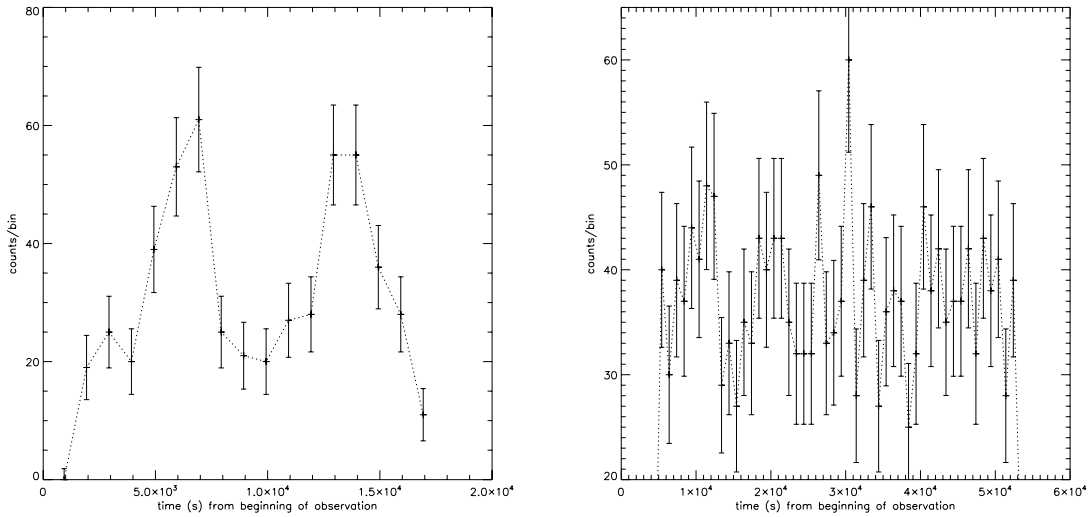

Figure 5.3 Lightcurves of the first and third observations of source M51 X-7. The lightcurve of the first observation suggests that the source is periodic, but the lightcurve for the third observation suggests that this is not the case. Note that the time interval covered in the third observation is around three times that covered in the first.

a more massive source. From the temperature, the radius of the inner disc can be estimated and, if this radius is assumed to be the smallest stable orbit, the mass of the black hole can be calculated (Miller & Colbert (2004)). Sources with temperatures in this range may therefore have masses in the range of thousands of solar masses.

A particularly interesting example of this class of sources is CXOU J140332.4+542103 in M101. Also called P098 in Pence et al. (2001), CXOU J140332.4+542103 is an extremely variable flaring source, and the brightest X-ray source identified in M101. In recent observations, its X-ray flux reaches 10^{41} erg s^{-1} (Kong et al. (2004)), making it one of the most luminous ULXs yet identified, and therefore a very good IMBH candidate. The source is highly variable, with low-state luminosity of around 10^{37} erg s^{-1}. A lightcurve of P098 is shown in figure 5.6.

The spectrum of CXOU J140332.4+542103 is best fit by a cool disc blackbody plus power-law ($kT = 0.13keV and\ \Gamma = 3.84$). However, the harder component is more poorly constrained. The reason for this is demonstrated by Mukai et al. (2003): the variability of the source is confined largely to the emission above 2 keV (see, in particular, their Figure 3). The cool disc temperature combined with the very high X-ray luminosity can imply (at least) two things: either the source is beamed by an uncomfortably high factor or the source is an IMBH with an implied mass of a few thousand solar masses.

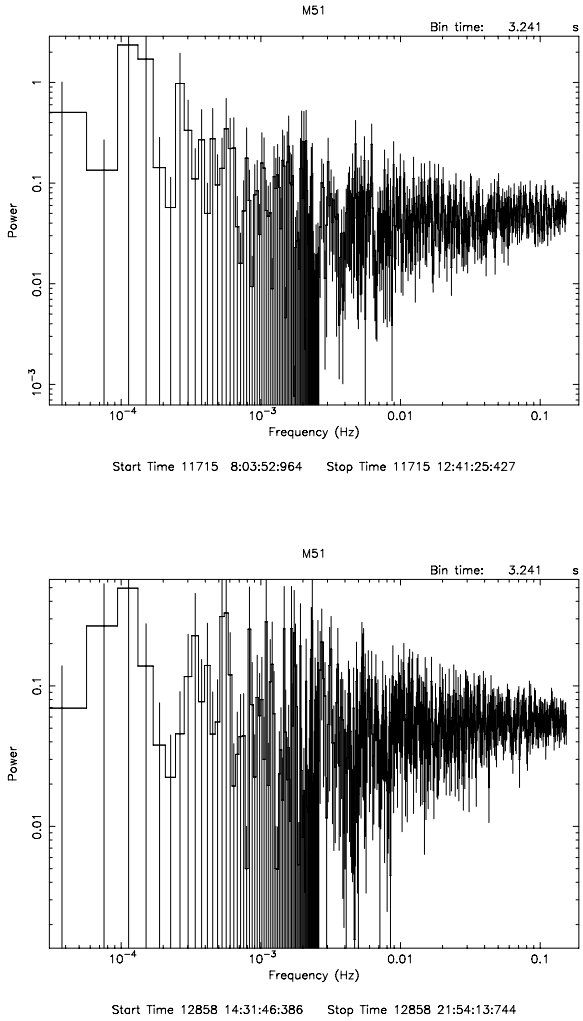

Figure 5.4 Power-density spectra of the first and third observations of M51 X-7. While there is the suggestion of a feature at a few thousand seconds, it is noise-dominated and therefore not statistically significant.

5.4.4 Disc blackbody plus power-law fits: the case of M74 X-1

Four of the sources require power-law plus disc blackbody models. These sources can be fit with either a cool disc blackbody plus power-law continuum (e.g. Miller et al. (2004)), implying that the source is an intermediate-mass black hole, or with a soft power-law plus warm disc component (e.g. Stobbart et al. (2004)). The most intriguing of these sources is CXOU J013651.1+154547 (a.k.a. M74 X-1, see Krauss et al. (2005)). M74 X-1 is a persistent X-ray source whose luminosity peaks at over 10^{40} erg s^{-1}. It has been observed twice with *Chandra* and twice with *XMM* (though we do not present results on the second *XMM* observation as the flux was too faint for detailed analysis). In each of the 3

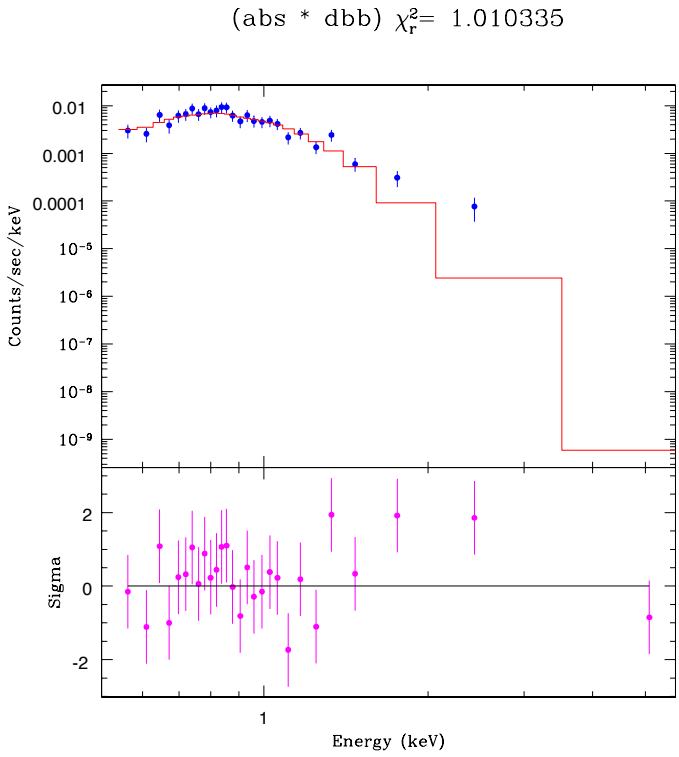

Figure 5.5 Spectrum of source CXOU J140341.3+541904 in M101. The spectrum is well characterised by a cool disc blackbody with $T_{in} = 0.13keV$ plus poorly-constrained soft power-law component. Sources with cool discs have been speculated to be intermediate mass black hole candidates.

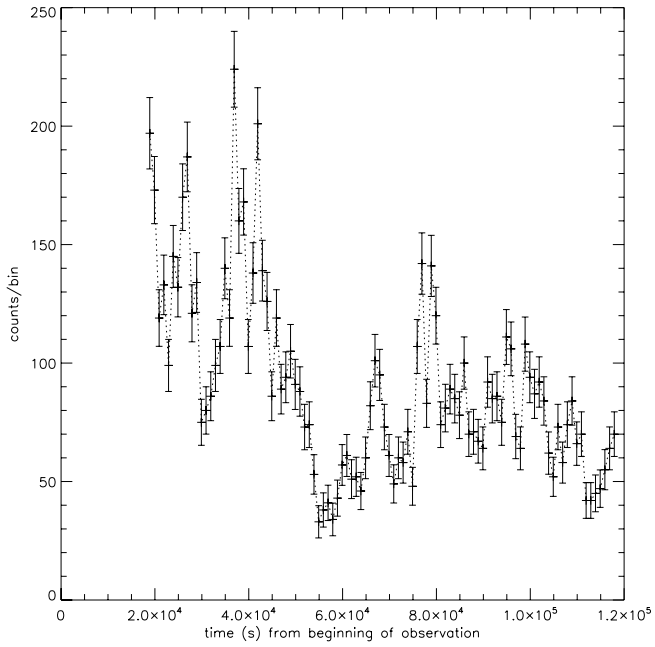

Figure 5.6 Lightcurve of CXOU J140332.4+542103 in M101. The flaring variability is clearly evident.

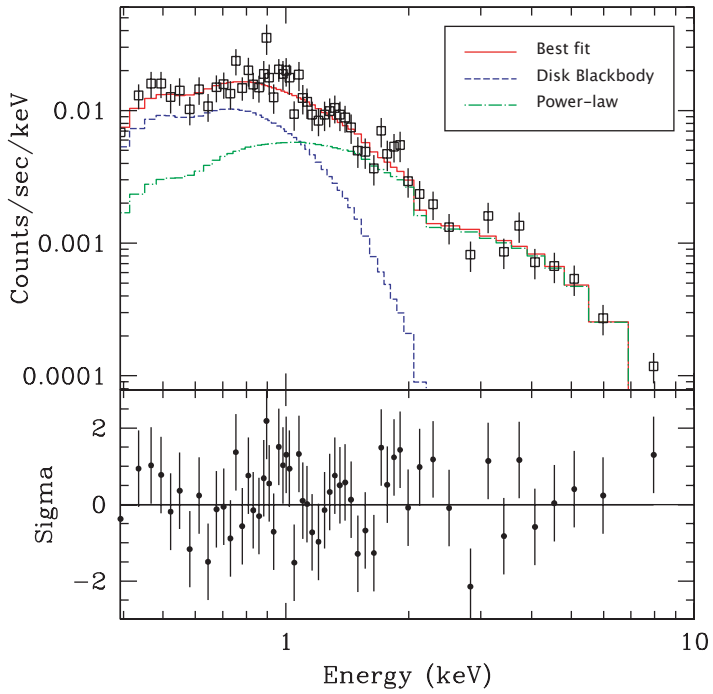

Figure 5.7 Spectrum of source CXOU J013651.1+154547 in M74. The spectrum requires a 2-component fit with power-law $\Gamma = 1.34$ and disc blackbody temperature $T_{in} = 0.25$ keV.

observations discussed here, the source exhibited clear flaring variability with broad QPOs in the power spectrum at frequencies of 3000-7000 seconds (see figure 5.8). This can be directly compared with the Galactic microquasar GRS 1915+105, whose black hole mass is $10 - 20$ $M_\odot$.

The spectrum of M74 X-1 is well-fit by either a power-law plus cool disc blackbody or power-law plus MEKAL model. As discussed above, the cool disc blackbody implies either an intermediate-mass black hole or microquasar-like (e.g Georganopoulos et al. (2002)) beaming. Due to the variability properties, which are similar to Galactic microquasars with observed jets, we prefer the jet model, though an IMBH cannot be ruled out. The MEKAL model also implies a solar-mass BH primary. In addition, M74 X-1 is located near, but not in, several OB associations. This correlation with a star-formation environment implies that M74 X-1 is likely a HMXB, which is consistent with all the spectral models.

We note that Liu et al. (2005) claim that the QPO frequency can be used to determine the black hole mass of the compact object using the $f_b - M$ scaling relation seen in the accretion disc of Galactic XRBs. Using this argument, they estimate the mass at either $2 - 20 \times 10^3$ $M_\odot$ or 10^5 $M_\odot$, depending upon which break frequency they assume to be observed. However, this argument is very suspect for 3 reasons: first, since no break frequency is observed in M74 X-1, one cannot assume that the

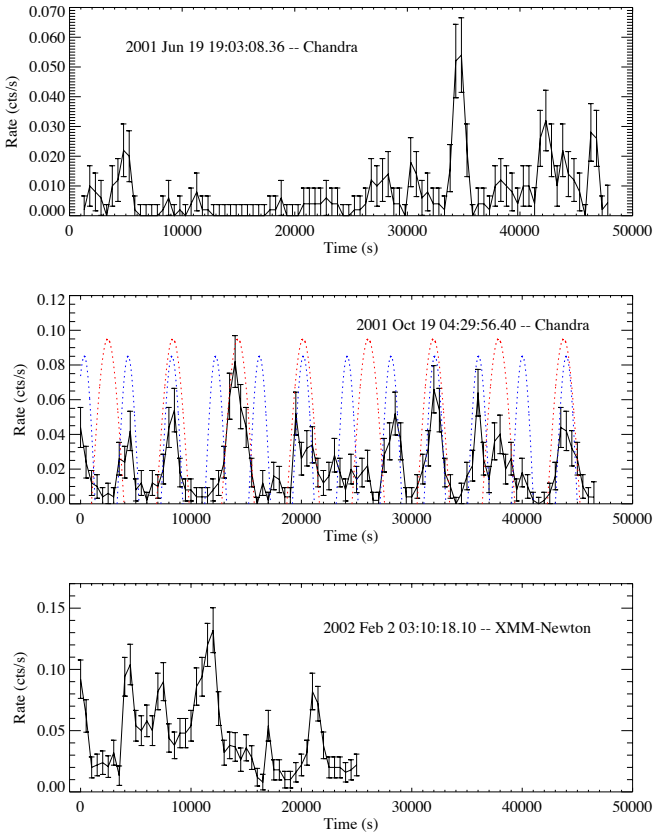

Figure 5.8 Lightcurves of source CXOU J013651.1+154547 in M74. As can be seen, the source is highly variable but non-periodic in all observations.

quasi-period corresponds to a break frequency; second, the QPOs seen within Galactic XRBs arise from a multitude of processes, none of which are necessarily correlated with mass (and the tentative correlation in such sources as Cygnus X-1 are considered speculative by many authors); and third, none of the QPOs in M74 X-1 are coherent periods, as are those seen in Galactic binaries where the QPO frequency is correlated with spin or orbital modulations. This speculative leap from QPO frequency to mass is unwarranted, given that there are no examples of such a correlation in any sources with independently determined masses for the primary.

5.4.5 power-law plus cool thermal component fits

11 sources require two component models which can be fit with a cool MEKAL component ($kT \sim 0.6keV$) plus a warm continuum component (power-law $\Gamma \sim 1.5 - 3.0$). These sources appear similar to hard state black hole binaries and may be stellar-mass black holes with thermal outflows from the

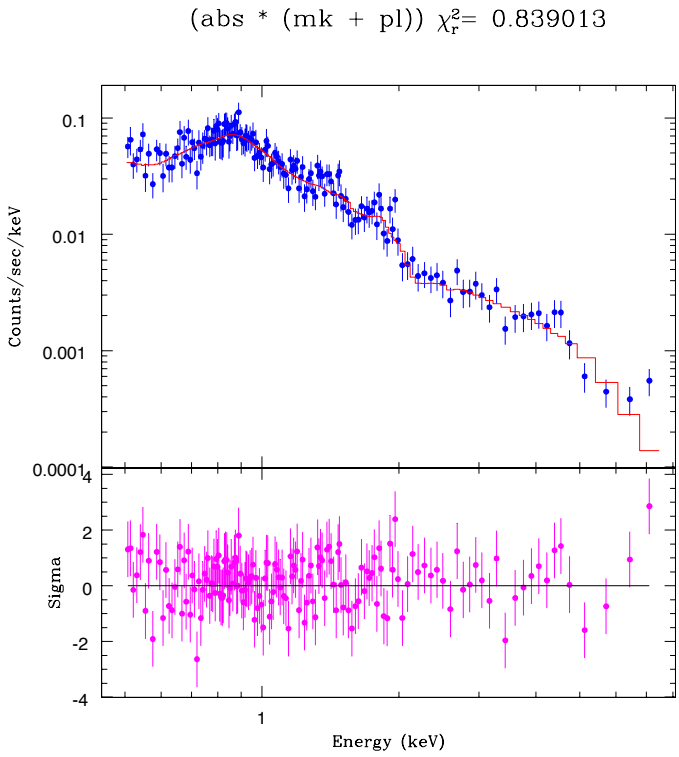

Figure 5.9 Spectrum of source CXOU J125053.1+410713 in M94. Best-fit values are MEKAL $kT = 0.65keV$ and power-law $\Gamma = 1.88$.

companion star. Another possibility is background contamination from diffuse hot gas in the discs of the galaxies. Still a third possibility is a bright background AGN with diffuse emission from the foreground galaxy (our target galaxy) confusing the spectrum. As can be seen in figure 5.10, though it is not required for the fit, there is the indication of $Fe\ K\alpha$ emission around 6.5 keV. While this may suggest that the source is a background AGN with the MEKAL component due to contamination of the spectrum by diffuse emission within our target galaxy, X-ray binaries can also exhibit $Fe\ K\alpha$ emission due to excitation of the accretion disc. We note that Roberts et al. (2004) find evidence for a cool MEKAL component in the ULX NGC 4559 X-4. They speculate that the thermal component is due to thermal outflow from a massive companion star which is excited by relativistic jets from the black hole (e.g. Georganopoulos et al. (2002) and Körding et al. (2002)). However, especially in galaxies with diffuse X-ray emission excited due to high star formation (e.g. M51 and M83), we cannot rule out contamination from the diffuse emission.

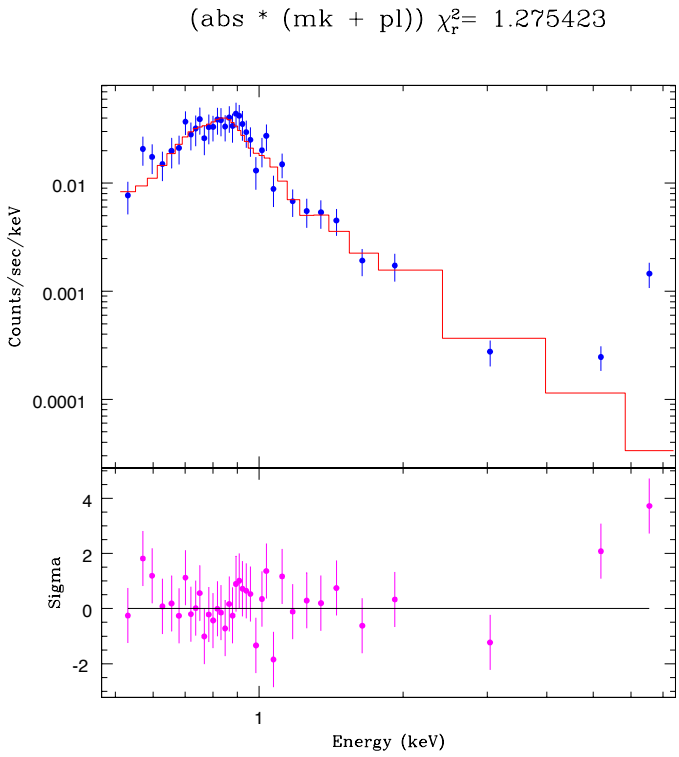

Figure 5.10 Spectrum of source CXOU J132952.7+471143 in M51. The indication of $Fe\ K\alpha$ emission around 6.5 keV suggests that the source is a background AGN.

5.5 Background sources

Three of the sources have very hard power-law spectra and are probably highly absorbed background AGN. We would expect 2-10 of the luminous sources to be background AGN based on the Giacconi et al. (2001) log(N)-log(S) results.

5.6 M82 Sources

The spectra of the M82 sources must be discussed slightly differently than that of the spirals sources due to the nature of the datasets. There are 13 sources in M82 with sufficient counts for spectral fitting, many of them with sufficient counts in the multi-epoch data. Therefore, in addition to the standard tables of best-fit parameters, we can discuss spectral evolution of many of the sources. In addition, there are count rates and inferred luminosities from the two *HRC* pointings available. The *HRC* data is tabulated in the discussion on source variability (6.2).

Table 5.1. Single-Model Spectral Fits to Luminous Spirals Sources. abs = photoelectric absorption, pl = simple power-law model, dbb = disc blackbody model, mk = MEKAL thermal plasma. T_{in} of disc blackbody and MEKAL models are given in keV.

Galaxy	Source	counts 0.3-8.0 keV	model	Γ/T_{in}	N_H ($10^{22} cm^{-2}$)	norm	χ^2_ν/d.o.f. 0.3-8.0 keV	flux ($erg\ cm^{-2}\ s^{-1}$) 0.3-8.0 keV	luminosity ($erg\ s^{-1}$
NGC 278	CXOU J005202.7+473308	67							
		906	abs*pl	1.50	0.41	4.53e-5	50.34/53	2.45e-13	2.12e39
NGC 1291	CXOU J031702.6-410714	666	abs*pl	2.82	0.27	2.56e-5	36.60/33	6.14e-14	5.82e38
		614	abs*pl	2.59	0.19	2.40e-5	28.89/28	5.35e-14	5.07e38
	CXOU J031713.9-411034	669	abs*pl	2.24	0.07	2.63e-5	36.13/32	7.54e-14	7.14e38
		585	abs*pl	2.56	0.12	2.79e-5	26.52/26	5.79e-14	5.49e38
NGC 2681	CXOU J085333.3+511705	450	abs*pl	2.09	0.03	6.68e-6	14.62/21	2.66e-14	2.10e38
		1161	abs*pl	1.84	0.13	2.23e-5	63.08/62	9.55e-14	2.52e38
NGC 3184	CXOU J101812.1+412421	254	abs*pl	1.80	0.11	1.49e-5	11.93/12	6.76e-14	9.96e38
		441	abs*pl	1.91	0.14	1.48e-5	18.09/22	5.92e-14	8.72e38
	CXOU J101823.0+412742	192	abs*pl	1.93	0.17	1.39e-5	4.81/9	5.36e-14	7.90e38
		500	abs*pl	1.90	0.20	2.10e-5	29.80/27	8.01e-14	1.18e39
M94	CXOU J125050.3+410712	1384	abs*pl	1.50	0.015	2.73e-5	86.04/73	1.83e-13	3.67e38
		45							
	CXOU J125052.5+410715	570	abs*pl	1.56	0.11	1.25e-5	29.06/30	7.28e-14	1.46e38
		21							
	CXOU J125052.7+410719	2691	abs*pl	1.83	0.047	6.04e-5	129.68/127	2.86e-13	5.75e38
		189							
	CXOU J125053.3+410714	5325	abs*pl	1.31	0.014	9.58-e5	266.63/244	7.89e-13	1.59e39
		234							
	CXOU J125053.7+410719	837	abs*pl	1.43	0.014	1.61e-5	37.47/43	1.16e-13	2.33e38
		30							
	CXOU J125056.3+410655	494	abs*pl	1.73	0.49	2.46e-5	26.69/27	2.87e-13	5.77e38
		0							
M51	CXOU J132943.3+471135	258	abs*dbb	0.10	0.22	669.825	8.24/6	3.04e-14	1.40e38
		358	abs*dbb	0.14	0.23	651.43	8.27/11	3.09e-14	1.40e38
	CXOU J132952.8+471147	304	abs*mk	0.032	0.43	1.74e-5	17.08/13	3.70e-14	1.70e38
		522	abs*mk	0.17	0.57	2.70e-5	21.71/23	4.02e-14	1.85e38
	CXOU J132953.3+471042	4							
		610	abs*pl	1.51	0.015	2.43e-5	33.17/33	1.61e-13	7.42e38
	CXOU J132953.7+471436	222	abs*pl	1.52	0.11	1.85e-5	7.16/10	1.13e-13	5.19e38
		413	abs*pl	1.20	0.020	1.50e-5	15.37/21	1.40e-13	6.45e38
	CXOU J133001.0+471344	523	abs*pl	1.16	0.054	3.39e-5	26.74/28	3.24e-13	1.49e39
		53							
	CXOU J133006.0+471542	222							
		382	abs*pl	1.39	0.056	1.55e-5	32.93/20	1.16e-13	9.79e38
	CXOU J133007.6+471106	911	abs*pl	2.27	0.11	9.50e-5	46.34/48	2.92e-13	1.34e39
		908	abs*pl	1.87	0.022	4.16e-5	52.69/49	1.97e-13	9.04e38
M83	CXOU J133649.1-295259	437	abs*pl	1.51	0.13	1.06e-5	22.34/21	6.38e-14	3.63e38
		12							
	CXOU J133659.8-295206	348	abs*pl	1.89	0.22	9.80e-6	21.89/17	3.73e-14	2.12e38
		67							
	CXOU J133700.5-295211	348	abs*dbb	0.11	0.48	653.739	19.16/14	8.99e-15	5.12e37
		63							
	CXOU J133703.9-294931	391	abs*pl	1.47	0.098	9.27e-6	9.38/20	5.97e-14	3.40e38
		55							
	CXOU J133707.1-295102	398	abs*pl	1.63	0.12	9.12e-6	15.95/18	4.89e-14	2.79e38
		55							
M101	CXOU J140214.1+542203	385	abs*pl	1.59	0.15	5.04e-6	23.53/17	2.80e-14	1.74e38
		79							
M101	CXOU J140252.9+542112	723	abs*pl	1.43	0.054	7.32e-6	45.14/38	5.13e-14	3.18e38
		56							
	CXOU J140307.4+541938	339	abs*pl	1.08	0.22	4.03e-6	10.30/16	3.97e-14	2.46e38
		13							
	CXOU J140312.5+542057	445	abs*pl	2.07	0.047	2.94e-6	13.43/13	1.27e-14	7.88e37
		26							
	CXOU J140312.5+542053	566	abs*pl	1.73	0.081	3.40e-6	3.98/13	1.76e-14	1.09e38
		45							
	CXOU J140318.1+541823	437	abs*pl	1.57	0.038	3.90e-6	13.62/19	2.38e-14	1.47e38
		45							
	CXOU J140321.5+541946	910	abs*pl	1.97	0.19	1.56e-5	50.07/49	5.60e-14	3.47e38
		110							
	CXOU J140324.2+541949	1049	abs*pl	1.73	0.51	2.37e-5	64.61/60	9.34e-14	5.80e38
		89							
	CXOU J140336.0+541925	1043	abs*pl	2.57	0.076	9.28e-6	33.16/35	2.56e-14	1.59e38
		106							
	CXOU J140341.3+541904	777	abs*dbb	0.13	0.52	118.633	25.26/25	1.12e-14	6.95e37
		26							
	CXOU J140353.8+542158	1499	abs*pl	2.69	0.11	1.53e-5	46.34/52	3.70e-14	2.29e38
		51							
	CXOU J140405.9+541602	1043	abs*pl	1.25	1.21	7.46e-6	29.64/24	4.80e-14	2.98e38
		OC							
	CXOU J140414.3+542604	4290	abs*pl	3.48	0.35	2.44e-4	211.56/204	2.64e-13	1.64e39
		OC							
	CXOU J140416.8+541615	1765	abs*pl	1.77	0.043	1.99e-5	65.05/80	1.00e-13	6.21e38
		OC							
	CXOU J140421.8+541921	1732	abs*pl	2.70	0.012	2.02e-5	64.61/60	6.22e-14	3.86e38
		76							

Table 5.2. Spiral multi-component fits, organized by spectral model, following the abbreviations in table 5.1.

Galaxy	Source	model	comp1	comp2	N_H ($10^{22} cm^{-2}$)	χ^2_ν/d.o.f.	flux ($erg\ cm^{-2}\ s^{-1}$)	luminosity ($erg\ s^{-1}$)
M74	CXOU J013651.1+154547	abs*(dbb+pl)	0.26	1.20	0.11	22.27/17	2.10e-14	1.95e38
		abs*(dbb+pl)	0.25	1.34	0.13	51.94/53	1.36e-13	1.26e39
NGC 2681	CXOU J085333.7+511929	abs*(dbb+pl)	0.11	1.43	0.025	13.27/11	2.41e-14	2.44e38
		abs*(dbb+pl)	0.20	1.75	0.054	17.82/17	2.72e-14	2.75e38
M51	CXOU J132952.4+471144	–						
		abs*(dbb+pl)	0.15	1.72	0.32	19.85/15	3.74e-14	1.72e38
M83	CXOU J133719.8-295349	abs*(bb+pl)	0.77	3.83	0.36	152.52/130	2.95e-13	1.68e39
		OC						
M101	CXOU J140332.4+542103	abs*(dbb+pl)[1]	0.13	3.84	0.15	217.96/160	2.73e-13	1.69e39
		–						
NGC 1291	CXOU J031718.6-410629	abs*(nei+dbb)	0.20	2.53	0.72	70.85/65	3.05e-13	2.89e39
		abs*(nei+dbb)	0.22	2.91	0.77	41.75/31	1.79e-13	1.70e39
M94	CXOU J125052.6+410702	abs*(MEKAL+pl)	0.65	2.97	0.23	24.96/38	5.83e-14	1.17e38
		–						
M94	CXOU J125052.8+410712	abs*(MEKAL+pl)	0.56	1.79	0.014	21.98/25	3.57e-14	7.18e37
		–						
M94	CXOU J125053.0+410711	abs*(MEKAL+pl)	0.62	1.52	0.014	83.37/77	1.62e-13	3.26e38
		–						
M94	CXOU J125053.1+410713	abs*(MEKAL+pl)	0.65	1.88	0.050	131.341/158	3.20e-13	6.44e38
		–						
M51	CXOU J132952.7+471143	abs*(MEKAL+pl)	0.54	2.02	0.038	25.89/21	1.03e-13	4.74e38
		abs*(mk+pl)	0.55	1.71	0.012	40.81/32	8.85e-14	4.07e38
M51	CXOU J132952.8+471139	abs*(dbb+MEKAL)	0.62	0.57	0.015	55.29/52		
		abs*(dbb+mk)	0.74	0.61	0.015	81.98/76		
M83	CXOU J133700.0-295151	abs*(MEKAL+pl)	0.95	1.50	0.099	17.06/17	3.64e-14	2.07e38
		–						
M83	CXOU J133700.5-295156	abs*(MEKAL+pl)	0.59	3.19	0.20	128.92/98	1.13e-13	6.44e38
		–						
M83	CXOU J133700.7-295206	abs*(MEKAL+pl)	0.62	1.47	0.096	58.72/39	5.87e-14	3.34e38
		–						
M83	CXOU J133700.9-295156	abs*(MEKAL+pl)	0.64	1.38	0.039	120.65/118	2.21e-13	1.26e39
M83	CXOU J133701.0-295203	abs*(MEKAL+pl)	1.10	2.42	0.12	91.86/89	1.38e-13	7.86e38
M101	CXOU J140229.9+542119	abs*(MEKAL+pl)	0.83	2.78	0.040	143.48/124	1.34e-13	8.31e38
M101	CXOU J140330.0+542229	abs*(MEKAL+pl)	0.77	2.48	0.62	20.49/19	2.33e-14	1.44e38
		–						
M51	CXOU J132959.6+471558	–						
		abs*(MEKAL+dbb)	0.35	1.17	0.32	27.65/20	7.72e-14	6.52e38
M83	CXOU J133659.5-294959	abs*(MEKAL+pl)	0.51	2.58	0.037	13.24/14	1.33e-14	2.81e37
		–						
M83	CXOU J133700.4-295160	abs*(MEKAL+pl)	0.61	2.88	0.093	134.32/106	1.21e-13	2.55e38
		–						
M83	CXOU J133700.6-295160	abs*(MEKAL+pl)	0.60	2.72	0.073	130.68/88	9.69e-14	2.04e38
		–						
M83	CXOU J133701.2-295157	abs*(MEKAL+dbb+pl)	0.61	0.99/4.52	0.074	55.01/39	4.09e-14	8.63e37
		–						
M83	CXOU J133704.3-295404	abs*(MEKAL+pl)	0.63	1.56	0.063	60.48/43	6.00e-14	1.27e38
		–						
M83	CXOU J133704.4-295122	abs*(MEKAL+pl)	0.63	1.40	0.047	128.87/126	2.86e-13	6.04e38
		–						

[1] This source is slightly piled up, with a pileup fraction of around 3%.

Table 5.3. Best single-model fits to M82 bright sources. The observations are listed in chronological order: ObsIDs 361, 1302, 378, 379, 380 and 2933.

Source	counts	model	Γ/T_{in}	N_H ($10^{22} cm^{-2}$)	norm	χ^2_ν/d.o.f.	flux ($erg\ cm^{-2}\ s^{-1}$)	luminosity ($erg\ s^{-1}$)
CXOU J095554.6+694101	373	abs*pl	2.59	4.37	3.23e-4	9.01/20	2.08e-13	3.79e38
	192	abs*pl	2.72	5.31	4.82e-4	5.60/8	2.35e-13	4.60e38
	39	IC						
	162	abs*pl	3.08	5.24	1.10e-3	1.93/6	3.22e-13	5.86e38
	65	IC						
	161	abs*pl	2.39	3.15	1.16e-4	8.14/6	1.15e-13	2.09e38
CXOU J095552.1+694053	1031	abs*pl	2.47	3.57	4.74e-4	47.95/62	3.97e-13	7.22e38
	527	abs*pl	2.87	4.47	1.05e-3	21.62/30	4.56e-13	8.30e38
	91	IC						
	164	abs*pl	2.01	2.07	9.55e-5	8.05/6	1.86e-13	3.38e38
	58	IC						
	245	abs*pl	2.86	0.04	6.55e-6	9.17/12	1.37e-14	2.49e37
CXOU J095546.4+694041	1237	abs*dbb	1.12	0.31	1.21e-2	78.55/72	2.82e-13	5.13e38
	585	abs*dbb	1.02	0.32	1.79e-2	31.74/33	2.81e-13	5.11e38
	179	IC						
	493	abs*dbb	1.09	0.28	2.04e-2	21.72/27	4.31e-13	7.84e38
	213	abs*dbb	1.23	0.27	1.07e-2	30.36/39	3.80e-13	6.92e38
	968	abs*dbb	1.89	0.095	2.14e-3	37.97/55	4.61e-13	8.39e38
CXOU J095551.4+694035	1136	abs*bb	1.01	0.04	2.20e-6	56.40/66	1.72e-13	3.13e38
	514	abs*bb	1.03	0.62	2.63e-6	34.41/29	1.80e-13	3.28e38
	199	abs*bb	0.83	0.04	3.28e-6	8.40/9	2.61e-13	4.75e38
	355	abs*bb	1.10	0.04	3.46e-6	8.44/19	2.66e-13	4.84e38
	223	abs*bb	0.80	0.34	3.43e-6	13.95/10	2.45e-13	4.46e38
	855	abs*bb	0.88	0.04	2.16e-6	60.78/48	1.71e-13	3.11e38
CXOU J095550.5+694043	967	abs*pl	2.78	3.02	5.11e-4	53.28/58	3.06e-13	5.57e38
	512	abs*pl	3.35	3.44	1.24e-3	19.57/28	3.35e-13	6.10e38
	153	abs*pl	1.83	0.89	1.24e-4	1.60//6	3.82e-13	6.95e38
	478	abs*pl	0.86	1.52	6.95e-5	23.59/27	7.83e-13	1.42e39
	203	abs*pl	1.38	1.03	8.20e-5	7.52/9	4.48e-13	8.15e38
	739	abs*pl	3.55	2.91	8.89e-4	34.31/43	2.14e-13	3.89e38
CXOU J095551.2+694043	1610	abs*dbb	1.85	18.06	2.18e-2	70.28/96	1.15e-12	2.09e39
	827	abs*dbb	2.87	19.28	4.92e-3	40.6748	1.51e-12	2.75e39
	399	abs*dbb	3.59	9.59	7.33e-5	12.10/21	1.94e-12	3.53e39
	418	abs*dbb	2.76	5.00	1.09e-3	16.54/23	5.29e-13	9.63e38
	474	abs*dbb	5.24	3.23	4.14e-4	37.54/26	1.90e-12	3.46e39
	1200	abs*dbb	8.71	8.61	6.08e-5	65.77/71	9.63e-13	1.75e39
CXOU J095551.9+694042	696	abs*pl	1.07	0.08	1.13e-5	28.10/41	1.17e-13	2.13e38
	320	abs*pl	1.25	0.040	9.59e-6	13.49/16	8.08e-14	1.47e38
	88		IC					
	141	IC						
	78	IC						
	385	poor data						
CXOU J095553.7+694050	301	abs*pl	0.98	7.88	3.24e-5	5.34/15	2.05e-13	3.73e38
	121	IC						
	31	IC						
	25	IC						
	22	IC						
	88	IC						
CXOU J095550.2+694022	262	abs*pl	1.66	0.40	1.26e-5	11.56/13	5.60e-14	1.02e38
	122	IC						
	26	IC						
	58	IC						
	34	IC						
	148	IC						
CXOU J095546.0+694026	201	abs*pl	1.34	0.04	6.08e-6	2.26/9	4.60e-14	8.37e37
	95	IC						
	27	IC						
	49	IC						
	22	IC						
	140	IC						
CXOU J095547.3+694059	214	abs*pl	1.31	0.43	7.88e-6	7.40/10	5.40e-14	9.83e37
	93	IC						
	23	IC						
	65	IC						
	31	IC						
	187	IC						
CXOU J095551.0+694051	471	abs*pl	5.73	4.02	1.72e-3	29.71/25	3.36e-14	6.11e37
	193	abs*pl	0.77	0.47	6.93e-6	8.96/8	1.00e-13	1.82e38
	55	IC						
	140	IC						
	86	IC						
	375	abs*pl	5.00	3.95	1.03e-3	23.74/20	4.09e-14	7.44e37

Table 5.4. Fits to the IMBH candidate source CXOU J095550.0+694046. As can be seen, the count rate leads to a very high pileup fraction in the *ACIS* data.

Source	model	Γ	pileup frac.	N_H	χ^2_ν/d.o.f.	flux ($erg\ cm^{-2}\ s^{-1}$)	luminosity ($erg\ s^{-1}$)
CXOU J095550.0+694046	(abs*pl)+pileup	1.41	0.19	1.06	210.31/229	2.18e-12	2.69e39
	(abs*pl)+pileup	1.35	0.19	0.98	100.44/115	2.25e-12	2.78e39
	(abs*pl)+pileup	4.19	0.94	0.04	178.55/93	3.52e-12	4.34e39
	(abs*pl)+pileup	1.39	0.17	1.26	68.67/75	2.84e-12	3.51e39
	(abs*pl)+pileup	1.80	0.19	1.92	43.01/39	2.36e-12	2.91e39
	(abs*pl)+pileup	0.76	0.26	0.97	203.15/167	3.66e-12	4.52e39

5.6.1 M82 Source Spectral Classes

As one would expect with a starburst galaxy where massive star formation has recently been triggered, most of the bright X-ray sources appear to be HMXBs in various spectral states. As can be seen in table 5.3, sources CXOU J095554.6+694101 and CXOU J095552.1+694053 show the characteristics of black hole binaries in the very high state (power-law slope $\Gamma > 2.4$, see Figure 5.12). The sources CXOU J095550.5+694043 and CXOU J095551.0+694051 appear to be in transition between a low/hard state and high/soft state. The sources CXOU J095546.4+694041 and CXOU J095551.4+694035 are in the high/soft state. We will examine these sources in more detail below.

Of the 16 luminous sources in M82, only two exhibit variability that is detectable in either the KS or Bayesian block tests discussed above. Source CXOU J095550.5+694043 is found to exhibit flares at the 99% confidence level in ObsID 378 only, whereas CXOU J095550.0+694046, the famous IMBH candidate, is found to be flaring in ObsIDs 361, 379, and 2933, as well as variability at the 99.5% level from the KS test in ObsID 380. A lightcurve with detected flares is plotted in figure 5.11.

The sources with single-epoch spectra are a bit harder to characterise, but generally appear to be black hole binaries in the low/hard state, though they could also be neutron star binaries in the high state.

M82 also has some spectral oddities. The source CXOU J095551.2+694043 is well fit by a high, varying temperature disc blackbody with little or no emission below 1 keV and very high N_H (up to $2x10^{24}cm^{-2}$, see Figure 5.13). The disc temperature of the source varies from 2 to 8 keV and the flux varies by a factor of 4. In addition, it is coincident with a radio-identified supernova remnant in M82 (McDonald et al. (2002). With such high temperature and no evidence of spectral features, it is unlikely that the X-ray source is a SNR, and the high luminosity (10^{39} erg s^{-1}) makes it unlikely to be

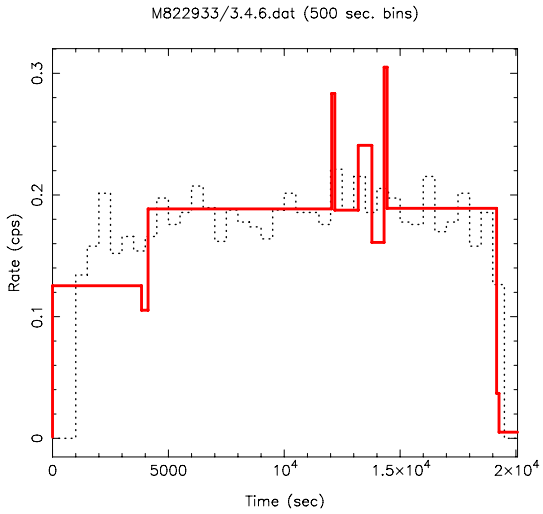

Figure 5.11 Lightcurve of M82 X-1, a.k.a. CXOU J095550.5+694043. The red curve shows flares which are statistically significant at the 99% confidence level.

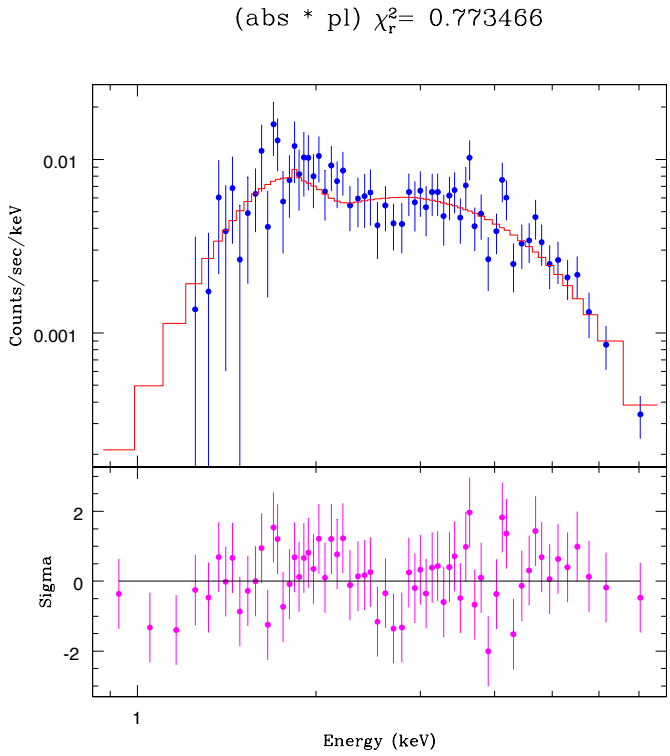

Figure 5.12 Spectrum of source CXOU J095552.1+694053. The spectrum is well fit by a power-law with $\Gamma = 2.47$, characteristic of a very high state BHXB.

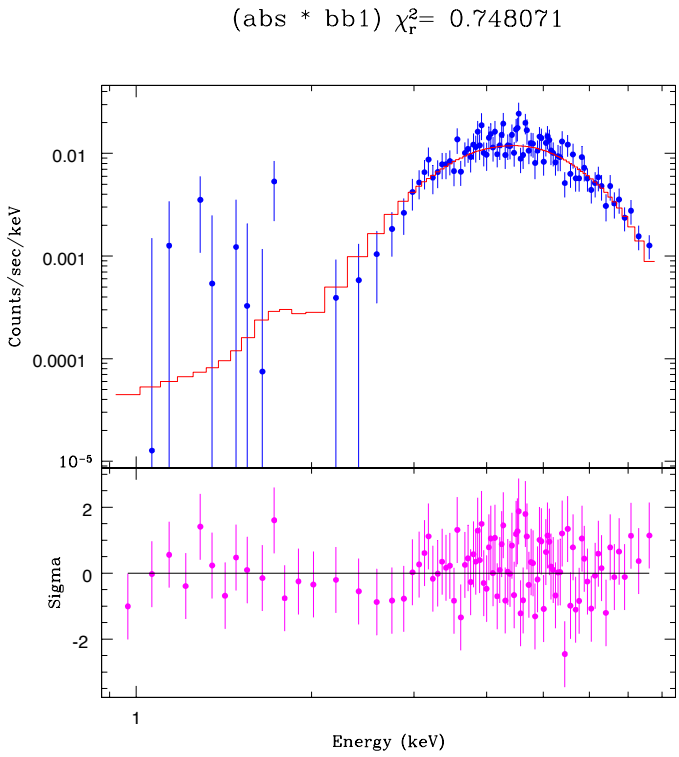

Figure 5.13 Spectrum of source CXOU J095551.2+694043. The spectrum is well fit by a high-temperature disc blackbody with very high absorption.

an isolated neutron star or black hole. It is most likely that the coincidence with the SNR indicates that the source is associated with recent massive star formation.

The source CXOU J095550.0+694046 is the famous intermediate-mass black hole candidate in M82 (see Kaaret et al. (2001) and Matsumoto et al. (2001)). As can be seen in table 5.4, the count rate of the source leads to quite high pileup fractions in the *ACIS* data. Thus, determination of the exact spectral shape of the source can be difficult. However, utilizing the pileup model of John Davis (Davis (2001)), we obtain best fit values of $\Gamma \sim 1.5$, which is comparable to a disc blackbody temperature of $T_{in} \sim 2.5$ keV (see Figure 5.14).. IMBH models, however, predict cool disc temperatures, since high disc temperatures would imply an inner disc radius within the event horizon of the black hole. Thus reconciling the high disc temperatures seen in the *ACIS* data with the luminosities above 10^{40} erg s^{-1} inferred from *HRC* count rates will be quite difficult. It is possible that the emission is Compton upscattered and thus not indicative of the disc temperature. It is further possible that the emission is beamed following the King model discussed above, though the QPO identified in the source by Strohmayer & Mushotzky (2003) would make beaming highly unlikely. If the emission is isotropic,

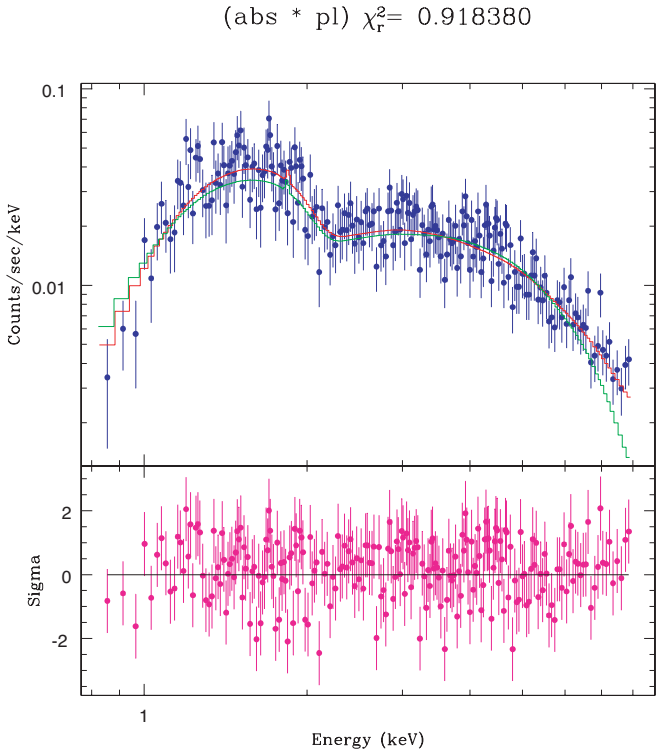

Figure 5.14 Spectrum of source CXOU J095550.0+694046. The best power-law fit with (red) and without (green) the pileup model. As can be seen, without the pileup model, the low energy range of the spectrum is overestimated and the high energy range is underestimated, leading to a much harder best-fit slope ($\Gamma = 0.78$ *vs.* $\Gamma = 1.41$. The pileup fraction for this dataset is around 19%.

the implied mass of the system is $\gtrsim 500\ \mathrm{M}_\odot$, whereas dynamical friction and position within M82 imply an upper limit of $10^5 - 10^6\ \mathrm{M}_\odot$. Two things must then be noted: first, if the mass of the system is closer to the upper range, then any cool disc emission may be below the Chandra energy range if it follows the σT^4 relation discussed in Miller & Colbert (2004); second, the high-flux ($> 10^{40}\ \mathrm{erg\ s^{-1}}$) state has only been observed with *HRC* and *ASCA*, so constraining the low-energy spectrum in that state has not been possible to date.

5.7 Conclusions

Most of the sources within the normal spirals (505/820, 62%) are contained within 4 of the 11 galaxies: M94, M51, M83, and M101. The fraction of sources above $2 \times 10^{38}\ \mathrm{erg\ s^{-1}}$ is even higher (55/64, 86%). This is likely due to higher star formation rates in those galaxies, as will be discussed further in later chapters. The other 7 spiral galaxies in our sample each contain zero to two sources with sufficient

counts for spectral fitting. This trend continues when examining the spectra of M82 sources, most if not all of which show characteristics indicative of black hole HMXBs. The normal spiral sources are also largely black hole binary candidates, likely with a mix of some neutron stars accreting close to the Eddington limit.

These luminous sources dominate the high end of the luminosity functions of the galaxies, as discussed in chapter 7. That the luminous source spectra are characteristic of HMXBs indicates that the number of luminous sources is directly correlated with star formation within galaxies; it is not a function of galaxy class, but rather one of star formation rate and recent star formation history. This correlation is further discussed in chapter 7.

Chapter 6

Source trends

colours, long-term variability, and multi-wavelength counterparts

> Interestingly, according to modern astronomers, space is finite. This is a very comforting thought– particularly for people who can never remember where they have left things.
>
> Woody Allen

6.1 Source Classification by X-ray Colours

6.1.1 Introduction

As has been stated previously, *Chandra* observations of nearby galaxies resolve a multitude of discrete sources. Ideally one would want to perform detailed spectral/temporal analysis of each source individually, but poor counting statistics makes this impossible. However, one can derive fairly accurate and consistent X-ray colours for sources with considerably fewer counts than are required for spectral fitting. In this chapter, I discuss a method for tentative source classification based upon X-ray colours. When this information is combined with variability properties and information about source environ-

ments within their host galaxies, only then can we completely discuss the X-ray source population of nearby galaxies.

The differences in the colours between bulge and disk sources indicates a difference in the source population, and can be used classify the sources in different systems. While it is impossible to classify any individual source with confidence on the basis of X-ray colours alone, it is valuable to be able to separate sources in a statistical sense for population studies.

For this exercise in colour classification, we utilize data taken from the bulge of M31 as a probable "pure" LMXB population in addition to data from the spiral galaxy sample. The M31 data was reduced via an identical procedure to all the other data in this thesis. As mentioned in previously, the bulge of our Galaxy and M31 as well as sources in elliptical galaxies are dominated by low mass X-ray binaries (Fabbiano, 1989; Grimm et al., 2002). We therefore suggest that the region of the X-ray colour-colour diagram populated by "bulge" sources contains many LMXBs. The "bulge" sources are in a region of the diagram characterized by a simple power law slope (photon index 1-2.5) with some intrinsic (to the source) absorption. This is typical of LMXBs (White et al., 1995). By cross-correlating our M31 inner bulge source list with the list given by Kong et al. (2002) we have rejected known foreground and background sources, supersoft sources, and sources for which there may be a contribution from hot gas (e.g. those associated with planetary nebula).

The soft sources (in the lower left of the colour-colour diagram) which appear almost exclusively in disks may be identified as thermal supernova remnants. Supernova remnants are found in regions of on-going star formation, and hence very few are found in elliptical galaxies. Thermal supernova remnants also have soft spectra (Long et al., 1996) consistent with the colours seen here. This is demonstrated in Figure 6.2. The purple boxes show the colours of several known thermal supernova remnants in the Small Magellanic Cloud with spectra measured by ASCA (Yokogawa et al., 2000). Most of these sources lie below the "XRB" region, in the part of the diagram populated by by soft sources. One absorbed SNR has $HC = -0.3$. Additional evidence that these sources are indeed thermal SNR comes from a detailed study of the discrete source population in M83 by Soria & Wu (2003). They find that two of the brightest soft sources have X-ray spectra dominated by emission lines, typical of SNR. However, it is important to stress that some of these soft disk sources may be absorbed supersoft sources (see discussion below.) SNR dominated by non-thermal emission (crab-like objects) may also contribute to the source population. These will have spectra somewhet harder than thermal SNR, and

will probably be located in the "XRB" or "absorbed sources" part of the diagram.

The green circles in Figure 6.2 show the colours of known binary pulsars observed by ASCA (Yokogawa et al., 2000). As noted earlier, most known HMXBs are associated with pulsars in binary systems. Therefore, the HMXBs shown in Figure 6.2 represent only pulsed (neutron star) binaries and not black hole binaries with early-type companions. These sources have spectra similar to black hole LMXB companions (van Paradijs, 1998), and probably are not well separated from black hole LMXB sources in the colour-colour diagram.

There are a small number of sources with essentially no counts above 1keV, and some are undoubtedly classical supersoft sources (Greiner et al., 1991). These "supersoft" sources seem to occur in both bulge and disk systems. They are frequently brighter than the sources identified as supernova remnants, and most are variable. Pence et al. (2001) have identified 10 sources in M101 as supersoft. We do not include 6 of these fainter sources because they have less than 20 counts. We detect the remaining four sources. It is also possible that some (or even all) of the soft sources identified as thermal SNR are absorbed supersoft sources. Absorption will decrease the flux in the lowest energy *Chandra* band, shifting the soft colour vertically upwards on the colour-colour plot (see also 6.1.2). If this is the case, we have identified a new population of faint, absorbed, accretion-powered soft sources in disk galaxies, probably associated with the young stellar population. We favor the hypothesis that the soft source population is dominated by SNR, but a new population of accretion-powered soft sources cannot be ruled out. An in-depth study of the variability and spectral characteristics of the soft sources (see Section 6.1.3) is required to distinguish between these two models.

6.1.2 Absorption and Overlap in Source Type

There will undoubtedly be some overlap in source type in the colour-colour diagram, both because different sources have intrinsically similar spectra (e.g. black hole binaries with high and low mass companions) and because of absorption.

Photons in the lowest energy *Chandra* band will be preferentially removed in an absorbed source, making SC "harder". This will move the source vertically up the colour-colour diagram, as illustrated in Figure 6.2. When the absorption becomes very severe ($n_H \sim 10^{22}$) photons in the medium *Chandra* band will also be removed, causing HC to become harder. The source will then curve to the right in

Figure 6.2, as shown by the tracks of increasing absorption. Absorption will cause supersoft sources to be confused with SNR, move SNR into the XRB region of the diagram, and blur the distinction between all sources once absorption becomes very high. Colour information in the *Chandra* bands will be very limited for highly inclined galaxies, where essentially all low energy photons are lost. In this case, sources distinguished primarily on the basis of their soft colour will be confused (SNR, supersoft sources, XRBs), and only a very rough separation on the basis of hard colour will be possible.

6.1.3 Luminosities, Variability and Spatial Distribution

The soft sources identified above as supernova remnants have considerably less scatter in their luminosities than do sources with harder colours – i.e. a higher fraction of the sources in the HMXB part of the diagram have luminosities $> 10^{37}$ erg s^{-1}. The larger scatter in the luminosities of sources with harder colours is naturally explained if many of these objects are accreting binaries. Binaries can reach much higher luminosities (especially in a flare state) than is typically observed in evolved SNR (10^{36}-10^{37} erg s^{-1}). The X-ray luminosities of the soft sources are typical of brighter SNR; there are certainly other soft sources below our detection threshold. Several of the brightest soft sources have very extreme colours (SC=-1) and have colours and luminosities characteristic of supersoft sources (Kahabka et al., 1994). These are probably accretion powered.

If the soft sources are supernova remnants, they should show little or no evidence for variability. When SNR are young ($\leq$ 1000 years) several emission mechanisms might contribute to the X-ray emission, and the flux may be variable (Schlegel, 1995). However, once the remnant enters the adiabatic phase the luminosity should decline gradually (Jones et al., 1981; Hamilton et al., 1983). In contrast, accretion-powered supersoft sources are known to be variable ((Kahabka et al., 1994; Kong et al., 2002), and detection of variability in a large fraction of the soft sources would support the hypothesis that they are accretion-powered. Both M101 and M83 have one deep exposure in the *Chandra* archive, with a second shorter observation. The second shorter exposure of M83 was taken 16 months after the first, and the second exposure of M101 taken 7 months after the first. In the long (100ks) pointing of M101 there are 28 soft sources (potential SNRs) detected. Most of these have 20-100 counts and are not detected in the short (10ks) observation. This does not provide very stringent constraints on the variability of the soft sources, since to be detected in the short observation they would have to increase in flux by factors of 5-10. There are two "soft" sources detected in both the long and short observation. One

source with $SC = -0.8$ shows no evidence for variability. Another source is significantly variable, and has a $SC = -0.78$ in the long observation. This source has a luminosity of $\sim 10^{39}$ erg s^{-1}, and is the brightest object in M101 (source 98 from Pence et al. (2001)). It is highly variable and is clearly an accretion source.

There are 28 soft (possible SNR) sources detected in M83 in the long (50ks) observation. A total of 7 sources with soft colours that were detected in the long observation were also detected in the short observation. Two of these are clearly variable, while the remaining 5 have approximately constant flux. Of the 28 soft sources detected in the long observation, 5 sources should have been detected in the short (10ks) observation, assuming no variability. Three of these have extremely soft colours, are clearly variable and are probably supersoft sources. The remaining two sources may have declined in flux between the two observations.

6.1.4 The X-ray Colour-Colour Diagram

The initial work on source classification by X-ray colours was presented in Prestwich et al. (2003). In this work, we discussed the apparent differences in source populations between bulge-dominated and disc-dominated systems in colour-space. This difference indicates a distinction in source population between the different galaxy types. As can be seen in figure 6.1, the sources in bulge systems are clustered in colour-space whereas those in disc systems are more spread in colour space.

It has been well demonstrated that the bulges of the Milky Way and M31 as well as sources in elliptical galaxies are dominated by LMXBs (see, e.g. Fabbiano (1989) and Grimm et al. (2002)). We therefore have suggested that the region of colour-space populated by bulge sources largely contains LMXBs. This is consistent with the typical X-ray spectra of LMXBs as discussed in 3.4.2. Similarly, the region of the colour-colour diagram populated by soft sources, which are predominantly found in the disc galaxies, is well-matched to the X-ray spectra of thermal supernova remnants (Long et al. (1996); Yokogawa et al. (2000)). In Prestwich et al. (2003), we further made the distinction between LMXBs and HMXBs. However, for the purpose of this work, I will not make the distinction in assigning an X-ray binary source class based entirely upon colour.

As discussed in 4.1, we have modified this colour classification scheme slightly to be more consistent with what has been done in the literature. This has an additional benefit: the colour bands are defined to

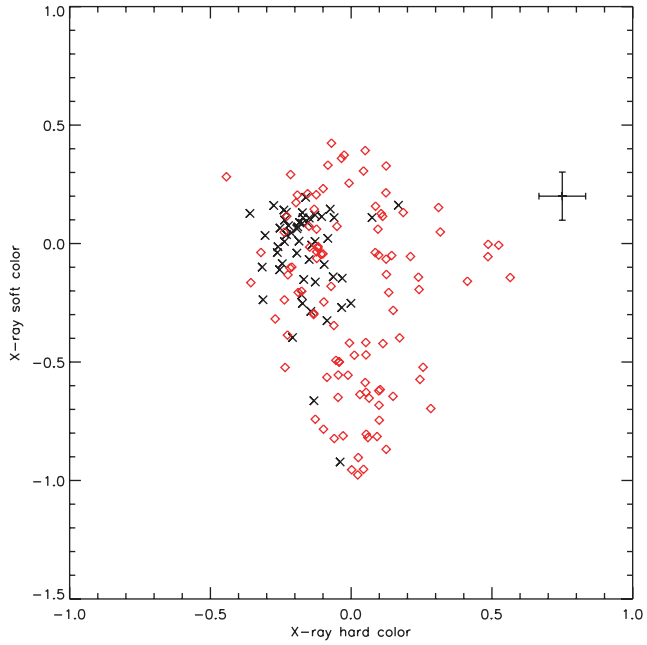

Figure 6.1 X-ray hard colour (x-axis) plotted against X-ray soft colour for the inner bulge of M31 (*crosses*) and the disc of M101 (*diamonds*). X-ray hard colour is defined as $H2 = (H - M)/T$, X-ray soft colour as $H1 = (M - 2)/T$. This is figure 1 from Prestwich et al. (2003).

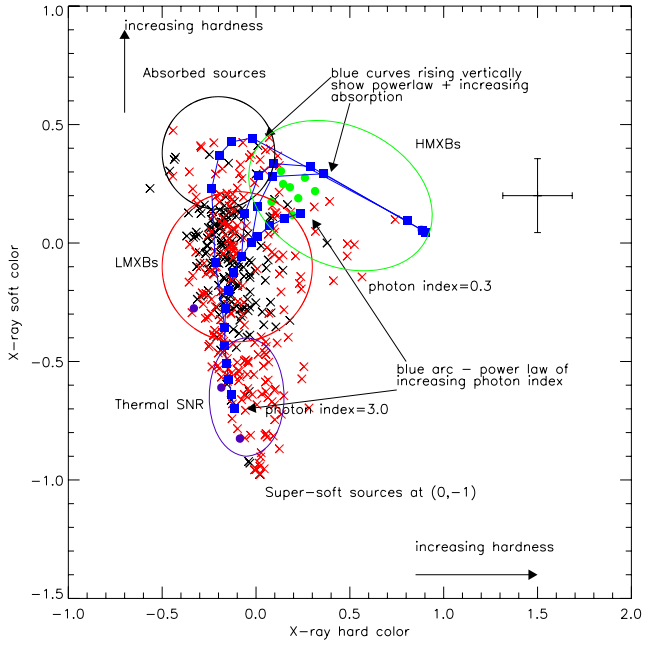

Figure 6.2 Proposed classification scheme from Prestwich et al. (2003). Note that we do not attempt to segregate HMXB and LMXB populations in this thesis, though we made a speculative attempt to do so in Prestwich et al. (2003). The blue arc of points stretching from (0.3,0.15) to (-0.1,-0.7) show the colours of a simple power law spectral model with photon index increasing from 0.7 to 3.0. The blue curves rising vertically show the effect of adding absorption to power law slopes of photon index 1.0, 1.2 and 2.0.

be self-consistent; that is, the numerator of each colour term does not contain a value not present in the denominator and vice versa. The advantage of this method is that the error propagation becomes much simpler; the hard colour error is not dependent upon the value of soft colour, nor is the soft colour error dependent upon the hard colour.

Presented in figure 4.1 is a colour-colour diagram, following the scheme in Prestwich et al. (2003) but in our modified colour bands, with no data plotted on it. The blue lines represent power laws of decreasing photon index (hardening spectrum). As absorption is added for a given photon index, sources travel up and to the right along the curves. Ellipses outline the major source categories.

The diagram contains a section called ”background sources” to the lower right. However, these sources are likely not typical AGN, and likely not background sources. They are found almost exclusively in M83 and M101 and have very large errors on the value of hard colour but much smaller errors on the soft colour. It is thus likely that these sources are soft sources, either SNRs or HMXBs, which are very bright in the soft band and have some emission component above 2keV but almost no detected photons in the medium band. It should be noted that, however, there is a similar class of ”hard/soft” sources in medium depth X-ray surveys, e.g. Wilkes et al. (2005), so the possibility that some of these sources are background sources cannot be ruled out, especially since M83 and M101 have the largest sky coverage of any of our observations.

Plotted in figures 6.3 through 6.8 are colour-colour diagrams for the 11 spiral galaxies in our sample and M82. in table 6.1 we list the number of sources per galaxy in each colour classification. Note that we only classify sources with greater than 25 net counts in one observation. Discussion about populations as derived from X-ray colours for each galaxy can be found in appendix 10.

6.2 Long-term variability

As was discussed in chapter 5, X-ray binaries exhibit variability on a myriad of timescales. Since we have at least two epochs of data for almost all our sources, it is possible to study variability on the scale of months to years. In addition, the luminous sources discussed previously have sufficient counts to allow for tests of short-term variability (timescales of tens to thousands of seconds) during each observation. We shall discuss both of these in turn.

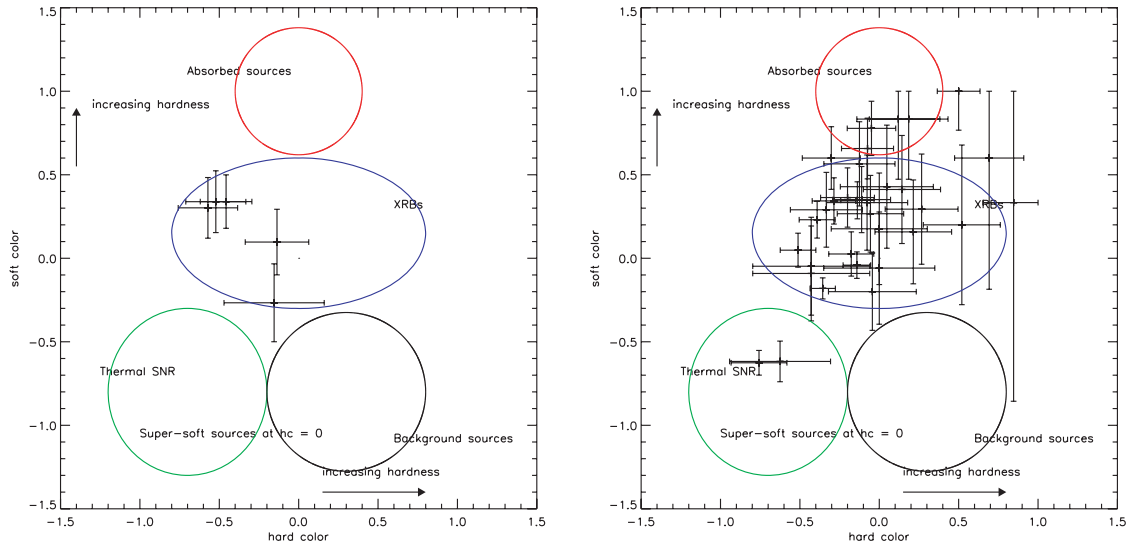

Figure 6.3 NGC 278 (left) and M74 (right).

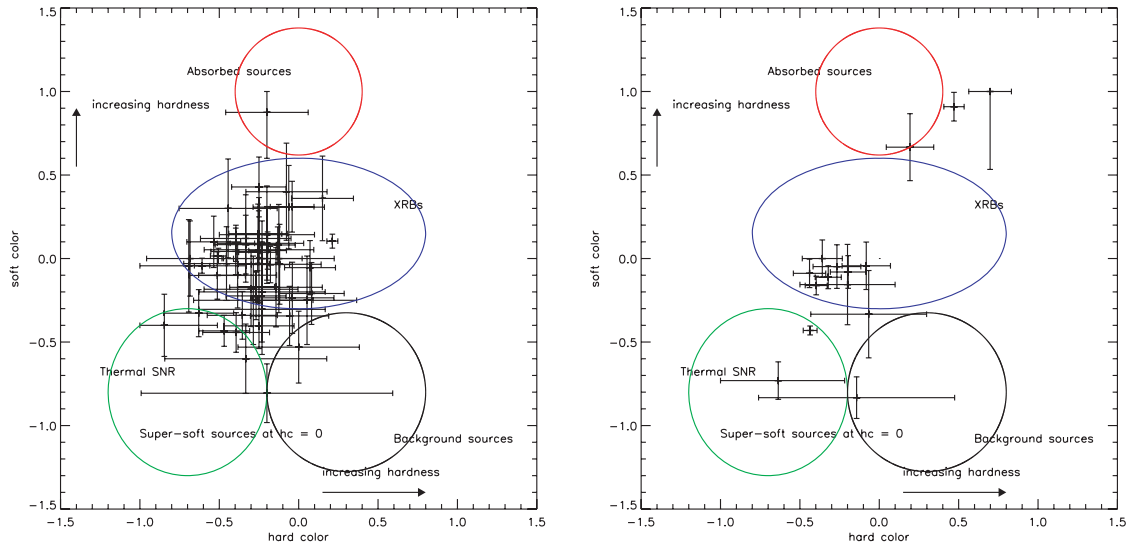

Figure 6.4 NGC 1291 (left) and NGC 2681 (right).

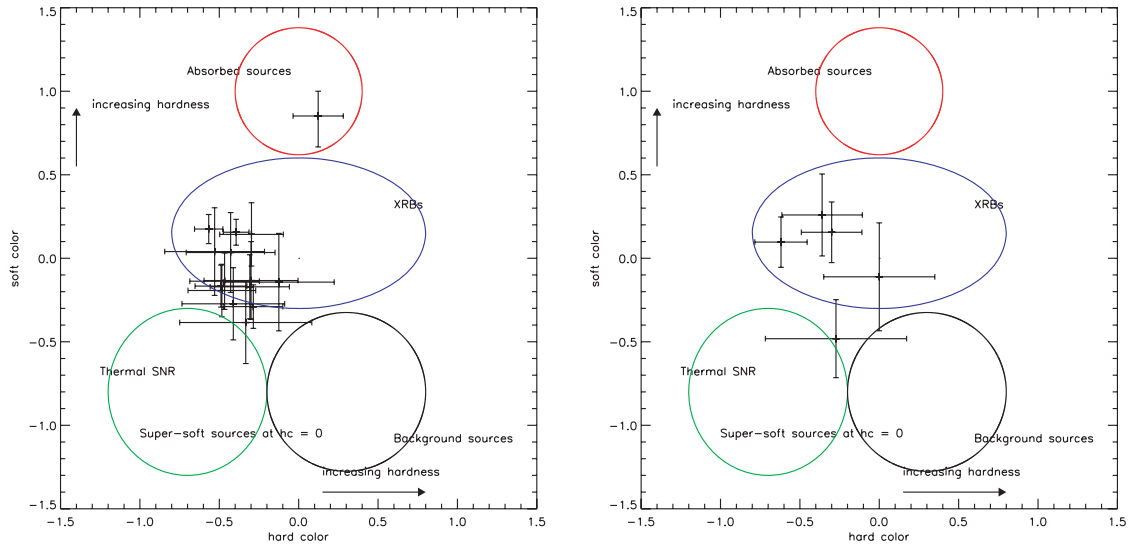

Figure 6.5 NGC 3184 (left) and NGC 4314 (right).

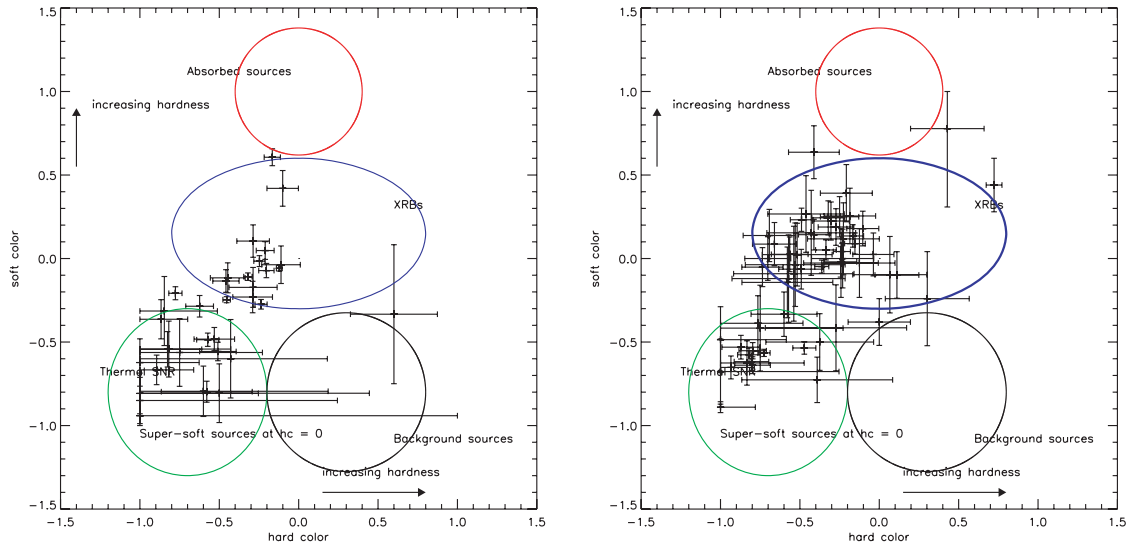

Figure 6.6 M94 (left) and M51 (right).

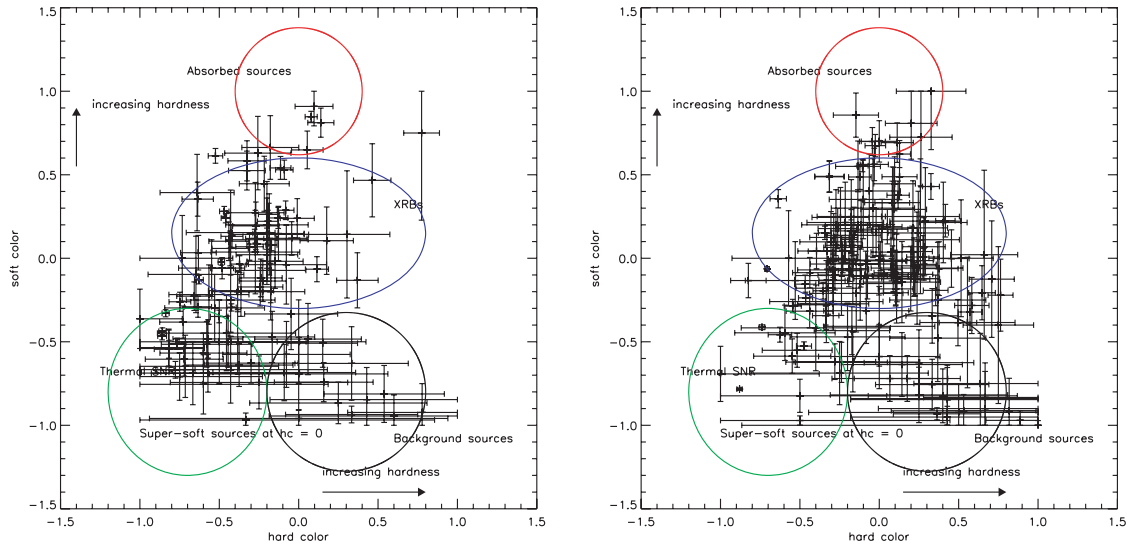

Figure 6.7 M83 (left) and M101 (right).

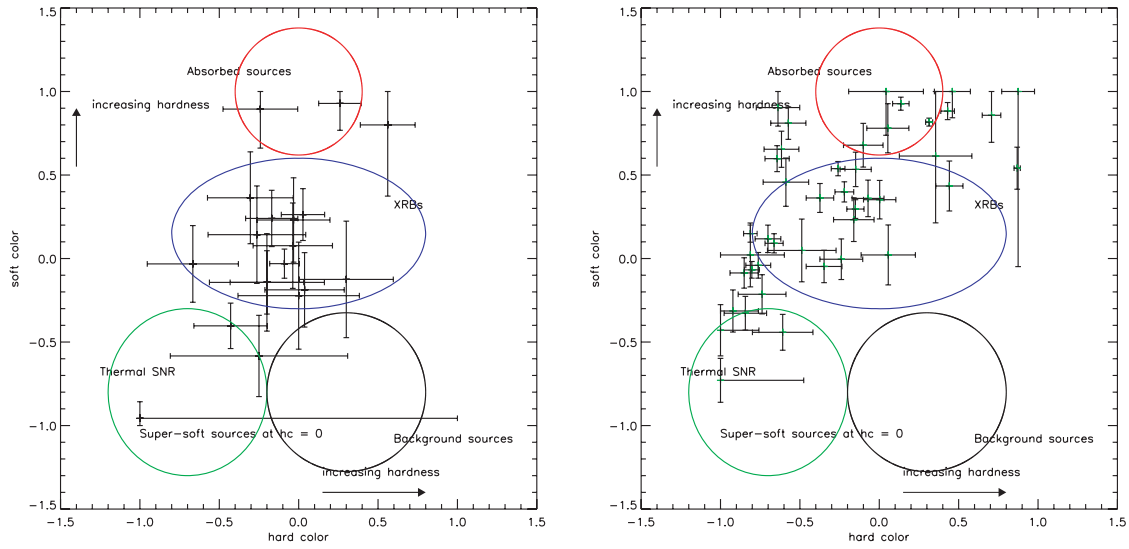

Figure 6.8 IC 5332 (left) and M82 (right).

Table 6.1. Results of colour-classification.

Galaxy	No srcs	No. srcs $\geq$ 25 cts	XRBs	SNRs	BKG	ABS
NGC 278	14	5	5	0	0	0
M74 (NGC 628)	67	33	26	2	5	0
NGC 1291	93	53	42	8	1	2
NGC 2681	23	17	12	2	2	1
NGC 3184	49	18	14	1	2	1
NGC 4314	19	5	4	1	0	0
M94 (NGC 4736)	50	35	16	17	1	1
M51 (NGC 5194/95)	116	42	27	13	1	1
M83 (NGC 5236)	131	115	61	29	8	17
M101 (NGC 5457)	208	163	106	16	9	30
IC 5332	50	19	13	3	3	0
M82	107	54	25	5	23	0

6.2.1 Long-term Variability of Spiral Source Population

As discussed previously, a large fraction of the source population is variable on both short and long timescales. It should be mentioned that all variability numbers quoted throughout are, necessarily, lower limits. For the purposes of this discussion, we consider only sources whose positions are on the detector in both *Chandra* observations. To determine the range of long-term variability we would expect to detect given our data, we performed variability simulations. The source data were allowed to vary randomly by fixed quantities (10, 20, and 50%) and Poisson noise was added. The data were then scaled to the duration of the second *Chandra* observation, and tested for statistically significant variability at the 90% level. The results are summarised in table 6.2: the simulations clearly demonstrate that a much larger fraction of sources must truly be variable (beyond those with detected variability) in order to arrive at the observed variability fractions. For example, in the case of M51, 31% of the sources are observed to vary. From the simulations, if 100% of the sources varied by 50%, we would only detect 24% of them as variable. This is largely due to the low flux of many of the sources.

Table 6.2. Results of variability simulations.

Galaxy	No. srcs [1]	Frac. srcs [2]	Frac. var [3]	Sim. var [4]	Det. var [5]
NGC 278	14	1.0	0.5	0.31/0.25	0.20
		0.5	0.5	0.15/0.12	
		1.0	0.2	0.04/0.04	
		0.5	0.2	0.02/0.02	
M74 (NGC 628)	67	1.0	0.5	0.27/0.26	0.23
		0.5	0.5	0.13/0.13	
		1.0	0.2	0.04/0.04	
		0.5	0.2	0.02/0.02	
NGC 1291	93	1.0	0.5	0.25/0.25	0.29
		0.5	0.5	0.12/0.13	
		1.0	0.2	0.03/0.05	
		0.5	0.2	0.01/0.03	
NGC 2681	23	1.0	0.5	0.37/0.38	0.43
		0.5	0.5	0.18/0.19	
		1.0	0.2	0.09/0.09	
		0.5	0.2	0.04/0.04	
NGC 3184	49	1.0	0.5	0.15/0.35	0.24
		0.5	0.5	0.08/0.17	
		1.0	0.2	0.01/0.08	
		0.5	0.2	0.01/0.04	
NGC 4314	19	1.0	0.5	0.17/0.17	0.14
		0.5	0.5	0.08/0.09	
		1.0	0.2	0.02/0.02	
		0.5	0.2	0.01/0.01	
M94 (NGC 4736)	50	1.0	0.5	0.15/0.16	0.14
		0.5	0.5	0.08/0.08	
		1.0	0.2	0.02/0.02	
		0.5	0.2	0.01/0.01	
M51 (NGC 5194/95)	117	1.0	0.5	0.24/0.24	0.31
		0.5	0.5	0.12/0.12	
		1.0	0.2	0.04/0.06	
		0.5	0.2	0.02/0.03	
M83 (NGC 5236)	131	1.0	0.5	0.27/0.31	0.24
		0.5	0.5	0.13/0.15	
		1.0	0.2	0.04/0.11	
		0.5	0.2	0.02/0.05	
M101 (NGC 5457)	208	1.0	0.5	0.14/0.13	0.10
		0.5	0.5	0.07/0.06	

Table 6.2—Continued

Galaxy	No. srcs [1]	Frac. srcs [2]	Frac. var [3]	Sim. var [4]	Det. var [5]
		1.0	0.2	0.01/0.05	
		0.5	0.2	0.01/0.02	
IC 5332	50	1.0	0.5	0.23/0.24	0.17
		0.5	0.5	0.12/0.12	
		1.0	0.2	0.03/0.03	
		0.5	0.2	0.02/0.02	

[1]Total number of sources detected in the galaxy

[2]Fraction of sources allowed to vary each iteration

[3]Fraction of flux by which the sources were allowed to vary

[4]Fraction of sources with detectable, statistically significant variability in the simulation for each *Chandra* observation

[5]Observed variability fraction

In section 6.1, we discussed how the colours of X-ray sources may allow insight into the nature of the sources (Prestwich et al., 2003). This colour sorting method, combined with the variability, should allow us to confirm if the sources fall into the coarse bins of XRBs and SNRs. Sources that are variable should, for the most part, fall outside the colour-space defined as SNRs, roughly colours $HC < -0.2$ and $SC < -0.3$. As can be seen in figure 6.9, the majority of sources that exhibit statistically significant variability between the two *Chandra* observations and that contain a sufficient number of counts in both observations to obtain accurate colours do indeed fall within the XRB band.

6.2.2 Long-term Variability of M82 Sources

With the sources in M82, it is not necessary to resort to 2-point variability calculations as with our spiral galaxy sample, since we have 8 epochs of data. In Figures 6.10 and 6.11, we present the 8-epoch lightcurves for the 16 brightest sources in M82. As can be seen from the lightcurves, most of the luminous sources are variable, again consistent with the interpretation of these sources as accretion-driven. As discussed in section 5.6.1, many of these sources may also exhibit short-term variability that is not detectable in our diagnostics due to the diffuse background.

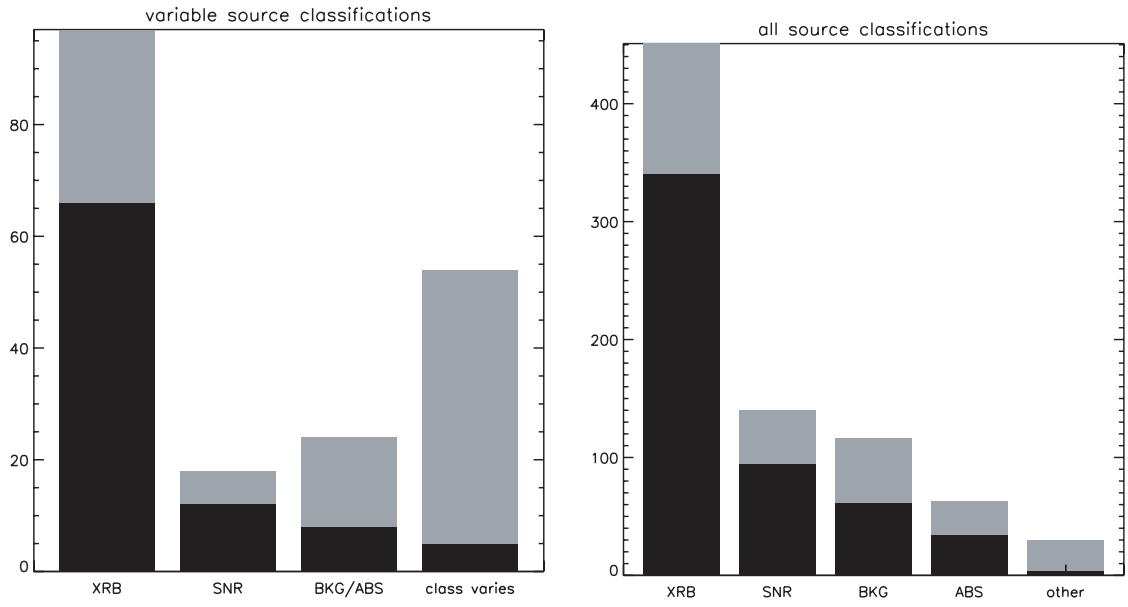

Figure 6.9 X-ray point source classifications for all sources in the 11 survey galaxies, using the colour classification scheme of Prestwich et al. (2003). The left-hand plot shows source classifications for the sources whose fluxes vary at the 90% level between *Chandra* observations. The black bars indicate sources with greater than 25 counts in both observations. The right-hand plot indicates source classifications for all sources, taken from the longer *Chandra* observation of each galaxy or, for observations of approximately equal length, the observation for which colours were best determined. Black bars indicate sources with greater than 25 counts. These plots suggest that the source classification scheme is good to a first approximation: Sources classified as XRBs or AGN tend to vary, whilst those classified as SNR do not.

6.3 Multiwavelength Counterparts and X-ray Source Environments

6.3.1 Introduction

The multiwavelength properties of X-ray sources can provide further insight into the nature of the sources. If one can identify a direct optical counterpart to an X-ray binary, for example, then one knows if the source is an LMXB or an HMXB. This in turn will tell us something about the star formation history of the host galaxy. In addition, by examining the environment of an X-ray source within its host galaxy, one may also learn something about the nature of the source. Kaaret et al. (2004) have demonstrated that X-ray sources in starburst galaxies are located near, but not often exactly coincident

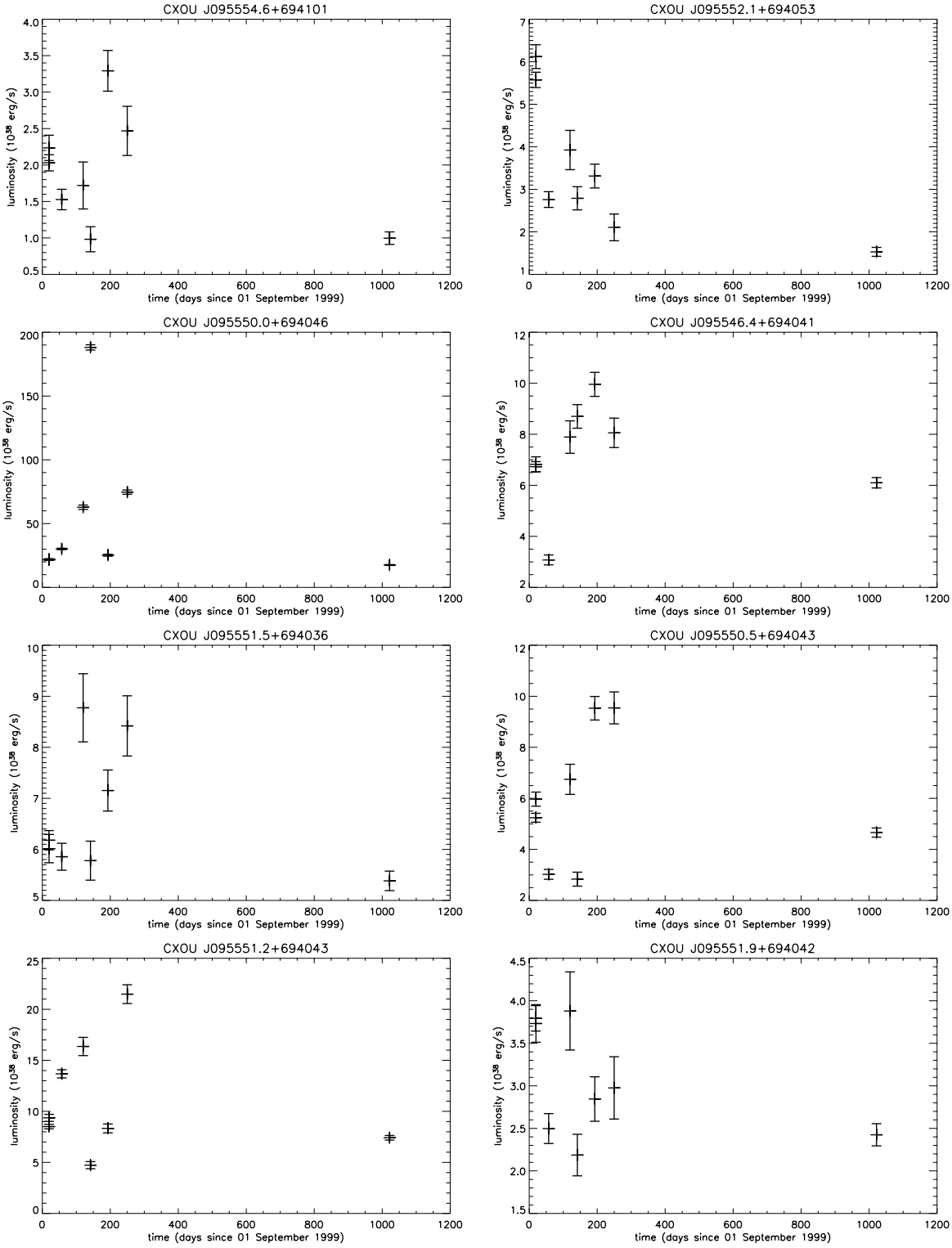

Figure 6.10 Lightcurves for 8 of the luminous X-ray sources in M82. Most of the sources exhibit obvious long-term variability.

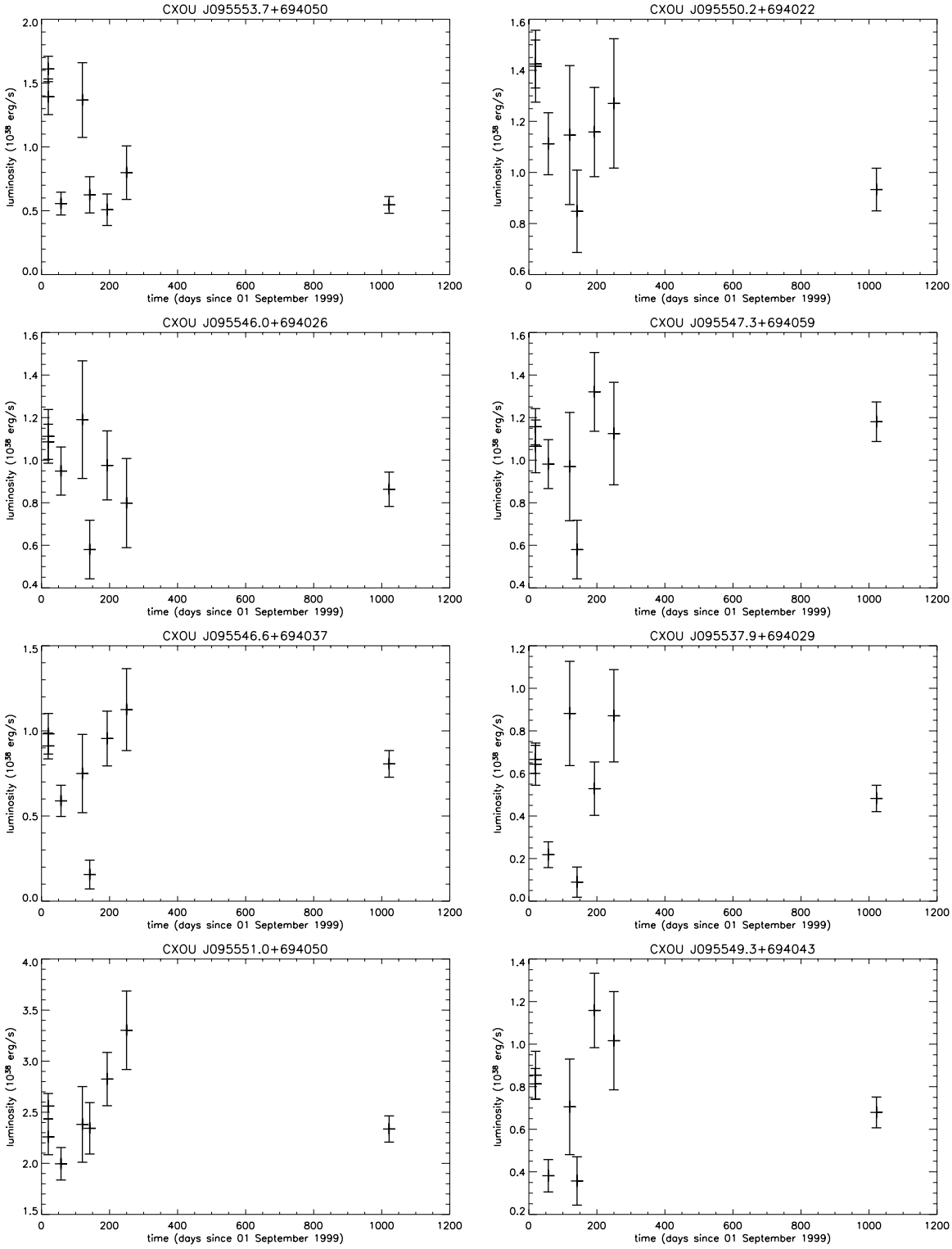

Figure 6.11 Lightcurves for 8 more of the luminous X-ray sources in M82. Most of the sources exhibit obvious long-term variability.

with, massive young star clusters. This indicates that the sources are likely associated with recent star formation. The displacements from the clusters indicates that the sources are likely XRBs that have been ejected from the clusters due to N-body interactions or supernova kicks.

In order to search for counterparts to X-ray sources, we first have conducted a thorough catalog search around the coordinates for the source. In addition, we have searched for optical counterparts in our own data obtained at the Fred L. Whipple Observatory 48" telescope on Mt. Hopkins, Arizona, and at the SARA 0.9-meter telescope on Kitt peak, Arizona. We have also analyzed archival optical data from the *Hubble Space Telescope*. In this chapter I provide a thorough analysis of any direct optical counterparts found for all our X-ray sources. I also discuss the environments of these sources within their host galaxies.

6.3.2 Data analysis

These results are based on catalog searches within $2''$ radius of the *Chandra* position, as well as $2''$ searches of the optical data mentioned above. Obviously the availability and quality of catalog data for the galaxies will affect the results presented; thus I will briefly discuss the data available for our sample. The search radius was chosen for two main reasons: that the *Chandra* source positions are good to within around $2''$ even in the most off-axis sources; and that the ground-based optical data was taken with seeing of around $2''$.

For all of the galaxies except NGC 1291, M83, and IC 5332, we have obtained data in the *Johnson U, B, V, R, and I* filters as well as $H\alpha$ and $[SII]$ line filters which have moderately broadened throughput for observing galaxies at a distance comparable to that of the Virgo cluster. These data were taken with the FLWO 48" telescope. For M83, we have observations in $Johnson\ V$, $H\alpha$ and the associated continuum filter, taken with the SARA 0.9 meter telescope. For NGC 1291 and IC 5332, which are located in the southern sky, we only have ground-based data from the digitized sky surveys.

Archival $HST/WFPC2$ data is available for all of the galaxies in our sample in an assortment of filters and exposure times. Where possible, we have utilized the available published catalogs from these HST observations rather than reanalyze all the data ourselves.

We also have obtained Gemini $g', r', and\ i'$ observations of M74, made available through the Gemini

early data release program. For M82, we will utilize the results from Kaaret et al. (2004).

All ground-based optical data were processed using $IRAFv.2.12$. Standard flat fielding and dark and bias corrections were performed. Bad pixel maps were constructed and corrections applied. The data were then aligned using the $SExtractor$ software available from the Smithsonian Astrophysical Observatory Telescope Data Center. Searches for stars and clusters were performed using the $DAOfind$ routine, and all matches were visually inspected.

6.3.3 Source Counterparts and environments

The search for direct counterparts is made quite difficult by the fact that, though X-ray imaging was advanced considerably with the launch of *Chandra*, the error ellipse for typical *Chandra* sources is still quite large as compared to the optical data. For example, an on-axis detection of a point source with *Chandra* will typically have a 3σ error ellipse of no smaller than $0.5''$ radius. This corresponds to a radius of 12 pc at 10 Mpc. If one registers the images using matches with foreground stars or background quasars, this can be improved by about a factor of 3, but this is still insufficient to establish a match with a star within a host galaxy. However, sources can be placed in or near young star clusters, SNRs, HII regions, etc., and this information can teach us a great deal about the likely star-formation scenario of the source.

Counterparts

One would expect a certain amount of contamination from foreground and background objects in any survey of this nature. In addition to providing a good means of image alignment, these sources also provide X-ray colours for sources not intrinsic to our source galaxies and hence another potential method of source classification (or at least decontamination). In our survey we find 4 sources coincident with foreground stars: one each in M74, NGC 2681, M94, and M101. We also find 2 background galaxies: a radio galaxy in M83 (Stockdale et al. (2006)) and a Seyfert 1 galaxy in M101 (Wang et al. (1999)).

There are also several X-ray sources whose coordinates are exact matches with catalog sources. We find 2 matches with recent supernovae: SN1999gi in NGC 3184 (Nakano & Kushida (1999) and SN1994i in M51 (Tongue et al. (1994)). It is worth noting that SN2002ap in M74 occurred after our *Chandra*

observations were taken. Since the position of X-ray sources is not known to that high an accuracy (as discussed above), I will discuss sources that are coincident with star clusters, HII regions, OB associations, and catalog stars and SNRs below.

6.3.4 Source Environments

If our argument that sources in late-type galaxies are largely LMXBs, we would expect to find few sources in or near star clusters, HII regions, and SNRs in those galaxies. Similarly, if the arguments of Kaaret et al. (2004) are correct, we would expect to find many matches in those galaxies with the highest SFR: NGC 4314, M94, M83, and M51. In the late-type spirals M74, NGC 3184, and IC 5332, we would expect to find occasional matches. As can be seen in table 6.3, this is indeed the case.

M101 is an anomaly in two important regards: first, the X-ray detection threshold is significantly lower than in the other galaxies in our sample; second, it is one of the most extensively observed objects in the sky. Thus not only is there a higher probability of X-ray sources matching optical sources due to the number density of X-ray sources but also due to the density of optical catalog objects. As such, we find significantly more matches to catalog sources in M101 than in the other galaxies in our sample.

As a further indication that the work discussed in section 6.1 is valid, one would expect that sources in or near SNR would fall in the SNR bin in the colour-colour diagram and sources near HII regions and star clusters would fall near the XRB bin. As can be seen in figures 6.12, 6.13, and 6.14, this is indeed largely the case. It also appears evident that X-ray sources coincident with radio sources are SNR, as is evident in the plots of M94 and M51. Curiously, X-ray sources coincident with bright stars intrinsic to M51 from Lamers et al. (2002) are tightly clustered in the SNR bin of the colour-colour diagram.

Though further multiwavelength observations are required, there is the indication that colour classification works to a first approximation. In order to refine the colour scheme further in the future, we will need to perform optical observations deep enough to detect discrete high-mass stellar counterparts, especially Be stars, since many Galactic HMXBs have Be stellar counterparts. However, the colour classification is a useful tool and can be applied to, e.g., analysis of luminosity functions, as is demonstrated in Chapter 7.

Table 6.3. X-ray source matches within 2″ .

Galaxy	*Cl[1]	HII reg[2]	SNR[3]	Gal*[4]	PN[5]	other[6]
NGC 278	0	0	0	0	0	0
M74	1	1	0	0	0	0
NGC 1291	0	0	0	0	0	0
NGC 2681	0	0	0	0	0	0
NGC 3184	0	0	1	0	0	0
NGC 4314	3	0	0	0	0	0
M94	0	0	0	0	2	3
M51	4	20	1	4	0	3
M83	2	0	0	0	0	4
M101	0	19	12	3	0	2
IC 5332	0	0	0	0	0	0

[1]Young star clusters, Larsen (1999, 2000); Benedict et al. (2002); Lamers et al. (2002)

[2]HII regions, Hodge et al. (1990); Petit et al. (1996); van Zee et al. (1998)

[3]supernova remnants, references in text and Matonick & Fesen (1997)

[4]stars in host galaxy, Sofue & Wakamatsu (1994); Lamers et al. (2002)

[5]Planetary nebulae, Douglas et al. (2000)

[6]matches of unidentified nature from radio, IR, and UV catalogs, Hill et al. (1984); Cowan & Branch (1985); Turner & Ho (1994); Kraemer et al. (2002)

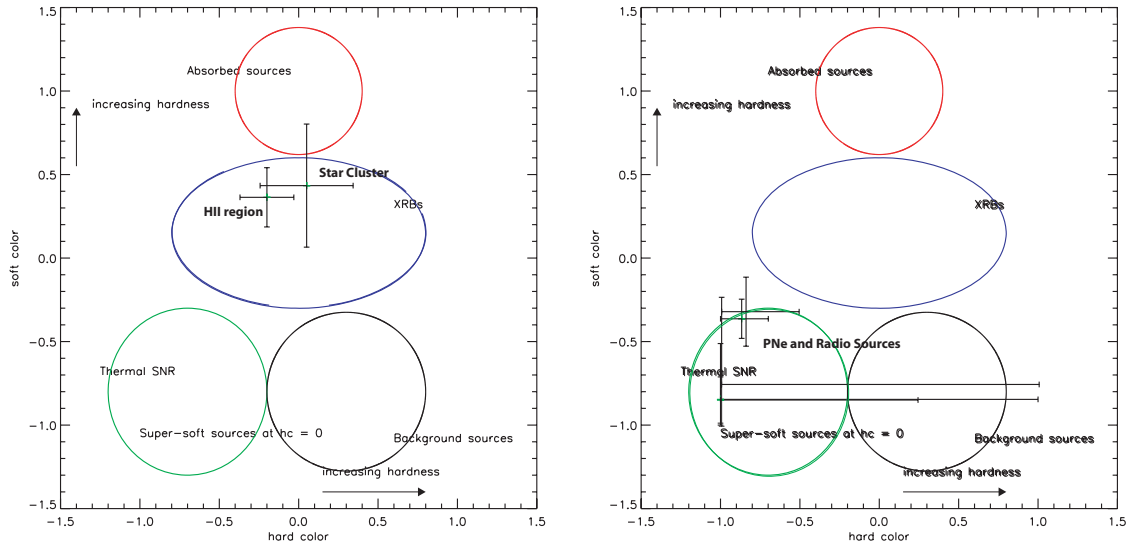

Figure 6.12 Colour-colour diagrams. Star cluster and HII region in M74 (left) and planetary nebulae and radio sources in M94 (right).

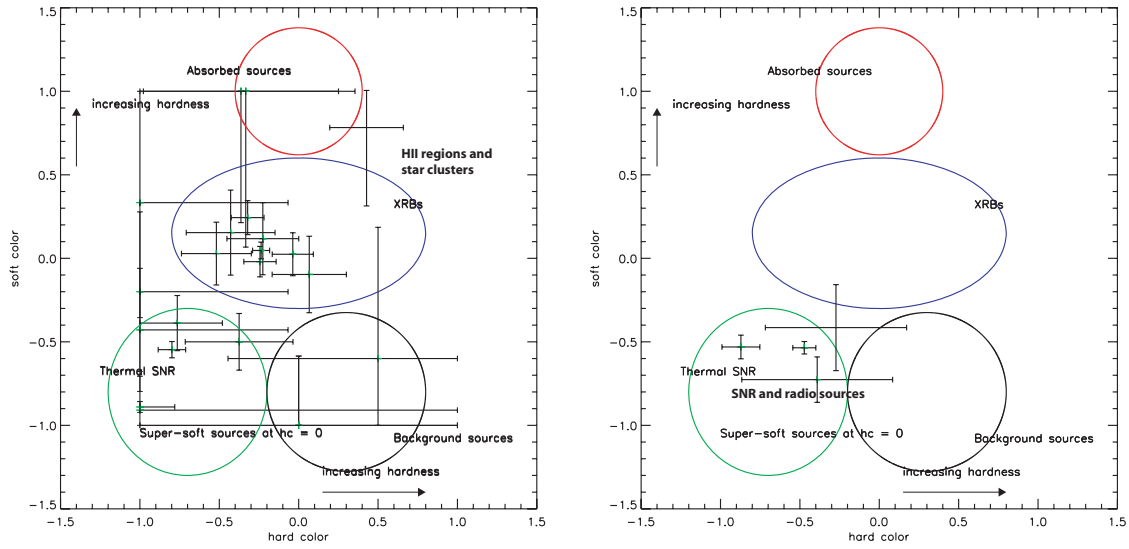

Figure 6.13 Colour-colour diagrams. HII regions and star clusters (left) and radio sources and SNR (right), both from M51.

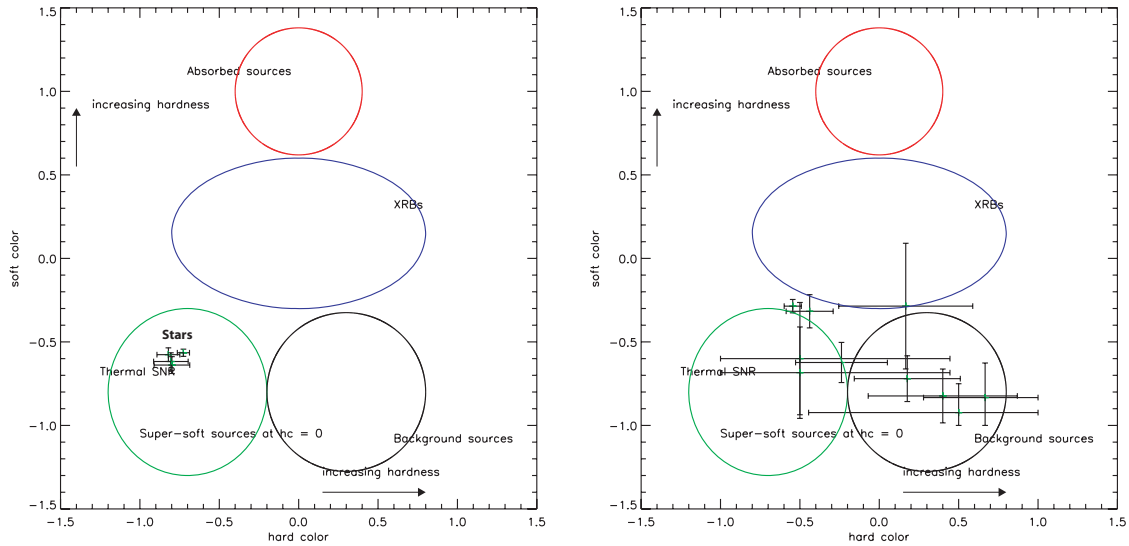

Figure 6.14 Colour-colour diagrams. Stars intrinsic to M51 (left) and SNR in M101 (right).

Chapter 7

Point Source Luminosity Functions

> There are 10^{11} stars in the galaxy. That used to be a huge number. But it's only a hundred billion. It's less than the national deficit! We used to call them astronomical numbers. Now we should call them economical numbers.
>
> Richard Feynman

In this chapter, we discuss the X-ray point source luminosity functions (LFs) in our sample of galaxies, as well as 2 additional starburst galaxies from the *Chandra* archive. Our results on the X-ray luminosity functions are presented in §7.1 and compared with previous results in §7.2. In §7.4 we discuss the multi-epoch LF of M82. In §7.5, we describe a simple model which attempts to relate the luminosity function to the age of the X-ray binary population in each galaxy. We present a discussion in §7.6.

7.1 Luminosity Functions of Spiral and Star Forming Galaxies

The cumulative luminosity functions for each galaxies are shown in appendix 10. In order to avoid incompleteness, we consider only the high luminosity range of the luminosity functions. For the nearest galaxies in our sample, we set an overall conservative completeness limit at the luminosity corresponding to a detection limit of 10 counts for NGC 1291, $L > 3 \times 10^{37}\,\mathrm{erg\,s^{-1}}$. In the case of the Antennae, this detection limit translates to $L > 9 \times 10^{37}\,\mathrm{erg\,s^{-1}}$. We derived power-law fits to the high luminosity range of the unbinned differential luminosity function using a maximum likelihood statistic following

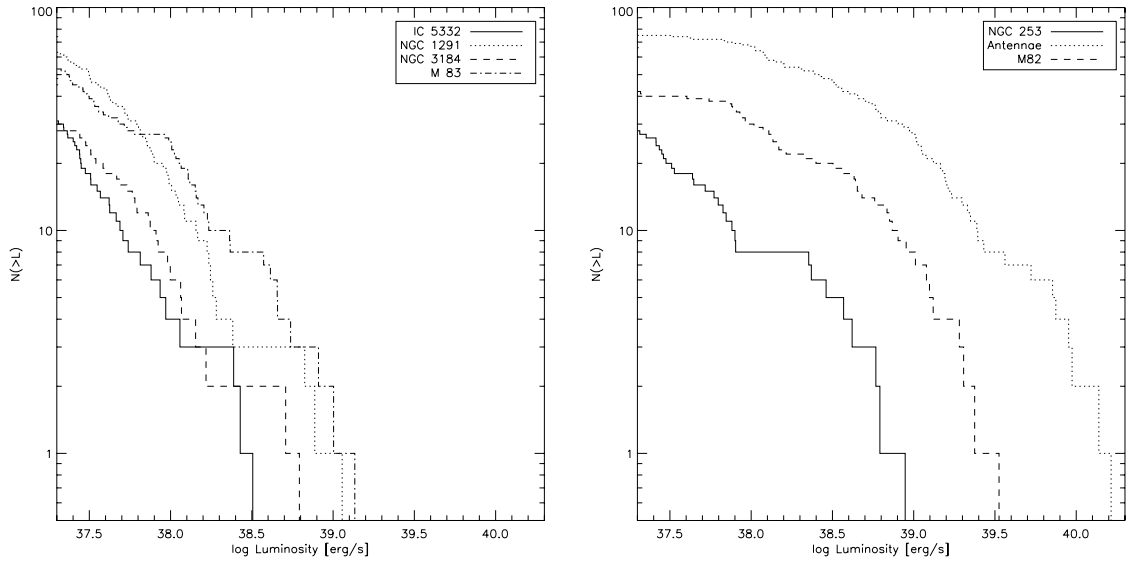

Figure 7.1 Cumulative Luminosity functions of spirals (left) and starbursts (right).

Crawford et al. (1970). Note that we plot cumulative functions for ease of visualisation only. The slopes range between 0.50 and 1.30; the fitted slopes, Γ, are shown in Tables 4.1 and 7.1. We evaluated the goodness of fit as discussed in section 4.1.

The early-type spiral NGC 1291 has been studied in detail by Irwin et al. (2002), who considered only bulge sources and found no sources above $L = 2.5 \times 10^{38}\,\mathrm{ergs\,s^{-1}}$. We include all sources in the galaxy within the S3 chip (which covers >80% of the total area of the galaxy), which adds some higher luminosity sources. It is possible that in NGC 1291 we are seeing two populations (bulge and disc) with the disc sources becoming more prominent at higher luminosities. However, there are only 2 disc sources brighter than $L > 3 \times 10^{38}\,\mathrm{ergs\,s^{-1}}$, so this suggestion must be treated with caution. Finally, we note that the LF of NGC 3184 may hint at a cut-off at $\sim 1.7 \times 10^{38}\,\mathrm{ergs\,s^{-1}}$, with a couple of higher luminosity sources skewing the high end of the fit, but the statistics are limited. A detailed study of the LF of the Antennae has been presented in Zezas & Fabbiano (2002). The parameters of the LF they derive are very similar to those presented here. Also, a study of the LF of M82 has been presented in Zezas et al. (2001). Their slope, although somewhat flatter is consistent with our results.

The most striking feature of the results in Fig. 7.1 and Table 7.1 is that the three starburst galaxies (NGC 253, M82 and NGC 4038/9) have flatter luminosity distributions than do the spirals. This implies that the starbursts have a larger fraction of higher luminosity sources relative to the total than do the spirals. This can most naturally be explained if systems with ongoing star formation have a population of X-

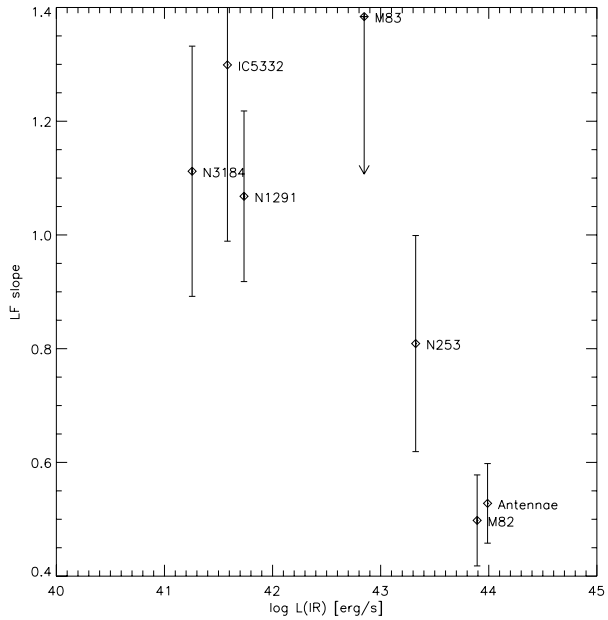

Figure 7.2 Cumulative luminosity function slope vs. 60 μ luminosity.

ray binaries that dominate the high end of the luminosity function. Due to the short time scales of the starbursts, 10-100 Myr, the high luminosity sources are most likely high-mass X-ray binaries, as the latency period for HMXBs becoming X-ray luminous is much shorter than for LMXBs. The hypothesis that the LF slope is related to star formation rate is supported by the plot in Figure 7.2, which shows the slopes of the luminosity functions of the galaxies discussed here plotted against the integrated 60μ luminosity from the IRAS faint source catalog (Moshir et al. (1992)). There is a clear correlation (above the 99% confidence level) between the 60μ luminosity – a measure of the star formation rate (Kennicutt (1998)) – and the slope of the X-ray luminosity function, in the sense that flatter slopes have higher star formation rates. The outlier is M83, which has a steep slope (deficit of high luminosity sources) relative to its 60 μ luminosity. It is worth noting that there are several bright sources within D_{25} but off the S3 chip which may well be associated with M83. The slope is therefore an upper limit.

There is evidence to suggest that galaxies with high star formation rates contain a greater number of ultraluminous X-ray sources ($L_x > 10^{39}\,\mathrm{erg\,s^{-1}}$). For example, there are several such sources in each of the starburst galaxies M82 (Zezas et al. (2001)), the Antennae (Fabbiano et al. (2001)), and NGC 3256 (Lira et al. (2002)). By contrast, none are found in the non-starburst/normal spiral galaxies IC 5332 or NGC 3184 (see Table 4.1). However, several biases must be considered that could affect such "anecdotal" evidence. More massive galaxies may have more ultraluminous X-ray sources because there is a greater likelihood of finding rare sources in larger systems. Nearby galaxies (e.g.

Local Group galaxies) have such large angular extents that *Chandra* surveys have been incomplete, and sources in unexplored regions may have been missed. The most important biases are probably source confusion,which can be addressed via variability studies, and higher source detection thresholds in more distant galaxies. Understanding these biases is crucial in discussion of LF slopes, as the brightest few sources dominate the LF for most galaxies.

One would like to separate the bulge and disc sources for each galaxy and compare the LFs to see if a discernible difference in slope is detected due to a difference in the underlying stellar population. However, the limited number of sources in each galaxy would render any results statistically insignificant except in the case of M101, which has over 200 point sources but essentially no bulge. We instead combine the galaxies with a primarily bulge population and a primarily disc population: NGC 278, NGC 1291, NGC 2681, & NGC 4314, and M74, NGC 3184, M101, & IC 5332, respectively. For these combined LFs, we consider only the longest available *Chandra* observation for each galaxy. In addition, we use only the data above the detection threshold for the galaxy with the highest detection threshold in each group. For M101, though the observations cover 78% of the galaxy, much of that data is on the front-illuminated ACIS CCDs, which have a much higher detection threshold. For the purposes of the combined LF, we consider only the data above the detection threshold for the front-illuminated CCDs. The LF slopes are 1.14 ± 0.17 for bulge sources and 1.17 ± 0.14 for disc sources. We also combine M51, M94, & M83, as they have higher star formation rates than the rest of the sample; M51 due to the recent interaction between the galaxies and M83 and the nuclear region of M94 due to mild nuclear starbursts. The combined LF slope of these galaxies is 0.70 ± 0.06, significantly flatter than the bulge-dominated and disc-dominated subsets (see figure 7.3). This is in agreement with the conclusions in Kilgard et al. (2002) as well as those in Colbert et al. (2004) and suggests that there may be an excess of high-mass X-ray binaries (HMXBs) created by the more recent star formation as compared with those galaxies dominated by a bulge population.

7.2 Comparison with Results from Literature

These results can be compared to studies of early-type systems in the literature, which are summarized in Table 7.2. The elliptical galaxy NGC 4697 has been studied by Sarazin et al. (2000), the S0 galaxy NGC 1553 by Blanton et al. (2001), and the bulge of M31 by Shirey et al. (2001). The luminosity

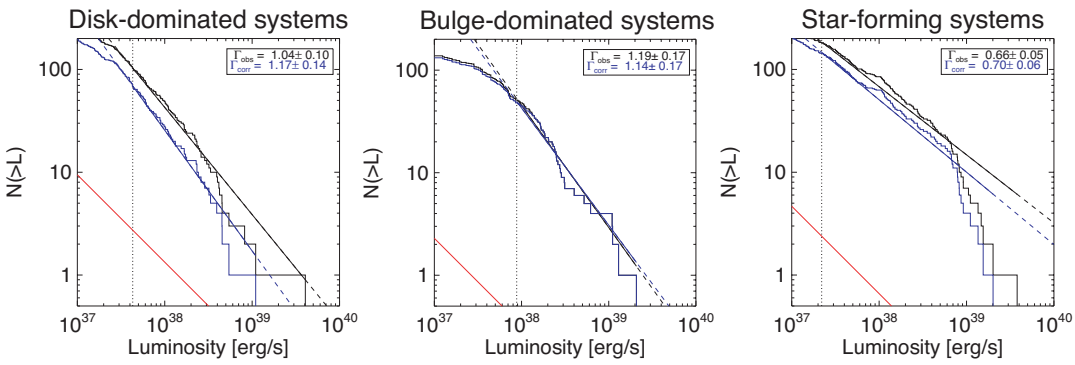

Figure 7.3 Cumulative luminosity function of the X-ray point sources in spiral galaxy subsets. The disc-dominated galaxies are M74, NGC 3184, M101, and IC 5332; the bulge-dominated galaxies are NGC 278, NGC 1291, NGC 2681, and NGC 4314; and the systems with high star formation are M94, M51, and M83.

distributions for NGC 4697, NGC 1553, and the bulge of M31 are not adequately described by single power-laws, but instead require broken power-laws. The exponents for the high luminosity parts of the cumulative distributions are $\Gamma = 1.79 \pm 0.26$ for M31 (Shirey et al. (2001); Primini et al. (1993)), $\Gamma = 1.76^{+1.81}_{-0.39}$ for NGC 4697 (Sarazin et al. (2000)), and $\Gamma = 1.7^{+0.7}_{-0.4}$ for NGC 1553 (Blanton et al. (2001)). For all three galaxies, the exponent is consistent with the range $\Gamma = 1.5 - 2.1$, steeper than the spirals and starbursts discussed above. This suggests that the trend of steeper slopes correlating with less star formation extends to early-type spirals and ellipticals. Two of these galaxies (NGC 4697 and NGC 1553) are of comparable distance to the Antennae and therefore confusion is potentially a problem. The effect of confusion on the luminosity function is complicated and depends on the clustering and luminosity properties of the sources. While a complete analysis of the effects of confusion is beyond the scope of this paper, we note that a similarly steep slope is observed in the bulge of M31 (Shirey et al. (2001); Primini et al. (1993)), lending support to the hypothesis that early type systems have steeper luminosity functions.

7.3 Universal X-ray Luminosity Functions?

It has been proposed that there exist "universal" X-ray luminosity functions for HMXBs (Grimm et al., 2003) and LMXBs (Gilfanov, 2004). The XLF of LMXBs is described as a complex function with slope at low L_X = 1, steepening around 10^{37} erg s^{-1} with a sharp cutoff on the order of 10^{39} erg s^{-1}.

The total number of LMBXs are the combined luminosity are said to be proportional to the stellar mass of the host galaxy. HMXBs are described by a simple power-law function with slope = 1.6 and a cutoff at a few times 10^{40} erg s^{-1} and normalisation proportional to the star-formation rate.

To consider the results from spiral galaxies in the context of universal luminosity functions, we take the X-ray population of M51 as an example. Included in this discussion is some work done after the conclusion of my thesis work that has been submitted to the Astrophysical Journal as Kilgard et al., 2007. Beyond the X-ray analysis included in this thesis, I also make use of data from the Advanced Camera for Surveys (ACS) on *Hubble Space Telescope*.

In order to construct "pure" HMXB or LMXB LFs for a spiral galaxy, it is necessary to include some information on optical counterparts and environments. We use the optical counterpart and environment identifications from Kilgard et al. (2007). X-ray sources are classified as coincident with individual supergiant O or B stars, coincident with bright young star clusters, coincident with Hα blobs, or coincident with nothing (no detected stellar or Hα match). For this example, we exclude sources in the optically confused nuclear region of M51, leaving a final sample of 90 X-ray sources.

7.3.1 X-ray sources coincident with individual stars

19 of the 90 X-ray sources are coincident with individual stars. Given that the stars are detected at all in the ACS observations, they are likely all O and B supergiants. Thus, the X-ray sources are (by definition) HMXBs. Presented in Figure 7.4 are the X-ray colour-colour diagram and LF for these sources. As can be seen from the colour-colour diagram, the sources largely have colours consistent with XRBs. The outlier in the bottom left is a supersoft source the luminosity of which is variable by more than two orders of magnitude. The sources at the bottom of the plot have zero counts detected above 1 keV and are thus impossible to classify by X-ray colours. As us discussed elsewhere in this chapter, the slope of the LF is associated with star-formation, with flatter XLF slopes indicative of a higher star formation rate (SFR). Further, work by Sarazin et al. (2000) and Kim & Fabbiano (2004) has suggested that there may be a break in the LF near the Eddington luminosity for a 1.4 $M_{\odot}$ neutron star ($\sim 2\times10^{38}$ erg s^{-1}), indicating the dropout in the neutron star contribution to the LF. The LF of these sources has no indication of a break and is relatively flat, suggesting that these sources are likely a homogeneous population, rather than a mix of black hole and neutron star binaries. Further,

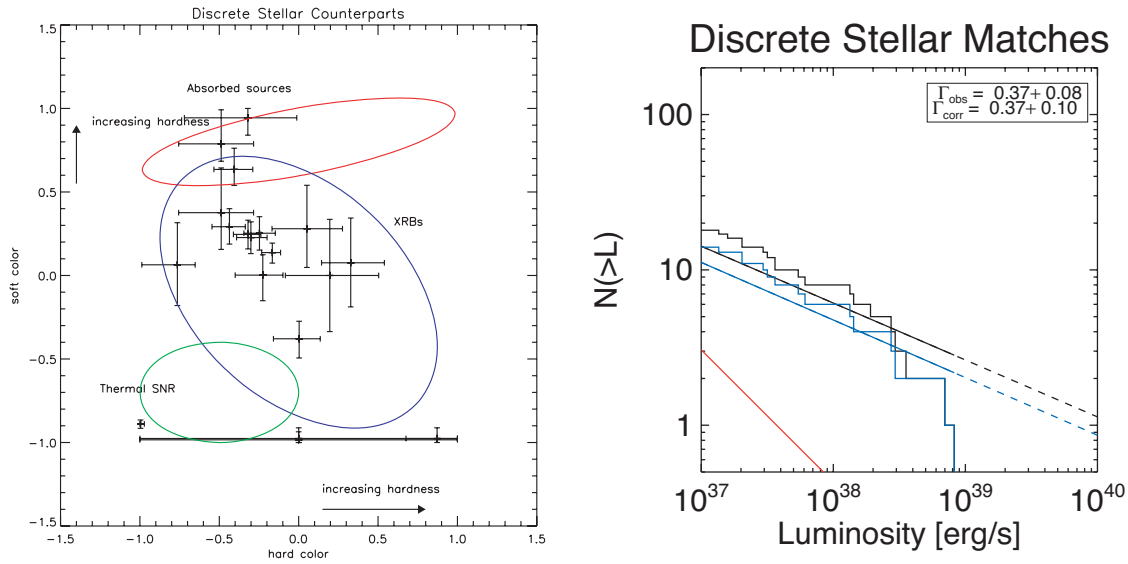

Figure 7.4 *Left:* X-ray colour-colour diagram for sources with discrete stellar counterpart candidates. The colours indicate that the sources are likely XRBs. *Right:* X-ray luminosity function for sources with discrete stellar counterparts. The black line is the raw data, the red line is an estimate of the contribution from background sources, and the blue line is the corrected XLF, with best fit power-law functions overplotted. The absence of Eddington break and suggestion of an exponential cutoff in the L_X suggests that the sources are neutron star HMXBs.

there is the suggestion of an exponential cutoff just below 10^{39} erg s^{-1}, though adding such a cutoff to the fit does not improve the goodness of fit significantly. The absence of sources more luminous than $8.2\times\ 10^{38}$ erg s^{-1} suggests that these sources are largely neutron star HMXBs.

2 of the 19 sources with discrete stellar counterparts are coincident with compact radio sources from Maddox et al. (2006). The first, CXOU J132939.0+471324, lies just outside the main part of the disc of M51. Its relatively soft X-ray spectrum and high radio flux suggest that it is a background AGN. The second, CXOU J133011.0+471041 has the highest radio flux of any of the radio/X-ray overlaps in M51. Maddox et al. (2006) suggest that the flat radio spectrum, high X-ray and radio fluxes and lack of Hα emission indicate that the source may be a microquasar in the radio-loud state.

7.3.2 X-ray sources coincident with star clusters

26 of the 90 X-ray sources are coincident with blue star clusters, OB associations or multiple blue stars. The colours of these sources (Figure 7.5, left) indicate a population of X-ray binaries, with a general trend towards softer spectra than for the sources with discrete counterparts. The association with blue stars and clusters suggests that these sources are also HMXBs. The LF (Figure 7.5, right) is slightly steeper than that of the sources with discrete stellar matches and there is the suggestion of a break near $2\times\ 10^{38}\ erg\ s^{-1}$. Further, the single power-law does not provide a good fit to the LF (likelihood parameter is 1.73) and fitting a broken power-law improves the fit significantly (likelihood parameter is 1.01), with a break luminosity of $1.1\times\ 10^{38}\ \mathrm{erg\ s^{-1}}$ (though the error on the break luminosity is quite large). The LF thus suggests that these sources are a mix of neutron star and black hole binaries. The softer spectra suggests that some of these sources may be HMXBs in the high-soft spectral state. The source CXOU J132949.1+471257 is coincident with a compact radio source identified by Maddox et al. (2006). Its radio spectrum is quiet steep, indicating a non-thermal emission mechanism. Given that the source is also highly absorbed in the X-ray, we have concluded that this source is likely a background AGN.

7.3.3 X-ray sources coincident with discrete Hα features

Perhaps most surprisingly, 27 of the 90 X-ray sources are coincident with discrete features in the Hα image, either shell-like structures or Hα point sources. The colour-colour diagram and LF are presented in Figure 7.6. The X-ray colours indicate that the sources are mostly SNRs, with a few X-ray binaries that are clearly separated in colour space. This is the most clear example thus far that the use of X-ray colours is a good first indicator of X-ray source classification. However, a few of the sources with SNR-like colours exhibit variability in their X-ray fluxes and are thus unlikely to be SNRs.

Excluding both the sources with XRB-like colours and those that are variable from the LF allows us to construct, for the first time, the LF of the X-ray bright SNR population of a galaxy. Thus, in Figure 7.6, we present the total LF of this sample, the LF of the SNR candidates, and the LF of the sources with Hα counterparts excluding the SNR candidates. The LF of the SNRs is quite steep with a cutoff below $10^{38}\ \mathrm{erg\ s^{-1}}$. The remaining sample of sources is likely to consist of HMXBs due to the association with Hα and thus star formation. The much flatter LF slope of these sources, combined with the lack of

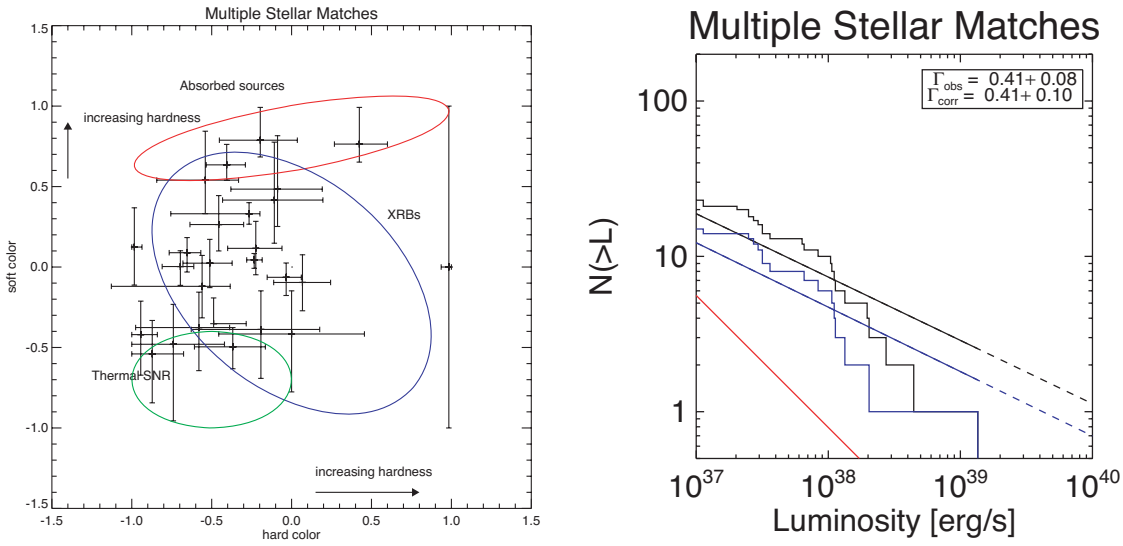

Figure 7.5 *Left:* X-ray colour-colour diagram for sources with multiple stellar counterpart candidates and those coincident with young star clusters. The colours suggest a mix of X-ray binaries, with the trend towards softer spectra suggesting that some of the sources may be HMXBs in the high-soft state. *Right:* X-ray luminosity function for sources with discrete stellar counterparts. The black line is the raw data, the red line is an estimate of the contribution from background sources, and the blue line is the corrected XLF, with best fit power-law functions overplotted. Fitting with a broken power-law significantly improves the fit, suggesting a mix of neutron star and black hole X-ray binaries.

Eddington break or exponential cutoff near 10^{39} erg s^{-1} indicates that they are likely black hole X-ray binaries.

Of these source, 9 are identified with compact radio sources by Maddox et al. (2006), of which 8 have thermal radio spectral indices. This indicates that these sources are likely SNRs, consistent with their X-ray identification, including the historical SN1994I. The one remaining source is CXOU J132955.0+470922, with non-thermal radio index and X-ray colours indicative of an XRB.

7.3.4 X-ray sources with no optical matches

18 of the 90 X-ray sources have no counterpart detected in the ACS images. These sources are largely found in dusty regions and include most of the X-ray sources detected in M51b. Given that M51b is an early-type (SB0) spiral, it is likely that these sources are mainly LMXBs. The colour-colour diagram

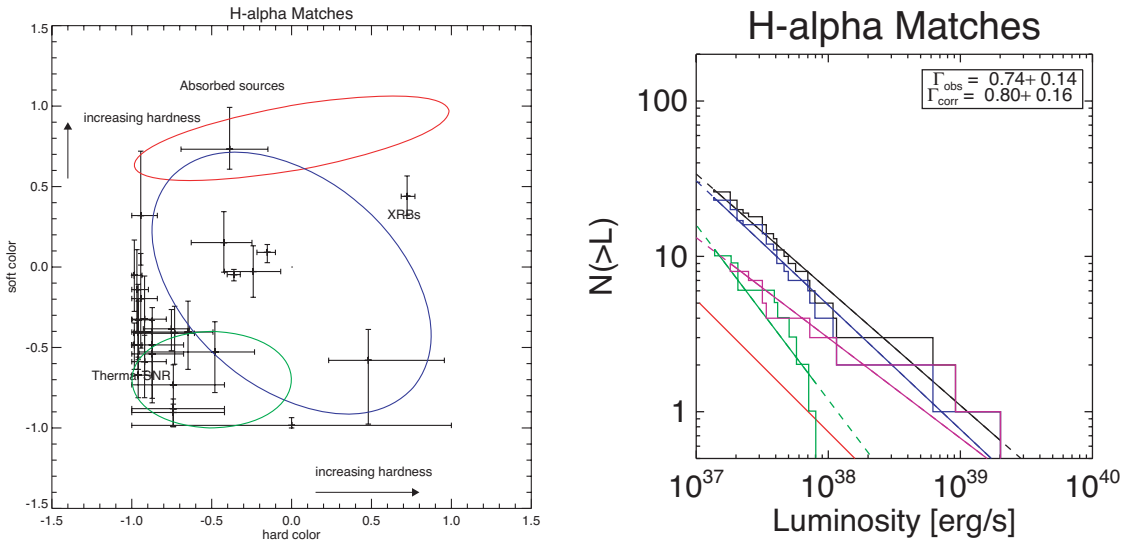

Figure 7.6 *Left:* X-ray colour-colour diagram for sources with Hα counterpart candidates. A clear divide can be seen between the SNRs and the typical X-ray binaries. *Right:* X-ray luminosity function for sources with Hα counterparts. The black line is the raw data, the red line is an estimate of the contribution from background sources, and the blue line is the corrected LF, with best fit power-law functions overplotted. The green line is the "pure" SNR LF, while the magenta line is the population excluding the SNR candidates.

and LF are presented in Figure 7.7. The X-ray colours indicate a uniform population of X-ray binaries and heavily absorbed sources. The LF shows evidence for an Eddington break. A broken power-law fit to the LF finds a break luminosity of $1.5\times\ 10^{38}$ erg s^{-1}, though the single power-law provides a statistically acceptable fit (likelihood = 1.18). The hard X-ray binary colours, absence of optical counterparts, and suggestion of a broken power-law LF indicate that these sources are likely LMXBs.

7.3.5 Implication for Universal Luminosity Functions

These results have provided a useful calibration of our X-ray diagnostic tools. The Hα results show that, using X-ray colour and variability, it is possible to classify the majority of X-ray bright SNRs. This is vital for the study of X-ray binary populations in galaxies, especially given the claims of a "universal" XLFs for both HMXBs (Grimm et al., 2003; Gilfanov et al., 2004) and LMXBs (Gilfanov, 2004). This is not to discount the work of these authors; indeed our results on HMXB candidates in M51 are consistent with their findings. However, given that SNRs likely make up $\sim 17\%$ of the X-ray

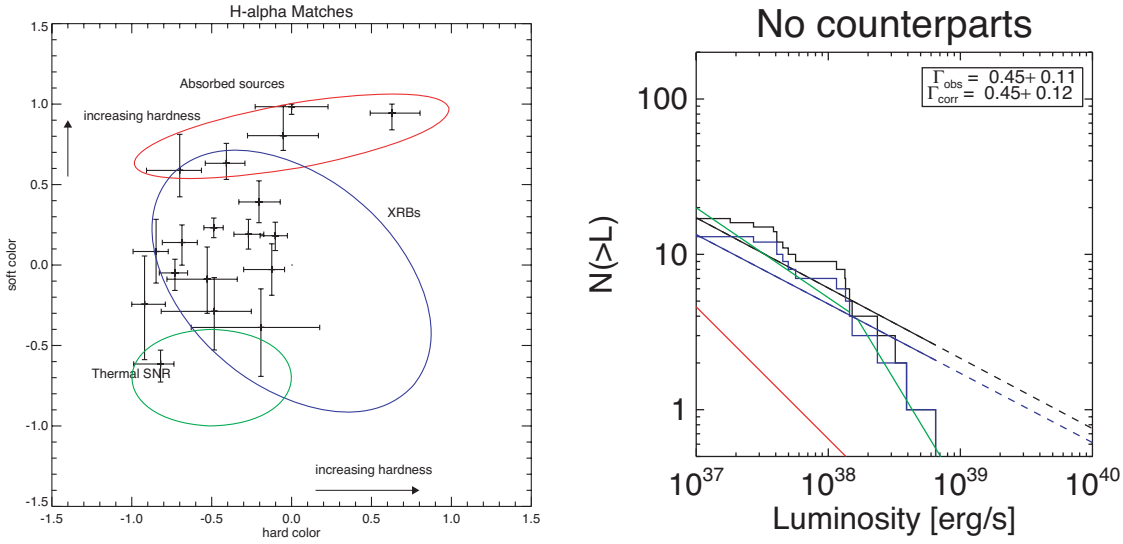

Figure 7.7 *Left:* X-ray colour-colour diagram for sources with no counterpart candidates. The colours indicate that the sources are primarily XRBs. *Right:* X-ray luminosity function for sources with no detected counterparts. The black line is the raw data, the red line is an estimate of the contribution from background sources, and the blue line is the corrected LF, with best fit power-law functions overplotted. The green line is the best-fit broken power-law, with break luminosity at $1.5\times\ 10^{38}$ erg s^{-1}.

point source population of M51, then any claims about SFR or history based upon the LF must take the SNRs into account.

This optical classification has allowed us, for the first time, to construct the XLF of SNRs in a galaxy. The slope is found to be much steeper ($\Gamma\ =\ 1.15$) as compared with any other sample of the population, and no SNRs are found to be more luminous than $8\ \times\ 10^{37}$ erg s^{-1}. The optical classes also allow us to distinguish between HMXBs and LMXBs, something that is not possible based upon X-ray properties alone. In the case of M51, more than half of the X-ray sources and two-thirds of the X-ray binary population appear to be HMXBs. This can be contrasted with the Milky Way, where LMXBs outnumber HMXBs by more than a factor of 5 (Grimm et al., 2002) in the same luminosity range. This is likely a factor of the differences in SFR, with the Milky Way SFR = 0.25M$_\odot$/yr and M51 SFR = 3.9M$_\odot$/yr (Grimm et al., 2002). In addition, we are able to classify many of the X-ray binaries as either neutron star or black hole HMXBs, with neutron star HMXBs identified with isolated high-mass stars and the black hole HMXBs associated with Hα emission and thus regions of on-going star formation.

Thus, the picture painted by Grimm et al. (2003) and Gilfanov (2004) does not appear to be quite so

simple. Our results on LMXBs show strong evidence for a break in the LF near 2×10^{38} erg s^{-1}. However, this break appears to also be present in HMXB populations with both neutron stars and black holes. As of yet, it is impossible to determine the cause of these breaks, whether due to the NS/BH separation in luminosity, different epochs of star formation, some combination of these factors, or something else entirely. It should be noted that Kim & Fabbiano (2004) see some evidence for the break in "pure" LMXB populations at slightly higher L_X, a result inconsistent with the interpretation of Gilfanov (2004).

For HMXBs, the situation is even murkier. Without good multiwavelength observations, it is impossible to disentangle the SNRs from HMXBs or coincident field LMXBs. Whilst the SNR population likely scales with star-formation rate, it will not be so simple a function as for HMXBs, since the X-ray bright phase for SNRs is much shorter than for HMXBs. Hence the contribution from SNRs is not just a factor of SFR but of duration since the last star-forming epoch. Given this evidence, I find the case for a universal HMXB luminosity function to be unclear and I would caution against extending such studies to more distant galaxies, as suggested in Grimm et al. (2003).

7.4 The Multi-Epoch Luminosity Function of M82

As can be seen in Table 4.2, the LF of M82 is relatively flat, with a mean slope of 0.9 above 4×10^{37} erg s^{-1}, the completeness limit in the shortest M82 observations. As one includes sources of lower luminosity, the LF flattens further, with slope of around 0.5 above 5×10^{36} erg s^{-1} (for ObsID 361, see 7.8). Over the full duration of the *Chandra* observations, the LF slope does not change within the statistical errors. Hence, whilst many of the sources are transient or highly variable, it does not change the overall shape of the LF.

7.5 Model Luminosity Distributions

As a first step in understanding the luminosity distributions, we adopt a simple model in which all of the X-ray sources are members of a single population with uniform properties except for luminosity and lifetime. Our goal is to show that this simple model provides an adequate framework for understanding

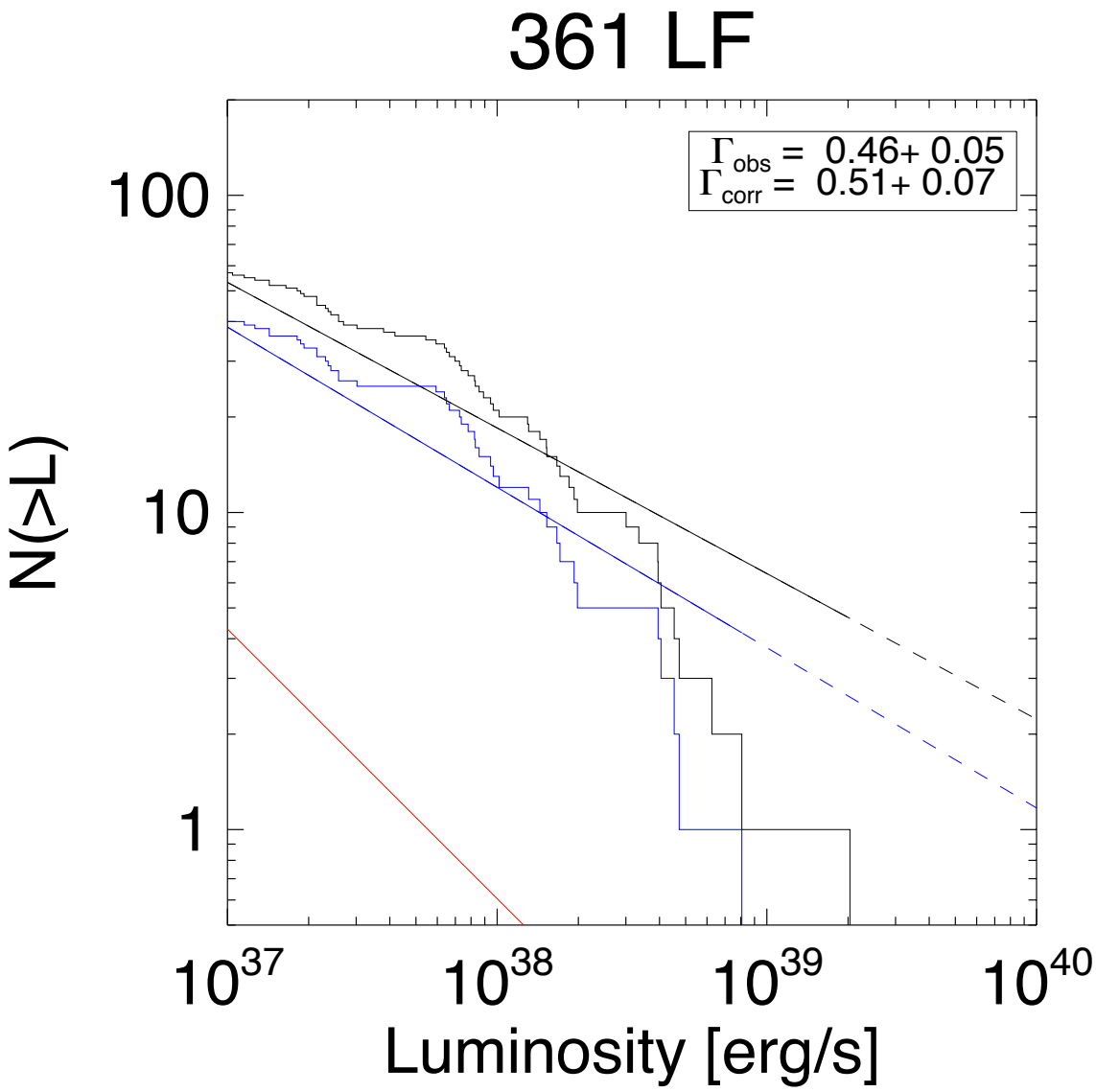

Figure 7.8 Luminosity function for M82 from ObsID 361. The best-fit slope is 0.51 ± 0.07. The flattening of the LF below 10^{38} erg s^{-1} is clearly evident.

the difference in luminosity function slopes between the various types of galaxies and the breaks in the luminosity functions of individual galaxies. More detailed modeling involving the distinctions between high-mass and low-mass X-ray binaries, and potentially including a distinct source class for the ultraluminous sources, should be done in the future. However, the basic results concerning the luminosity function derived here will remain true for each individual population of X-ray binaries in a more complex model.

The number of X-ray point sources is described at each instant in time, t, by the number of sources, $n(t, L, T)$, of luminosity, L, and of age, T. The source birth rate is specified by a function $b(L, t)$ which is, in general, time dependent. The death rate should be proportional to the number of sources with the constant of proportionality given by a function $f(L, T)$ which depends on the source properties, but not explicitly on time. In general, the evolution of sources after birth may include luminosity evolution as well as a luminosity dependent lifetime. For simplicity, we assume that each source has a constant luminosity through its lifetime. The time evolution of n is then

$$\frac{d}{dt}n(t, L, T) = b(L, t)\delta(T) - f(L, T)n(t, L, T) \tag{7.1}$$

where the Dirac delta function $\delta(T)$ enforces the condition that sources are born with zero age.

The function $f(L, T)$ determines the shape of the source lifetime distribution. We choose $f = \delta(T - \tau(L))$. In this case, each source of luminosity L lives a time $\tau(L)$ and then promptly dies. To specify the lifetime $\tau(L)$, we note that the lifetime of an X-ray binary is determined by the time required to accrete the companion star onto the compact object. Implicit in this assumption is that the entire mass of the donor is consumed; however, this will not be the case in all binaries. However, including a term to describe the fraction of mass consumed is beyond the scope of this toy model. Since the luminosity is proportional to the accretion rate, $L = \eta\dot{M}c^2$ where $\eta \sim 0.1 - 0.4$ is the efficiency for conversion of accreted matter to luminosity, the lifetime will depend on the luminosity as $\tau = \eta\bar{M}_2c^2/\epsilon L$, where $\bar{M}_2$ is the average mass of the companion stars and ϵ is the duty cycle of emission (King et al. (2001)). We assume that $\bar{M}_2$ and ϵ are the same for all members of the population.

We note that Wu & Tennant (2001) presented a model in which the source population is described only by the number of sources as a function of L and t, $n(t, L)$, i.e. no information is retained concerning the age of the sources. This is equivalent to choosing a constant for the function f in our model.

This choice leads to a source lifetime distribution which is a decaying exponential. Such a lifetime distribution has a great spread in ages at fixed luminosity, with many sources dying immediately after birth and some having extremely long lifetimes. Our more general model allows a narrower lifetime distribution.

We assume a power-law form for the birth rate distribution, $b(L) \propto L^{-\alpha}$. The power-law form is purely empirical, and provides an adequate fit to the data as discussed below. Populations synthesis models by Belczynski et al. (2004) show that the situation is more complicated. The XLFs of older populations are dominated by mass-transfer systems. Young populations have some contribution from the most massive compact objects in wind-fed systems, but these systems have short lifetimes. Roche-lobe overflow systems do not become X-ray luminous until the populations has aged to about 170 Myr. Each of these components contributes to the shape of the XLF, with the younger sources leading to a flattening of the XLF shape. Thus, the dependence on birth rate distribution is nonmonotonic, but is fairly well described as such for old populations. We also assume that the binaries turn on in X-rays instantaneously after they are formed.

If the star formation is dominated by a recent impulsive event, then the cumulative luminosity distribution shortly after the burst will be determined by the birth rate distribution,

$$N(>L) \propto L^{1-\alpha}. \tag{7.2}$$

If the population is allowed to evolve with no subsequent X-ray binary formation, then the high end of the luminosity distribution will be truncated as the highest luminosity sources, with the shortest lifetimes, die. The sharpness of the cutoff is determined by the sharpness of the age distribution. With the form chosen above for f, the luminosity cutoff will be extremely sharp. More realistic age distributions would produce more gradual cutoffs. Due to the limited statistics available in constraining such cutoffs, we expect that our choice for the age distribution is adequate for the present data. In this case, the differential luminosity distribution is $n(L) \propto L^{-\alpha}$ for $L < L_B$ and $n(L) = 0$ for $L \geq L_B$, where the break luminosity, L_B, is determined by the time since the burst, t_B, as $L_B = \eta \bar{M}_2 c^2 / \epsilon t_B$. The cumulative luminosity distribution is:

$$\begin{aligned} N(>L) &\propto \left(\tfrac{L}{L_B}\right)^{1-\alpha} - 1 \quad \text{for } L < L_B \\ N(>L) &= 0 \qquad\qquad\qquad\quad \text{for } L \geq L_B \end{aligned} \tag{7.3}$$

Now consider the case of gradual and long-term star formation, leading to an equilibrium between X-ray binary formation and death. If the lifetimes of the longest lived members of the X-ray point source population are significantly shorter than the interval over which star formation has been proceeding steadily, then equilibrium will have been reached. The death rate at a given L will be proportional to the number of sources divided by the lifetime $\tau(L)$ and must equal the birth rate. Since τ is inversely proportional to L (King et al., 2001), the equilibrium luminosity distribution must be proportional to the birth rate distribution divided by L. The cumulative luminosity distribution is then:

$$N(>L) \propto L^{-\alpha}. \tag{7.4}$$

This luminosity distribution is steeper than that of the impulsive case with an exponent that differs by one due to the (inverse) linear dependence of lifetime on luminosity.

At sufficiently low luminosities, the source lifetimes will be longer than the interval over which star formation has been proceeding steadily t_S. In general, the luminosity function will have the form of Eq. 7.2 for source luminosities corresponding to source lifetimes longer than t_B and the form of Eq. 7.4 for higher luminosities. This leads to a broken power-law form for the luminosity distribution with the break luminosity, L_S, determined by the time since the burst, t_S, with the same relation as between L_B and t_B. The differential distribution below the break will have the same slope as that of the birth distribution, whilst above the slope will be steeper by one. The cumulative luminosity distribution is then

$$\begin{aligned} N(>L) &= \tfrac{N_0 L_S}{\alpha-1}\left[\left(\tfrac{L}{L_S}\right)^{1-\alpha} - 1\right] + \tfrac{N_0 L_S}{\alpha} \quad \text{for } L < L_S \\ N(>L) &= \tfrac{N_0 L_S}{\alpha}\left(\tfrac{L}{L_S}\right)^{-\alpha} \qquad\qquad\qquad\quad \text{for } L \geq L_S \end{aligned} \tag{7.5}$$

where N_0 is the normalisation of the differential luminosity distribution at L_S. Plots of this distribution for several values of t_S are shown in Fig. 7.9. The older systems have a steep slope in the high luminosity range. The younger systems, analogous to the starbursts, have a flatter slope over the same

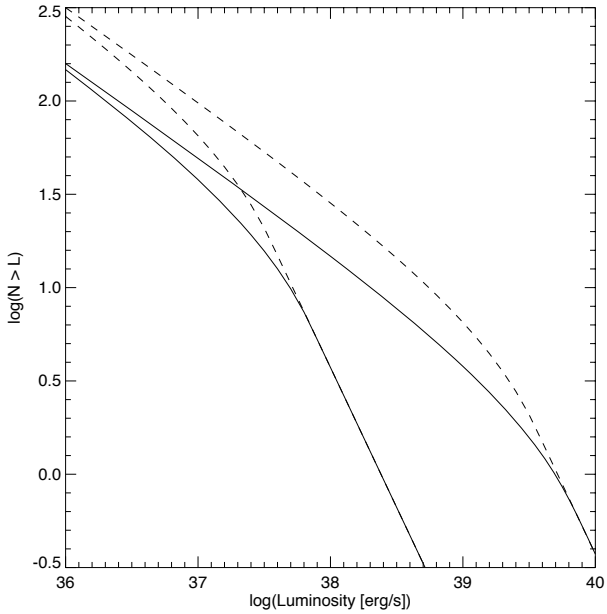

Figure 7.9 Model cumulative luminosity functions. The upper solid and upper dashed curves are continuous star formation for 10 Myr (solid) and 20 Myr (dashed). The lower solid and lower dashed curves are for 1 Gyr (solid) and 2 Gyr (dashed) with a star formation rate lower by a factor of 100.

luminosity range and distributions extending to higher luminosities. The break luminosity depends on the duration over which X-ray binary formation has been occurring.

If X-ray binary formation proceeds continuously for some interval and then shuts off, the resulting distribution will be sharply truncated at high luminosities with the cutoff luminosity determined by the time since the shut off of X-ray binary formation. If the duration of the continuous formation interval is longer than the time since the shut off of formation, then the (differential) distribution will consist of two power-laws and a sharp high luminosity cutoff. If the opposite situation holds, the luminosity distribution will be as in Eq. 7.3.

As noted above, we have assumed that all of the X-ray sources are members of a single population with uniform properties except for luminosity and lifetime. In reality two types of X-ray binaries are known, low-mass and high-mass systems, which have different evolutionary paths. High-mass X-ray binaries (HMXBs) are the progeny of rapidly evolving high mass stars, whilst low-mass X-ray binaries (LMXBs) are descendants of slowly evolving low mass stars leading to a long latency period between star formation and the turn on in X-rays of the binaries. In the impulsive star formation case described above, the long latency of the LMXBs precludes any significant contribution from LMXBs to the

luminosity distribution. Hence, the X-ray sources in starbursts are likely HXMBs, as noted above. There is also likely to be some delay between the onset of star formation and the appearance of the first HMXBs, due to time required for the first stars to go supernova. However, this can be as short as a few million years, so the assumption made above of instantaneous turn on of the X-ray binaries is reasonable for star formation episodes with durations in excess of 10 Myr.

Conversely, the luminosity distribution for old systems is likely to be dominated by LMXBs because of the much longer lifetimes of the low-mass companions. For the equilibrium distributions, LMXBs and HMXBs will likely have different formation rates, companion masses, and duty cycles. This would lead to different luminosity distributions for each population, each of which taken individually would be described by the equations presented above. The observed distribution would then be the sum of the distributions for each population.

7.6 Discussion

Recent *Chandra* observations show that the X-ray source luminosity distributions of the early-type galaxies are steeper than those of the starburst galaxies with an exponent that differs by approximately one. This is similar to the difference between the slopes for our models of a burst of star formation and steady-state star formation. We suggest that the luminosity distribution of the starburst galaxies directly reflects the birth luminosity distribution, whilst the other galaxies have a similar birth luminosity distribution and an observed luminosity distribution modified by the effects of an aging X-ray binary population. The slopes of the spirals are intermediate between the two cases, which may arise from a combination of the two components, as suggested above for NGC 1291.

For galaxies where the LF is measured over a broad luminosity range, it may be possible to detect breaks in the luminosity function and relate them to the galaxy's star formation history (Wu & Tennant (2001)). Shirey et al. (2001) reports a break in the LF for M31's bulge near $3 \times 10^{37}\,\mathrm{ergs\,s^{-1}}$. Applying the relation found above between the break luminosity and age of the X-ray binary population, we find t_B of the order of 10 Gyr for $\epsilon = 0.02$, $\eta = 0.1$, and $\bar{M}_2 = 2M_\odot$. The difference in slope above and below the break is 1.32 ± 0.26, close to the difference of 1 predicted in our simple model. The breaks in NGC 4697 and NGC 1553 are at higher luminosities, suggesting shorter t_B. However, the break luminosities are uncertain due to the distance uncertainties. There are suggestions of breaks at

Table 7.1. Properties of starbursts not included in our general sample.

Galaxy	Hubble type	ObsID	Exposure (sec)	$n_{\rm H}$ (10^{20} cm)	D_{25} fraction	Distance (Mpc)	LF Slope	60 μ luminosity (10^{40} erg/s)
NGC 253	SAB	969	12207	1.43	0.45	3.0	0.81 ± 0.15	324
Antennae	SA/SB(pec)	315	70813	3.95	0.85	25.5	0.53 ± 0.07	1350

even higher luminosities, above $10^{39}\,{\rm ergs\,s^{-1}}$ in the starbursts M82 and the Antennae. In the context of the model presented above, this would be consistent with the rather short ($\lesssim 100\,{\rm Myr}$) durations of the starburst events in these galaxies.

An alternate explanation of the luminosity function breaks is that they are due to the transition between neutron star and black hole X-ray binaries (Sarazin et al. (2000)). This suggestion is motivated by the observation that the break luminosity in the elliptical galaxies is close to the Eddington limit of a 1.4 $M_\odot$ neutron star (Sarazin et al. (2000)). However, the lower break luminosity found in M31 and the higher, although only marginally detected, break luminosities in the starbursts would argue against this interpretation. Additional X-ray luminosity function measurements are required to determine whether the break luminosity is the related to the Eddington luminosity or to the star-formation history of each galaxy as suggested here.

The striking differences in the luminosity functions and the progress that can be made in understanding the distributions with a simple model indicate that X-ray point source luminosity distributions should prove to be a powerful tool in understanding the evolutionary history of massive star populations in external galaxies. New *Chandra* observations of a large sample of galaxies across the full Hubble sequence coupled with detailed stellar evolution models should provide new insights into the compact object populations of external galaxies.

Table 7.2. LF slope and 60 μ luminosity of early-type galaxies

Galaxy	Hubble type	LF Slope	60 μ luminosity (10^{40}erg/s)	Reference
NGC 1553	S0	$1.7^{+0.7}_{-0.4}$	37.7	Blanton et al. (2001)
NGC 4697	E6	$1.76^{+1.81}_{-0.39}$	59.5	Sarazin et al. (2000)
M31 (bulge)	Sb	1.79 ± 0.26	102	(Shirey et al., 2001; Primini et al., 1993)

Chapter 8

Conclusions and Future Work

In science, "fact" can only mean "confirmed to such a degree that it would be perverse to withhold provisional assent." I suppose that apples might start to rise tomorrow, but the possibility does not merit equal time in physics classrooms.

Stephen Jay Gould

8.1 Putting together the pieces

8.1.1 Luminous Sources

As has been demonstrated in this work and others, the majority of the bright discrete X-ray sources in galaxies are accreting X-ray binary systems. This is clear from their spectral properties (sections 5.4 and 5.6) and their variability properties (sections 5.4, 5.6 and 6.2.1). In this Thesis, the spectra of XRBs are shown to be consistent with a population made up almost entirely of black hole binaries, either in the low/hard or high/soft state (5.4.1). Indeed, this is exactly what is expected for this population, given that all the sources with sufficient counts for spectral fitting have luminosities in excess of the Eddington limit for accretion onto a 1.4 $M_{\odot}$neutron star.

Further, spectral state transitions are evident in many of the more luminous sources, thus providing another clue as to the XRB nature of the sources. Sources whose spectral characteristics are more typical

of high-mass X-ray binaries are more often found in late-type spirals and galaxies with higher star-formation rates. The luminous source population of M82, for example, appears to be almost entirely made up of HMXBs. Since many of these sources have soft spectra, it is likely that they are HMXBs in the high/soft state (3.5.1).

The short-term variability of the luminous sources demonstrates that many sources exhibit characteristic timescales to their variability; the timescales of variability observed (1000s of seconds) indicate that the sources are likely black hole binaries, since the accretion discs of neutron stars should (and do, in the Galaxy) exhibit QPOs on much shorter timescales (5.4.2).

8.1.2 Source Trends

While most bright X-ray sources are binaries, some sources are supernova remnants and super-soft sources–likely white dwarf accretors. We have demonstrated that the colours of X-ray sources provide a good first estimate of source class (section 6.1). The supernova remnants, as expected are found in galaxies that have experienced relatively recent star-formation.

The long-term variability of sources indicates that a large fraction of the population is variable and, hence, probably accretion-powered. Further, sources whose colours indicate that they are likely XRBs tend to be variable; sources whose colours indicate that they are SNR tend not to be variable. This holds true exclusive of source luminosity and is thus not a selection affect. This lends further support to the colour classification scheme.

Sources coincident with optically identified young clusters tend to have X-ray colours indicative of XRBs. Sources coincident with optically identified SNR or radio sources (likely SNR) tend to have X-ray colours indicative of SNR. Not only does this demonstrate that the colour classification scheme works quite well, but it prevents a single-point of failure in source identification: if a source has an XRB colour, is variable, and is coincident with a star cluster, it's an XRB.

I clearly demonstrated that slopes of galaxy XLFs are linked directly to the star formation rates within those galaxies: the galaxies with higher star formation rates have flatter luminosity function slopes. I present toy models that demonstrate that the high-SFR galaxy XLFs are dominated by luminous HMXBs (likely black hole binaries) with neutron star binaries becoming more important at the low

luminosity end. Conversely, early-type galaxies (old stellar populations, hence largely LMXBs) have steeper XLF slopes. These galaxies also show evidence for a break in the XLF near the Eddington luminosity that canonically separates NS binaries from BH binaries. High SFR galaxies do not clearly show this break. Rather, they show a high luminosity cut-off in the XLF. This indicates that there is an upper limit to the luminosity obtained by normal XRBs. Hence, whilst some of the sources in this sample may be IMBHs, there is no systematic requirement for IMBHs. Our results on HMXB-dominated and LMXB-dominated XLFs is consistent with work the work done by Grimm et al. (2003) on the "universal" luminosity function of HMXBs and the work of Kim & Fabbiano (2004) on the XLF of elliptical galaxies.

All galaxies show some evidence for a flattening of the XLF at low luminosities. It is important to understand whether this is due to incompleteness or an actual turnover in source density. If the latter, this is very important for understanding star-formation within galaxies, as it has a significant impact on population synthesis codes, which rely heavily on knowing the fraction of XRBs in quiescence and outbursts.

8.2 How do we get there from here?

While we have made substantial progress in understanding the X-ray binary population of nearby galaxies, there is much work still to be done: We have not yet completely classified the luminous X-ray source population of a single galaxy; we haven't extended the XLF of external galaxies to luminosities substantially below 10^{36} erg s^{-1}; we haven't probed the connection between star formation and X-ray populations in regions of galaxy interaction; we haven't determined the impact of incompleteness on our X-ray analysis; we haven't constructed XLFs segregated by population type; and we haven't fully harnessed the power of multiwavelength data available to us. Below, I describe projects now underway to try to resolve these problems and truly understand the X-ray emission from normal galaxies.

8.2.1 Optical Counterparts

In order to definitively classify sources as high- or low-mass X-ray binaries, SNR or something else entirely, it is necessary to directly detect optical counterparts to the X-ray sources. We have currently

begun an archival project to analyze deep *Hubble Space Telescope* Advanced Camera for Surveys imaging of M51 to search for counterparts to X-ray sources and initial results are encouraging. 25% (25/100) of the sources have clear, apparently unambiguous optical counterparts: about 9/25 are foreground or background objects, whilst 16/25 are coincident with bright O or B stars. A further 9/100 sources are coincident with young star clusters. Both the sources coincident with O and B stars and those coincident with clusters exhibit XRB X-ray colours. Another 24/100 sources are coincident with compact features in the $H\alpha$. Most of these have SNR X-ray colours and 7 are also coincident with 20cm sources. Preliminary results on this project were presented at the IAU Symposium #230 in Dublin in August, 2005, with publication to follow shortly.

8.2.2 The Low-Luminosity End of the XLF

It is important to understand what happens to the X-ray luminosity function below $10^{36}\ \mathrm{erg\ s^{-1}}$, ultimately down to the luminosity of quiescent XRBs at or below $10^{34}\ \mathrm{erg\ s^{-1}}$. While observations of M31 and M33 from *Chandra* and *XMM* do extend down to $\sim 10^{35}$, they are not complete to that level. We will shortly be starting two projects that will help resolve this question. First, we will be obtaining a deep, 100ks *XMM* observation of the Fornax Dwarf Spheroidal galaxy. The Fornax Dwarf is mostly old population II objects with several globular clusters. Second, we will be observing the nearby dwarf starburst IC 10 with *Chandra* for 90 ks. These two datasets will allow for us to probe the low luminosity range of the XLF for old and young stellar populations separately. Since most X-ray binaries are transient, we must reach the luminosities at which they spend most of their time in order to understand the relation between the number and fraction of XRBs and the star formation rates and histories within the host galaxies. This information also provides valuable feedback to those writing population synthesis codes.

8.2.3 Interaction and Tidal Tails

Interacting systems show a multitude of X-ray sources within the galaxies. However, little analysis has been done of tidal tails. Recent optical studies have shown star formation triggered in the tidal tail of the M81 system, particularly in the HI bridge connecting M81 and NGC 3077 (Durrell et al. (2004)). In addition, studies with *ROSAT* showed a statistical excess of X-ray sources in this region (Bi et al.

(1994)). We have recently obtained *XMM* and *Chandra* observations of a portion of the M81 HI bridge as a case study of interaction with the goal of determining the timescale for XRB formation induced by interaction. We have also obtained deep optical images for parts of this field in an effort to determine whether there are young stellar counterparts to the X-ray sources or whether the apparent excess is due to statistical fluctuations in the X-ray background.

8.2.4 Incompleteness and Colour-Segregated XLFs

In order to better understand the relation between XLFs and star formation, we must construct XLFs segregated by population type, but we must also do simulations to determine the incompleteness of this data. A project, led by Andrea Prestwich at the CfA, has begun to perform these simulations for our spiral galaxy data. Initial results show that the population of HMXB-candidates and LMXB-candidates are indeed different, with the HMXBs exhibiting flatter XLF slope and no evidence of a break, whilst the LMXB sources have a steeper slope, with break near the value obtained by Kim & Fabbiano (2004) for early-type galaxies. This work was also presented at the IAU Symposium #230.

8.2.5 Multiwavelength Observations

The final step in completely classifying the X-ray population of galaxies will be to obtain multiwavelength data across the entire spectrum. As such, we have begun a project to accumulate as much of this data as possible: 20cm and 6cm observations from the VLA; *Spitzer* IRAC and MIPS images from 3.6$\mu$to 160μ; 2MASS and UKIRT WFCAM J, H and K images; ground based optical in U, V, B, R, I, Hα and [SII]; *Hubble Space Telescope* WFPC and ACS data with many broad and narrow filters; *XMM* EPIC and OM; and GALEX NUV and FUV. We have currently obtained most of this data and begun analysis, though it will be quite some time before the project is complete.

The VLA observations will help distinguish SNR as well as removing many background radio-loud AGN. Obtaining both 20cm and 6cm observations is important in making this distinction, as we can determine the spectral index of the sources. *Spitzer* observations are important in determining regions of star-formation within the galaxies (from 8μ PAH emission) and to accurately map the extinction due to dust (from 3.6 and 4.5μ emission). X-ray sources that have LMXB colours but are coincident with

regions of high star-formation as determined by 24μ observations are probably obscured HMXBs. The near-IR and wide-band optical images will allow us to determine accurate colours and metallicities of different regions within the galaxies. The narrow optical filters will help identify SNR. The UV observations will be important in the study of SSSs and ULXs that have cool disc temperatures. The superior collecting area of *XMM* will allow us to make accurate temperature maps of the diffuse X-ray emission within our galaxies and possibly even determine elemental abundances.

The unique opportunities now available thanks to the current generation of X-ray telescopes are allowing us, for the first time, to perform detailed studies of the X-ray source populations of galaxies. These studies have demonstrated that the properties of X-ray sources in galaxies can actually be used to study the physics of star formation within those galaxies. It is imperative that future X-ray missions maintain the high standard of large collecting area and high spatial resolution, or we will once again be blind in the only wavelengths where many of the most energetic processes in the universe are visible.

Acknowledgements

I would like to thank everyone at Leicester and at CfA for putting up with my incredibly hectic travel schedule over the last 4+ years, especially Steve Beikman, Lucy Byrne, Tricia Buckley, Rob Hewitt, Ann Kite, Lisa Paton, and Pat Russell. These are the dedicated souls who found me offices, worked out endless computer problems, and constantly changed flights and hotel arrangements.

Within the department at Leicester (past and present), I would like to thank Tim Roberts, Leigh Jenkins, Bob Warwick, Masaaki Sakano, Darach Watson, Paul O'Brien, Alex Hands, Simon Good, Nick Schurch, and Melvyn Davies for their collaborations, comments, and curry. At CfA, I wish to thank Andreas Zezas, Pepi Fabbiano, Frank Primini, Phil Kaaret, Rosanne Di Stefano, Mike Garcia, Fred Seward, and Jonathan McDowell.

From a past life, I owe a great debt to all the folks at VSU: Ken Rumstay, Martha Leake, and especially Dennis Marks. If I become half the scholar, teacher, and person that he is, I will consider my life a success.

Many others have been great friends and supporters over the years. A few of them are Derek Buzasi, Heather Preston, Brent and Kim Collier (and little Hoju), Jason Westlake, Lee Carpenter, and, of course, Chris Roush (who I cannot thank enough for his friendship).

I must thank everyone involved with the *Chandra* project. Without the dedication of hundreds of people, *Chandra* would not be the remarkable instrument that it is, and this thesis would not be possible.

I also must thank all the dungeon-dwellers of B-102 past and present. In particular, I would like to thank Eli Beckerman, John Bright, John Hayes, Mike Raley, Anil Seth, Joe DePasquale, and especially Mihoko Yukita.

A few people deserve individual thanks:

Harvey Tananbaum, whose encouragement and support has made me feel like much more than a kid from Georgia who got really lucky.

Anil Dosaj, for being the social-organizer's social organizer and for being a wonderful true friend.

Martin Ward, who came up with the crazy scheme of living on an airplane for 3 years.

Andrea Prestwich, to whom I owe my thesis, my career, and so much more. I cannot possibly thank you enough for everything.

To Miriam, the most wonderful person I've ever met. Your love and support have made the last 5+ years of my life the best. I would not have been able to make it through without you.

And finally, to my family–the most supportive family I could ever ask for. My parents have always been there for me with love and caring and have always stood by every decision I've ever made. Amy and Keith have always offered advice, sympathy (especially about writing!), and love. And Grammie has been the most wonderful grandmother in the world.

I would like to dedicate this thesis to the memory of my grandfather, William Edwards, who instilled in me his love for the stars at a very early age. I hope I have made him proud.

Chapter 9

Appendix A: Chronology

> Anything that happens, happens. Anthing that, in happening, causes something else to happen, causes something else to happen. Anthing that, in happening, causes itself to happen again, happens again. It doesn't necessarily do it in chronological order, though.
>
> Douglas Adams

This chapter provides a general overview of the history of X-ray point sources in external galaxies. It is not intended to be a complete history of the field of X-ray astronomy. Rather, it is intended to generally cover the science topics most relevant to the materials discussed herein, including X-ray binaries (XRBs) in external galaxies, supersoft sources(SSSs), extragalactic supernova remnants (SNR), and ultraluminous X-ray sources (ULXs).

On 18 June, 1962, a rocket was launched from White Sands, N.M., U.S.A., with the goal of detecting florescent solar X-rays reflected off the surface of the Moon. The moon was indeed detected, but a far brighter, more powerful cosmic X-ray sources was seen. It was given the name Sco-X1 because of its location w within the constellation Scorpius. The mission was significant also for its detection of a soft X-ray background, as well as the suggestion of a secondary X-ray source in the direction of supernova remnant Cassiopeia A and radio galaxy Cygnus A, both of which are now known to be strong X-ray sources. The speculated mechanism for X-ray production from those sources is based on existing radio data. Synchrotron radiation in the Galactic magnetic fields gives rise to the observed X-rays. These four discoveries are all the more remarkable given that the observing time on the flight was around 5

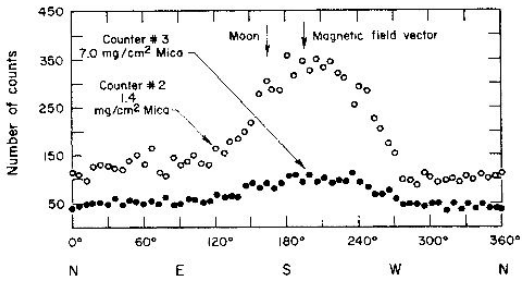

FIG. 1. Number of counts versus azimuth angle. The numbers represent counts accumulated in 350 seconds in each 6° angular interval.

Figure A-1 Original strip scan of the detection of Sco X-1.

minutes! (Giacconi et al., 1962)

1965 April 25. Another rocket flight made the first definite detections of extragalactic X-ray sources: the well-known radio galaxies M87 and Cygnus A. Significantly, Cassiopeia A was also conclusively identified as an X-ray source. The source Cygnus X-1 is found to be at only 1/4 the flux of observations from the previous year. It was this reduction in the flux of Cyg X-1 that made possible the detection of Cygnus A. The strong variability of Cygnus X-1 was further evidence that the source was accretion-powered. This mission also found that the cosmic X-ray background is anisotropic and likely results from man unresolved sources. (Byram et al., 1966)

Friedman et al. (1967) make the first estimate of the X-ray luminosity of the Milky Way: 7×10^{39} erg s^{-1} in the 1 to 10 keV range. They also estimate that the average luminosity of Galactic sources is 5×10^{36} erg s^{-1} and that the Galaxy contains around 1250 such sources. We now know that these numbers are within a factor of a few of being correct and are typical values for a normal spiral galaxy, as will be discussed later.

1968 October 28. A 5-minute rocket flight from Johnston Atoll in the South Pacific led to the detection of the LMC in X-ray. It was detected at 4σ with $F_x \approx 1.5\times10^{-9}$ erg cm^{-2} s^{-1}, $L_x \approx 4\times10^{38}$ erg s^{-1}. It was determined that the X-ray luminosity to mass ratio was approximately the same for the LMC and Milky Way. Though the scan region covered the SMC, it was not detected on this flight. A remarkable finding from this mission is that the 1.5-10.5 keV spectrum of the LMC was found to be softer than that of the "isotropic background". Though the authors don't discuss this finding in detail, it is clear that they have observed the largely AGN nature of the X-ray background as compared with the largely

X-ray binary nature of the LMC spectrum. (Mark et al., 1969)

1970 September 24. Another rocket launch detected both the SMC and the LMC. It was determined that the peak X-ray emission is offset from the peak optical emission and that the spectrum of the SMC is harder than that of the LMC. The emission of each object is extended. The luminosity of the LMC is $L_x \approx 6 \times 10^{38}\ \mathrm{erg\ s^{-1}}$ with two strong emission regions, one close to the star cluster 30 Doradus. The SMC has luminosity $L_x \approx 5 \times 10^{38}\ \mathrm{erg\ s^{-1}}$. Both luminosities are in the 1.5-12 keV band. It is speculated that the emission is dominated by a few sources, each with luminosity close to $10^{38}\ \mathrm{erg\ s^{-1}}$. (Price et al., 1971)

1970 December 21, 30, & 31, and 1971 January 4, 6, 7, 8, & 20. *Uhuru* observed the LMC for a total exposure time of 1ks. 3 discrete sources were detected and named LMC X-1, X-2, and X-3. LMC X-2 is possibly extended. LMC X-1 is near, but not coincident with, 30 Doradus. Faint diffuse emission is also detected in the LMC. 1971 January 1, 12, 13, 16, & 17. *Uhuru* observed the SMC for 1.1ks. One source was detected and dubbed SMC X-1. It is highly variable, with a peak $L_x \approx 1.2 \times 10^{38}\ \mathrm{erg\ s^{-1}}$ in the 2-7 keV band with spectral state changing along with the luminosity. No diffuse emission is detected in the SMC. LMC X-1 and X-3 are each about $7 \times 10^{37}\ \mathrm{erg\ s^{-1}}$ in 2-7 keV, and are likely the same class of source as the (as yet unclassified) Galactic sources Cyg X-2 and Sco X-1. LMC X-2 may be a cluster of sources. SMC X-1 is the first *unambiguous* observation of a source of stellar dimensions in an external galaxy. These observations are also significant because they produce the first clear X-ray maps of external galaxies.(Leong et al., 1971)

1971 January. Observations with *Uhuru* of SMC X-1 determine that the source is a binary star with an eclipse period of 3.9 days, but no pulse periods are found. This is the first clear detection of an eclipse period in an extraglactic binary, and only followed verly closely on the heals of the detection of periods in Galactic X-ray binaries (e.g. Schreier et al. (1972)). It is concluded that the X-ray emission (in excess of $10^{38}\ \mathrm{erg\ s^{-1}}$) is accretion powered, close to the Eddington limit for a 1.4 solar mass neutron star. (Schreier et al., 1972)

1972. An optical counterpart for SMC X-1 is found. It is determined to ba a B0 I star, Sanduleak 160 (Webster et al., 1972), with period identical to the X-ray period (Liller, IAUC #2469, confirmed by Petro et al. (1973)). Thus SMC X-1 is the first conclusively identified extragalactic high-mass X-ray binary.

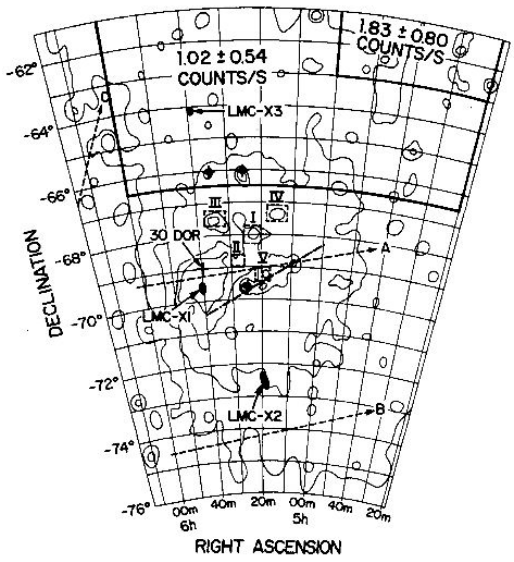

FIG. 2.—Map of the Large Magellanic Cloud. In addition to the three sources there is a diffuse emission whose intensity, averaged over the whole region shown in the map is (0.57 ± 0.16) counts s^{-1}. The heavy rectangles show areas in which additional excess emission appears. Some radio and optical features are shown for comparison: the bar is represented by the dash-dot line (— • — •); the constellations (Bok 1966), by the rectangles; the three supernova remnants by the symbol ⊕; and 1410-MHz isophote contours at levels of 0, 2, 6, and 10 × 0.17° K are given by the thin lines (Matthewson and Healey 1964). Scan tracks of the center of the field of view of the 0°.5 FWHM detector for the three scans shown in Fig. 1 are given by the dashed lines.

Figure A-2 *Uhuru* map of the LMC.

Bowyer et al. (1974) detect M31 in a 1973 rocket flight. In 0.5-5 keV, $L_x = 2.2 \times 10^{39}$ erg s^{-1}, comparable to the summed X-ray luminosity of the 25 brightest X-ray binaries in the Milky Way. The spectrum is also similar. It is proposed that the X-ray emission of M31 and, by extension, all normal galaxies is dominated by a population of a few bright XRBs. This indeed turns out to be the case for all galaxies not dominated by emission from an AGN.

1975. Bahcall and Ostriker propose that the X-ray emission from globular clusters is due to massive black holes at the cluster centres. Though this turned out to likely be incorrect for Galactic (and other local group) globular clusters, it was the first discussion of luminous X-ray sources as possible "intermediate mass black holes", though the authors do not use that term. (Bahcall & Ostriker, 1975)

1976. Pulsations are discovered from SMC X-1, making SMC X-1 the first X-ray identified pulsar. The pulse period is 0.716 seconds with a pulse fraction of 25-35%. The discovery is made with an Aerobee rocket and an Apollo spacecraft. (Lucke et al., 1976).

1977. All 7 known (by that time) point sources in the LMC are shown to be variable on a variety

of timescales, consistent with the theory that the sources are accretion-powered. This is a major step towards proof that the X-ray luminosity of all normal galaxies is dominated by emission from discrete accretion-powered binaries. (Griffiths & Seward, 1977)

Ward et al. (1978) identify M82 as an X-ray source in the 2A catalog and suggest that more normal galaxies will be found with $L_x \sim 10^{39}$ erg s^{-1} from the cumulative luminosity of a few bright sources. It is the first starburst galaxy identified in the X-ray.

1978 November 12. The *Einstein* Observatory (HEAO-2) is launched. It features 4 instruments: the IPC, HRI, SSS, and FPCS. (Giacconi et al., 1979) Prior to the launch of *Einstein*, only 4 non-AGN, non-Seyfert (that is to say, "normal") galaxies had been detected in X-rays: M31, the Milky Way, and the Small and Large Magellanic Clouds. *Einstein* can be considered the true predecessor to *Chandra*, as its main advantage over previous missions was high angular resolution. (Helfand, 1984)

Clark et al. (1978) note that the X-ray luminosities of the LMC and SMC sources are higher than the luminosities of similar Galactic sources. They surmise that this is due to lower metal abundances in the clouds and, thus, lower opacity of the accreting material.

1978, 1981, 1983. X-ray eclipses (1.4 day), flux modulations (30.5 day), and pulsations (13.5s) are all observed in LMC X-4, thus confirming it as the second identified extragalactic X-ray binary. (Li et al., 1978; Lang et al., 1981; Kelley et al., 1983)

1978, 1979, 1980, 1982. LMC X-5 is detected; outbursts are seen in excess of 10^{39} erg s^{-1}; an outburst recurrance scale of 16.7 days is determined (with not all predicted outbursts occuring); and the counterpart is determined to be a B star. LMC X-5 is the first neutron star detected with peak $L_x > 10^{39}$ erg s^{-1}. This is very significant, as many people will forget during the early days of *Chandra* that neutron stars can achieve luminosities in excess of 10^{39} erg s^{-1}. (White & Carpenter, 1978; Johnston et al., 1979, 1980; Skinner et al., 1982)

An *Einstein* survey of M31 in 1979 reveals 69 discrete X-ray sources. The position of many of the sources within the bulge implies that the sources are largely Population II (LMXBs). Many of the sources lie in globular clusters, contrary to the bright X-ray sources in the Milky Way. (van Speybroeck et al. (1979) and subsequent works.)

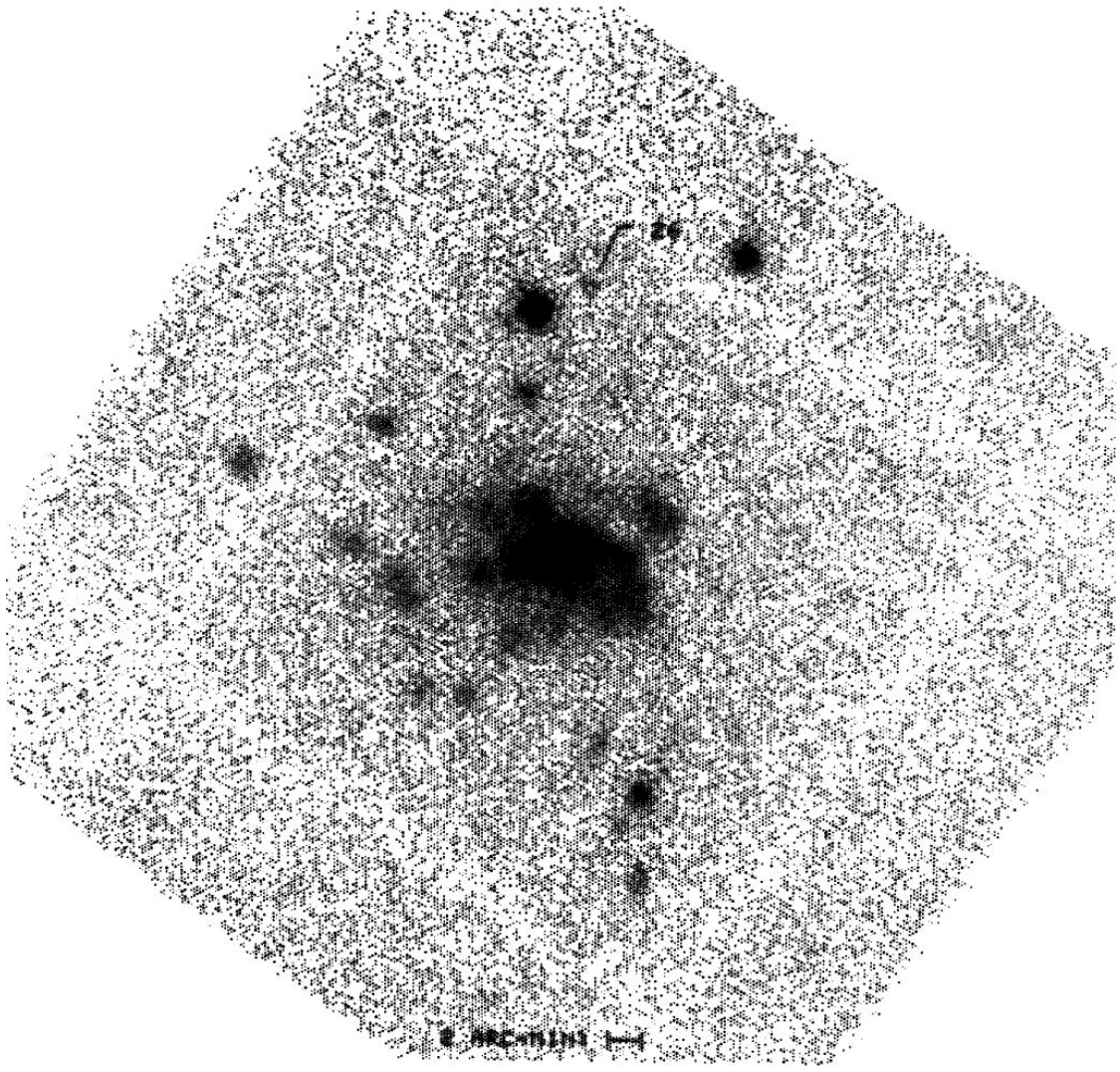

Figure A-3 *Einstein* IPC image of the central region of M31.

McKee et al. (1980) observe the supernova remnant N132D in the LMC. This is the first detection of an extragalactic supernova remnant in X-rays. The X-ray spectrum is softer than that of XRBs.

An *Einstein* survey of the SMC in 1981 discovers several soft X-ray sources for which counterparts cannot be found. These will become the first historical supersoft X-ray sources (SSSs) though the term is not used at the time. An *Einstein* survey of the LMC also finds lots of soft sources. They are tentatively identified as supernova remnants, though the authors acknowledge that they may be a new class of object. (Seward & Mitchell, 1981; Long et al., 1981)

1983. An *Einstein* survey of nearby galaxies reveals the first detected point sources (probably XRBs)

in galaxies beyond the local group: M101, NGC 247, and NGC 253. The survey also detects the first very luminous, non-nuclear point sources in galaxies beyond the local group (ULXs, though that therm is not used). These sources are found to be variable (hence discrete), and it is proposed that they are accreting binaries with black holes as the compact objects, since the luminosities are higher than those from pure Eddington accretion onto a neutron star. (Lewin & van den Heuvel (1983), pp. 117-118)

1984. Optical counterparts for 22 of the 24 known point sources in the LMC are identified. 13 are foreground stars, 3 are background AGN, and 6 are members of the LMC. Of these 6, 5 are probable XRBs and one is a SNR. The advantage of multiwavelength data for classification of X-ray point sources is very clearly demonstrated. (Cowley et al., 1984)

Cowley et al. (1984) determine that LMC X-3 is a black hole with mass between 7 and 13 $\mathrm{M}_{\odot}$. The calculation is made given the spectroscopic mass of the companion B3 V star (4-8 $\mathrm{M}_{\odot}$), the orbital period determined by radial velocity variations (1.7049 days), and the inclination determined by X-ray eclipses ($\lesssim 65\,\mathrm{deg}$). This is the first confirmed detection of an extragalactic stellar-mass black hole.

A LMC survey and follow-up with *Einstein* reveals 103 point sources. About 50% are in the LMC and 50% of those are SNRs. A SMC survey and follow-up reveals 45 sources, again dominated by SNRs (see Helfand (1984) and references therein). These observations demonstrate that, as lower luminosity thresholds are reached, sources besides XRBs contribute significantly to the discrete X-ray source luminosity function of galaxies.

Fabbiano & Trinchieri (1985) demonstrate that there is a strong correlation between L_x and L_B in normal galaxies, indicating that the X-ray population is predominantly Population I objects associated with young star formation. HMXBs dominate the high luminosity end of the luminosity function of galaxies and contribute the most to the total X-ray luminosity.

Fabbiano (1988) presents the first fits to the X-ray point source luminosity functions of external galaxies (M31 and M81). She proposes that the LFs are fit by a powerlaw with a low-luminosity turnover.

Fabbiano, Trinchieri, and others establish firmly that the L_x of normal spirals is dominated by discrete point sources, largely XRBs, whereas the emission from early-type galaxies and starburst galaxies is due to a mix of discrete sources and a hot, gaseous component (see, e.g., Fabbiano (1989) and references therein).

Trinchieri et al. (1990) propose that there may be a "universal" luminosity function (LF) for X-ray point sources in all spiral galaxies. The LF is a powerlaw with slope between 0.6 and 0.8 (differential) and a low-luminosity turnover. They observe that the LF of M101 may be flatter than M31 and propose that M101 may have a population of luminous high-mass binaries on top of an older population similar to M31. This is a particularly impressive observation as there were only 10 sources thusfar detected in M101.

1990 June 1. The German and U.S. Rontgen Satellite, *ROSAT*, is launched. If features 3 instruments: the PSPC, HRI, and WFC. *ROSAT* was the premier X-ray observatory of its era and provided a wealth of data on normal galaxies.

The term "supersoft sources" is first used in 1991 to describe two LMXBs in the LMC. They may represent a new class of objects: binaries with white dwarf primaries accreting matter at a super-Eddington rate. The X-ray emission would result from nuclear burning directly on the surface of the white dwarf. (Greiner et al., 1991)

Primini et al. (1993) publish the *ROSAT* LF of M31. They find a slope of $\Gamma \approx 1.7$ (cumulative) for sources above $L_x = 2 \times 10^{37}\ \mathrm{erg\ s^{-1}}$. They also conclude that there is a flattening of the LF at low L_x. They assume the flattening is real and, therefore, only 15-26% of the diffuse emission in the bulge of M31 can be accounted for by discrete sources. They also find that 45% of the X-ray sources in the bulge are variable.

Di Stefano et al. (1995) demonstrate that the ionization nebulae associated with SSSs may in fact be planetary nebulae, thus strengthening the argument that SSSs are white dwarfs, since one would expect to see SNR around compact objects from more massive parent stars.

The term "ultra-luminous compact X-ray" source is first used to describe a source with $L_x > 10^{39}\ \mathrm{erg\ s^{-1}}$. The *ASCA* results for ULXs show that the source spectra are well fit by cool disk blackbody models, thus implying a large inner accretion disk radius and a more massive compact object. The sources may then be black holes with $M > 50\ \mathrm{M_\odot}$. (Mizuno et al., 1999)

Roberts & Warwick (2000) show that there are a large number of "superluminous" X-ray sources in nearby galaxies, defined as sources with $L_x > 2 \times 10^{38}\ \mathrm{erg\ s^{-1}}$, the Eddington luminosity for a $1.4\ \mathrm{M_\odot}$neutron star. Many of the sources have luminosities in excess of $10^{39}\ \mathrm{erg\ s^{-1}}$. This is the first

true sample of ULXs in nearby galaxies, though, again, the term is not used.

Results from *ASCA* show that many ULXs have high L_x but also high T_in, incompatible with the theory of ULXs as black holes with masses larger than 100 $M_\odot$. It is suggested that a Kerr (rotating) black hole can explain both these properties. The comparison to Galactic microquasars GRO J1655-40 and GRS 1915+105 is made. (Makishima et al., 2000)

Chapter 10

Appendix B: Notes on Individual Galaxies

Light thinks it travels faster than anything but it is wrong. No matter how fast light travels it finds that darkness has always got there first and is waiting for it.

Terry Pratchett

B-1 NGC 278, Sb

At just over $2'$ in diameter, NGC 278 is the least extended galaxy in our sample. As can be seen in Figure B-2, the X-ray emission consists of around 15 point sources embedded in extensive unresolved emission. Due to the small spatial extent, we anticipate 0-1 background sources within the galaxy D_{25} radius (red line on Figure B-1). An additional 63 sources in the field were excluded as outside the D_{25} radius. This number is quite large in the case of NGC 278 due to the long exposure times of the observations. The completeness limit for each observation is $3.7 \times 10^{37} ergs^{-1}$. Though some of this emission is likely due to point source confusion, the ability of *Chandra* to resolve point sources in galaxies of similar distance in a similar exposure time (e.g. M74, see secion B-2) implies that either 1) much of the unresolved emission is due to hot gas and not faint point sources, or 2) the shape of the LF of NGC 278 is drastically different from other more nearby galaxies (e.g. M31) which show an LF turnover at lower luminosities (Shirey et al., 2001). Though the Galactic $\mathrm{n_H}$ in the direction of NGC 278 ($1.29 \times 10^{21}\ cm^{-2}$) is the highest in our sample, it is still relatively low and should not hamper

the detection of faint sources.

Plotted in Figure B-1 is the cumulative point source luminosity function for both *Chandra* observations of NGC 278 with best fit single power law slopes. Though the relatively steep slopes indicate an evolved stellar population, since there are only 14 point sources, the parameters of the luminosity function (LF) cannot be accurately determined. Figure B-3 shows an optical image of NGC 278 with the X-ray point sources marked. Following the method of Prestwich et al. (2003) for source classification by X-ray colours, the population appears to be dominated by low-mass X-ray binaries (LMXBs) with evidence for high absorption (see figure 6.3). 20% of the sources exhibit statistically significant variability between the two *Chandra* observations at the 90% level.

B-2 M74 (NGC 628), Sc

M74 has been observed twice with *Chandra* and twice with *XMM-Newton*. The first *XMM-Newton* observation was performed as a target of opportunity (TOO) observation to observe a recent supernova in M74, SN2002ap. A detailed study of those data is presented in Soria & Kong (2002). The emission is dominated by 67 point sources with little evidence of unresolved emission. At only 8.8 Mpc, the Sc spiral M74 offers one of the best comparisons to the Milky Way in our sample. 13 sources in the field were excluded as outside the D_{25} radius. We anticipate that fewer than 10 of the detected sources within the D_{25} radius are background sources.

The most interesting aspect of the M74 observations is the ultraluminous source CXOU J013651.1+154547 which is discussed in detail in Krauss et al. (2003). This remarkable source exhibits quasi-periodic flaring and changes in spectral state, suggesting that it is likely a microquasar similar to the Galactic microquasar GRS 1915+105.

The LF slope of M74 is relatively steep (1.16) as compared with star-forming galaxies, indicating that the X-ray source population is dominated by LMXBs. The completeness limit for each observation is $1.6 \times 10^{37} ergs^{-1}$. The X-ray colours indicate a mix of high- and low-mass binaries with a few possible supernova remnants (SNRs). There is no radial dependence of the source colours, indicating no clear separation of bulge and disc sources. 23% of the sources exhibit long-term variability. Plotted in figures B-4 through B-6 are the LF, smoothed 3-colour X-ray image and optical image with X-ray

source overlays.

B-3 NGC 1291, S0/a

NGC 1291 is one of the best examples of an X-ray bright S0 galaxy in the local universe. It has been observed twice with *Chandra* with results presented in Irwin et al. (2002). We build on their work by extending the source catalog from 48 to 93 discrete sources. An additional 8 sources in the field were excluded as outside the D_{25} radius. Note the relatively steep luminosity function in figure B-7, which is characteristic of early-type galaxies (Sarazin et al., 2000). The X-ray colours indicate a population dominated by LMXBs. There is clear evidence of spiral structure in the unresolved X-ray emission which is not evident in optical images. 29% of the sources exhibit long-term variability. Plotted in figures B-7 through B-9 are the LF, smoothed 3-colour X-ray image and optical image with X-ray source overlays. The completeness limit for the two observations are $1.8 \times 10^{37} ergs^{-1}$ and $2.9 \times 10^{37} ergs^{-1}$. We anticipate 10-12 of the detected X-ray sources within NGC 1291 are background sources.

B-4 NGC 2681, S0/a

NGC 2681 is an early type galaxy with evidence for a bar-like structure present in the unresolved X-ray emission. The colours indicate an LMXB population. 43% of the X-ray source population (10 of 23 sources) exhibits long-term variability. An additional 56 sources in the field were excluded as outside the D_{25} radius. Plotted in figures B-10 through B-12 are the LF, smoothed 3-colour X-ray image and optical image with X-ray source overlays. The completeness limit for each observation is $1.0 \times 10^{37} ergs^{-1}$. We estimate that 2 of the 23 detected sources are background sources.

B-5 NGC 3184, Scd

NGC 3184 was observed twice with *Chandra*, the second time as a target of opportunity observation to observe a recent supernova, SN 1999gi (Schlegel, 2001). The LF is less steep than the early-type

spirals NGC 1291 and NGC 2681, though still not as flat as the actively star-forming M83 (B-9). The X-ray colours show a mix of low- and high- mass binaries and SNRs. There is a slight enhancement in the unresolved emission towards the southwest, coincident with the optical spiral arm in that direction. 24% of the population exhibits long-term variability. Plotted in figures B-13 through B-15 are the LF, smoothed 3-colour X-ray image and optical image with X-ray source overlays. The completeness limit for the two observations are $4.3 \times 10^{37} ergs^{-1}$ and $2.5 \times 10^{37} ergs^{-1}$. 25 sources in the field were excluded as outside the D_{25} radius. Approximately 10 of the detected X-ray sources are likely due to background.

B-6 NGC 4314, SBa

NGC 4314 is a bright SB galaxy with a ring of circumnuclear star formation. Unresolved emission in the star forming region dominates the emission, with only 22 point sources detected. An additional 23 sources in the field were excluded as outside the D_{25} radius. NGC 4314 has been studied extensively with HST (see Benedict et al. (1992) and subsequent papers) showing clear evidence for star formation in a circumnuclear ring. We detect enhanced unresolved X-ray emission coincident with this ring. We estimate that 4-5 of the detected sources may be due to background.

The X-ray colours indicate an LMXB dominated population, though insufficient exposure time prevents the detection of faint ($L_X < 10^{37} ergs^{-1}$) potential SNRs in the nuclear starburst region. The LF slope is fairly flat, though the low number of sources prevents the parameters of the LF fit from being precisely determined. 14% of the population exhibits long-term variability. Plotted in figures B-16 through B-18 are the LF, smoothed 3-colour X-ray image and optical image with X-ray source overlays. The completeness limit for each observation is $8.8 \times 10^{37} ergs^{-1}$.

B-7 M94 (NGC 4736), Sab

M94 has several bright nuclear sources, none of which is clearly an AGN. The observation was performed with a 1/4 subarray (reducing the frametime from 3.2 to 0.84 seconds) in order to mitigate the effects of pileup on the cout rates and spectra of the nucleus and other bright sources. As such, we only

observe a slice $2' \times 8'$ of the galaxy and the luminosity functions should therefore be taken as indicative of the nuclear region rather than the full galaxy. An analysis of the longer (47ks) M94 observation is presented in Eracleous et al. (2002), and we extend their analysis to include a short (2ks) observation and catalog an additional 16 point sources. No sources in the field were excluded as outside the D_{25} radius. Due to the small fraction of sky covered in the subarray, we estimate that only 0-1 sources are contributed by the background.

The LF of M94 is quite flat, and the X-ray source population is dominated by potential SNRs and X-ray binaries (XRBs). This implies a high star formation rate in the nucleus, in agreement with $H\alpha$ and radio measurements (Pogge 1989 & Turner & Ho, 1994). This can be contrasted with the nucleus of M31, where the LF slope is quite steep, indicating a population dominated by LMXBs (Kong et al., 2003). The spiral nucleus shows clear unresolved emission tracing the spiral arms. 14% of the sources exhibit long-term variability, though this should be considered an extreme lower limit as the first observation was around 20 times the duration of the second. Plotted in figures B-19 through B-21 are the LF, smoothed 3-colour X-ray image and optical image with X-ray source overlays. The completeness limit for the two observations are $3.1 \times 10^{36} ergs^{-1}$ and $6.3 \times 10^{37} ergs^{-1}$.

B-8 M51 (NGC 5194/95), Sbc

At just over 6 Mpc, M51 is the closest example of a face-on interacting galaxy pair. It contains a wealth of point sources and unresolved emission clearly tracing the spiral arms in both galaxies. There are 4 ULXs. A detailed analysis of M51 is presented in Terashima & Wilson (2004). We extend their catalog by an additional 15 sources and include sources on the ACIS S2 chip. An additional 34 sources in the field were excluded as outside the D_{25} radius. We estimate that 15 sources within the D_{25} ellipse are due to background.

The LF slope is also quite flat (almost as flat as the LFs of starburst galaxies, Kilgard et al. 2002) and the X-ray colours indicate a mix of SNRs and low- and high-mass binaries, as well as some supersoft sources (SSSs). 31% of the sources exhibit long-term variability. Plotted in figures B-22 through B-24 are the LF, smoothed 3-colour X-ray image and optical image with X-ray source overlays. The S3 completeness limit for the two observations are $4.1 \times 10^{37} ergs^{-1}$ and $2.2 \times 10^{37} ergs^{-1}$. The FI chip completeness limit for the two observations are $5.7 \times 10^{37} ergs^{-1}$ and $3.2 \times 10^{37} ergs^{-1}$.

B-9 M83 (NGC 5236), Sc

The X-ray observations of M83 consist of many bright point sources and unresolved emission tracing the spiral arms. M83 harbors a nuclear starburst, so it, like M51, bridges the gap between the normal spirals in our sample and more extreme starbursts like the Antennae (Fabbiano et al., 2001). A detailed study of the first observation of M83 is presented in Soria & Wu (2002) and Soria & Wu (2003). We extend their catalog by an additional 54 sources, many falling on the neighboring ACIS S2 and S4 chips. An additional 12 sources in the field were excluded as outside the D_{25} radius. We estimate that 7-8 of the detected sources within the D_{25} ellipse are due to background.

The LF slope of M83 is quite flat, consistent with a high star formation rate in its recent past (e.g. Harris et al., 2001). The X-ray colours indicate a mix of high- and low-mass binaries with quite a lot of potential SNRs and SSSs as compared with the other galaxies in our sample. There is also the suggestion of an overabundance of soft sources near the nuclear region, indicating that these sources are indeed SNRs in the nuclear starburst region. 34% of the population exhibits long-term variability; a lower limit since the first observation was 5 times the duration of the second. Plotted in figures B-25 through B-27 are the LF, smoothed 3-colour X-ray image and optical image with X-ray source overlays. The S3 completeness limit for the two observations are $4.1 \times 10^{36} ergs^{-1}$ and $1.9 \times 10^{37} ergs^{-1}$. The FI chip completeness limit for the two observations are $5.1 \times 10^{36} ergs^{-1}$ and $2.6 \times 10^{37} ergs^{-1}$.

B-10 M101 (NGC 5457), Scd

M101 is the (spatially) largest galaxy in our sample at just under 1/2 a degree across and was observed for the longest single exposure (100ks). Not surprisingly, it also contains the most point sources. Analysis of the longer *Chandra* pointing has been presented in Pence et al. (2001), which focuses on the ACIS-S3 chip. Building on their work, we include analysis of both *Chandra* observations and a set of five ACIS chips (I2, I3, S2, S3, & S4) to more than double their source catalog. Since the second *Chandra* pointing is only 1/10 the length of the first observation, many of the sources are not detected in the second and it therefore may not be too useful to compare the luminosity functions of the two observations. Since the front-illuminated ACIS CCDs have much higher detection thresholds than do the back-illuminated chips, in fitting the LFs we only consider sources above the detection thresholds

for a front-illuminated CCD.

M101 contains 3 ultraluminous X-ray sources. One is a SSS, with almost no photons detected above 1 keV. This source exhibits extreme flaring variability. An analysis of these sources is presented in Mukai et al. (2003).

The LF slope of M101 is moderately steep. The X-ray colours indicate a mix of low- and high-mass binaries with many SNRs and SSSs. In the case of M101, we speculate that the abundance of SNR candidates is not due to a higher than average SFR but rather due to the much deeper observation of M101 as compared with the other galaxies in the sample. There is the suggestion of an overabundance of soft sources towards the nucleus, but we believe this is a selection effect due to the decreased sensitivity of the outlying front-illuminated ACIS chips to low-energy photons. Though the X-ray colours of the sources on the front-illuminated chips have been weighted to approximate colours on the S3 chip, the detection threshold is still quite a bit higher on those chips, due both to the lower effective area at low energies of the FI chips and the large off-axis angles. 10% of the population is variable, again an extreme lower limit due to the factor of 10 difference in exposure times of the two observations. Plotted in figures B-28 through B-30 are the LF, smoothed 3-colour X-ray image and optical image with X-ray source overlays. The S3 completeness limit for the two observations are $4.4 \times 10^{36} ergs^{-1}$ and $4.6 \times 10^{37} ergs^{-1}$. The FI chip completeness limit for the two observations are $6.3 \times 10^{36} ergs^{-1}$ and $6.4 \times 10^{37} ergs^{-1}$. We exclude 4 sources beyond the D_{25} radius of M101. We estimate that 10-15 of the X-ray sources on the S3 chip are due to background. The contribution in the front-illuminated CCDs is much more difficult to estimate, and could be up to 50% of those sources in all cases.

B-11 IC 5332, Sd

IC 5332 is another good Milky Way analog with emission consisting almost entirely of resolved point sources. The completeness limit for each observation is $1.4 \times 10^{37} ergs^{-1}$. The LF slope is quite steep and the X-ray colours indicate a mix of high- and low-mass binaries. There is no clear detection of a nuclear source. Though there is the suggestion of unresolved X-ray emission towards both the NE and SE, these are actually two background clusters of galaxies outside the radius of IC 5332. 17% of the sources exhibit long-term variability. Plotted in figures B-31 through B-33 are the LF, smoothed 3-colour X-ray image and optical image with X-ray source overlays. 22 sources in the field were excluded

as outside the D_{25} radius. We estimate that 10 of the detected sources in IC 5332 are likely background sources.

B-12 M82, Irr0, starbusrt

M82 is the prototypical starburst galaxy in the nearby universe. Viewed nearly edge-on, one can clearly see diffuse emission from the starburst-induced superbubble. In our *Chandra* observations, the completeness limits are as cited in table 4.2. The LF slope is very flat, at around 0.6. The X-ray colours indicate a mix of bright X-ray binaries (most likely HMXBs, due to the recent star formation) and SNR, though the colours also appear quite absorbed. Presented in figures B-34 and B-35 are the smoothed 3-colour X-ray image and optical image with X-ray source overlays. Figures B-36 through B-38 show the LFs for all 8 observations of M82. We exclude 34 sources beyond the D_{25} radius. Due to the relative shallowness of each of the observations of M82, we anticipate that only around 5 sources are due to background.

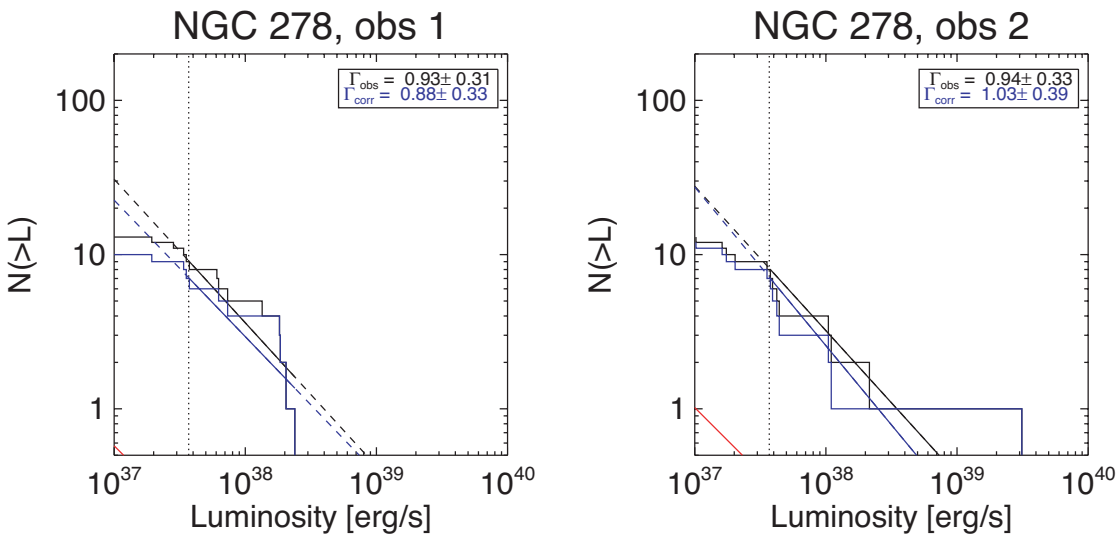

Figure B-1 Cumulative luminosity function of the X-ray point sources in NGC 278. LFs for both *Chandra* observations are plotted. Solid lines indicate the range of data used for the fit. nuclear sources and sources below the detection completeness limit are excluded.

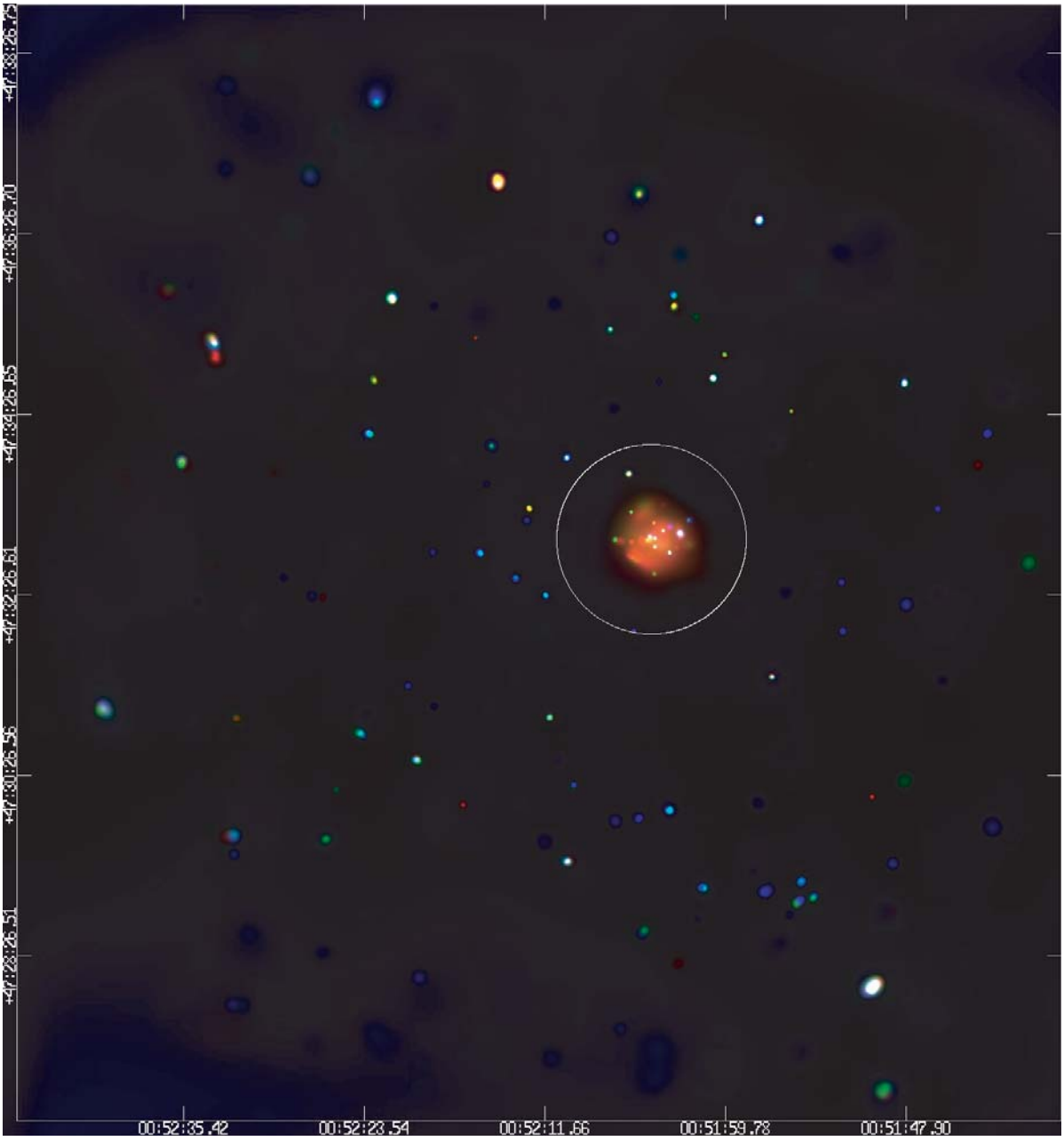

Figure B-2 Merged Chandra observation of NGC 278. Adaptively smoothed. Red is 0.3-1 keV, green 1-2 keV, and blue 2-8 keV. Overplotted is the galaxy D_25 ellipse.

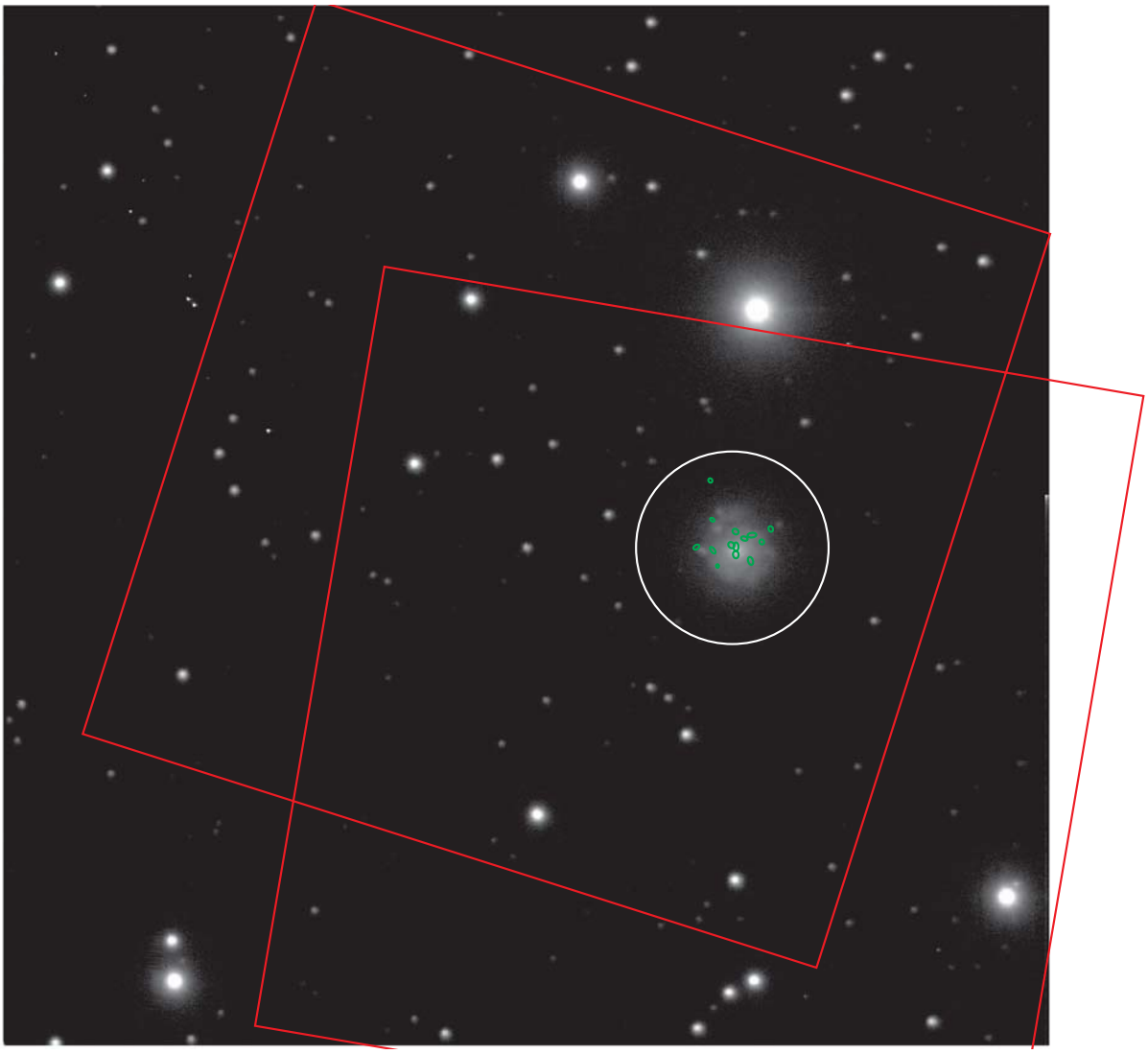

Figure B-3 Optical image of NGC 278 with Chandra sources overlayed. The white circle is the D25 extent of the galaxy. The scale of the image is $4' \; x 4'$.

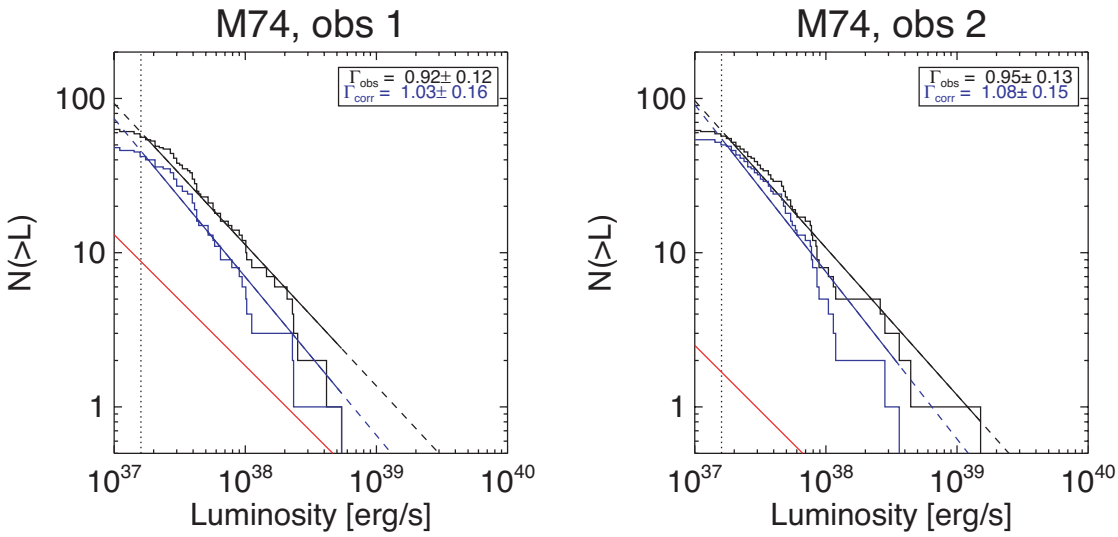

Figure B-4 Cumulative luminosity function of the X-ray point sources in M74.

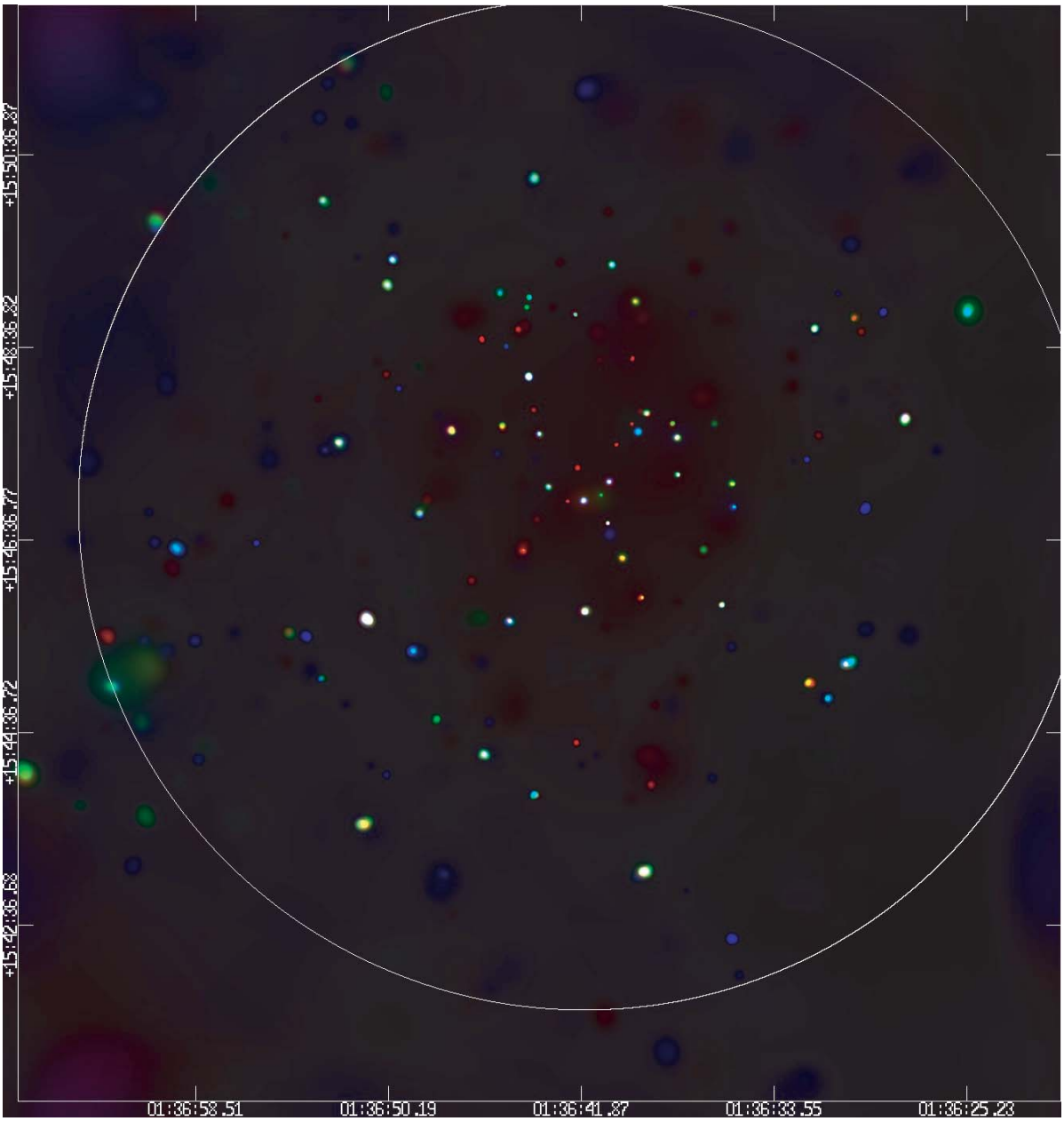

Figure B-5 Merged Chandra observation of M74. Adaptively smoothed. Red is 0.3-1 keV, green 1-2 keV, and blue 2-8 keV.

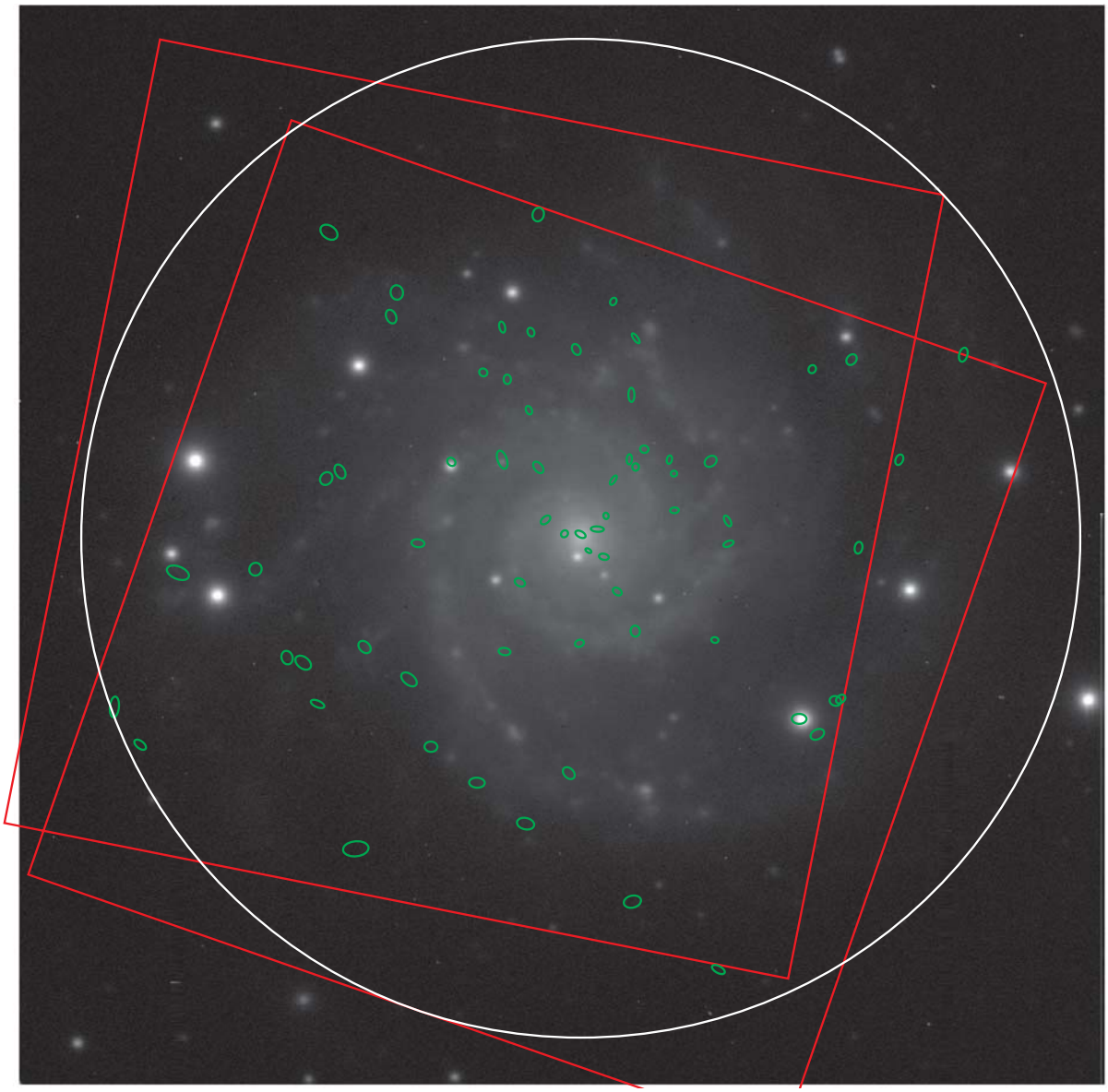

Figure B-6 FLWO optical image of M74 with Chandra sources overlayed. The white circle is the D25 extent of the galaxy. The scale of the image is $10' \; x 10'$.

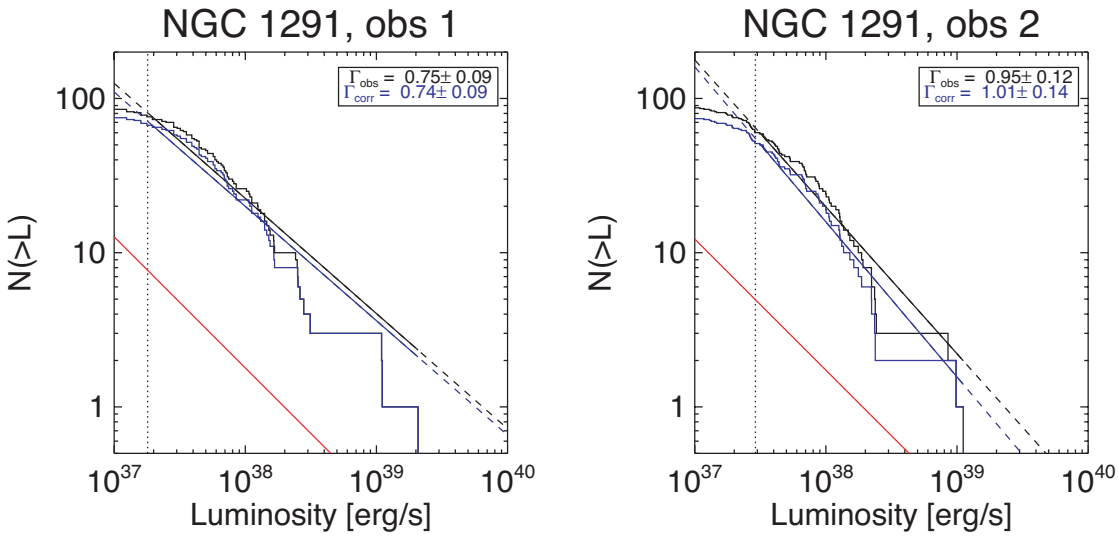

Figure B-7 Cumulative luminosity function of the X-ray point sources in NGC 1291.

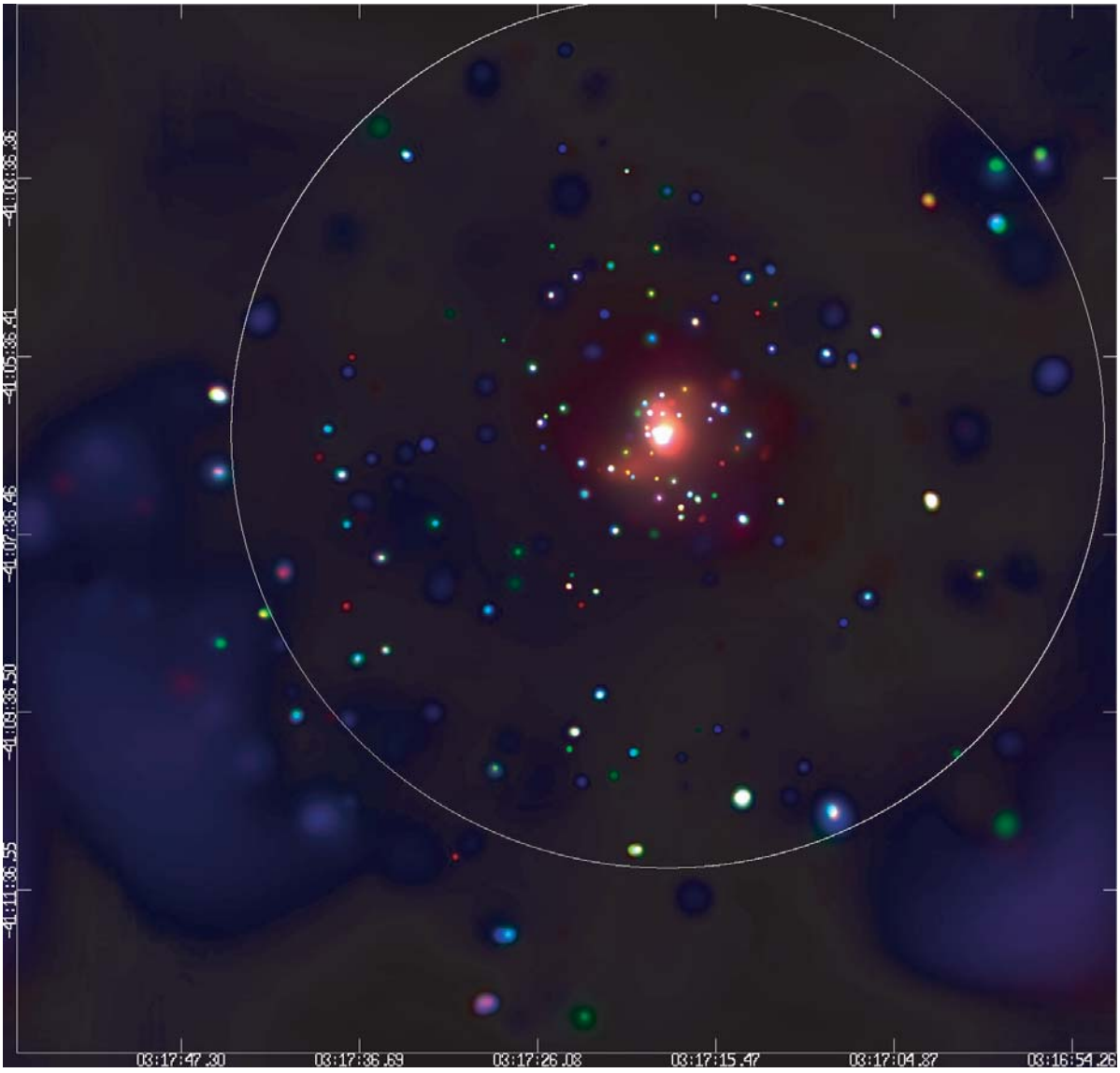

Figure B-8 Merged Chandra observation of NGC 1291. Adaptively smoothed. Red is 0.3-1 keV, green 1-2 keV, and blue 2-8 keV.

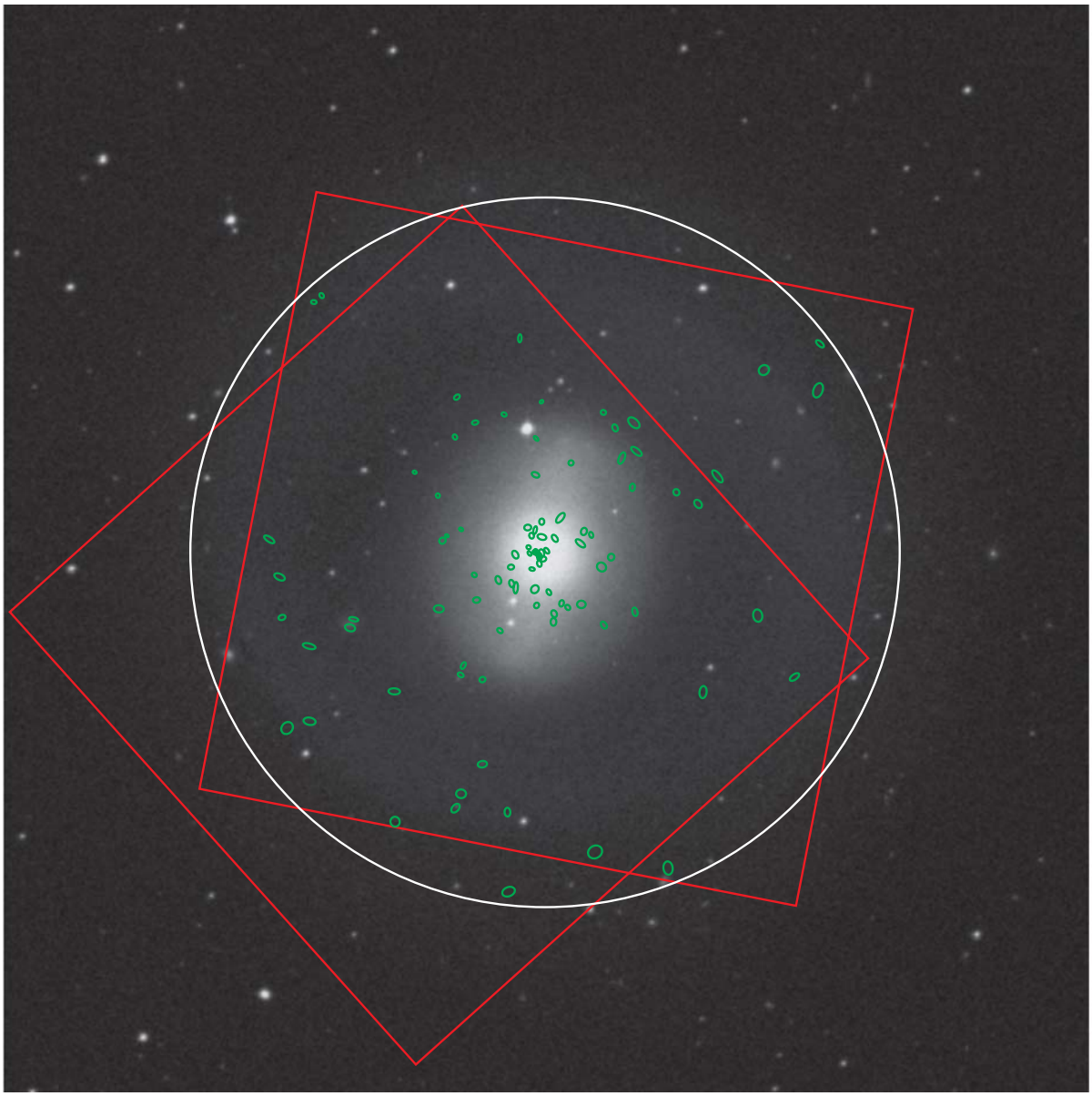

Figure B-9 DSS optical image of NGC 1291 with Chandra sources overlayed. The white circle is the D25 extent of the galaxy. The scale of the image is $10' \; x 10'$.

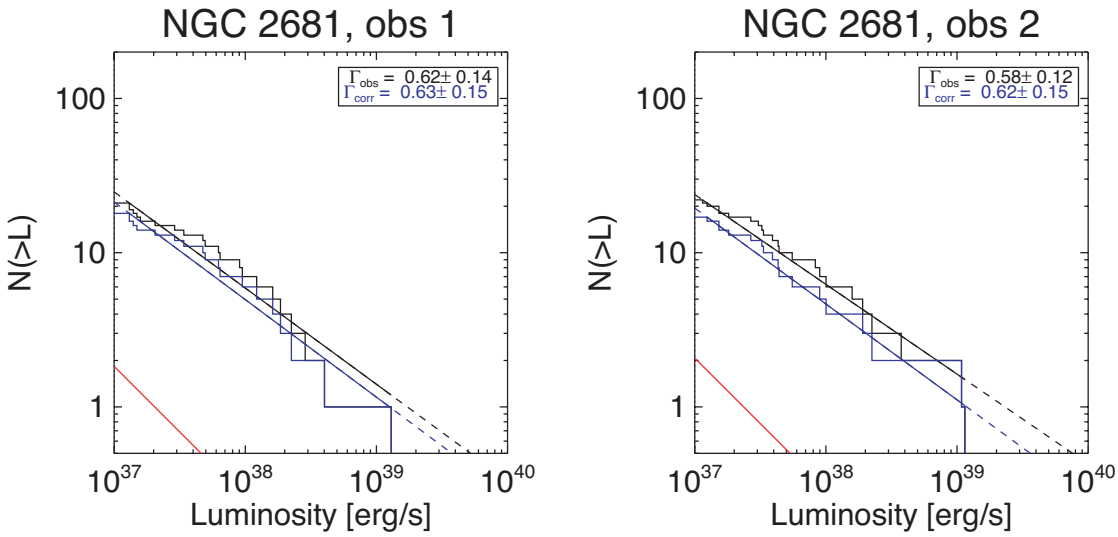

Figure B-10 Cumulative luminosity function of the X-ray point sources in NGC 2681.

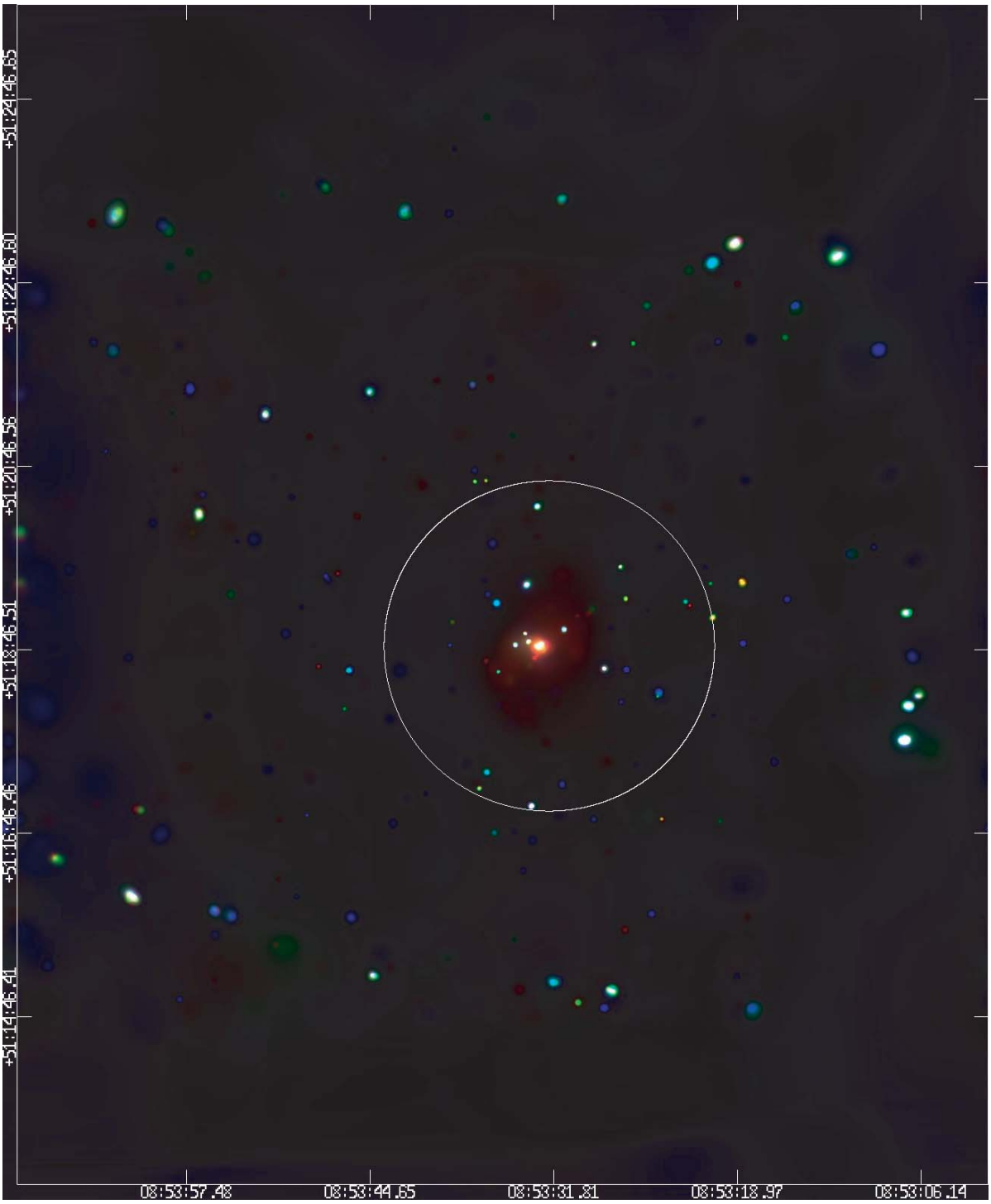

Figure B-11 Merged Chandra observation of NGC 2681. Adaptively smoothed. Red is 0.3-1 keV, green 1-2 keV, and blue 2-8 keV.

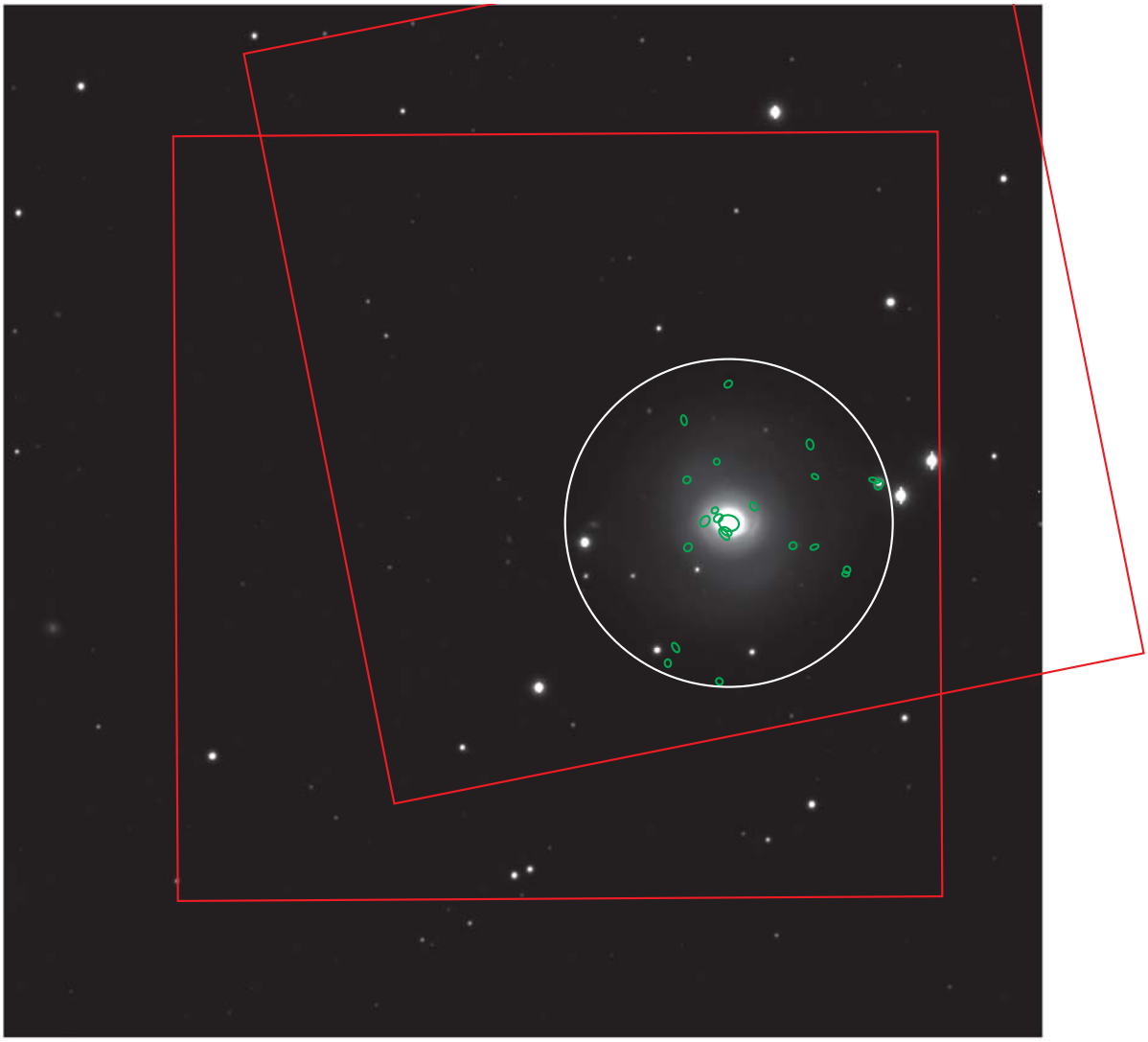

Figure B-12 FLWO optical image of NGC 2681 with Chandra sources overlayed. The white circle is the D25 extent of the galaxy. The scale of the image is $10' \; x 10'$.

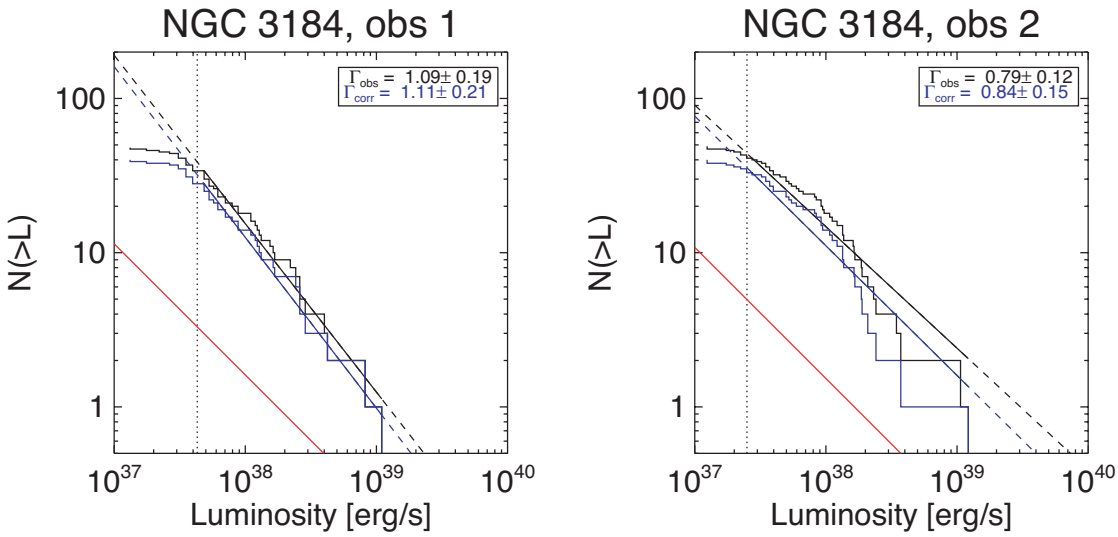

Figure B-13 Cumulative luminosity function of the X-ray point sources in NGC 3184.

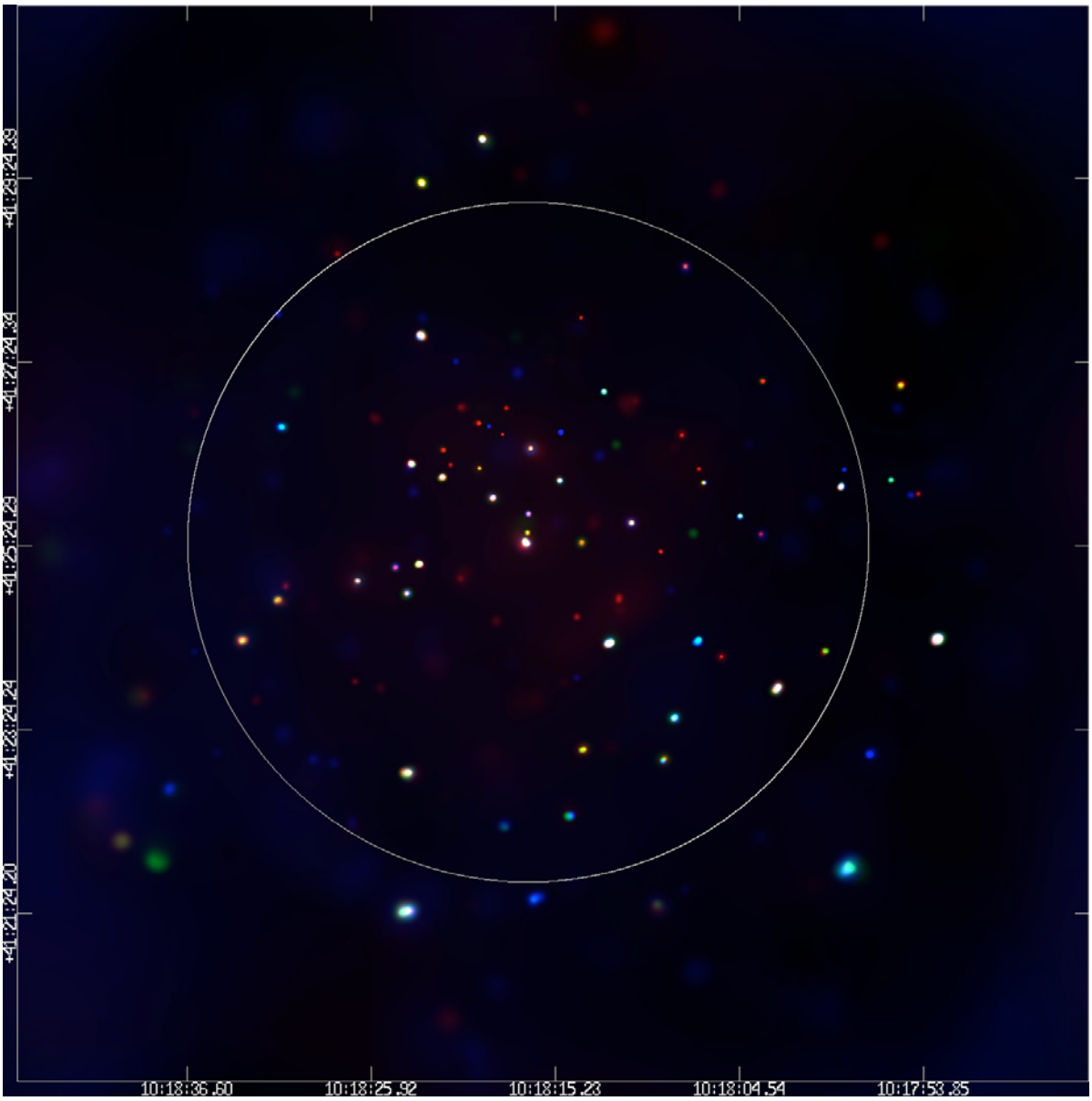

Figure B-14 Merged Chandra observation of NGC 3184. Adaptively smoothed. Red is 0.3-1 keV, green 1-2 keV, and blue 2-8 keV.

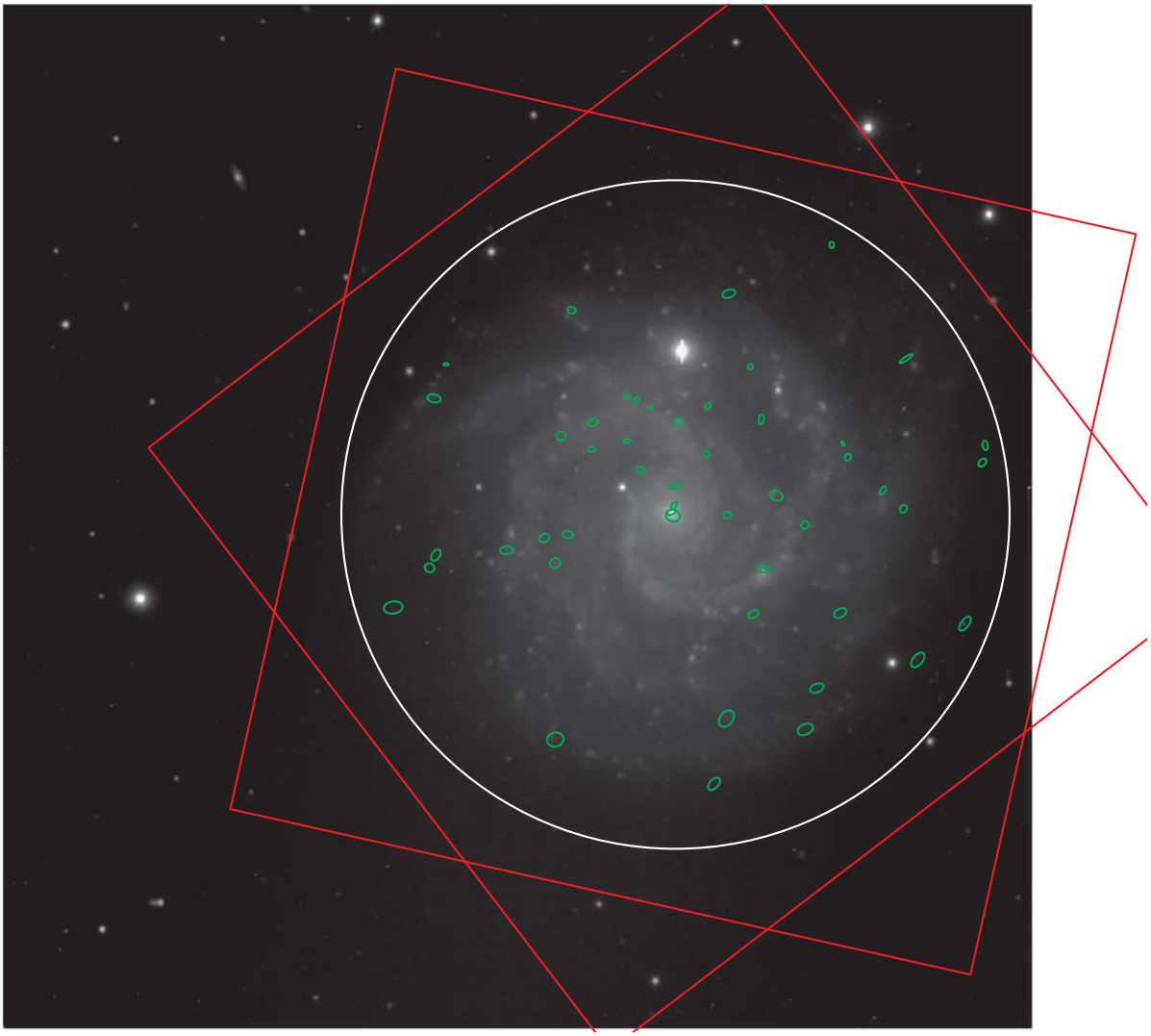

Figure B-15 FLWO optical image of NGC 3184 with Chandra sources overlayed. The white circle is the D25 extent of the galaxy. The scale of the image is $10' \; x10'$.

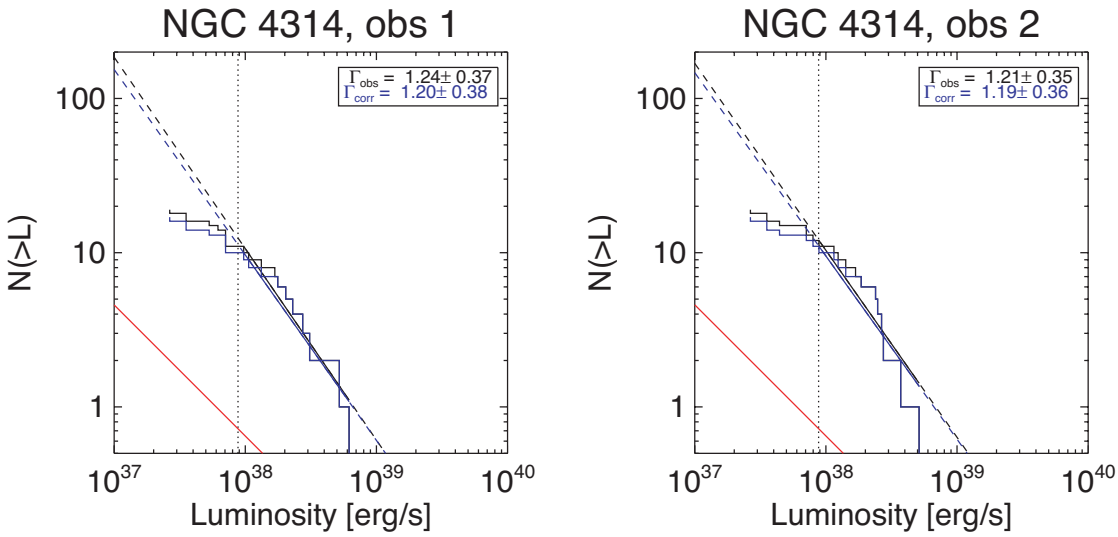

Figure B-16 Cumulative luminosity function of the X-ray point sources in NGC 4314.

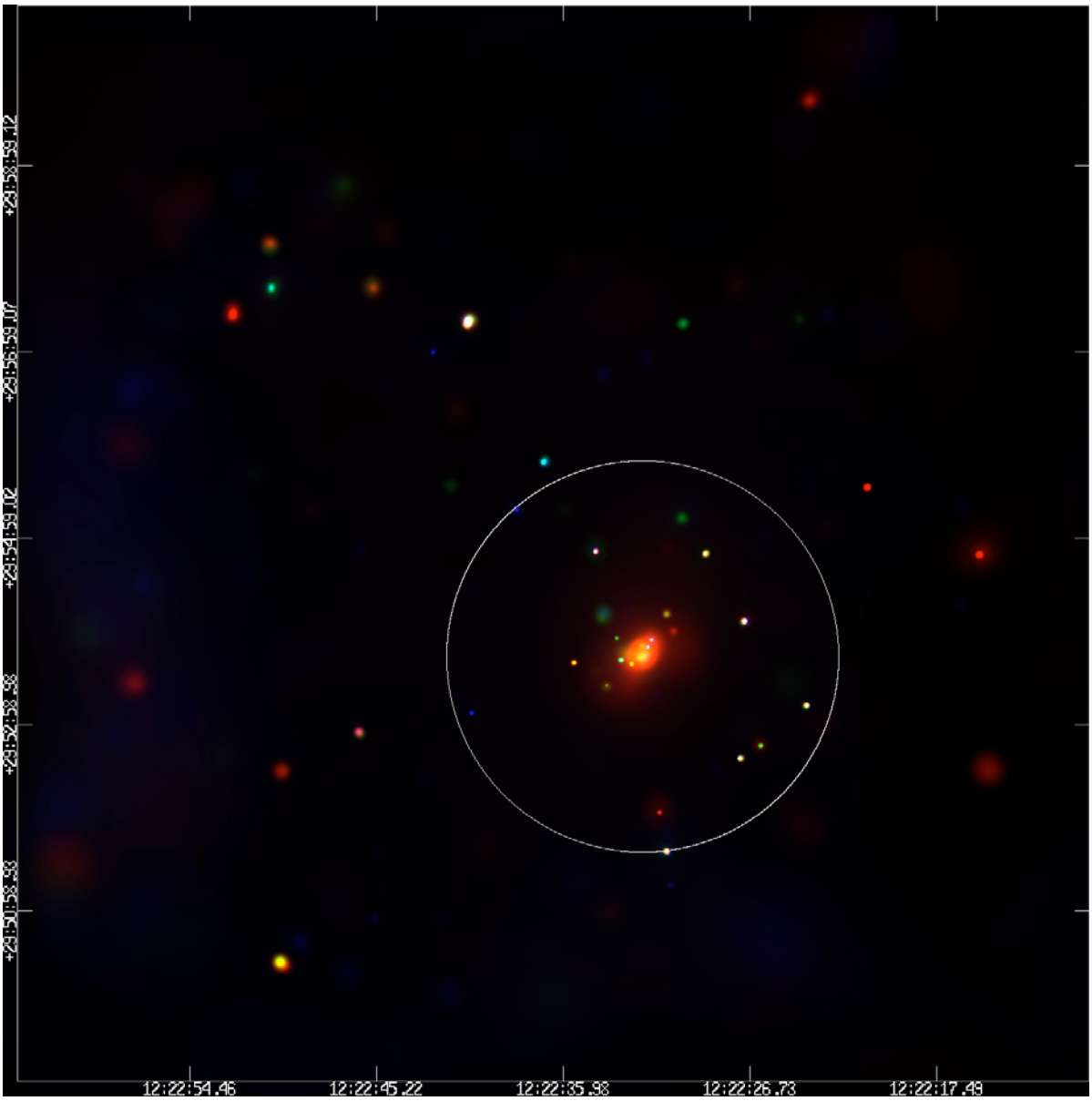

Figure B-17 Merged Chandra observation of NGC 4314. Adaptively smoothed. Red is 0.3-1 keV, green 1-2 keV, and blue 2-8 keV.

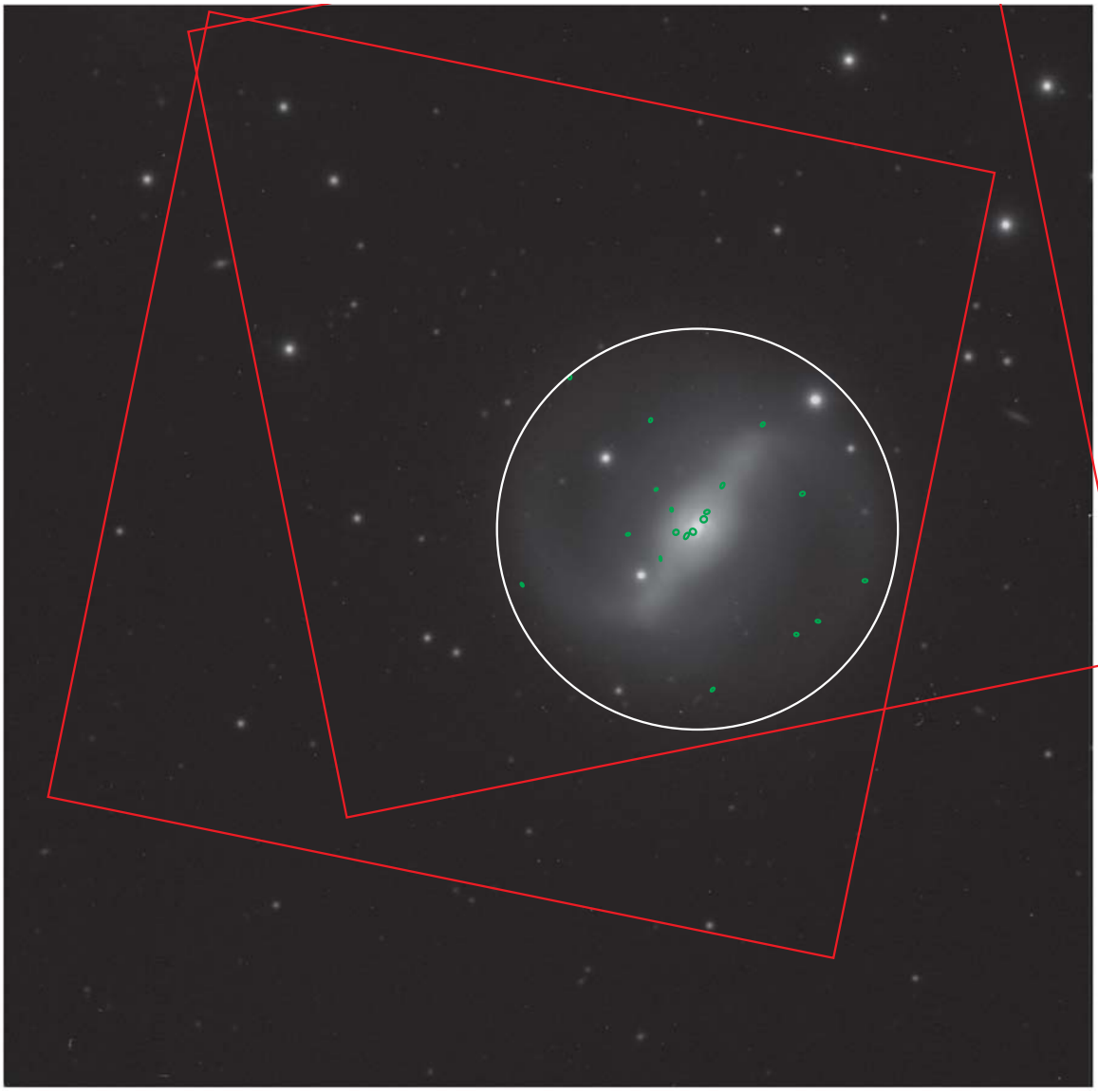

Figure B-18 FLWO optical image of NGC 4314 with Chandra sources overlayed. The white circle is the D25 extent of the galaxy. The scale of the image is $10' \; x 10'$.

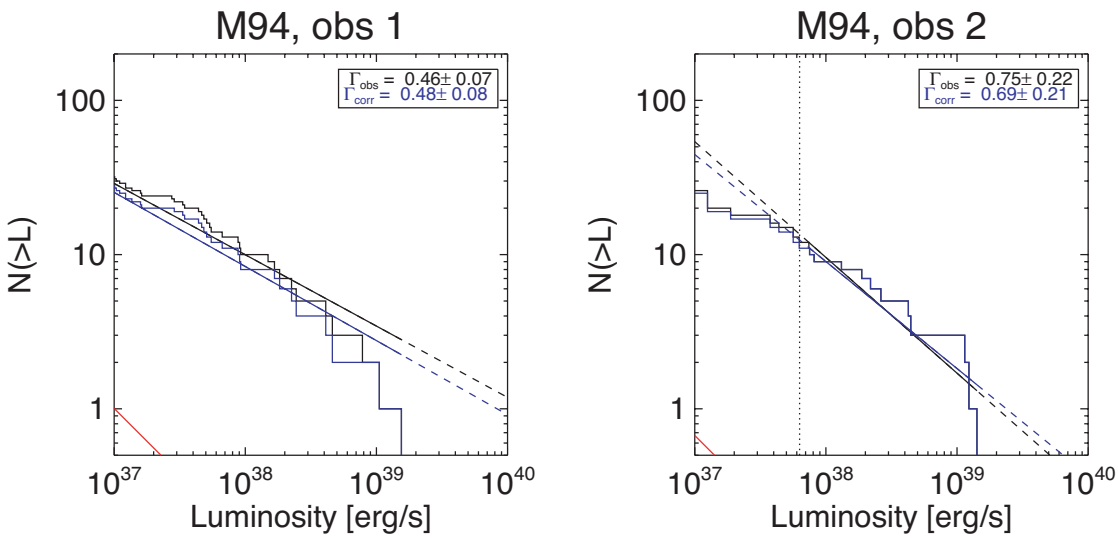

Figure B-19 Cumulative luminosity function of the X-ray point sources in M94. Note that the observations cover only the nuclear region of the galaxy and, as such, the LF should be considered indicative of the star-forming nuclear region and not the galaxy as a whole.

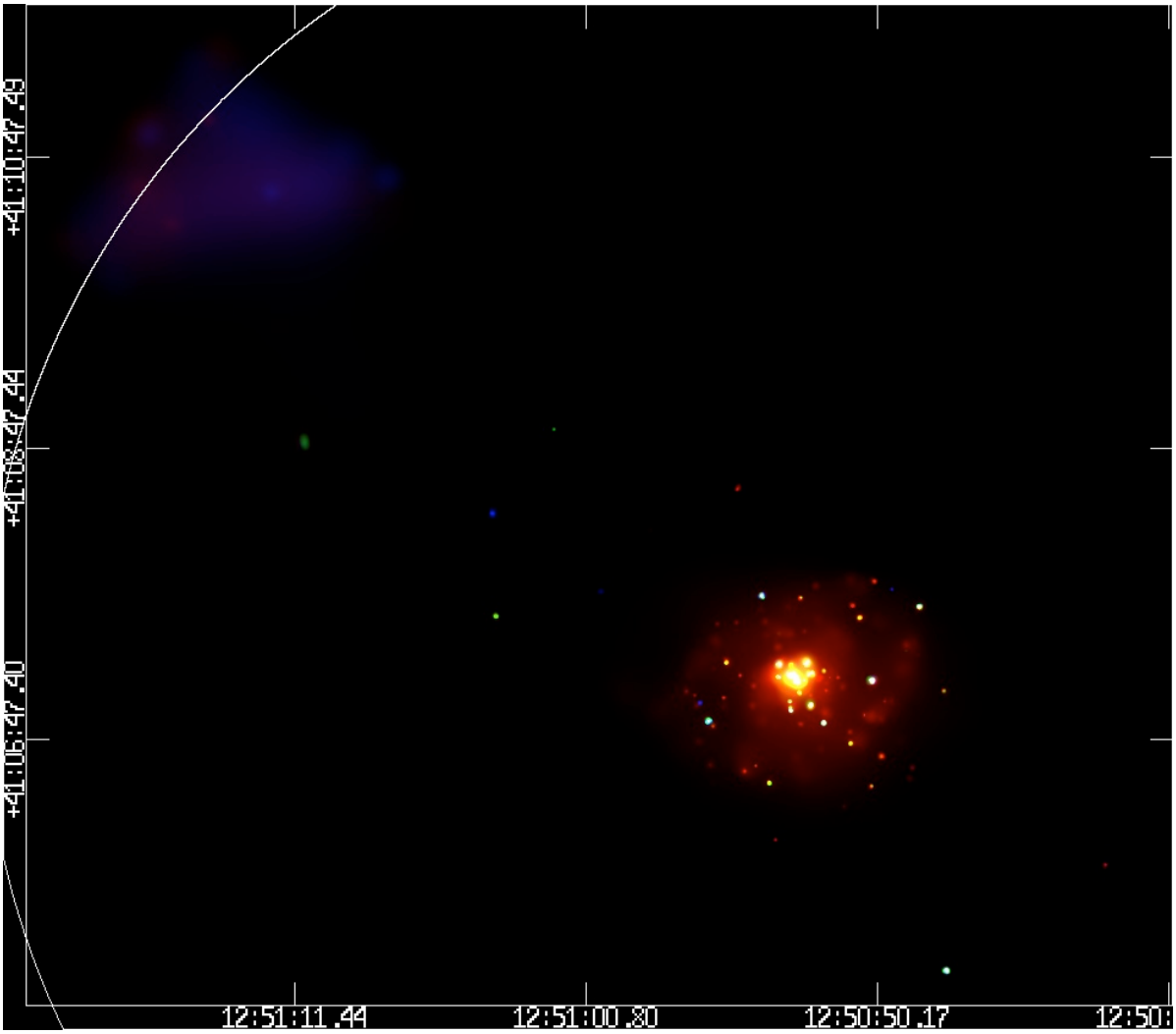

Figure B-20 Merged Chandra observation of M94. Adaptively smoothed. Red is 0.3-1 keV, green 1-2 keV, and blue 2-8 keV.

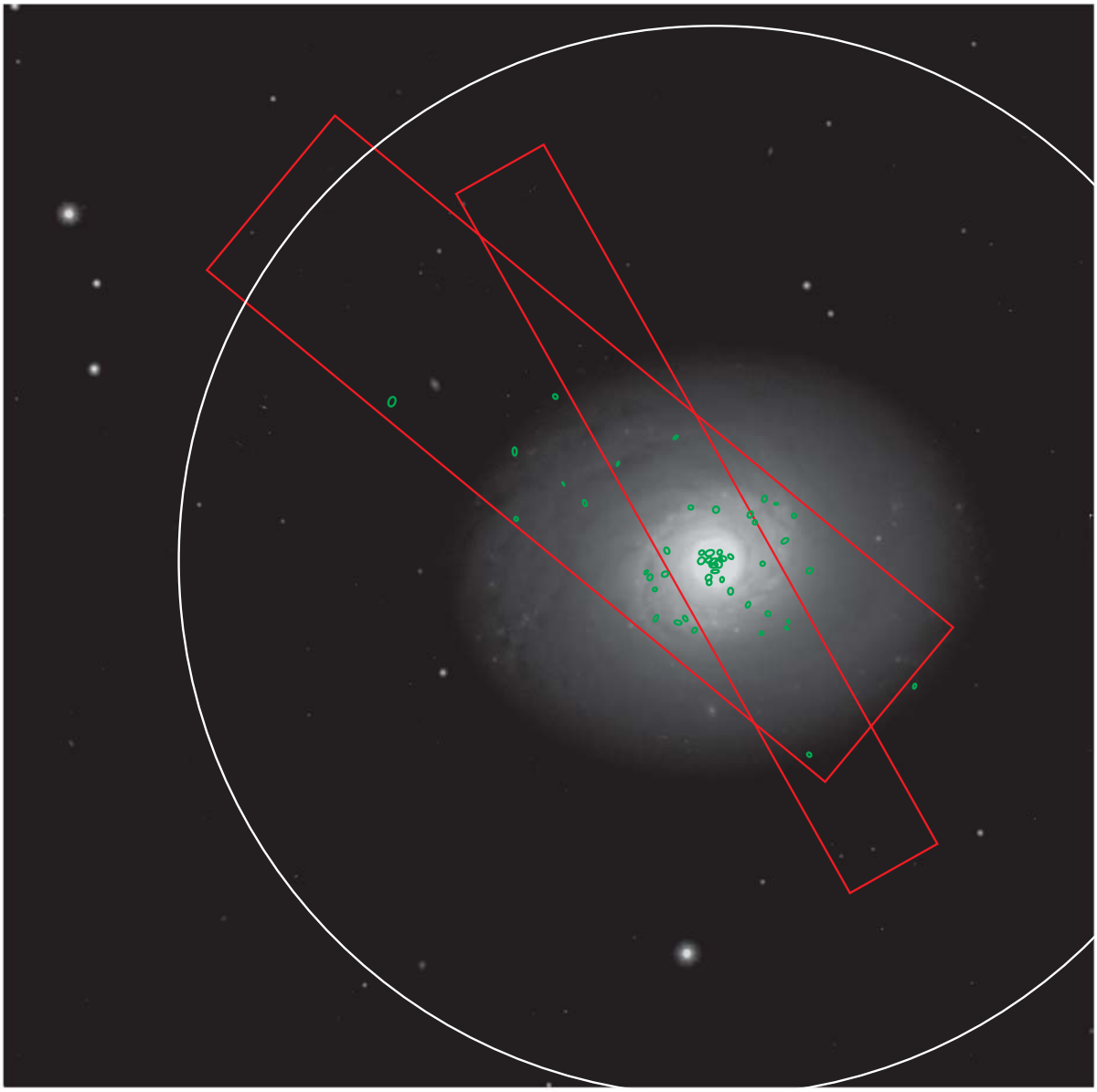

Figure B-21 FLWO optical image of M94 with Chandra sources overlayed. The white circle is the D25 extent of the galaxy. The red boxes show the locations of the ACIS-S3 subarray during the two Chandra observations (the wider box is the longer observation). The scale of the image is $10' \; x 10'$.

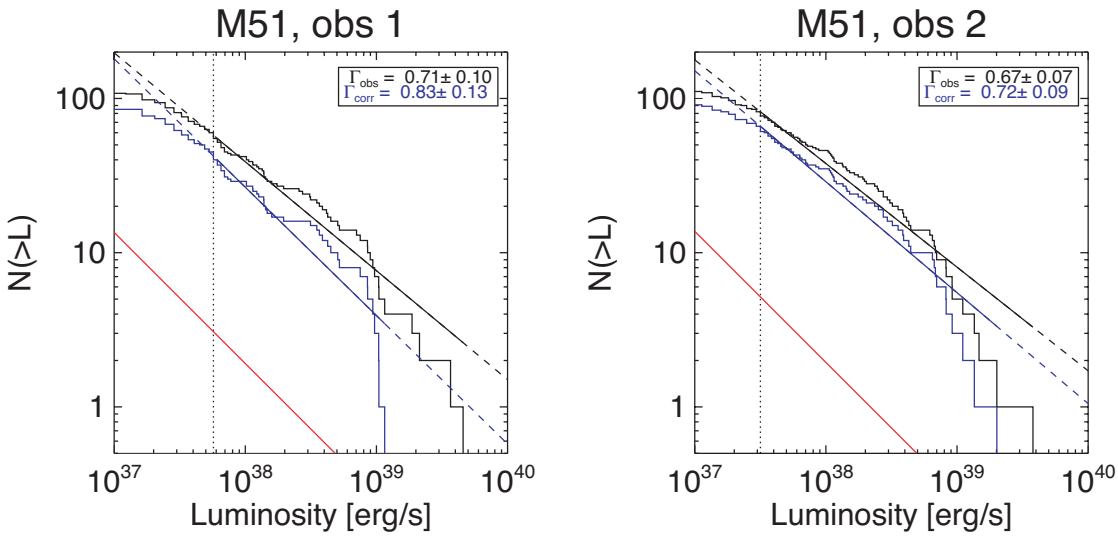

Figure B-22 Cumulative luminosity function of the X-ray point sources in M51.

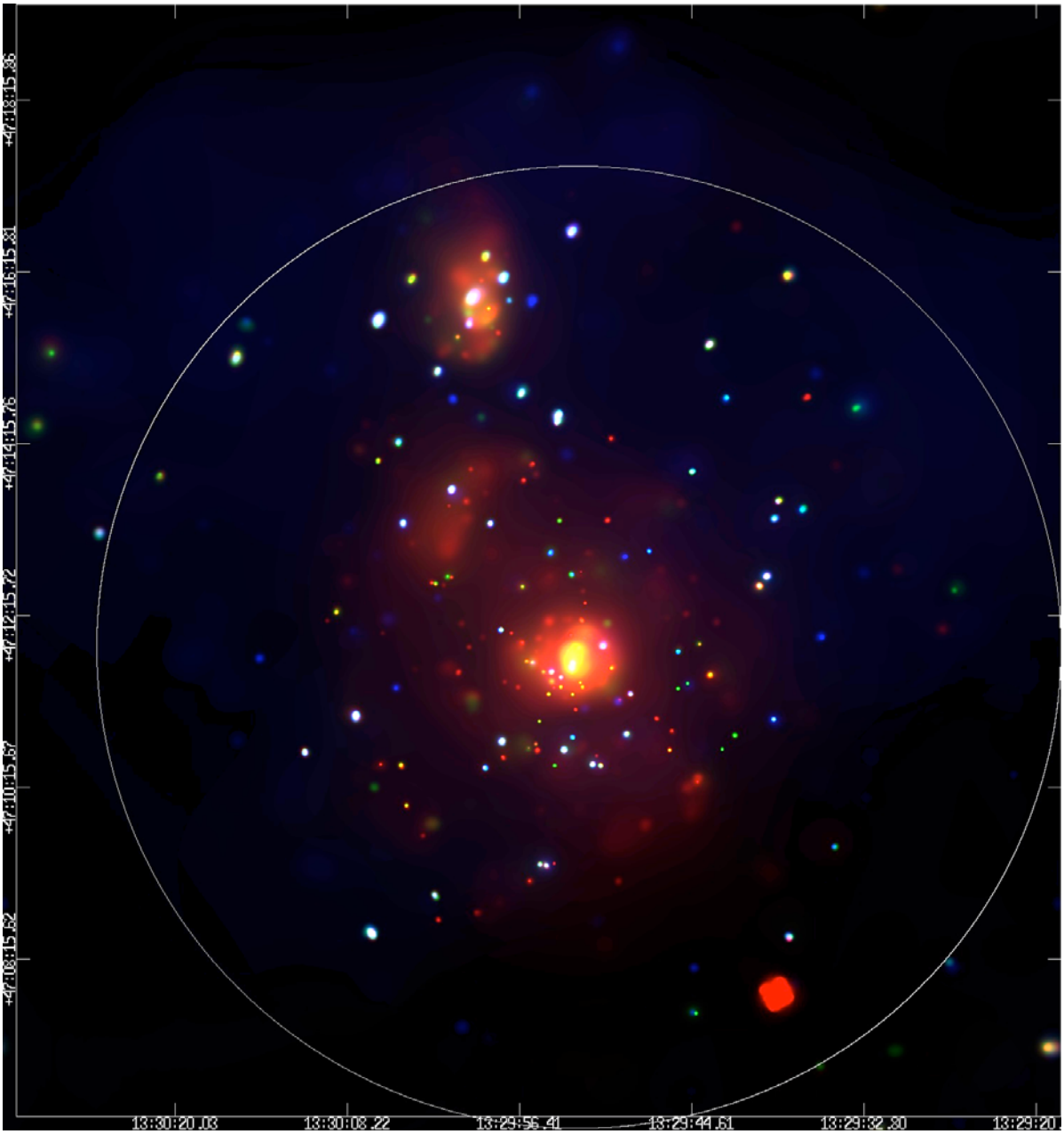

Figure B-23 Merged Chandra observation of M51. Adaptively smoothed. Red is 0.3-1 keV, green 1-2 keV, and blue 2-8 keV.

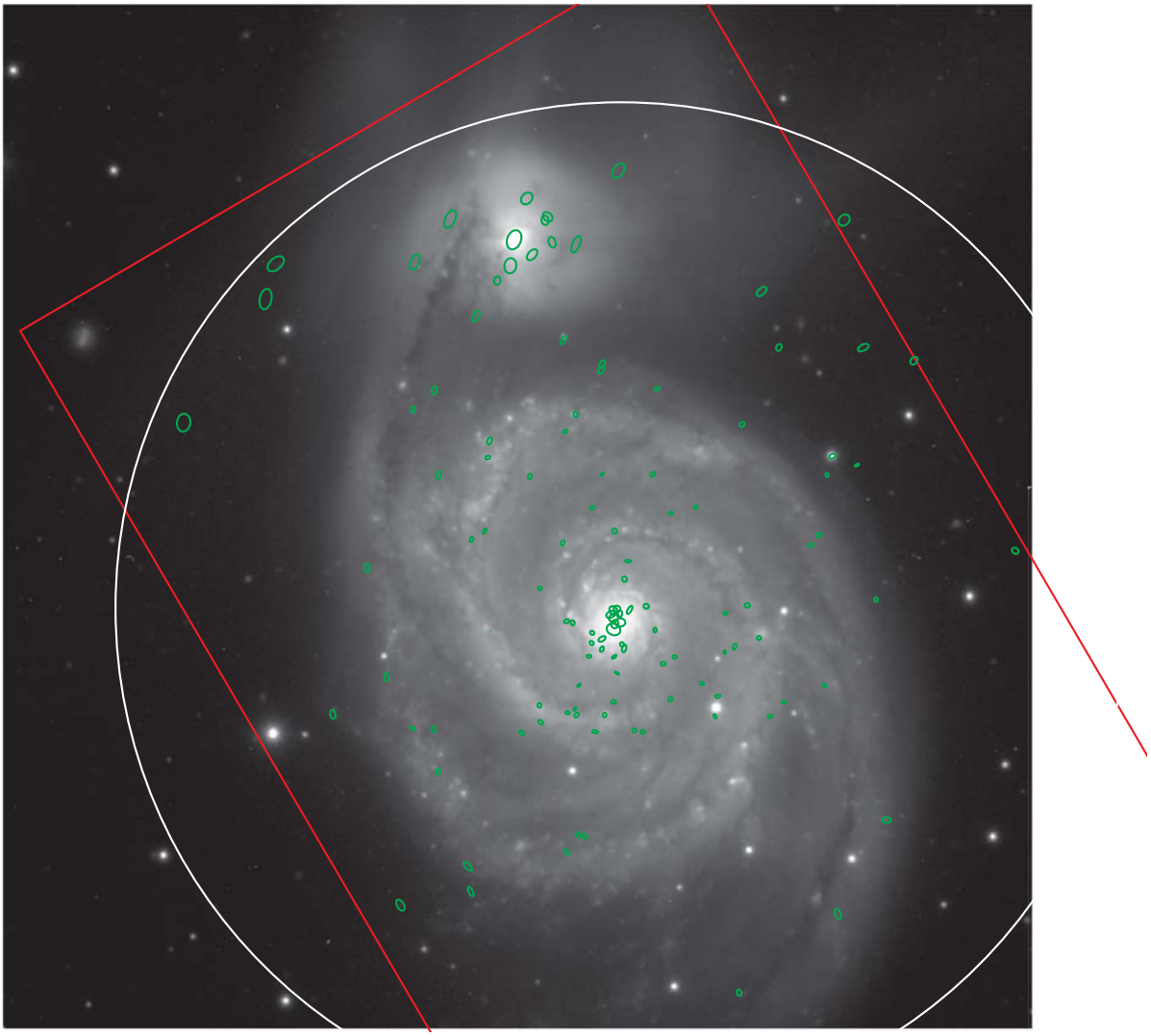

Figure B-24 FLWO optical image of M51 with Chandra sources overlayed. The white circle is the D25 extent of the galaxy. The scale of the image is $10' \; x10'$.

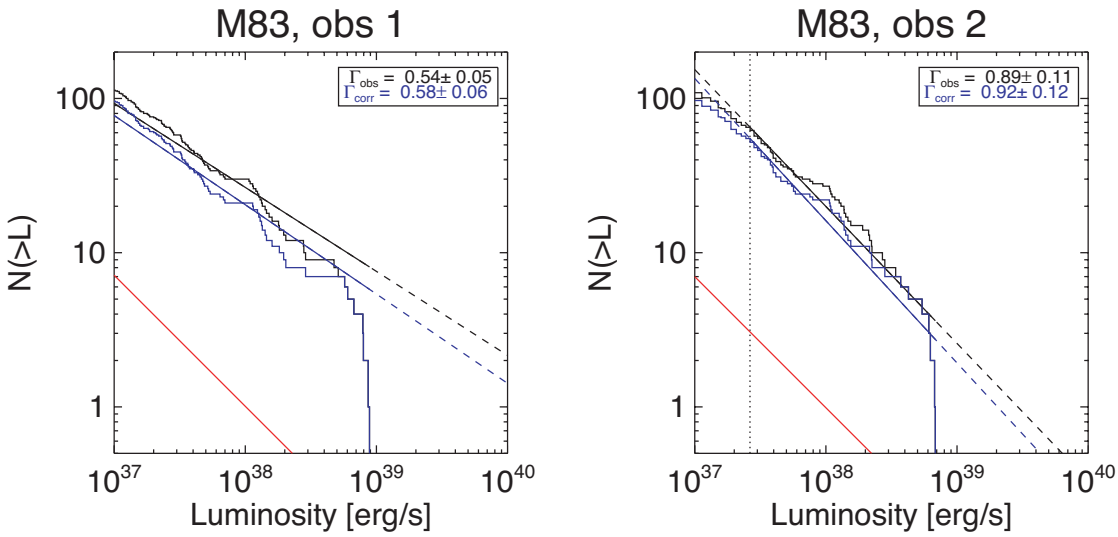

Figure B-25 Cumulative luminosity function of the X-ray point sources in M83.

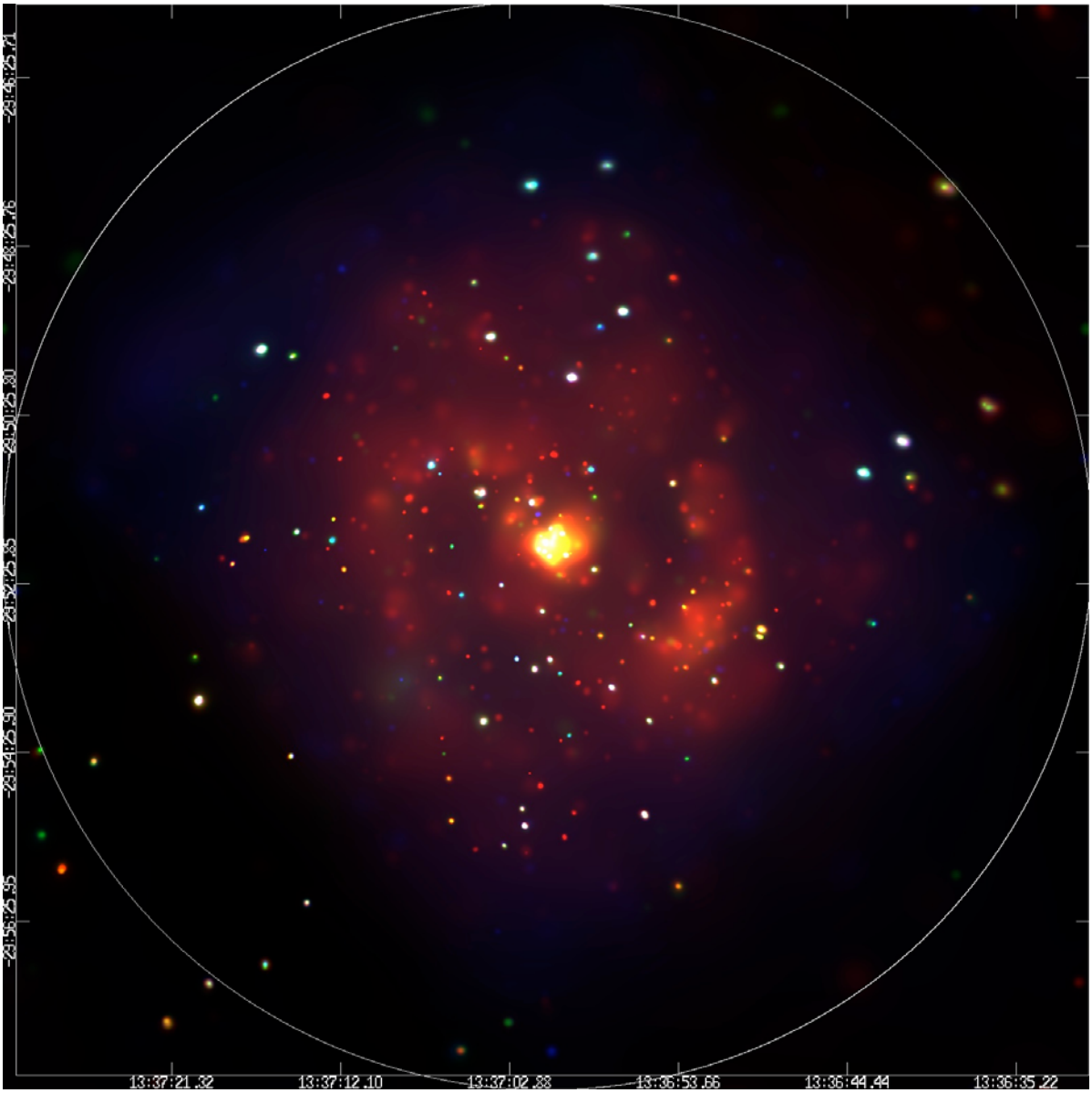

Figure B-26 Merged Chandra observation of M83. Adaptively smoothed. Red is 0.3-1 keV, green 1-2 keV, and blue 2-8 keV.

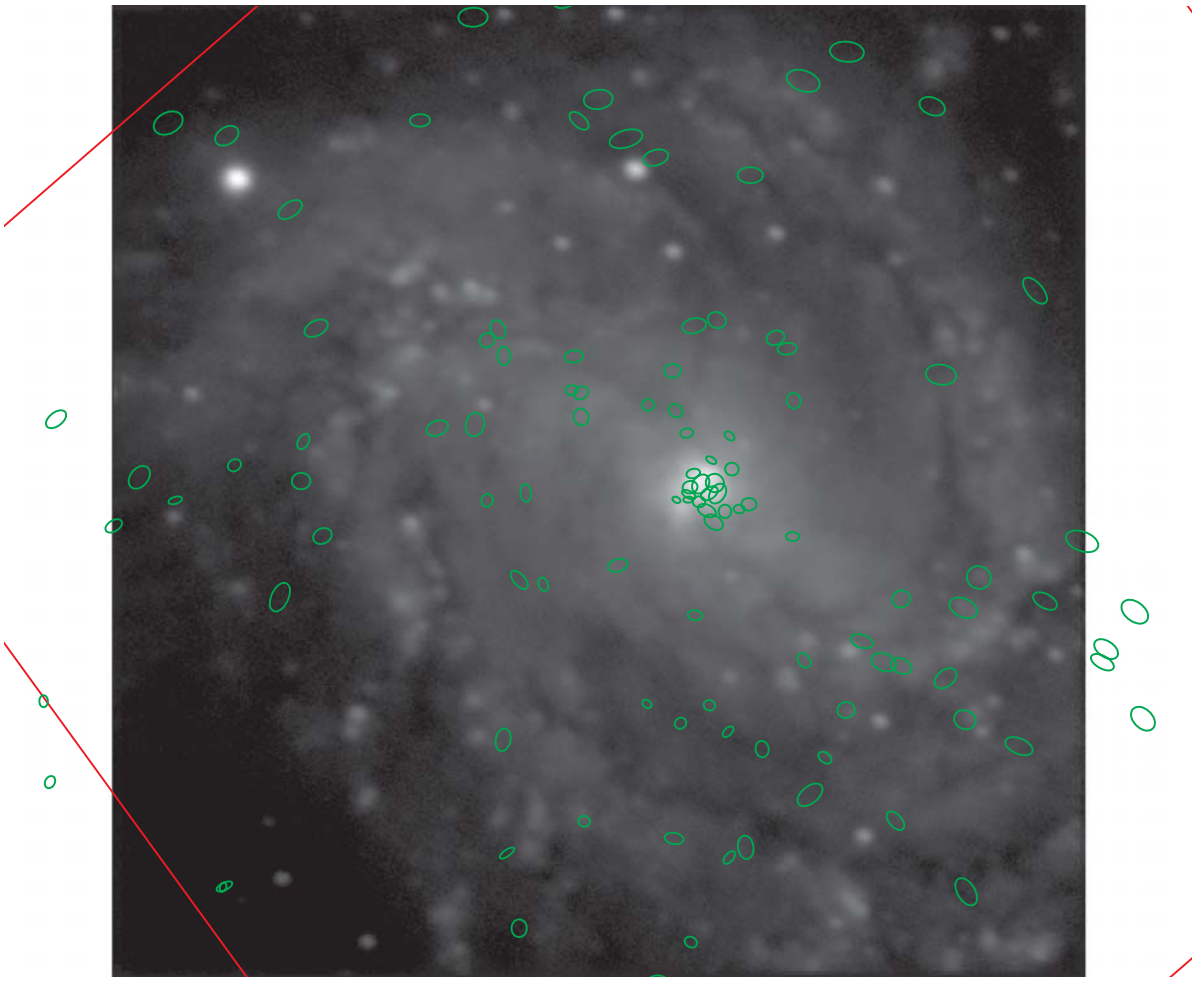

Figure B-27 SARA optical image of M83 with Chandra sources overlayed. The white circle is the D25 extent of the galaxy. The scale of the image is $6' \; x 6'$.

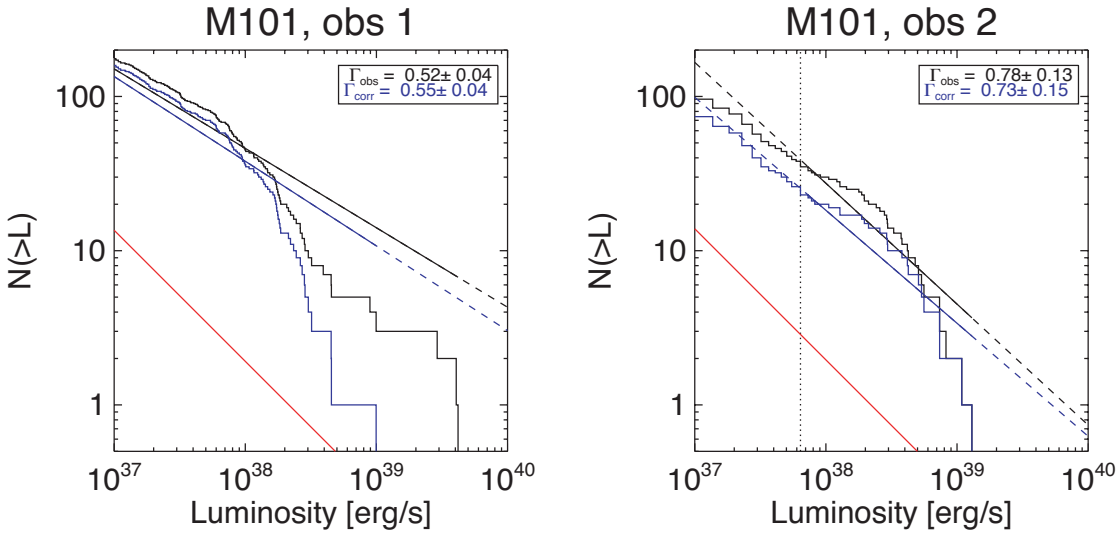

Figure B-28 Cumulative luminosity function of the X-ray point sources in M101.

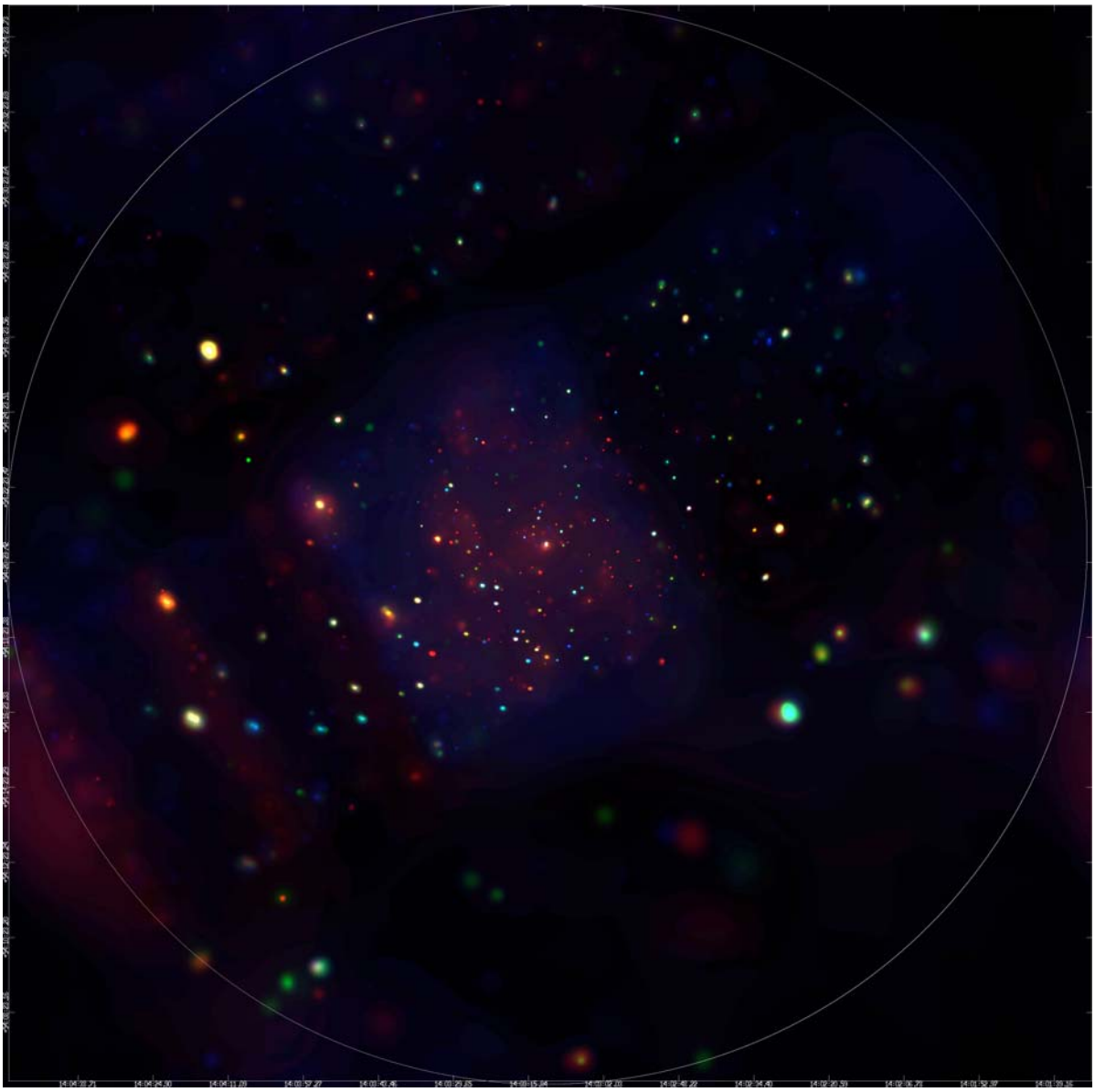

Figure B-29 Merged Chandra observation of M101. Adaptively smoothed. Red is 0.3-1 keV, green 1-2 keV, and blue 2-8 keV.

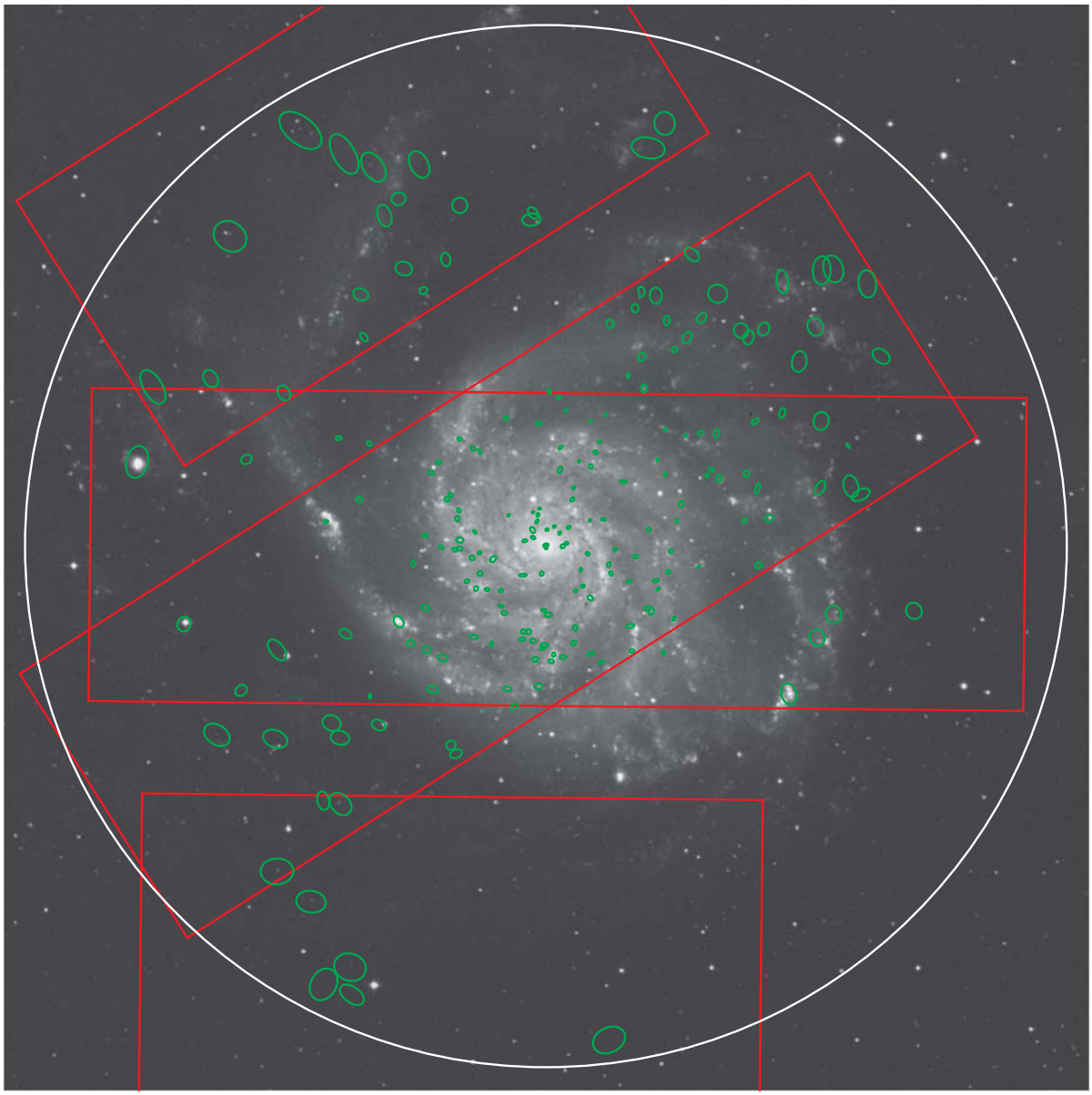

Figure B-30 DSS optical image of M101 with Chandra sources overlayed. The white circle is the D25 extent of the galaxy. The scale of theimage is $30' \; x30'$.

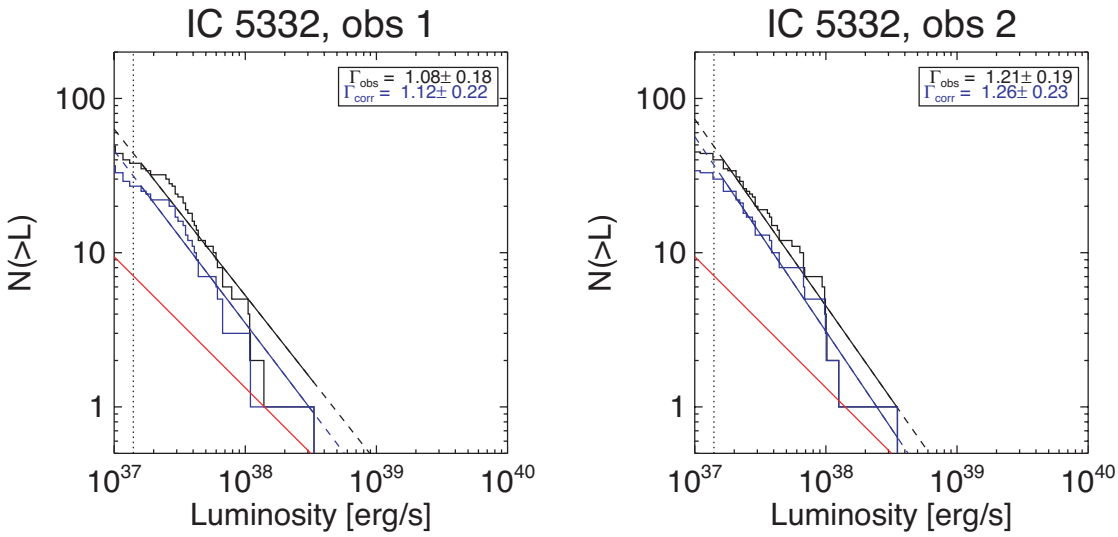

Figure B-31 Cumulative luminosity function of the X-ray point sources in IC 5332.

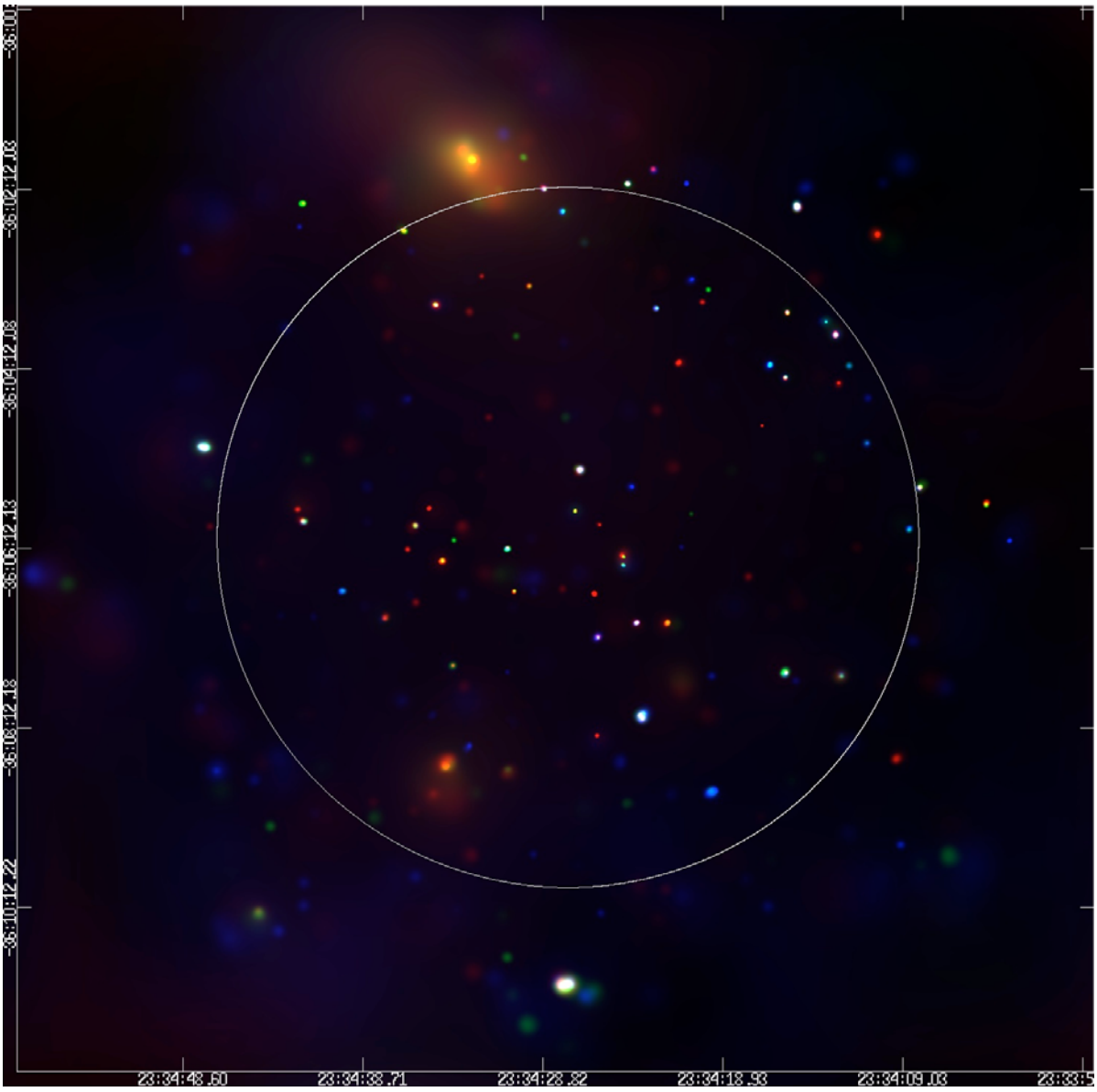

Figure B-32 Merged Chandra observation of IC 5332. Adaptively smoothed. Red is 0.3-1 keV, green 1-2 keV, and blue 2-8 keV.

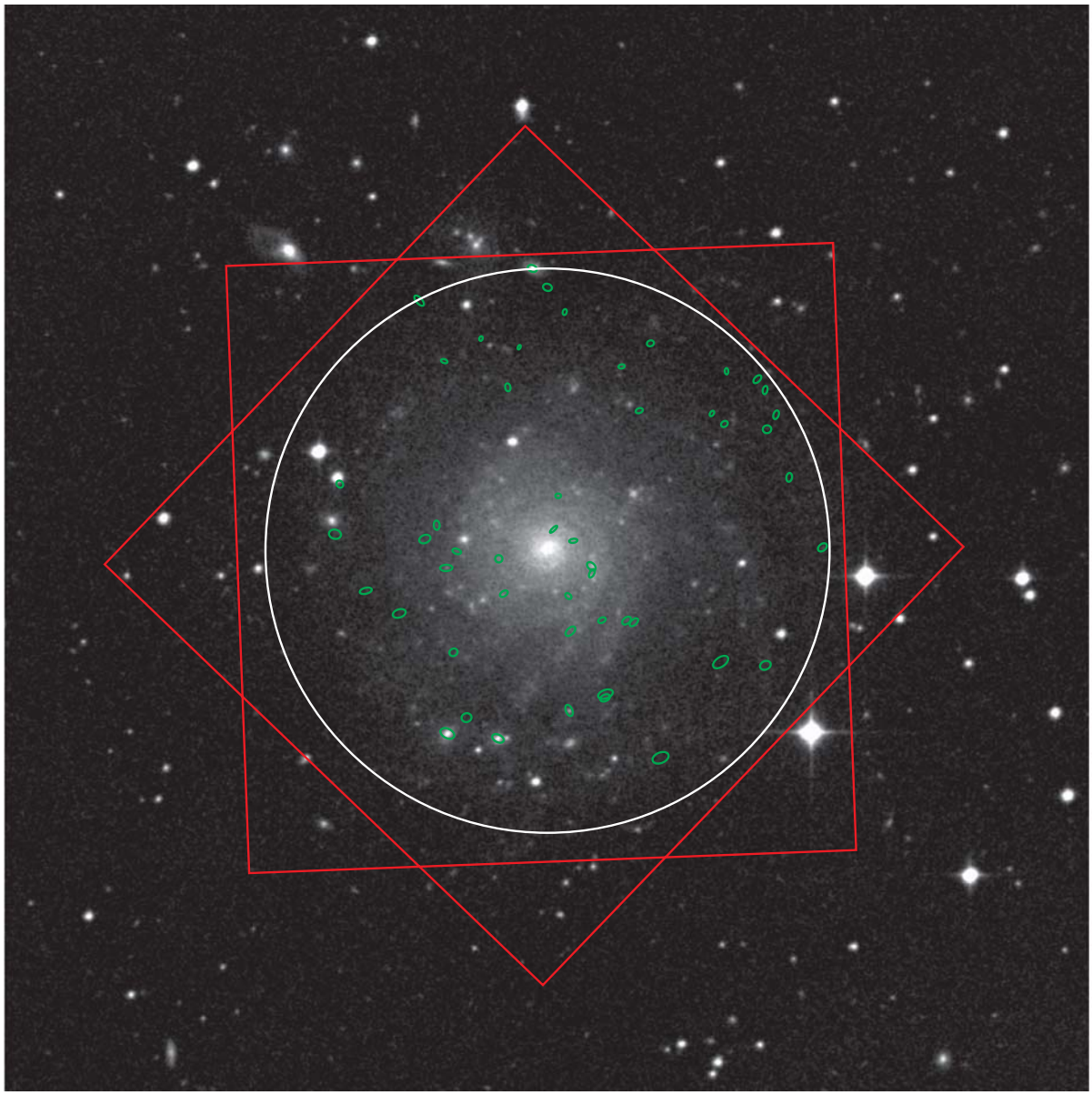

Figure B-33 DSS optical image of IC 5332 with Chandra sources overlayed. The white circle is the D25 extent of the galaxy. The scale of the image is $10' \; x 10'$.

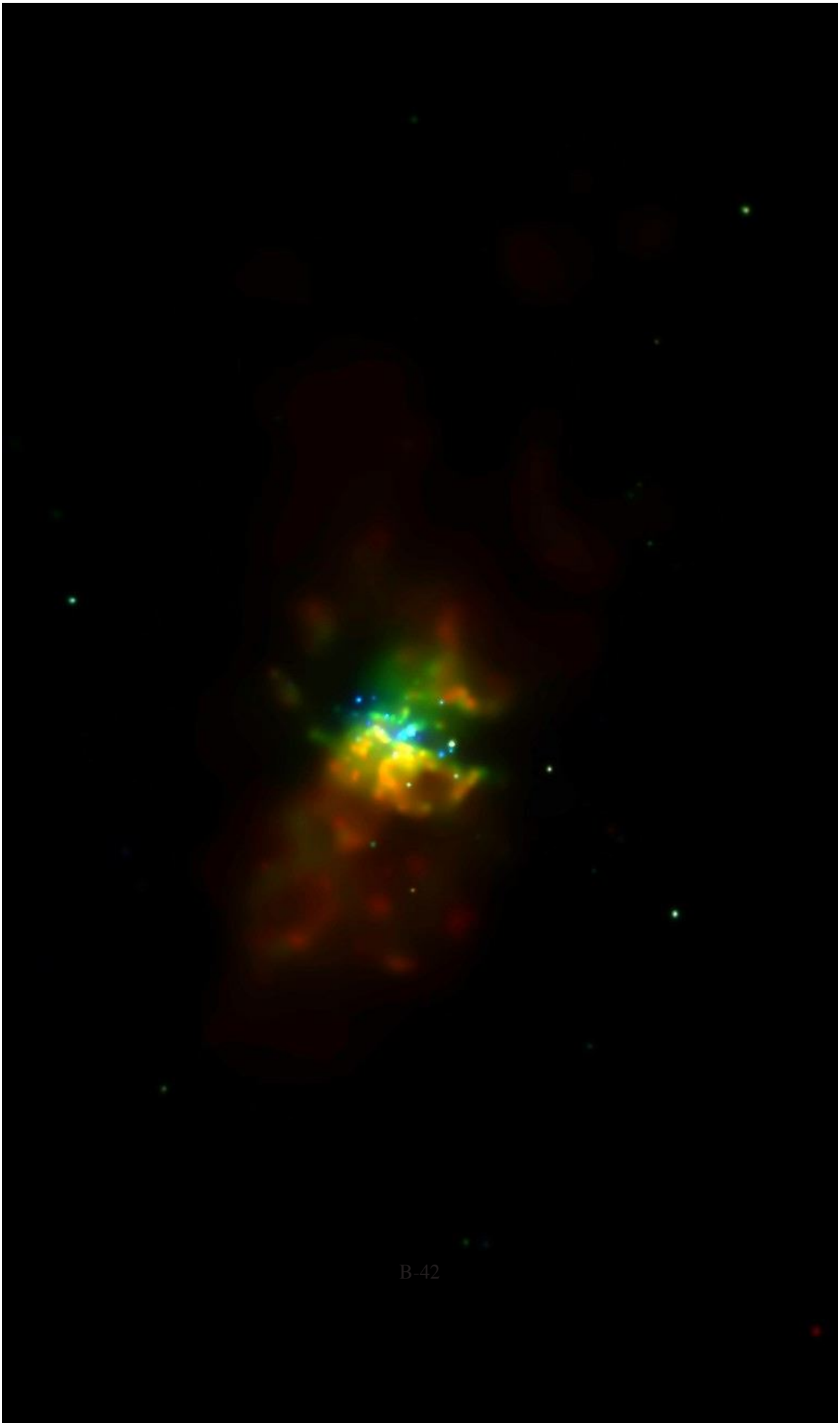

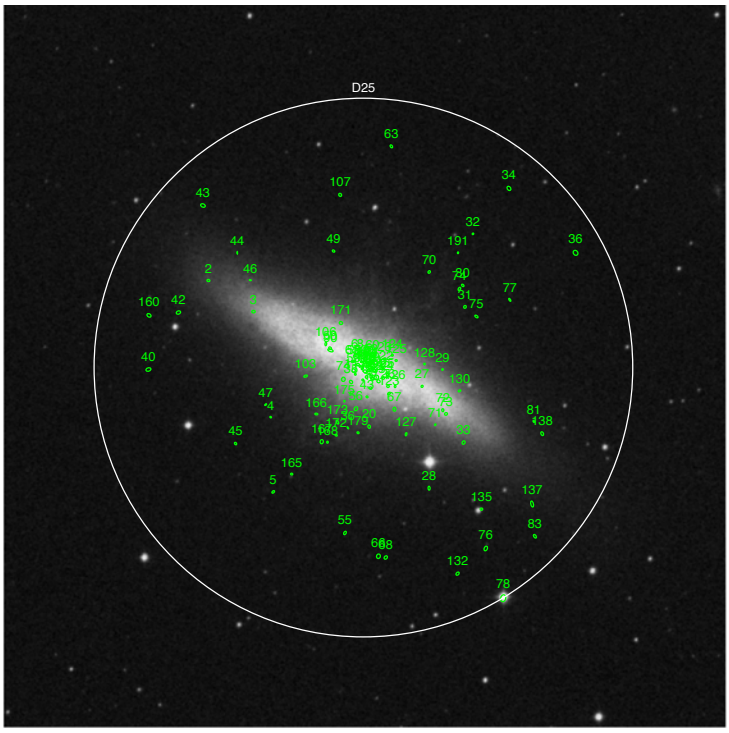

Figure B-35 DSS optical image of M82 with Chandra sources overlayed. The white circle is the D25 extent of the galaxy. The scale of the image is $15' \; x 15'$.

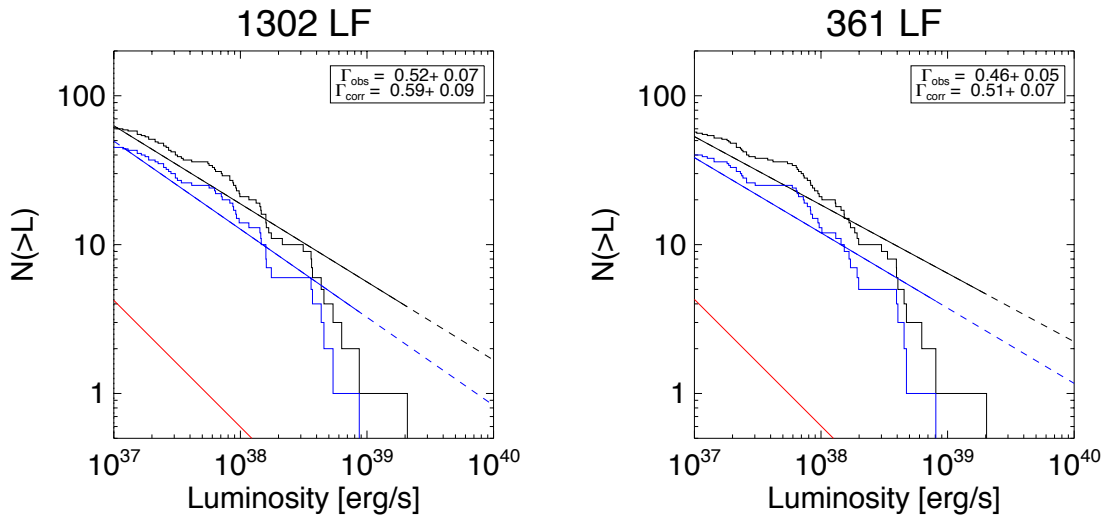

Figure B-36 Cumulative luminosity function of the X-ray point sources in M82. ObsIDs 1302 (left) and 361 (right).

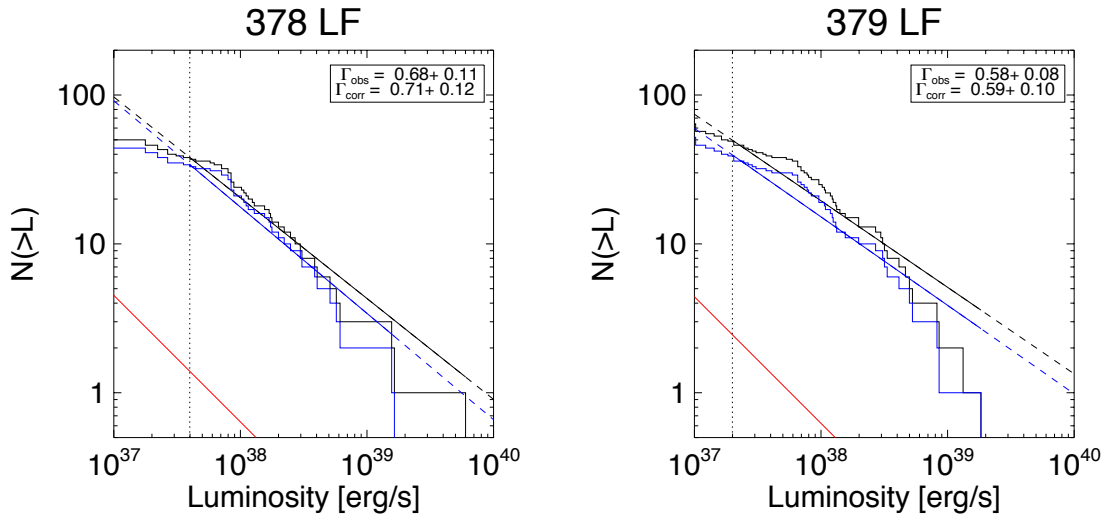

Figure B-37 Cumulative luminosity function of the X-ray point sources in M82. ObsIDs 1302 (left) and 361 (right).

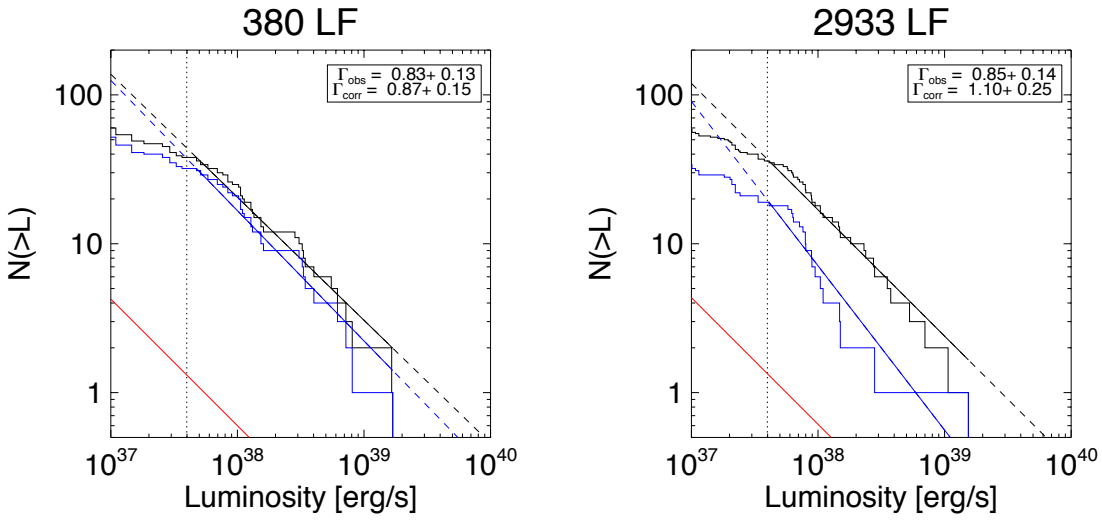

Figure B-38 Cumulative luminosity function of the X-ray point sources in M82. ObsIDs 1302 (left) and 361 (right).

BIBLIOGRAPHY

Bahcall J. N., Ostriker J. P., 1975, *Nature*, 256, 23

Belczynski K., Kalogera V., Zezas A., Fabbiano G., 2004, *ApJL*, 601, L147

Benedict F. G., Smith B. J., Kenney J. D. P., 1996, *AJ*, 111, 1861

Benedict G. F., Higdon J. L., Tollestrup E. V., Hahn J. M., Harvey P. M., 1992, *AJ*, 103, 757

Benedict G. F., Howell D. A., Jørgensen I., Kenney J. D. P., Smith B. J., 2002, *AJ*, 123, 1411

Bi H. G., Arp H., Zimmermann H. U., 1994, *A&A*, 282, 386

Blanton E. L., Sarazin C. L., Irwin J. A., 2001, *ApJ*, 552, 106

Bowyer S., Margon B., Lampton M., Cruddace R., 1974, *ApJ*, 190, 285

Byram E. T., Chubb T. A., Friedman H., 1966, Science, 152, 66

Chevalier R. A., Clegg A. W., 1985, *Nature*, 317, 44

Clark G., Doxsey R., Li F., Jernigan J. G., van Paradijs J., 1978, *ApJL*, 221, L37

Colbert E. J. M., Heckman T. M., Ptak A. F., Strickland D. K., Weaver K. A., 2004, *ApJ*, 602, 231

Colbert E. J. M., Ptak A. F., 2002, *ApJS*, 143, 25

Collura A., Reale F., Schulman E., Bregman J. N., 1994, *ApJL*, 420, L63

Cowan J. J., Branch D., 1985, *ApJ*, 293, 400

Cowley A. P., Crampton D., Hutchings J. B., Helfand D. J., Hamilton T. T., Thorstensen J. R., Charles P. A., 1984, *ApJ*, 286, 196

Cowley A. P., Crampton D., Hutchings J. B., Remillard R., 1984, in IAU Symp. 108: Structure and Evolution of the Magellanic Clouds Evidence for a Black-Hole in Large Magellanic CLOUD-X-3. pp 241–+

Crawford D. F., Jauncey D. L., Murdoch H. S., 1970, *ApJ*, 162, 405

da Costa L. N., Pellegrini P. S., Davis M., Meiksin A., Sargent W. L. W., Tonry J. L., 1991, *ApJS*, 75, 935

Davis J. E., 2001, *ApJ*, 562, 575

de Grijs R., O'Connell R. W., Gallagher III J. S., 2001, *AJ*, 121, 768

de Vaucouleurs G., 1975, *ApJS*, 29, 193

de Vaucouleurs G., de Vaucouleurs A., Corwin H. G., Buta R. J., Paturel G., Fouque P., 1991, Third Reference Catalogue of Bright Galaxies. Volume 1-3, XII, 2069 pp. 7 figs.. Springer-Verlag Berlin Heidelberg New York

DeCesar M. E., Durrell P. R., Ciardullo R., Hurley-Keller D., Feldmeier J. J., 2003, American Astronomical Society Meeting Abstracts, 203,

Di Stefano R., Paerels F., Rappaport S., 1995, *ApJ*, 450, 705

Douglas N. G., Gerssen J., Kuijken K., Merrifield M. R., 2000, *MNRAS*, 316, 795

Durrell P. R., Ciardullo R., DeCesar M. E., Feldmeier J. J., 2003, American Astronomical Society Meeting Abstracts, 203,

Durrell P. R., Decesar M. E., Ciardullo R., Hurley-Keller D., Feldmeier J. J., 2004, in IAU Symposium A CFH12K Survey of Red Giant Stars in the M81 Group. pp 90–+

Eracleous M., Shields J. C., Chartas G., Moran E. C., 2002, *ApJ*, 565, 108

Fabbiano G., 1988, *ApJ*, 325, 544

Fabbiano G., 1989, *ARA&A*, 27, 87

Fabbiano G., Trinchieri G., 1985, *ApJ*, 296, 430

Fabbiano G., Zezas A., Murray S. S., 2001, *ApJ*, 554, 1035

Feldmeier J. J., Ciardullo R., Jacoby G. H., 1997, *ApJ*, 479, 231

Feldmeier J. J., Durrell P. R., Ciardullo R., Jacoby G. H., 2003, in IAU Symposium A Search for Intra-group Planetary Nebulae in the M81 Group. pp 605–+

Freeman P. E., Kashyap V., Rosner R., Lamb D. Q., 2002, *ApJS*, 138, 185

Friedman H., Byram E. T., Chubb T. A., 1967, Science, 156, 374

Gallagher J. S., Smith L. J., 1999, *MNRAS*, 304, 540

Gehrels N., 1986, *ApJ*, 303, 336

Georganopoulos M., Aharonian F. A., Kirk J. G., 2002, *A&A*, 388, L25

Giacconi R., Branduardi G., Briel U., Epstein A., Fabricant D., Feigelson E., Forman W., Gorenstein P., 1979, *ApJ*, 230, 540

Giacconi R., Gursky H., Paolini F. R., Rossi B. B., 1962, Physical Review Letters, 9, 439

Giacconi R., Rosati P., Tozzi P., Nonino M., Hasinger G., Norman C., Bergeron J., Borgani S., Gilli R., Gilmozzi R., Zheng W., 2001, *ApJ*, 551, 624

Gilfanov M., 2004, *MNRAS*, 349, 146

Gilfanov M., Grimm H.-J., Sunyaev R., 2004, *MNRAS*, 347, L57

Greiner J., Hasinger G., Kahabka P., 1991, *A&A*, 246, L17

Griffiths R. E., Seward F. D., 1977, *MNRAS*, 180, 75P

Grimm H.-J., Gilfanov M., Sunyaev R., 2002, *A&A*, 391, 923

Grimm H.-J., Gilfanov M., Sunyaev R., 2003, *MNRAS*, 339, 793

Hamilton A. J. S., Chevalier R. A., Sarazin C. L., 1983, *ApJS*, 51, 115

Hasinger G., van der Klis M., 1989, *A&A*, 225, 79

Helfand D. J., 1984, *PASP*, 96, 913

Hill J. K., Bohlin R. C., Stecher T. P., 1984, *ApJ*, 277, 542

Hodge P. W., Gurwell M., Goldader J. D., Kennicutt R. C., 1990, *ApJS*, 73, 661

Huchra J. P., Vogeley M. S., Geller M. J., 1999, *ApJS*, 121, 287

Irwin J. A., Sarazin C. L., Bregman J. N., 2002, *ApJ*, 570, 152

Johnston M. D., Bradt H. V., Doxsey R. E., Griffiths R. E., Schwartz D. A., Schwarz J., 1979, *ApJL*, 230, L11

Johnston M. D., Griffiths R. E., Ward M. J., 1980, *Nature*, 285, 26

Jones E. M., Smith B. W., Straka W. C., 1981, *ApJ*, 249, 185

Kaaret P., Alonso-Herrero A., Gallagher J. S., Fabbiano G., Zezas A., Rieke M. J., 2004, *MNRAS*, 348, L28

Kaaret P., Prestwich A. H., Zezas A., Murray S. S., Kim D.-W., Kilgard R. E., Schlegel E. M., Ward M. J., 2001, *MNRAS*, 321, L29

Kahabka P., Pietsch W., Hasinger G., 1994, *A&A*, 288, 538

Kelley R. L., Jernigan J. G., Levine A., Petro L. D., Rappaport S., 1983, *ApJ*, 264, 568

Kennicutt R. C., 1998, *ARA&A*, 36, 189

Kilgard R. E., Cowan J. J., Garcia M. R., Kaaret P., Krauss M. I., McDowell J. C., Prestwich A. H., Primini F. A., Stockdale C. J., Trinchieri G., Ward M. J., Zezas A., 2005, *ApJS*, 159, 214

Kilgard R. E., Kaaret P., Krauss M. I., Prestwich A. H., Raley M. T., Zezas A., 2002, *ApJ*, 573, 138

Kim D.-W., Fabbiano G., 2004, *ApJ*, 611, 846

King A. R., Davies M. B., Ward M. J., Fabbiano G., Elvis M., 2001, *ApJL*, 552, L109

Kong A. K. H., Di Stefano R., Yuan F., 2004, *ApJL*, 617, L49

Kong A. K. H., DiStefano R., Garcia M. R., Greiner J., 2003, *ApJ*, 585, 298

Kong A. K. H., Garcia M. R., Primini F. A., Murray S. S., Di Stefano R., McClintock J. E., 2002, *ApJ*, 577, 738

Körding E., Falcke H., Markoff S., 2002, *A&A*, 382, L13

Kraemer K. E., Price S. D., Mizuno D. R., Carey S. J., 2002, *AJ*, 124, 2990

Krauss M. I., Kilgard R. E., Garcia M. R., Roberts T. P., Prestwich A. H., 2003, AAS/High Energy Astrophysics Division, 7,

Krauss M. I., Kilgard R. E., Garcia M. R., Roberts T. P., Prestwich A. H., 2005, *ApJ*, 630, 228

Lamers H. J. G. L. M., Panagia N., Scuderi S., Romaniello M., Spaans M., de Wit W. J., Kirshner R., 2002, *ApJ*, 566, 818

Lang F. L., Levine A. M., Bautz M., Hauskins S., Howe S., Primini F. A., Lewin W. H. G., Baity W. A., Knight F. K., Rotschild R. E., Petterson J. A., 1981, *ApJL*, 246, L21

Larsen S. S., 1999, *A&AS*, 139, 393

Larsen S. S., 2000, *MNRAS*, 319, 893

Leonard D. C., Filippenko A. V., Li W., Matheson T., Kirshner R. P., Chornock R., Van Dyk S. D., Berlind P., Calkins M. L., Challis P. M., Garnavich P. M., Jha S., Mahdavi A., 2002, *AJ*, 124, 2490

Leong C., Kellogg E., Gursky H., Tananbaum H., Giacconi R., 1971, *ApJL*, 170, L67+

Lewin W. H. G., van den Heuvel E. P. J., eds, 1983, Accretion-driven stellar X-ray sources

Li F., Rappaport S., Epstein A., 1978, *Nature*, 271, 37

Lira P., Ward M., Zezas A., Alonso-Herrero A., Ueno S., 2002, *MNRAS*, 330, 259

Liu J., Bregman J. N., Irwin J., Seitzer P., 2002, *ApJL*, 581, L93

Liu J., Bregman J. N., Lloyd-Davies E., Irwin J., Espaillat C., Seitzer P., 2005, *ApJL*, 621, L17

Long K. S., Charles P. A., Blair W. P., Gordon S. M., 1996, *ApJ*, 466, 750

Long K. S., Helfand D. J., Grabelsky D. A., 1981, *ApJ*, 248, 925

Lucke R., Yentis D., Friedman H., Fritz G., Shulman S., 1976, *ApJL*, 206, L25

Maddox L. A., Cowan J. J., Kilgard R. E., Lacey C. K., Prestwich A. H., Stockdale C. J., Wolfing E., 2006, *AJ*, 132, 310

Makishima K., Kubota A., Mizuno T., Ohnishi T., Tashiro M., Aruga Y., Asai K., Dotani T., Mitsuda K., Ueda Y., Uno S., Yamaoka K., Ebisawa K., Kohmura Y., Okada K., 2000, *ApJ*, 535, 632

Mark H., Price R., Rodrigues R., Seward F. D., Swift C. D., 1969, *ApJL*, 155, L143+

Matonick D. M., Fesen R. A., 1997, *ApJS*, 112, 49

Matsumoto H., Tsuru T. G., Koyama K., Awaki H., Canizares C. R., Kawai N., Matsushita S., Kawabe R., 2001, *ApJL*, 547, L25

McClintock J. E., Remillard R. A., 2004, in Compact Stellar X-ray Sources Black Hole Binaries

McDonald A. R., Muxlow T. W. B., Wills K. A., Pedlar A., Beswick R. J., 2002, *MNRAS*, 334, 912

McKee J. D., Fritz G., Cruddace R. G., Shulman S., Friedman H., 1980, *ApJ*, 238, 93

Miller J. M., Fabian A. C., Miller M. C., 2004, *ApJL*, 614, L117

Miller M. C., Colbert E. J. M., 2004, International Journal of Modern Physics D, 13, 1

Mitsuda K., Inoue H., Koyama K., Makishima K., Matsuoka M., Ogawara Y., Suzuki K., Tanaka Y., Shibazaki N., Hirano T., 1984, *PASJ*, 36, 741

Mizuno T., Ohnishi T., Kubota A., Makishima K., Tashiro M., 1999, *PASJ*, 51, 663

Moshir M., Kopman G., Conrow T. A. O., 1992, IRAS Faint Source Survey, Explanatory supplement version 2. Pasadena: Infrared Processing and Analysis Center, California Institute of Technology, 1992, edited by Moshir, M.; Kopman, G.; Conrow, T. a.o.

Mukai K., Pence W. D., Snowden S. L., Kuntz K. D., 2003, *ApJ*, 582, 184

Mulder P. S., van Driel W., 1993, *A&A*, 272, 63

Muno M. P., Remillard R. A., Chakrabarty D., 2002, *ApJL*, 568, L35

Nakano S., Kushida R., 1999, *IAU Circular*, 7329, 1

Pence W. D., Snowden S. L., Mukai K., Kuntz K. D., 2001, *ApJ*, 561, 189

Petit H., Hua C. T., Bersier D., Courtes G., 1996, *A&A*, 309, 446

Petro L., Feldman F., Hiltner W. A., 1973, *ApJL*, 184, L123+

POG 2003, Chandra Proposers' Observatory Guide. 6.0 edn

Prestwich A. H., Irwin J. A., Kilgard R. E., Krauss M. I., Zezas A., Primini F., Kaaret P., Boroson B., 2003, *ApJ*, 595, 719

Price R. E., Groves D. J., Rodrigues R. M., Seward F. D., Swift C. D., Toor A., 1971, *ApJL*, 168, L7+

Primini F. A., Forman W., Jones C., 1993, *ApJ*, 410, 615

Ptak A., Griffiths R., 1999, *ApJL*, 517, L85

Remillard R. A., 2004, in AIP Conf. Proc. 714: X-ray Timing 2003: Rossi and Beyond X-ray QPOs from Black Hole Binary Systems. pp 13–20

Rieke G. H., Lebofsky M. J., Thompson R. I., Low F. J., Tokunaga A. T., 1980, *ApJ*, 238, 24

Roberts T. P., Warwick R. S., 2000, *MNRAS*, 315, 98

Roberts T. P., Warwick R. S., Ward M. J., Goad M. R., 2004, *MNRAS*, 349, 1193

Sakai S., Madore B. F., 1999, *ApJ*, 526, 599

Sarazin C. L., Irwin J. A., Bregman J. N., 2000, *ApJL*, 544, L101

Scargle J. D., 1998, *ApJ*, 504, 405

Schlegel E. M., 1995, Reports of Progress in Physics, 58, 1375

Schlegel E. M., 2001, *ApJL*, 556, L25

Schreier E., Giacconi R., Gursky H., Kellogg E., Tananbaum H., 1972, *ApJL*, 178, L71+

Schreier E., Levinson R., Gursky H., Kellogg E., Tananbaum H., Giacconi R., 1972, *ApJL*, 172, L79+

Schulz N. S., Hasinger G., Truemper J., 1989, *A&A*, 225, 48

Seward F. D., Mitchell M., 1981, *ApJ*, 243, 736

Shakura N. I., Sunyaev R. A., 1973, *A&A*, 24, 337

Shirey R., Soria R., Borozdin K., Osborne J. P., Tiengo A., Guainazzi M., Hayter C., La Palombara N., Mason K., Molendi S., Paerels F., Pietsch W., Priedhorsky W., Read A. M., Watson M. G., West R. G., 2001, *A&A*, 365, L195

Skinner G. K., Bedford D. K., Elsner R. F., Leahy D., Weisskopf M. C., Grindlay J., 1982, *Nature*, 297, 568

Sofue Y., Wakamatsu K., 1994, *AJ*, 107, 1018

Soria R., Kong A. K. H., 2002, *ApJL*, 572, L33

Soria R., Wu K., 2002, *A&A*, 384, 99

Soria R., Wu K., 2003, *A&A*, 410, 53

Stetson P. B., Saha A., Ferrarese L., Rawson D. M., Ford H. C., Freedman W. L., Gibson B. K., Graham J. A., et al., 1998, *ApJ*, 508, 491

Stobbart A.-M., Roberts T. P., Warwick R. S., 2004, *MNRAS*, 351, 1063

Stockdale C. J., Maddox L. A., Cowan J. J., Prestwich A., Kilgard R., Immler S., 2006, *AJ*, 131, 889

Strickland D. K., 2004, ArXiv Astrophysics e-prints

Strohmayer T., Bildsten L., 2003, ArXiv Astrophysics e-prints

Strohmayer T. E., Mushotzky R. F., 2003, *ApJL*, 586, L61

Tanaka Y., Shibazaki N., 1996, *ARA&A*, 34, 607

Terashima Y., Wilson A. S., 2004, *ApJ*, 601, 735

Thim F., Tammann G. A., Saha A., Dolphin A., Sandage A., Tolstoy E., Labhardt L., 2003, *ApJ*, 590, 256

Thorsett S. E., Arzoumanian Z., McKinnon M. M., Taylor J. H., 1993, *ApJL*, 405, L29

Tongue T., Graham M., Stanley M., Truesdell L., Westpfahl D., Mikuz H., 1994, *IAU Circular*, 5990, 2

Trinchieri G., Fabbiano G., Romaine S., 1990, *ApJ*, 356, 110

Turner J. L., Ho P. T. P., 1994, *ApJ*, 421, 122

van Paradijs J., 1998, in Buccheri R., van Paradijs J., Alpar A., eds, NATO ASIC Proc. 515: The Many Faces of Neutron Stars. Neutron Stars and Black Holes in X-Ray Binaries. pp 279–+

van Speybroeck L., Epstein A., Forman W., Giacconi R., Jones C., Liller W., Smarr L., 1979, *ApJL*, 234, L45

van Zee L., Salzer J. J., Haynes M. P., O'Donoghue A. A., Balonek T. J., 1998, *AJ*, 116, 2805

Wang Q. D., Immler S., Pietsch W., 1999, *ApJ*, 523, 121

Ward M. J., Wilson A. S., Penston M. V., Elvis M., Maccacaro T., Tritton K. P., 1978, *ApJ*, 223, 788

Watson M. G., Stanger V., Griffiths R. E., 1984, *ApJ*, 286, 144

Webster B. L., Martin W. L., Feast M. W., Andrews P. J., 1972, Nature Physical Science, 240, 183

White Nargase Parmar 1995, The Properties of X-ray Binaries. pp 1–+

White N. E., Carpenter G. F., 1978, *MNRAS*, 183, 11P

Wilkes B., Kilgard R., Kim D.-W., Kim M., Polletta M., Lonsdale C., Smith H., Owen F., Franschini A., Surace J., 2005, American Astronomical Society Meeting Abstracts, 207,

Wu K., Tennant A., 2001, in Two Years of Science with Chandra, Abstracts from the Symposium held in Washington, DC, 5-7 September, 2001, meeting abstract. Luminosity function of X-ray binaries in nearby galaxies

Yokogawa J., Imanishi K., Tsujimoto M., Nishiuchi M., Koyama K., Nagase F., Corbet R. H. D., 2000, *ApJS*, 128, 491

Yun M. S., Ho P. T. P., Lo K. Y., 1993, *ApJL*, 411, L17

Zezas A., Fabbiano G., 2002, *ApJ*, 577, 726

Zezas A., Fabbiano G., Prestwich A., Murray S., Ward M., 2001, in ASP Conf. Ser. 249: The Central Kiloparsec of Starbursts and AGN: The La Palma Connection Chandra Observations of the Stellar Populations and Diffuse Gas in Nearby Galaxies. pp 425–+